Experimentelle Physik

Heavy Ion Collimation at the Large Hadron Collider
- Simulations and Measurements -

Inaugural-Dissertation
zur Erlangung des Doktorgrades
der Naturwissenschaften im Fachbereich Physik
der Mathematisch-Naturwissenschaftlichen Fakultät
der Westfälischen Wilhelms-Universität Münster

vorgelegt von
Pascal Dominik Hermes
aus
Saarlouis

-2016-

Dekan:	Prof. Dr. Christian Weinheimer
Erster Gutachter:	Prof. Dr. Johannes P. Wessels
Zweiter Gutachter:	Dr. John M. Jowett
Tag der mündlichen Prüfung:	
Tag der Promotion:	

Für Julia

Contents

Abstract

The CERN Large Hadron Collider (LHC) stores and collides proton and $^{208}Pb^{82+}$ beams of unprecedented energy and intensity. Thousands of superconducting magnets, operated at 1.9 K, guide the very intense and energetic particle beams, which have a large potential for destruction. This implies the demand for a multi-stage collimation system to provide protection from beam-induced quenches or even hardware damage. In heavy-ion operation, ion fragments with significant rigidity offsets can still scatter out of the collimation system. When they irradiate the superconducting LHC magnets, the latter risk to quench (lose their superconducting property). These secondary collimation losses can potentially impose a limitation for the stored heavy-ion beam energy. Therefore, their distribution in the LHC needs to be understood by sophisticated simulations. Such simulation tools must accurately simulate the particle motion of many different nuclides in the magnetic LHC lattice and simulate their interaction with the collimators. Previous simulation tools used simplified models for the simulation of particle-matter interaction and showed discrepancies compared to the measured loss patterns. This thesis describes the development and application of improved heavy-ion collimation simulation tools. Two different approaches are presented to provide these functionalities. In the first presented tool, called STIER, fragmentation at the primary collimator is simulated with the Monte-Carlo event generator FLUKA. The ion fragments scattered out of the primary collimator are subsequently tracked as protons with ion-equivalent rigidities in the existing proton tracking tool SixTrack. This approach was used to prepare the collimator settings for the 2015 LHC heavy-ion run and its predictions allowed reducing undesired losses. More accurate simulation results are obtained with the second presented simulation tool, in which SixTrack is extended to track arbitrary heavy ions. This new tracking tool, called hiSixTrack, is actively coupled to FLUKA to simulate the interaction of heavy ions with matter. The new software is used to study the collimation performance for future LHC configurations. The simulation results are combined with experimental input from a quench test experiment to deduce potential intensity limitations and define required upgrades of the collimation system for High Luminosity LHC.

1. Introduction

The CERN[1] Large Hadron Collider (LHC) [B$^+$04b] is the world's largest particle accelerator, capable of storing proton and $^{208}Pb^{82+}$ beams at an unprecedented energy[2] of 7 Z TeV. In the seven years after starting its operation, the LHC has continuously demonstrated to be a powerful scientific tool which produced unrivaled luminosities for the four main detectors ATLAS [Col08b], ALICE [Col08a], CMS [Col08c] and LHCb [Col08d]. The most outstanding scientific achievement so far is the discovery of the Higgs boson, announced in 2012 [Col12a, Col12b].

After the Intersecting Storage Rings (ISR) [JJ84] and the Relativistic Heavy Ion Collider [H$^+$03], the LHC is the third heavy ion collider that was ever built and operated. Approximately one month per operational year is dedicated to heavy-ion operation with $^{208}Pb^{82+}$ beams. One of the main aims of the LHC heavy-ion program is the study of the quark gluon plasma (QGP), a state of matter hypothesized in quantum chromo-dynamics (QCD) which is believed to have existed shortly after the big bang [SSS10]. The QGP is classified by a deconfinement of the quarks, which is expected to occur at extreme temperatures and densities. The experimental investigation of the QGP could hence deliver important evidence to validate or disprove current theories about the evolution of the early universe. Furthermore, a deeper understanding of QCD is expected from these experiments. The energy required to reproduce these extreme conditions can be deliberated in collisions of heavy nuclei at relativistic energies.

Thousands of superconducting magnets, cooled with liquid helium, are used to guide and focus the very rigid LHC beams. In order to achieve the ambitious target luminosity, the LHC stores proton beams of a total beam energy of 362 MJ, which has never been achieved before. This corresponds to the energy required to melt 300 kg of copper. A tiny fraction of this energy is sufficient to damage the LHC hardware if it is instantaneously deposited [Bra09]. An even smaller fraction can make the superconducting LHC magnets lose their superconductivity (magnet quench). During operation, particle losses are omnipresent because several processes diffuse the beam particles to large amplitudes. This implies the demand for a collimation system to protect the machine hardware from uncontrolled beam loss [B$^+$04b].

[1] European Organization for Nuclear Research

[2] Z is the particle charge number.

The LHC collimation system consists of approximately 100 movable absorbers with the aim of intercepting particles at amplitudes far from the main beam axis [B$^+$04b, A$^+$06]. The collimation system has proven to be very efficient for proton operation, in which only a tiny fraction of the energy lost in the collimators is lost in superconducting magnets. For heavy-ion beams, the system is less efficient, because interactions of heavy ions with the collimator materials can lead to fragmentation into other isotopes. These ion fragments with different magnetic rigidity can scatter out of the collimators and continue moving towards the superconducting magnets. The latter act as a spectrometer and deviate the fragments into their aperture. The particles scattered out of the collimation system can hence cause a magnet quench. This scenario is undesired, because it interrupts the operation by the time the magnet requires to recover.

If the origin of potentially dangerous losses is known, they can possibly be mitigated by appropriate countermeasures. Therefore, it is important to have sophisticated simulation tools which can anticipate the locations in the accelerator that are exposed to large amounts of collimation losses. Such tools are also used to define the requirements for collimation system upgrades in future operation with higher beam intensities. So far, tools to simulate heavy-ion collimation used approximations which led to discrepancies compared to the measured loss distributions.

In this thesis, the development, benchmarking and application of improved heavy-ion collimation simulation tools is presented. Two different types of simulations are required to accurately predict the loss distribution of the residual heavy-ion fragments scattered out of the collimators. First, the interaction of beam particles with the collimator materials must be simulated. Secondly, the particle motion of the ion fragments through the accelerator magnets, possibly over many turns, must be accurately computed. The loss locations are then predicted by comparing the particle amplitudes to the dimension of the beam pipe.

In a first approach, the particle-matter interaction with the primary collimator (which is exposed to the highest amount of losses) is simulated with the simulation tool FLUKA [FSFR05, B$^+$14b]. The motion of the ion fragments scattered out of this collimator is subsequently simulated with SixTrack [Sch94, TJ94, RD$^+$05a, Tam14], an existing tool to simulate proton motion particle accelerators. The mass to charge ratio of the individual heavy ions is incorporated into the momentum of the tracked protons, to obtain proton rigidities equivalent to the heavy ions. This framework, referred to as SixTrack with ion-equivalent rigidities (STIER), shows a better agreement with the measured loss patterns than previous simulation tools. Shortly after its introduction in late 2014, it became the standard simulation tool for heavy-ion collimation at CERN. In the 2015 LHC heavy-ion run, predictions made by STIER were experimentally confirmed.

The next generation tool heavy-ion SixTrack (hiSixTrack) was developed as a successor of STIER, to further enhance the agreement with the measurements. hiSixTrack was developed with the aim of accurately predicting the motion of arbitrary heavy-ion species in the accelerator magnets. The fragmentation into lighter heavy ions is simulated by an active coupling to the Monte-Carlo event generator FLUKA. This integrated framework for heavy-ion collimation simulation is referred to as the hiSixTrack-FLUKA coupling. It is deployed to simulate the collimation performance for the future High Luminosity LHC (HL-LHC). The results of these simulations are combined with experimental data from a quench experiment to derive possible intensity limitations for HL-LHC and define required collimation system upgrades.

In the next chapter, the theoretical background for the understanding of particle motion in the LHC is presented. The LHC and its collimation system are presented in Chap. 3. Simulation tools important for the development of the hiSixTrack-FLUKA coupling are introduced in Chap. 4. Measurements of heavy-ion collimation losses are presented and compared to simulations with the previous standard tool in Chap. 5. The new simulation tool STIER is presented and benchmarked in Chap. 6. The further improved tracking tool hiSixTrack and its coupling to FLUKA are described and benchmarked in Chap. 7. In Chap. 8, STIER is applied to the LHC configuration in the 2015 heavy-ion run to evaluate the collimation performance and to develop mitigation strategies for critical losses. Also, collimation simulations of HL-LHC with and without potential collimator upgrades are presented in this chapter. They are carried out with the hiSixTrack-FLUKA coupling. In the following Chap. 9, the LHC heavy-ion collimation quench test conducted in 2015 is presented and analyzed. The hiSixTrack-FLUKA coupling is applied to simulate the loss distribution during the quench test and to define performance limitations for HL-LHC. An outlook on potential future upgrades of the hiSixTrack-FLUKA coupling is given in Chap. 10. In the final chapter, the content of the thesis is summarized.

2. Particle Accelerator Physics

Particles in the magnetic lattice of high-energy synchrotrons like the LHC perform quasi-harmonic transverse oscillations around a reference trajectory. Furthermore, the accelerating devices lead to longitudinal oscillations. Obviously, these types of particle motion are important for the description of the collimation system and the simulation of particle motion for residual particles created in it. In this chapter, the theoretical background to quantify the transverse and longitudinal motion is briefly introduced. Since the new simulation tool to be developed aims for the tracking of multiple different isotopes, the magnetic bending is quantified for different isotopes in the first section of this chapter. The second section quantifies the transverse quasi-harmonic oscillations of beam particles in a lattice of bending and focusing magnets. The last section describes the longitudinal particle motion.

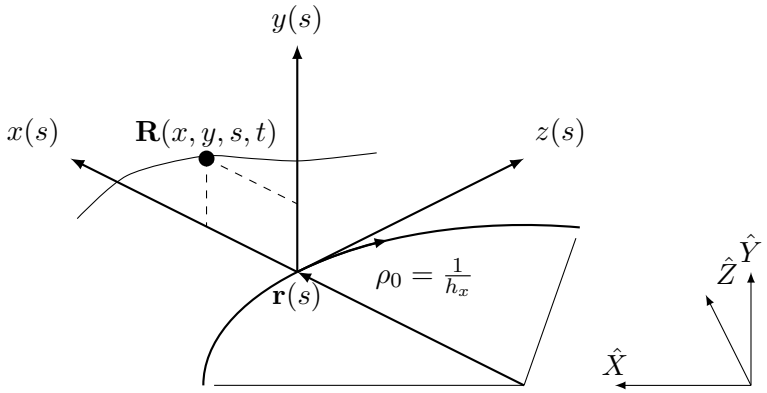

Figure 2.1: Accelerator coordinate system (x, y, z) moving with $\mathbf{r}(s)$. The radius of the bent trajectory is $\rho_0 = \frac{1}{h_x}$. Figure taken from [DMFF15].

2.1 Particle Dynamics in Electromagnetic Fields

2.1.1 Reference Frame

Particle beams in circular accelerators are bent by means of magnetic dipole fields. With the design of the machine, a closed reference trajectory is defined. Typically the ideal trajectory goes through the center of the beam pipes and magnets. This trajectory corresponds to the orbit of a particle at design momentum without transverse offsets, which is referred to as the reference (or ideal) particle.

The position of the reference particle in a curvilinear reference frame of curvature $h_x = \frac{1}{\rho_0}$, where ρ_0 is the bending radius, is defined as $\mathbf{r}(s)$ with the parametrization s. The latter is the distance the reference particle has traveled from a reference point. The position $\mathbf{R}(s)$ of an arbitrary particle can then be defined as

$$\mathbf{R}(x, y, z, s) = \mathbf{r}(s) + x\,\mathbf{e}_x + y\,\mathbf{e}_y + z\,\mathbf{e}_z\,, \tag{2.1}$$

where $\mathbf{r}(s)$ now serves as a support vector defining the origin of the moving coordinate system spanned by the unitary vectors $\mathbf{e}_x(s)$, $\mathbf{e}_y(s)$ and $\mathbf{e}_z(s)$ as shown in Fig. 2.1. Usually, the magnetic bending fields are aligned with y, such that the bending force acts in the horizontal plane x.

2.1.2 Magnetic Bending of Charged Particles

In the upcoming sections, the motion of heavy ions with mass and charge unmatched to the magnetic lattice of the accelerator shall be accurately described. For particles of the main beam species (mono-isotopic case), dispersive effects arise only from momentum offsets. For particles of other species, additional dispersive offsets are caused by the different mass and charge with respect to the reference isotope. In this section, basic definitions are introduced to quantify the rigidity offset of heavy ions with respect to the main beam. In Chap. 7.2, they shall be used to derive the equations of motion and thereupon transfer maps for the individual accelerator elements.

General Case

The accelerator lattice is designed to provide bending and focusing fields for a reference particle of a defined particle species. Consider a heavy-ion accelerator with magnetic fields matched to the reference species

$${}^{A_0}X_0^{(Z_0-n_{e,0})+}\,, \tag{2.2}$$

where X_0 is the element name, A_0 is the number of nucleons, $Z_0 = q_0/e$ is the nuclear charge multiplicity and $n_{e,0}$ is the number of electrons attached to the ion. Furthermore, m_0 is defined as the rest mass of this heavy ion. Here and in the following, quantities sub-scripted with zero refer to the reference particle. We want to describe the magnetic bending of an arbitrary ion, which is not necessarily of the same species as the reference particle:

$$ {}^{A}X^{(Z-n_e)+} \,. \tag{2.3}$$

The rest mass of this ion shall be given as m. Charged particles moving in electromagnetic fields are subject to the Lorentz force [Gri13]

$$ \mathbf{F} = q\,(\mathbf{E} + \mathbf{v} \times \mathbf{B})\,, \tag{2.4}$$

where q is the particle charge, $\mathbf{E}$ is the electric field vector, $\mathbf{v}$ is the particle velocity vector, and $\mathbf{B}$ is the magnetic field vector. In absence of an electric field, the Lorentz force becomes purely transverse and the interplay between the centrifugal force and the Lorentz force bends the particle trajectory by a certain radius ρ, defined by [Wie99]

$$ B\rho = \frac{P}{q}\,. \tag{2.5}$$

Here, P is the particle momentum and $B\rho$ is referred to as the magnetic rigidity. The relativistic particle momentum and energy can be expressed as

$$ P = m\,\beta\,\gamma\,c\,, \quad \text{and} \quad E = m\,\gamma\,c^2\,, \tag{2.6}$$

where $\beta = \frac{v}{c}$ is the particle speed normalized by the speed of light c and the Lorentz factor is defined as $\gamma = \frac{1}{\sqrt{1-\beta^2}}$. Following Eq. (2.5), the design rigidity can be expressed in terms of the momentum per rest mass $\bar{p}_0 = P_0/m_0 = \beta_0\,\gamma_0\,c$ of the reference particle:

$$ B\rho_0 = \frac{P_0}{q_0} = \frac{m_0\,\bar{p}_0}{Z_0\,e}\,. \tag{2.7}$$

The rigidity of an arbitrary ion with a different momentum per rest mass $\bar{p}_i = \bar{p}_0 + \Delta\bar{p}$ can then be expressed in the generic way

$$ B\rho = \frac{m\,(\bar{p}_0 + \Delta\bar{p})}{Z\,e}\,. \tag{2.8}$$

Merging these two equations and applying elementary transformations, the contributions from velocity offset and the mass to charge ratio with respect to that of the reference isotope can be

separated into two different factors. The rigidity of an arbitrary ion can then be expressed in terms of the rigidity $B\rho_0$ of the reference particle as

$$B\rho = \frac{m}{m_0}\frac{q_0}{q} B\rho_0 \left(1 + \frac{\bar{p} - \bar{p}_0}{\bar{p}_0}\right) = B\rho_0 \frac{(1+\delta)}{\chi} . \tag{2.9}$$

Apparently, $\frac{(1+\delta)}{\chi}$ is the offset in rigidity relative to the main beam. The quantities χ and δ are independent from each other and define the dispersive offset a particle acquires in the magnetic accelerator lattice. Following Eq. (2.9), the relative momentum per mass offset δ can be expressed in terms of the full ion momenta or the relativistic $\beta\gamma$ as

$$\delta = \frac{P\frac{m_0}{m} - P_0}{P_0} = \frac{\bar{p} - \bar{p}_0}{\bar{p}_0} = \frac{\beta\gamma - \beta_0\gamma_0}{\beta_0\gamma_0} . \tag{2.10}$$

In the latter expression the dependence of the ion masses is fully eliminated so it is a pure function of the particle velocity. The relative mass to charge offset χ scales with the mass to charge ratio relative to the reference species, defined as

$$\chi = \frac{q}{q_0}\frac{m_0}{m} . \tag{2.11}$$

An alternative way to derive the relation described in Eq. (2.9) is by considering the ratio of the rigidities defined in Eq. (2.7) and Eq. (2.5):

$$\frac{B\rho}{B\rho_0} = \frac{P}{P_0}\frac{q_0}{q} = \frac{q_0}{q}\frac{m}{m_0}\frac{\beta\gamma}{\beta_0\gamma_0} = \frac{(1+\delta)}{\chi} . \tag{2.12}$$

Both δ and χ shall become the fundamental quantities in the description of multi-isotopic particle motion, presented in Chap. 7.2. The rigidity of an ion with $\chi \neq 1$ and arbitrary δ is identical to that of an ion of the reference species ($\chi = 1$) having an effective momentum offset

$$\delta_{\text{eff}} = \frac{(1+\delta)}{\chi} - 1 . \tag{2.13}$$

Hence, the motion of an arbitrary ion with momentum offset δ and mass/charge offset χ in a magnetic field is identical to that of a particle of the reference species with the momentum offset δ_{eff}. This relation will be of importance in Chap. 6.

Mono-Isotopic Case

The mono-isotopic scenario (all particles are of the same species as the reference isotope) is the standard case which is discussed in literature (see [Wie99, Lee12]). The mono-isotopic equations are obtained from the generic multi-isotopic relations by the following substitutions

$$m \to m_0, \qquad q \to q_0, \qquad \chi \to 1\,. \tag{2.14}$$

In this case, Eq. (2.10) yields the standard expression used in literature

$$\delta = \frac{P - P_0}{P_0} = \frac{\beta\gamma - \beta_0\gamma_0}{\beta_0\gamma_0}\,. \tag{2.15}$$

Note that the latter expression remains unchanged, so δ is always a pure function of the particle velocity, which can be drawn back to the velocity dependence of the Lorentz force. Furthermore, the quantity δ is also a relative momentum offset in the mono-isotopic case and a relative momentum per mass offset if multiple ion types are present.

2.2 Linear Transverse Dynamics

The particle beams in a high-energy synchrotron are guided and focused by means of dedicated magnetic fields of different multipole orders. The magnets are assembled to a beam line to guide the beam on the foreseen trajectory and to confine its transverse dimensions. An example of a short section in the region IR1 of the beam line of the CERN Large Hadron Collider (see Chap. 3) is shown in Fig. 2.2. In this subsection, a brief overview of the functionality of the different beam line elements is given. The equations of transverse particle motion in a lattice of accelerator magnets are described and solved in the next subsection.

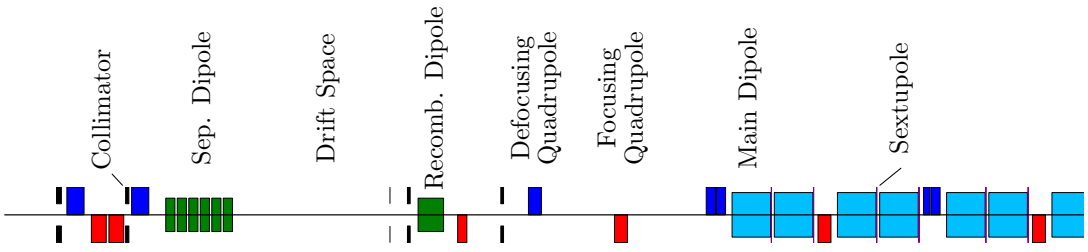

Figure 2.2: Example for a short section of an accelerator beam line. The individual symbols represent different beam line elements which are described on top.

2.2.1 Magnetic Beam Line Elements

Dipole Magnets

Dipole magnets provide uniform transverse magnetic fields to bend the beam orbit. The main dipoles (light blue rectangles in Fig. 2.2) provide the bending force to keep the beams on a circular trajectory.

If the beam orbit differs from the ideal orbit, it can be corrected with correction (kicker) magnets. Compared to the main dipoles, the reference trajectory in the kicker magnets is not bent, thus $h_x = 0$. Also the crossing angle and the separation bumps are created by kicker magnets.

Close to the experiments, where the beams collide, the two counter-rotating beams have to be guided from separated beam pipes into a common beam pipe. The recombination and separation dipoles serve this purpose. In the beam line plot they are shown as green rectangles.

Quadrupole Magnets

Quadrupole magnets (see Fig. 2.3) are used to provide focusing in order to confine the transverse dimensions of the particle beams. The magnetic field strength in a quadrupole increases linearly with the transverse distance from the quadrupole center, as described by

$$B_y = g\,x\,, \quad \text{and} \quad B_x = -g\,y\,. \tag{2.16}$$

The magnetic field gradient g, measured in T/m, defines the strength of the quadrupole. The quantity g is often expressed normalized by the rigidity, which is referred to as the focusing strength k with the unit m^{-2}

$$k = \frac{q_0}{P_0}\,g\,. \tag{2.17}$$

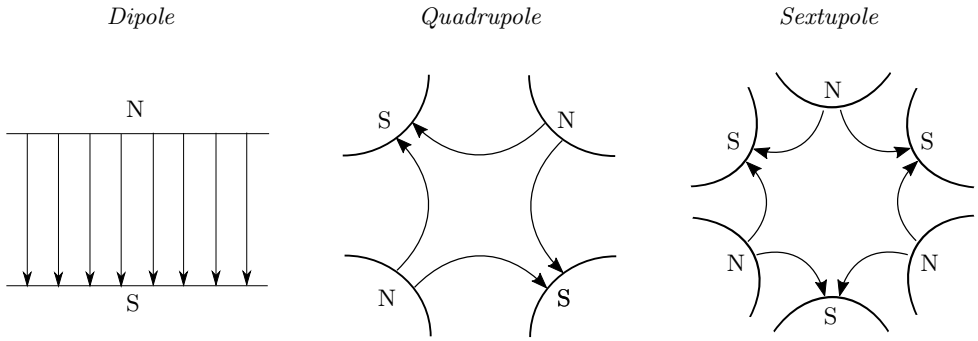

Figure 2.3: Schematic illustration of the magnetic field lines in different magnet types.

If a particle is not moving through the center of the quadrupole it is subject to a transverse force which is focusing (directed towards the ideal trajectory) in one transverse direction and defocusing in the other. Therefore, the effective confinement of the beam dimensions in both transverse directions requires multiple quadrupole magnets which are arranged in a specific manner. Given that the ideal particle is not exposed to a magnetic field, the reference trajectory in a quadrupole is straight and $h_x = 0$.

Sextupole Magnets

The Lorentz force depends on the magnetic rigidity of the particle traversing the magnetic field. Thus, the focal length of a quadrupole magnet depends on the particle momentum, so the guidance of the optical lattice becomes momentum dependent. In circular accelerators this momentum dependence, together with an inevitable spread in momentum between the beam particles, can lead to instabilities and resonances. They are compensated by means of sextupole magnets, with a cross-section shown on the right hand side of Fig. 2.3. Sextupoles are shown in the beam line plot as pink rectangles.

2.2.2 Equation of Motion

General Solution

The transverse motion can be described in leading order by expanding the magnetic dipole and quadrupole fields and considering the equation of motion in the approximation of small x, y and δ [Lee12]. Higher orders are ignored in this approach. The resulting equation of motion for the case of $\chi = 1$ in horizontal direction[1] is given by:

$$x'' - \left(k(s) - h_x^2(s)\right) x = \delta\, h_x(s)\,, \tag{2.18}$$

where $x' = \frac{\mathrm{d}x}{\mathrm{d}s}$. The general solution of the homogeneous part of this equation is described by

$$\begin{pmatrix} x \\ x' \end{pmatrix} = \begin{pmatrix} C_x(s) & S_x(s) \\ C_x'(s) & S_x'(s) \end{pmatrix} \begin{pmatrix} x_0 \\ x_0' \end{pmatrix}\,, \tag{2.19}$$

[1] This chapter refers to the horizontal direction as x. The derivation for y is equivalent with the difference that the reference radius in vertical direction yields $h_x = 0$. Furthermore it should be kept in mind that the quadrupole is always focusing in one and defocusing in the other plane.

where, x_0 and x_0' are the initial conditions and the quantities $S_x(s)$, $C_x(s)$ are defined as

$$S_x(s) = \frac{1}{\sqrt{K}} \sin\left(\sqrt{K}\, s\right) \qquad \text{and} \quad C_x(s) = \cos\left(\sqrt{K}\, s\right) \qquad \text{for } K > 0\,, \tag{2.20}$$

$$S_x(s) = \frac{1}{\sqrt{-K}} \sinh\left(\sqrt{-K}\, s\right) \quad \text{and} \quad C_x(s) = \cosh\left(\sqrt{-K}\, s\right) \quad \text{for } K < 0\,, \tag{2.21}$$

using the substitution $K(s) = -k(s) + h_x^2(s)$. The particle trajectories in any dipoles and quadrupoles are thus either harmonic oscillations or exponential functions depending on the sign of K. A widely used application of the general solution in Eq. (2.19) is the derivation of transfer matrices for the individual beam line elements, defined by their length L and strength K. The particle coordinates x, x' at the end of the beam line element are then related to the coordinates x_0, x_0' at its beginning by means of the matrix multiplication

$$\begin{pmatrix} x \\ x' \end{pmatrix} = \begin{pmatrix} C_x(L) & S_x(L) \\ C_x'(L) & S_x'(L) \end{pmatrix} \begin{pmatrix} x_0 \\ x_0' \end{pmatrix} = \mathcal{M} \begin{pmatrix} x_0 \\ x_0' \end{pmatrix} . \tag{2.22}$$

The transfer matrix $\mathcal{M}$ is specific for every beam line element. The transformation of the particle coordinates by a sequence of beam line elements can be described by a combined matrix obtained by a matrix multiplication of all involved transfer matrices. Using Eq. (2.22), the transfer matrices $\mathcal{M}_D$ of a drift space ($K = 0$), $\mathcal{M}_{Q,f}$ of a focusing quadrupole ($K > 0$) and $\mathcal{M}_{Q,d}$ of a defocusing quadrupole ($K < 0$) yield

$$\mathcal{M}_D = \begin{pmatrix} 1 & L \\ 0 & 1 \end{pmatrix} , \tag{2.23}$$

$$\mathcal{M}_{Q,f} = \begin{pmatrix} \cos\left(\sqrt{K}L\right) & \frac{1}{\sqrt{K}} \sin\left(\sqrt{K}L\right) \\ -\sqrt{K}\, \sin\left(\sqrt{K}L\right) & \cos\left(\sqrt{K}L\right) \end{pmatrix} , \tag{2.24}$$

$$\mathcal{M}_{Q,d} = \begin{pmatrix} \cosh\left(\sqrt{|K|}L\right) & \frac{1}{\sqrt{|K|}} \sinh\left(\sqrt{|K|}L\right) \\ \sqrt{|K|}\, \sinh\left(\sqrt{|K|}L\right) & \cosh\left(\sqrt{|K|}L\right) \end{pmatrix} . \tag{2.25}$$

Thin Lens Approximation

The analytic treatment of the transfer matrices can be significantly simplified if the magnet length L is small compared to $1/KL$. The magnetic bending can then be treated as a point-like transverse kick which is given to the particle at the center of the magnet. In the rest of the element length, the particle trajectory remains undisturbed, hence behaves like a drift space

(see Fig. 2.4). Mathematically, this thin lens approximation [RS95] corresponds to the limit

$$L \to 0 \quad \text{with} \quad K\,L = \text{const.} \tag{2.26}$$

The transfer matrix for a quadrupole magnet simplifies in the thin lens approximation to

$$\mathcal{M}_{Q,f/d} = \begin{pmatrix} 1 & L \\ KL & 1 \end{pmatrix} , \tag{2.27}$$

which is equivalent to the transfer matrix of a thin optical lens with focal length $f = \frac{1}{KL}$.

Periodic Solution and Betatron Motion

An alternative to the solution of the homogeneous part of the equation of motion, given before in matrix form, is given by

$$x(s) = \sqrt{\tilde{\epsilon}_x}\,\sqrt{\beta_x(s)}\,\cos\left(\psi_x(s) + \phi\right) , \tag{2.28}$$

where $\tilde{\epsilon}$ and ϕ are mathematically the integration constants and represent the initial conditions of the particle. The function $\beta_x(s)$ is called the betatron function. The latter is related to the maximum amplitude the particle trajectory can take at the position s.

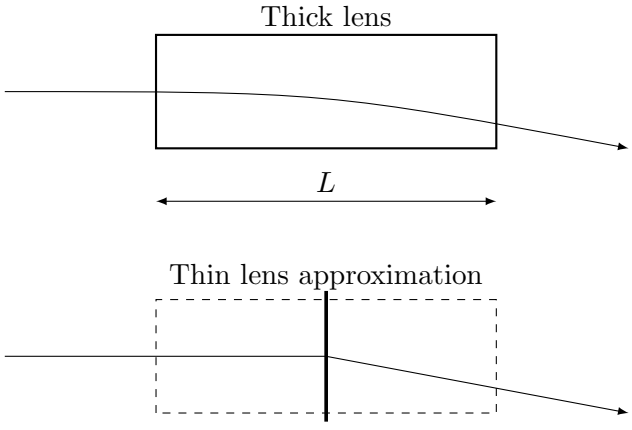

Figure 2.4: Schematic illustration of the thin lens approximation. The transverse bending of a magnet of length L is approximated by a point-like kick the particle receives only at the center of the magnet. Left and right of the magnet center the transverse particle momentum remains unchanged.

In circular accelerators the quantity $K(s)$ is periodic with the same period as the machine circumference C

$$K(s) = K(s + C). \tag{2.29}$$

The equation of motion (2.18) with periodic $K(s)$ is the Hill differential equation [Wie99]. The solution of Hill's equation is identical to Eq. (2.28), but the periodicity implies that also $\beta_x(s)$ is periodic in s with period C

$$\beta_x(s) = \beta_x(s + C)\,. \tag{2.30}$$

The betatron function is purely defined by the magnetic lattice in the accelerator. The particles perform transverse quasi-harmonic oscillations in x, around the ideal trajectory. The local amplitude of these so-called betatron oscillations is defined by $\tilde{\epsilon}_x$, the betatron function $\beta_x(s)$ and the betatron phase $\psi_x(s)$, defined as

$$\psi_x(s) = \int_0^s \frac{\mathrm{d}s}{\beta_x(s)}\,. \tag{2.31}$$

The total number of betatron oscillations over one turn is called the machine tune

$$Q_x = \frac{1}{2\pi}\int_0^C \frac{\mathrm{d}s}{\beta_x(s)}\,. \tag{2.32}$$

From Eq. (2.28) and its derivative, it can be deduced that $\tilde{\epsilon}_x$ is a constant of motion, mathematically the Courant-Snyder invariant, for the individual particle and can be expressed as

$$\tilde{\epsilon}_x = \gamma_x(s)\, x^2(s) + 2\,\alpha_x(s)\, x(s)\, x'(s) + \beta_x(s)\, x'^2(s)\,. \tag{2.33}$$

The quantities $\beta_x(s)$, $\alpha_x(s)$ and $\gamma_x(s)$ are the so-called Twiss parameters [Wie99]. They are defined by the magnetic lattice in the machine which transforms the beam equivalently to a lattice of lenses in classical optics. The Twiss parameters are therefore also referred to as the optical functions, and the configuration of the magnetic lattice as the beam optics.

The derivative of the betatron function $\beta_x(s)$ defines the two remaining Twiss parameters as

$$\alpha_x(s) = -\frac{1}{2}\beta_x'(s) \qquad \gamma_x(s) = \frac{1 + \alpha_x(s)^2}{\beta_x(s)}\,. \tag{2.34}$$

The evolution of an initial set $(\alpha_{x,0}, \beta_{x,0}, \gamma_{x,0})$ of Twiss parameters in the accelerator depends on the lattice elements and is, equivalent to the transformation of the particle coordinates in

Eq. (2.22), described by their transfer matrices as follows

$$\beta_x(s) = C_x^2\,\beta_{x,0} - 2\,S_x^2\,C_x^2\,\alpha_{x,0} + S_x^2\,\gamma_{x,0}\,. \tag{2.35}$$

Furthermore, the expression in Eq. (2.33) is the parametric representation of an ellipse in x, x' enclosing a phase space surface of $\pi\tilde{\epsilon}_x$. Shape and orientation of the phase space ellipse are changing as a function of the Twiss parameters. The surface in phase space that is enclosed by the ellipse remains unchanged if only conservative forces act on the beam particles (Liouville's theorem) [Wie99]. Following Eq. (2.28), the largest possible amplitude in x and x' the individual particle can reach yields (see Fig. 2.6):

$$x_{\max} = \sqrt{\tilde{\epsilon}_x\,\beta_x(s)} \quad \text{and} \quad x'_{\max} = \sqrt{\tilde{\epsilon}_x\,\gamma_x}\,. \tag{2.36}$$

The quantity $x_{\max}$ is hence related to the peak amplitude of the betatron oscillation for a given β-function. If many particles compose the beam, the RMS value of the individual $\tilde{\epsilon}_x$ is referred to as the emittance, which is directly related to the RMS beam size $\sigma_x(s)$:

$$\sigma_x(s) = \sqrt{\epsilon_x\,\beta_x} \quad \text{with} \quad \epsilon_x = \langle\tilde{\epsilon_x}\rangle_{\text{rms}}\,. \tag{2.37}$$

The quantity $\sigma_x(s)$ defines an RMS beam envelope at the position s which contains $1\,\sigma_{\text{rms}}$ of the beam particles. In Fig. 2.5, the betatron motion of particles with different initial conditions within ϵ_x is shown in a periodic lattice of quadrupoles and bending dipoles. It is clearly visible how the individual particle tracks are confined by σ_x.

The emittance is a measure for the beam quality and should be as small as possible. If the particle beam is accelerated, only the longitudinal momentum is increased. It can be shown that the ratio of transverse momentum to longitudinal momentum decreases $\frac{1}{\beta\gamma}$, which is referred to as

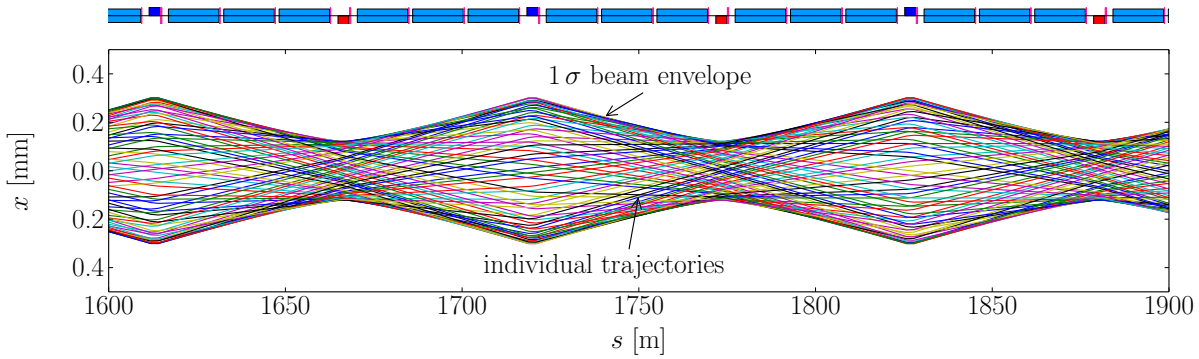

Figure 2.5: Individual particle trajectories in a periodic quadrupole lattice.

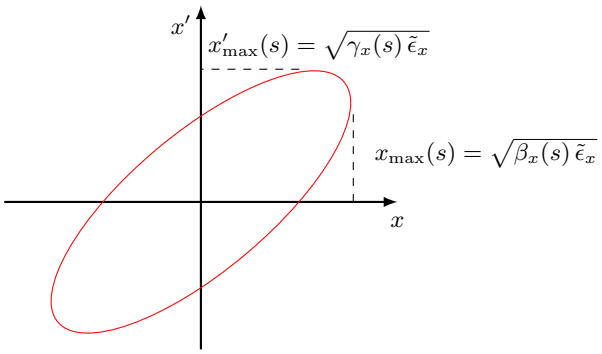

Figure 2.6: Phase space ellipse with $x_{\max}$ and $x'_{\max}$.

adiabatic damping [Wie99]. Consequently, the normalized horizontal emittance is defined as

$$\epsilon_N = \epsilon_x \, \beta\gamma \,, \tag{2.38}$$

and remains constant for all particle energies, assuming that, besides the acceleration, only conservative forces act on the beam. The emittance is measured in units of μm rad.

Solution of the inhomogeneous Equation of Motion

The solution of the inhomogeneous equation of motion Eq. (2.18) can be expressed as

$$x(s) = x_h(s) + x_i(s) \,, \tag{2.39}$$

where $x_h(s)$ is the solution of the homogeneous equation shown in Eq. (2.19) and x_i is one particular solution of the inhomogeneous equation, for example

$$x_i(s) = \bar{D}_x(s)\,\delta \,. \tag{2.40}$$

The dispersion function $\bar{D}_x(s)$ is a periodic function in s with period length C, depending on the magnetic elements in the entire ring. It is defined as

$$\bar{D}_x(s) = -\frac{\beta_x(s)}{2\,\sin(\pi\,Q_x)} \int_{s_0}^{s_0+C} h_x(\tilde{s})\,\sqrt{\beta(\tilde{s})}\,\cos\left[2\pi\,\left(\psi(\tilde{s}) - \psi(s_0) - \frac{Q_x}{s}\right)\right] \mathrm{d}\tilde{s} \,. \tag{2.41}$$

In order to be coherent with the definition in the simulation tools used, in the following the dispersion function will be expressed in terms of $D_x(s)$, defined as

$$D_x(s) = -\bar{D}_x(s) \,. \tag{2.42}$$

As shown in Eq. (2.39), the dispersion function relates the momentum offset of the particle to an additional transverse amplitude. The quantity $D_x(s)\,\delta$ hence gives the closed orbit around which off-momentum particles perform betatron oscillations. For multi-isotopic beams, Eq. (2.42) still applies, but the relative momentum offset is replaced by δ_{eff}.

It is often useful to also define the local dispersion function $\tilde{D}_x(s)$, which quantifies the dispersive offset an off-rigid particle acquires between two defined locations. This becomes important, when the rigidity of a particle changes at a given location and the particle trajectory should be followed from the location at which the rigidity offset was acquired.

Note that this mathematical description represents a linear approximation and higher order dispersive effects are not taken into account. For particles with large momentum offsets, a more accurate description is given by a fully symplectic transformation without truncation, which can be derived from the accelerator Hamiltonian (see Chap. 7.2.1).

2.3 Longitudinal Particle Dynamics

The beams in the LHC are accelerated and longitudinally confined by means of radio frequency cavities (RF cavities) [Wie99]. They consist of a periodic resonator structure (illustrated in Fig. 2.7) and are operated with RF waves and provide a longitudinal electric field $V(t)$ of a defined frequency $\phi_{\text{RF}} = \omega_{\text{RF}}\, t$

$$V(t) = V_0\, \sin(\phi_{\text{RF}} + \phi_s)\,, \tag{2.43}$$

where V_0 is the peak amplitude of the electric field and $\phi_s = \omega_s\, t$ is the phase of the synchronous particle. The frequency of the RF cavity is adapted to the revolution frequency f_{rev} of the synchronous particle, to provide the same accelerating voltage at every turn

$$f_{\text{RF}} = h\, f_{\text{rev}}\,, \tag{2.44}$$

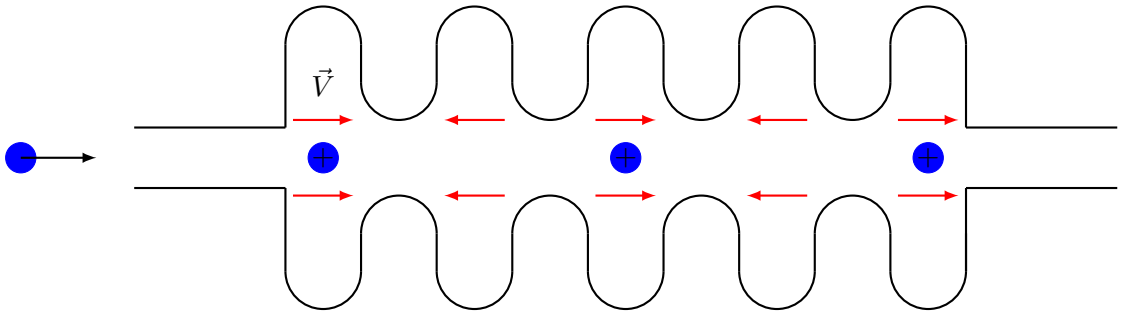

Figure 2.7: Schematic illustration of an accelerating cavity.

where h is the harmonic number. Assuming that $q = q_0$, the energy ΔE transferred to a particle arriving at phase ϕ compared to the phase of the synchronous particle ϕ_s is given by [CAS14]

$$\Delta E = q_0 \, V_0 \, (\sin\phi - \sin\phi_s) \, . \tag{2.45}$$

The phase dependence of the energy transfer leads to a different energetic kick for particles arriving at different times than the synchronous particle. If ϕ_s is correctly chosen, particles with momentum P smaller than the reference momentum P_0 (which arrive with time delay), receive a larger momentum transfer and those with $P > P_0$ receive a smaller momentum transfer than the synchronous particle. This is illustrated in the top plot of Fig. 2.8.

It can be shown [CAS14] that the difference in phase $\Delta\phi = \phi - \phi_s$ with respect to the reference particle obeys the differential equation

$$\frac{\mathrm{d}^2}{\mathrm{d}t^2}\phi + \frac{\Omega_s^2}{\cos\phi_s}(\sin\phi - \sin\phi_s) = 0 \quad \text{with} \quad \Omega_s^2 = \frac{h\,\eta\,\omega_{\mathrm{rs}}\,q_0\,V_0\,\cos\phi_s}{C\,P_0} \, . \tag{2.46}$$

Here, h is the harmonic number, $\eta = \frac{\Delta\omega_{\mathrm{r}}/\omega_{\mathrm{rs}}}{\Delta P/P_0}$ is the slip factor which quantifies the change in revolution frequency implied by a change in momentum, ω_{rs} is the revolution frequency of the synchronous particle and C is the circumference of the machine.

For small phase deviations $\Delta\phi_s$, the expression in Eq. (2.46) can be simplified to [CAS14]

$$\frac{\mathrm{d}^2}{\mathrm{d}t^2}\phi + \Omega_s^2\,\Delta\phi = 0 \, , \tag{2.47}$$

which describes a harmonic oscillation (the so-called synchrotron oscillation) in P and ϕ, with frequency Ω_s. Stability of the longitudinal motion implies that $\Omega_s^2 > 0$, which is the case when $\eta\cos\phi > 0$, as illustrated in Fig. 2.8.

Stable and unstable regions in the $\phi, \Delta P/P_0$ plane are separated by the so-called separatrix, which defines the largest amplitude in ϕ, $\frac{\Delta P}{P_0}$ that is compatible with stable synchrotron oscillations. The region inside the separatrix is called RF bucket.

By virtue of the periodicity of the electric field in the RF cavity, multiple buckets are available to store particles in the machine. The concrete number of buckets is determined by the harmonic number. Thus, the accelerating RF cavities imply a bunching of the particle beam.

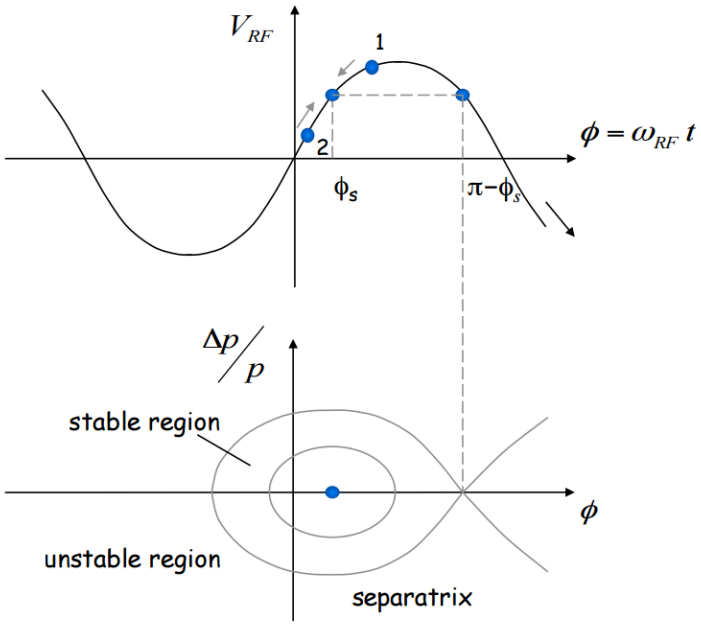

Figure 2.8: Top panel: longitudinal electric field V as a function of the particle phase ϕ. Particles with $P < P_0$ which arrive later than the reference particle (1) receive a larger energy transfer. Accordingly, particles arriving before the reference particle (2) receive a smaller energetic kick. The particles perform an oscillation in the $\phi, \frac{\Delta P}{P_0}$-plane (bottom panel). The stable region in $\phi, \Delta P/P_0$ is defined by a separatrix. Figure courtesy of [CAS14].

3. The Large Hadron Collider

The Large Hadron Collider (LHC) is the world's largest particle accelerator, designed to store and accelerate proton and $^{208}Pb^{82+}$ beams at unprecedented energies of $7\,Z$ TeV. The LHC is a synchrotron of 26.7 km length, installed in the underground tunnel built for the Large Electron Positron Collider (LEP) at the CERN[1] research center near to Geneva, Switzerland. With the Relativistic Heavy-Ion Collider (RHIC) at the Brookhaven National Laboratory and the former CERN Intersecting Storage Rings (ISR) [JJ84], it is one of the three heavy-ion colliders ever built and operated [FJ14]. In the first operational period (Run 1), the LHC reached energies up to $4\,Z$ TeV with proton and $^{208}Pb^{82+}$ beams. With the collected data, the discovery of the long sought Higgs boson was announced in July 2012 [Col12a, Col12b]. After a phase of machine and detector upgrades from 2013 to 2015, the LHC restarted into Run 2 and accelerated proton beams to the unprecedented energy of 6.5 TeV and $^{208}Pb^{82+}$ beams to $6.37\,Z$ TeV.

In this chapter the LHC is presented with the sub-systems relevant for the development of heavy-ion collimation simulation tools presented later-on. Particular emphasis is given to the LHC collimation system and the interaction of particles with the collimator material, which has an important influence on the efficiency of the collimation system.

3.1 The CERN Accelerator Complex

The LHC is a high-energy synchrotron operated at the end of a complex chain of injectors which pre-accelerate and prepare the beam for its requirements. The ensemble of accelerators currently operated at CERN is referred to as the CERN accelerator complex. It is schematically illustrated in Fig. 3.1.

The LHC injector chain starts with two different ion sources, respectively delivering proton or heavy-ion beams. The generation of proton beam starts at a hydrogen ion source feeding the linear accelerator LINAC2, in which the proton beam is accelerated to a momentum[2] of 50 MeV

[1] Centre Européen pour la Recherche Nucléaire.

[2] For clarity, in this chapter the momentum is given in natural units. All given momenta shall correspond to the correct unit of eV/c. Furthermore, the energies for the non fully stripped ions are given in terms of momentum per nucleon, while for the fully stripped ions, the general convention of using the momentum per charge is followed.

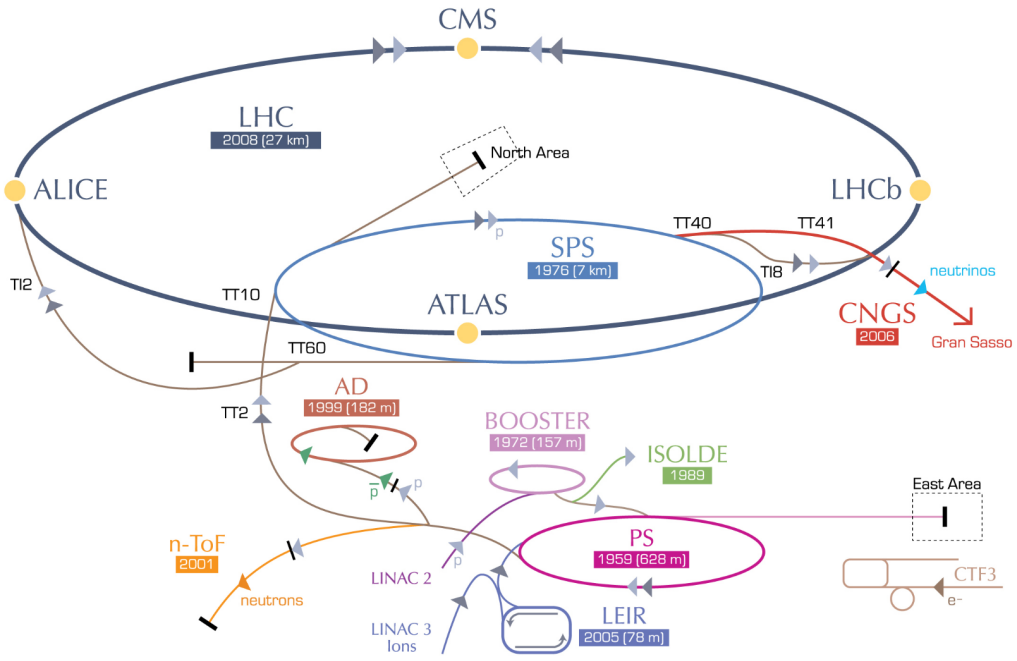

Figure 3.1: The CERN Accelerator Complex [Lef08].

and injected into the Proton Synchrotron Booster (PSB). This synchrotron accelerates the beam to 1.4 GeV, the injection energy of the Proton Synchrotron (PS) which provides acceleration up to 25 GeV. After the subsequent injection into the Super Proton Synchrotron (SPS), the beams are brought to 450 GeV, the injection energy of the LHC [B+04b].

Heavy-ion beams start from the ion source upstream of the linear accelerator LINAC3. The ions are generated from a block of lead, enriched with the isotope ^{208}Pb, by means of an Electron Cyclotron Resonance Source [B+04b]. The source delivers ions at a momentum of 2.5 keV/A, which are sent to a spectrometer in order to extract the desired Pb^{27+} charge state. After the filtering, a multi-stage RF system accelerates the selected ion species to a momentum of 4.2 MeV/A. The following 300 nm thick stripper foil removes more electrons, such that an ion beam of Pb^{53+} is extracted from LINAC3 and transferred to the circular accelerator LEIR (Low Energy Ion Ring). In the latter, the ion beams are cooled, e.g. the transverse emittance is reduced by an adiabatic process using electron scattering. In parallel, the beam is accelerated to a momentum of 72 keV/A at which it is extracted and transferred into the PS. In this machine, the ion bunches are re-shaped, accelerated to a momentum of 5.9 GeV/A and finally sent to the SPS. Another stripper foil in the transfer line between PS and SPS removes the remaining electrons, such that the ion arriving at the SPS is $^{208}Pb^{82+}$. The SPS provides the acceleration to the energy of 450 Z GeV at which the beams are injected into the LHC [B+04b].

3.2 LHC Design and Performance

3.2.1 Global Layout

The global LHC layout is illustrated in Fig. 3.2. The LHC houses eight straight sections (also called insertion regions, IR). Four of them host the main experiments ATLAS [Col08b], ALICE [Col08a], CMS [Col08c] and LHCb [Col08d]. The remaining four IRs provide operational functionalities, namely betatron and momentum cleaning in IR3 and IR7 (see Chap. 3.4), acceleration in IR4 and the beam dump in IR6. The straight insertion regions are separated by the LHC arc regions. In the latter, a periodic array of superconducting dipole magnets and superconducting quadrupole magnets provides the guiding and focusing forces required to transport the beam between the IRs.

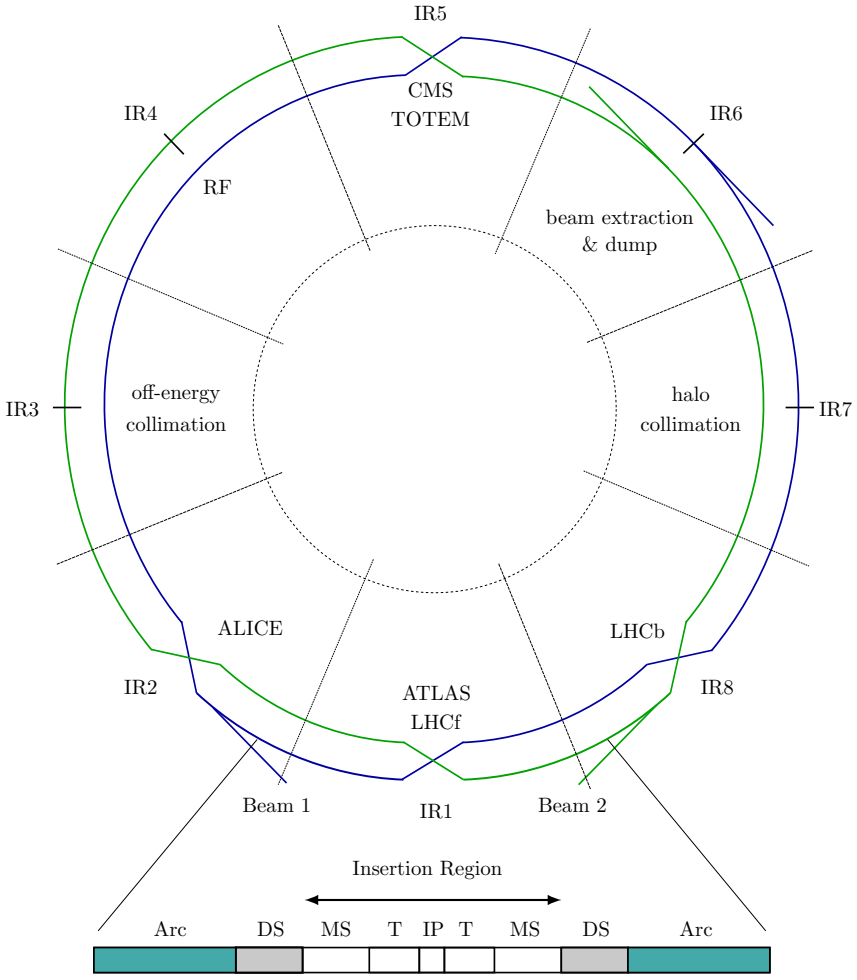

Figure 3.2: The layout of the LHC. Based upon [BBM12, B$^+$04b].

3.2.2 Naming Conventions

The two counter-rotating LHC beams are called Beam 1 (B1), which circulates in clockwise direction and Beam 2 (B2), which circulates in counter-clockwise direction. The position s in the LHC is measured from IP1 in clockwise direction.

Each element of the LHC is associated with a cell number, indicating the number of quadrupoles between the closest IP and the respective location. For example the name MQY.4L5.B1 denotes a quadrupole of the MQY type (see [B$^+$04b]) in cell 4 left of IP5 for Beam 1.

3.2.3 Optics and Insertion Region Layout

The schematic layout of the experimental insertion regions is shown together with the β functions in Fig. 3.3. Downstream of the main arcs (1) in which the beams are transported between the IRs, the dispersion suppressor (DS) region (2) serves the purpose of reducing the periodic dispersion function. This is reached by means of a missing dipole structure, in which one of the three dipoles of the regular arc lattice is omitted [B$^+$04b]. In between the surrounding DS regions, the IR is free of the main dipoles and therefore straight. After the DS, the matching section (3) adjusts the β functions to the requirements of the following sections. The separation/recombination dipoles (4) and (5) guide the beams from the separated beam pipes into a common beam pipe. The superconducting triplet magnets (6) provide the final focusing for the interaction point (7) (IP), where the beams are brought into collision.

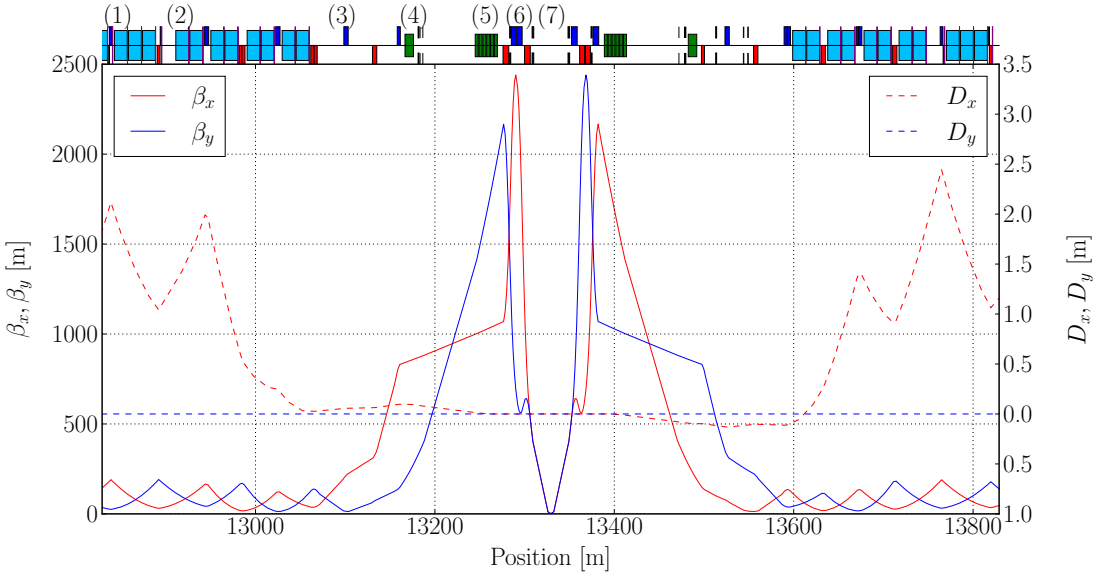

Figure 3.3: Optical functions of B1 at the experimental insertion IR5 with $\beta^* = 1\,\mathrm{m}$ for a flat machine (no separation or crossing bump).

Table 3.1: Minimum β^* values in LHC operation compared to the design values.

Configuration	Species	β^* [m] IP1/IP5	β^* [m] IP2	β^* [m] IP8	Energy [Z TeV]
Design	p	0.55	10.0	10.0	7.0
2011	p	1.0	10.0	3.0	3.5
2012	p	0.6	10.0	3.0	4.0
2015	p	0.8	10.0	3.0	6.5
2016	p	0.4	10.0	3.0	6.5
Design	Pb	0.5	0.5	10.0	7.0
2011	Pb	1.0	1.0	3.0	3.5
2013	p-Pb	0.8	0.8	2.0	4.0
2015	Pb	0.8	0.8	3.0	6.37

The experiments ATLAS and CMS demand for the highest possible luminosity in order to gain enough statistics for the study of rare processes (see Chap. 3.2.5). As discussed later, the luminosity is inversely proportional to the β value at the IP (denoted as β^*), thus the optics is optimized to minimize the β^* value. Following Liouville's theorem, small β functions imply a large divergence (large α function) at the IP and, due to the absence of magnets between IP and triplet, the β functions (and associated with it the beam size) at the superconducting triplets increase with smaller β^*. The dimensions of the triplet aperture therefore impose a lower limit on the achievable β^*. The transition to the smallest β^* settings (referred to as squeeze) is performed either at top energy or during the last part of the energy ramp (see Chap. 3.2.6), because the beam sizes decrease with energy due to the adiabatic damping. At injection energy, the optics in IR1 and IR5 are set to $\beta^* = 11\,\mathrm{m}$ while IP2 and IP8 are set to $\beta^* = 10\,\mathrm{m}$. A summary of the minimum β^* values achieved at top energy during the past LHC runs is given in Table 3.1.

In the central part of the experimental insertions, both beams are moving in a common vacuum pipe to bring them into collision at the IP. In order to avoid unwanted collisions of the counter-rotating beams, a separation bump is applied when collisions are not supposed to occur. In addition, a crossing angle avoids secondary collisions at parasitic bunch encounters when the beams are brought into collision. The crossing and separation bumps in the high luminosity insertions are orthogonal to each other. Both bumps are shown for the example of IR5 in Fig. 3.4. The IRs without experiments are not equipped with triplet magnets and the optics is adjusted for the purpose of the installed hardware. The layout, functionality and optics of the collimation insertion regions are discussed in Chap. 3.4.

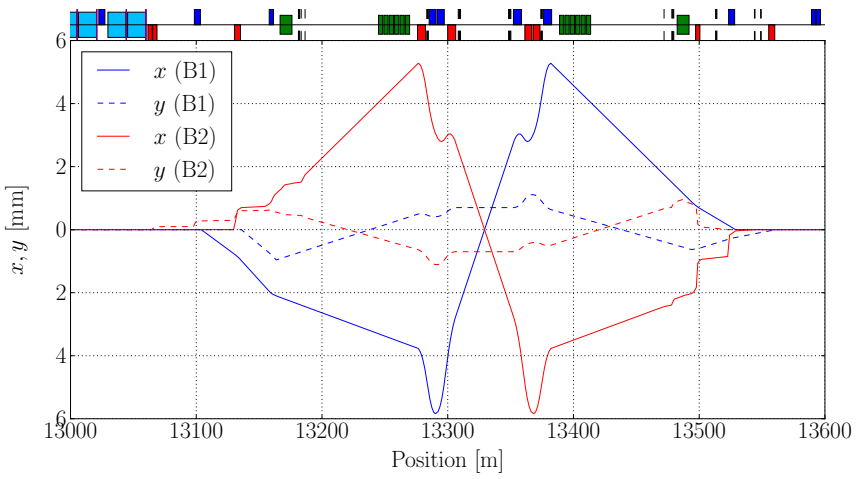

Figure 3.4: Separation and crossing bumps in IR5 during the 2011 heavy-ion run with $\beta^* = 1\,\mathrm{m}$.

3.2.4 Operational Cycle

The LHC operational cycle is a defined protocol which ensures safe operation and avoids uncertainties of the magnetic fields which could possibly arise from hysteresis. In Fig. 3.5, the LHC cycle is illustrated for an ideal $^{208}\mathrm{Pb}^{82+}$ physics fill in the 2015 heavy-ion run.

In the *injection* mode (1) at a beam energy of 450 Z GeV, the machine is ready to receive particle bunches from the injectors. The beams are not squeezed in this configuration, to obey the tight aperture restrictions. The optics in the injection insertions IR2 and IR8 are designed to optimize the phase advance between the injection septum the injection protection collimators.

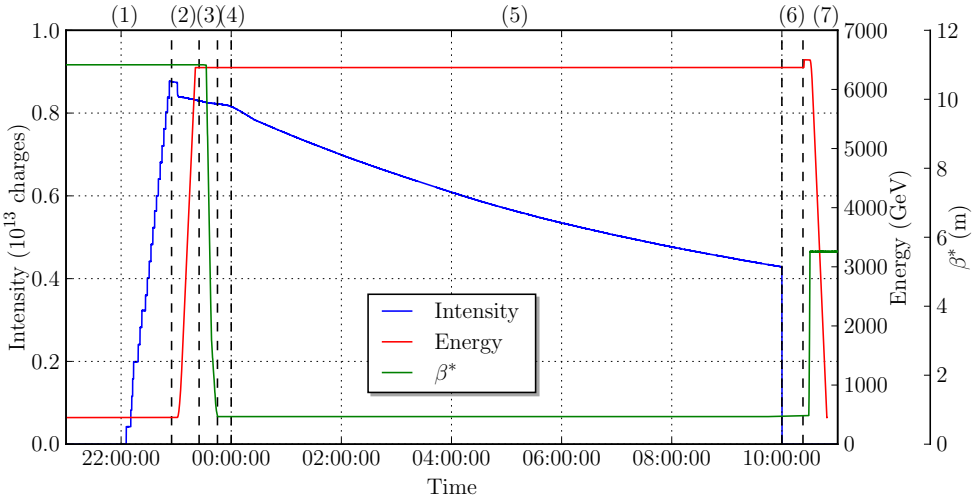

Figure 3.5: Beam energy, intensity and β^* during the LHC cycle.

Once the LHC is filled with beam, the mode is changed to *prepare ramp* (2), in which the injection protection collimators are retracted to allow for the following *ramp* (3), the acceleration to top energy. During the ramp, power converters, RF and collimators are synchronously adjusted to follow the beam energy and the decreasing beam size.

After the ramp, the *squeeze* (4) is a stepwise optical sequence in which the β^* value in the high luminosity IRs is smoothly reduced to the final value for collision. Finally, the beam mode changes to *adjust* (5), in which the separation bump is collapsed and small additional bumps are introduced to correct for deviations in the closed orbit and maximize the luminosity in the experiments. Once the collisions in the experimental IRs are established, the beam mode is referred to as *stable beams* (6). The stable beam mode is maintained for several hours until the luminosity has decreased below a certain level. Then the beams are intentionally dumped (7). The magnet currents are then reduced (*ramp down*, (7)) to a level below the injection level to eliminate hysteresis effects before the following injection mode. Note that for heavy-ion operation in 2015, the last part of the cycle was carried over from the previous proton run in which the protons had larger rigidities. The ramp down therefore included an increase of the magnet currents from the operational setting at $6.37\,Z$ TeV to the proton setting at 6.5 TeV.

In 2016, the formerly distinct steps of ramp and squeeze have been merged to reduce the time to set up the stable beams configuration and thus increase the integrated luminosity. This combined ramp and squeeze [R$^+$12b] synchronously accelerates the beams to 6.5 TeV and reduces the β functions at IP1 and IP5 to $\beta^* = 3\,\mathrm{m}$.

3.2.5 Luminosity

An important measure for the performance of a collider is the luminosity. The instantaneous luminosity $\mathcal{L}(t)$ is the proportionality between the cross section σ_p of a physical process and the expected event rate $\frac{\mathrm{d}N_p}{\mathrm{d}t}$ in a given machine configuration [Wie99]:

$$\frac{\mathrm{d}N_p(t)}{\mathrm{d}t} = \mathcal{L}(t)\,\sigma_p\,. \tag{3.1}$$

The luminosity is proportional to the number of bunches n_B, the square of the number of particles per bunch N_B, the revolution frequency in the machine f_{rev}, the relativistic γ and inversely proportional to the β^* value and the normalized emittance[3]:

$$\mathcal{L} = \frac{n_B N_B^2 f_{\mathrm{rev}} \gamma}{4\pi\epsilon_N \beta^*}\,F\,. \tag{3.2}$$

[3]This formula applies for round beams; e.g. when β^* and the emittance ϵ are identical in both planes for both beams.

The additional factor F takes into account for the luminosity reduction due to the fact that the colliding bunches are not fully overlapping when a crossing angle θ_C is applied.

The correction factor depends on the longitudinal RMS beam size σ_l, the transverse beam size at the IP ($\sigma_x = \sigma_y = \sigma^*$) and the crossing angle as follows [Her03]:

$$F = \frac{1}{\sqrt{1 + \left(\frac{\theta_C \, \sigma_l}{2 \, \sigma^*}\right)^2}} \,. \tag{3.3}$$

For heavy-ion collisions, it is important to measure the number of colliding nucleons, rather than nuclei. This is especially true if the collider produces asymmetric collisions (e.g. p-Pb collisions) or if the luminosity with different isotopes should be compared. The nucleon-nucleon luminosity $\mathcal{L}_{\mathrm{NN}}$ is defined as

$$\mathcal{L}_{\mathrm{NN}} = A_1 \, A_2 \, \mathcal{L} \,, \tag{3.4}$$

where A_1 and A_2 are the nuclear mass numbers of the colliding nuclei.

Following Eq. (3.2), the luminosity is measured in the unit $\mathrm{cm}^{-2}\,\mathrm{s}^{-1}$, which corresponds to $10^{24}\,\mathrm{b}^{-1}\,\mathrm{s}^{-1}$. The latter expression in combination with the definition given in Eq. (3.1) elegantly illustrates the dependence of the number of expected events with a given cross section (measured in barns) per time unit. Even more information on the performance of the accelerator can therefore be obtained if the instantaneous luminosity is integrated over the total time T the machine is operated in stable beams. This quantity is referred to as the integrated luminosity:

$$\mathcal{L}^{\mathrm{int}} = \int_0^T \mathcal{L}(t) \, \mathrm{d}t \,. \tag{3.5}$$

Obviously, it is of great interest to maximize the integrated luminosity, in order to allow the study of rare events. This can be done either by increasing the instantaneous luminosity (if not restricted by the experiments) or by optimizing the operational cycle of the machine, to maximize the time the machine can be operated in the stable beams mode.

The instantaneous luminosity can be increased if smaller β^* values are applied, the emittance is reduced, the stored beam intensity is increased or if the luminosity reduction factor is enlarged. While the achievable emittance, number of bunches and bunch intensity depend strongly on the performance of the LHC injectors, the β^* value is imposed to a lower limit due to aperture restrictions in the triplet magnets [BAR15]. The geometrical luminosity reduction factor F could be improved by reducing the crossing angle, which has a lower limit imposed by the long range beam-beam interaction.

3.2.6 LHC Performance in Previous Runs

In this section, the LHC program so far is briefly introduced. The achieved beam parameters in operation with p-p, p-Pb and Pb-Pb are summarized and compared to the design parameters Table 3.2 and Table 3.3.

Proton Beams

The LHC proton program started with the first data taking phase in 2010. In this first operational period the LHC was operated with small beam intensities at 3.5 TeV, half the design energy. With the operational experience gained, the stored beam intensity could be increased by almost one order of magnitude in 2011, and a significant amount of integrated luminosity was collected. The 2012 proton operation was fully dedicated to luminosity production and the integrated luminosity could be doubled with respect to the precedent year. In this year the maximum particle energy was increased to 4 TeV [P$^+$16b].

At the beginning of 2013, the operation of the LHC stopped for long shutdown 1 (LS1), a consolidation and upgrade phase with the main purpose of consolidating the superconducting splices in order to reach proton momenta of 6.5 TeV to 7.0 TeV [B$^+$13a]. After a successful restart in 2015, the LHC was operated at an unprecedented proton energy of 6.5 TeV. In the following year, the LHC operated the first time at nominal luminosity due to the reduced β^* value and increased bunch intensity.

Table 3.2: Comparison of the LHC design beam parameters for proton beams [AF$^+$13, B$^+$16]. The quantity n_B describes the number of bunches, E_s the total stored beam energy and N_B the number of particles per bunch. The data for 2016 is as of July 2016 and may be subject to change.

		Nominal	Achieved in the LHC				
Year			2010	2011	2012	2015	2016
E	[TeV]	7	3.5	3.5	4.0	6.5	6.5
γ		7460.5	3730.3	3730.3	4263.2	6927.6	6927.6
n_B		2808	368	1380	1380	2244	2220
N_B	[10^{11}]	1.15	1.0	1.3	1.5	1.1	1.1
ϵ_N	[μm rad]	3.75	2.6	2.4	2.4	3.5	3.4
E_s	[MJ]	362	23	112	143	277	266
$\mathcal{L}_{\text{peak}}$	[$10^{34}\,\text{cm}^{-2}\,\text{s}^{-1}$]	1.0	0.021	0.35	0.77	0.51	1.2
$\mathcal{L}^{\text{int}}$	[fb^{-1}]		0.0048	5.5	22.8	4.2	8.1

Heavy-Ion Beams

The first LHC run with heavy ions took place in 2010, in which mostly operational experience at 3.5 Z TeV was collected. The second heavy-ion run in late 2011 was carried out at 3.5 Z TeV and delivered half the design luminosity [J$^+$11]. In 2013 a mixed particle mode was established, in which protons were collided with $^{208}Pb^{82+}$ ions at 4 Z TeV [J$^+$13b].

The 2015 operational period with heavy ions started with a reference proton run at 2.51 TeV per beam in order to obtain the same center of mass energy as in the p-Pb run of 2013. For the same reason, the ensuing Pb-Pb operation was carried out at an energy of 6.37 Z TeV, instead of the 6.5 Z TeV which would have been possible after the precedent proton operation at equivalent rigidity [J$^+$16b]. This allows the experiments to compare data at the same center of mass energy for three different collision types: p-p, p-Pb and Pb-Pb. In the 2015 Pb-Pb running period, the LHC exceeded the design value of the stored $^{208}Pb^{82+}$ beam energy more than twice, due to the better-than-nominal performance of the LHC injectors. The bunch intensity has tripled with respect to the design value. This remarkable performance led to an excess of the design luminosity by a factor three [J$^+$16b].

Table 3.3: Comparison of the LHC design beam parameters for heavy-ion beams compared to the values achieved in the previous LHC heavy-ion runs [B$^+$04b, J$^+$13b, J$^+$13a, J$^+$11, J$^+$12]. The parameters given for p-Pb operation refer to the $^{208}Pb^{82+}$ beam. The integrated luminosity is given in terms of nucleon-nucleon encounters [J$^+$16b].

		Nominal	Achieved in the LHC			
Year			2010	2011	2013	2015
Species		Pb-Pb	Pb-Pb	Pb-Pb	p-Pb	Pb-Pb
E	[TeV]	7 Z	3.5 Z	3.5 Z	4.0 Z	6.37 Z
γ		2963.5	1481.8	1481.8	1693.4	2696.8
n_B		592	137	358	338	518
N_B	[10^8]	0.7	1.12	1.20 ± 0.25	1.40 ± 0.27	2.2 ± 0.3
ϵ_N	[μm rad]	1.5	2.0	1.7 ± 0.2	-	1.50 ± 0.15
E_s	[MJ]	3.81	0.71	1.98±0.42	2.18± 0.42	9.54±1.30
$\mathcal{L}_{\text{peak}}$	[10^{27} cm^{-2} s^{-1}]	1 (Pb-Pb) 115(p-Pb)	0.03	0.5	110	3.0
$\mathcal{L}_{\text{NN}}^{\text{int}}$	[pb^{-1}]		0.4	19.9	20.2	76.0

3.2.7 High Luminosity LHC

For the future of the LHC, a drastic increase of the luminosity is foreseen for both proton and heavy-ion operation, to improve the potential for discoveries. The future LHC configuration with increased luminosity is referred to as High Luminosity LHC (HL-LHC) [A$^+$14, BR16].

An essential keystone for this objective is the increase of the bunch intensity and, for heavy ions, the possible number of bunches that can be stored in the machine. This is made possible by the LHC injectors upgrade (LIU) [G$^+$11, M$^+$15], a modification of the injector chain with hardware upgrades and even the replacement of LINAC2 by a new H^- accelerator LINAC4 [M$^+$15]. The schedule to reach the HL-LHC parameters foresees a stepwise luminosity increase in which double of the design luminosity shall be reached after LS2 in 2020 [BR16].

The current baseline envisages the commissioning of the High Luminosity LHC (HL-LHC) adapted for a peak luminosity with proton beams more than seven times the LHC design value as of 2025. To allow for this increase, extensive hardware upgrades in IR1 and IR5 are required, one of them being the installation of crab cavities [A$^+$14]. Furthermore, the replacement of several magnets is required. The inner magnets in IR1 and IR5 (including the triplet magnets, separation/recombination dipoles and Q4 and Q5) are replaced by new magnets with a larger aperture to allow for smaller β^* values [A$^+$14]. Presently, it is foreseen to apply $\beta^* = 0.15\,\text{cm}$ for protons and $\beta^* = 0.48\,\text{m}$ for heavy-ion beams in IR1 and IR5. Further upgrades concern the LHC collimation system, which is discussed in Chap. 8.3.1.

Optimistic estimates for the heavy-ion beam parameters after the LIU and HL-LHC upgrade are compared to the design values and those achieved in 2015 in Table 3.4.

Table 3.4: Comparison of heavy-ion beam parameters: design parameters [B$^+$04b], achieved in the 2015 heavy-ion run, envisaged parameters for LIU and HL-LHC [Jow16]. The baseline for the heavy-ion species is $^{208}Pb^{82+}$ for all cases.

	E [Z TeV]	n_B	ϵ_N μm rad	N_B [10^7 ions]	E_s [MJ]
Design	7.0	592	3.75	7	3.81
2015	6.37	518	1.5±0.15	22±3	9.54±1.30
LIU baseline	7.0	1152	1.2	17	18.0
HL-LHC request	7.0	1248	1.3	21	24.1

3.3 The LHC Magnets

Many different types of magnets provide the guiding and confining forces required for the operation of the LHC. Except the magnets in the inner part of the experimental insertions, where the two beams are brought into collision, the LHC magnets are double-bore magnets in which both beams circulate in separated beam pipes, as shown in Fig. 3.6. In this section, the superconducting LHC main dipoles and quadrupoles are briefly introduced and their superconducting properties are discussed. The risk of beam induced quenches (transition from superconducting to normal conducting state) for these magnets is one of the motivations for the LHC collimation system explained in the following section. More detailed information can be found in [B$^+$04b].

3.3.1 Main Dipoles

The 1232 superconducting LHC main dipoles (MB) are horizontal bending magnets of 14.3 m magnetic length, capable of delivering a maximum magnetic field of 8.3 T. They are designed to provide a bending radius of $\rho_0 = \frac{1}{h_x} = 2804$ m, yielding a maximum particle energy of 7 Z TeV. To keep the NbTi coils in a superconducting state, they are cooled with liquid helium to be operated at a temperature of 1.9 K. More information on the superconducting LHC dipoles can be found in [B$^+$04b].

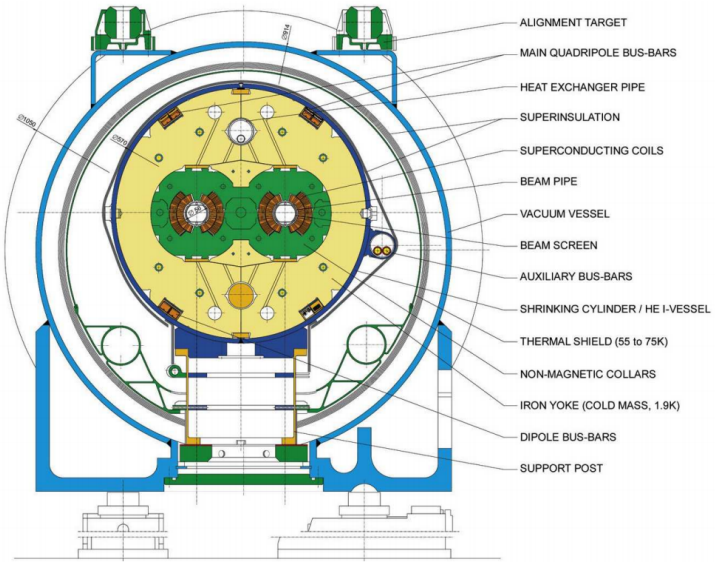

Figure 3.6: Cross section of the LHC double bore main dipole magnet [Duv01].

3.3.2 Quadrupoles

The LHC is equipped with many different quadrupoles to provide the focusing required to confine the beams in the LHC arcs and prepare their optical functions for the collision in the IPs. Depending on their purpose, they are normal or superconducting (and hence can provide different field gradients), have different lengths and provide various bore diameters depending on the local aperture requirements [B$^+$04b].

The beam transport from IR to IR in the LHC arc regions is provided by a structure of 392 alternating focusing and defocusing quadrupoles, which are referred to as the main quadrupoles (MQ). Their maximum magnetic field gradient is 223 T/m. The superconducting quadrupoles in the matching section of the experimental insertions are of five different types which are summarized in [B$^+$04b]. The superconducting triplet magnets MQXA and MQXB provide the final focusing for the experiment with a maximum magnetic field gradient of 215 T/m.

3.3.3 Quench Limit

The superconducting LHC magnets are type-II superconductors [Tin04]. Their superconducting state can be maintained if the temperature T, the applied magnetic field B and the current density J in the NbTi coils fulfill certain conditions. This can be described by a critical surface in the (T, B, J)-space underneath of which the magnet is superconducting [Iwa09].

For a given set of two parameters, a critical value for the third parameter can be found at which the magnet changes from its superconducting to the normal conducting state (quench). As shown in Fig. 3.7, the critical temperature for a LHC magnet operated at 9 T and a current density of 1.5 to 2.0 kA/mm^2 is 1.9 K, compared to 4.2 K at $B = 5$ T [BC07]. The critical temperature is hence higher if lower magnetic fields are applied.

The superconducting LHC magnets are sensitive to beam losses on their coils. They can quench if the energy deposited by impacting beam particles and their secondary showers exceeds a defined threshold. This threshold is referred to as the quench limit. Typically, three different time regimes of losses are distinguished, depending on the time scale τ_L at which they occur [A$^+$15]:

- Short duration: $50\,\mu\text{s} > \tau_L$,
- Intermediate duration: $50\,\mu\text{s} < \tau_L < 5\,\text{s}$,
- Steady state losses: $\tau_L > 5\,\text{s}$.

For every time scale of losses different physical mechanisms are relevant for the quench risk. They are explained in detail in [A$^+$15]. For short and intermediate duration losses, the quench limit is measured in terms of the minimum quench energy density (MQED) in units of mJ/cm^3.

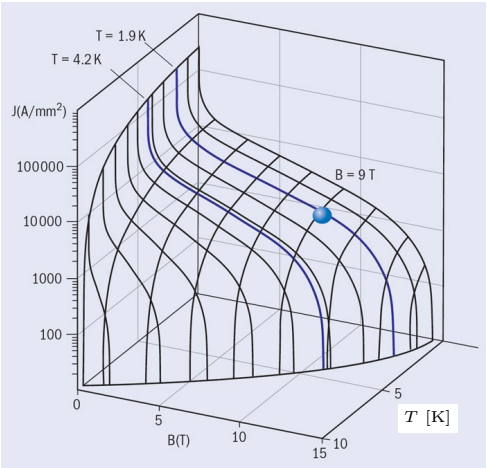

Figure 3.7: Critical surface of the superconducting NbTi coils used for the superconducting LHC magnets operated at 1.9 K [Sie13].

The energy deposited from steady state losses is effectively reduced by heat transfer of the superfluid helium, such that the quench limit is rather quantified by the minimum quench power density (MQPD) in terms of mW/cm^3 [J$^+$96, A$^+$15]. The dependence of these quantities on the loss duration is illustrated in Fig. 3.8.

Quenches interrupt the operation of the LHC and are therefore undesired. In 2015, three beam-induced quenches have occurred in standard proton operation of the LHC, all caused by UFO events [P$^+$16a]. So far, no quench has yet been induced by circulating beam losses in physics operation, even with the large stored beam energies achieved in 2016. With the envisaged higher stored beam intensities, beam-induced quenches might become a serious issue for the interrupted operation of the LHC.

Two beam-induced quenches have occurred with heavy-ion beams in 2015 during dedicated quench tests. They are described in detail in [S$^+$15a] and Chap. 9.

Table 3.5: Quench limit estimates for steady state losses at 7 TeV for the LHC main dipoles.

Author	Reference	MQPD [mW/cm^3]	Year
Schaumann *et al.*	[S$^+$15a]	13	2016
Auchmann *et al.*	[A$^+$15]	27-49	2015
Granieri *et al.*	[GvW14]	47-49	2014
Bocian *et al.*	[BDS09]	12	2008
Jeanneret *et al.*	[J$^+$96]	5	1996

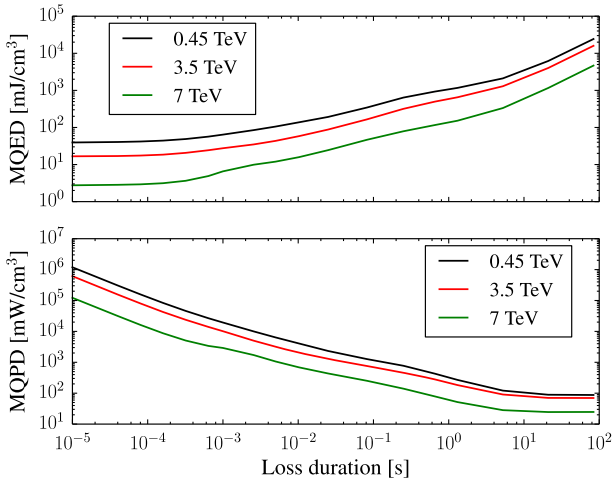

Figure 3.8: Simulated quench limits of LHC main dipoles for different loss durations (courtesy of [A$^+$15]).

Reliable predictions of beam intensity limitations due to the risk of quenches require accurate estimates of the quench limit. Theoretically, these are not easy to access, because the effective heat transfer to the superconducting coils depends on the loss scenario, the coil geometry, the type of insulation, heat capacities, the rate at which the superfluid helium can remove thermal energy from the coils and many more [S$^+$13a]. Accordingly, the estimated quench limits are associated to rather large uncertainties and have changed drastically over time when improved simulation models became available and by taking into account experimental data from quench tests. An incomplete summary of the temporal evolution of the estimated quench limits in the MB coils at 7 TeV is given in Table 3.5.

3.4 The LHC Collimation System

At design momentum and intensity, the LHC will store protons of a combined energy of 362 MJ per circulating beam. This corresponds to the energy deliberated in an explosion of 78 kg of TNT and is more than two orders of magnitude larger than the stored beam energy achieved in previous particle accelerators [B+04b, A+06] (see Fig. 3.9).

Uncontrolled deposition of the beam energy into the machine equipment can cause severe hardware damage and even tiny fractions of the LHC beams can cause magnet quenches. On the other hand, a variety of physical processes inevitably scatters particles to large transverse amplitudes out of the beam core, and they risk to be lost in the aperture of the superconducting magnets. To intercept these particles and remove them from the beam in a safe and controlled manner, the LHC is equipped with a multi-stage collimation system. The collimation system consists of approximately 100 absorbers which are adjusted around the circulating beams.

This section describes the design and functionality of the LHC collimation system. Particles can still scatter out of the collimators and be absorbed in superconducting LHC magnets. Definitions to quantify this cleaning inefficiency are introduced in this chapter.

Protons interact differently with the material of the collimators than heavy ions. The heavy-ion-matter interactions lead to fragmentation into other isotopes with rigidities very different from the main beam. As it shall be shown in Chap. 6.1, this is the reason why the cleaning performance for heavy-ion beams is worse than for proton beams. It is hence important to understand interactions of particles with the material of the collimators. A brief description of these processes is given at the end of this section.

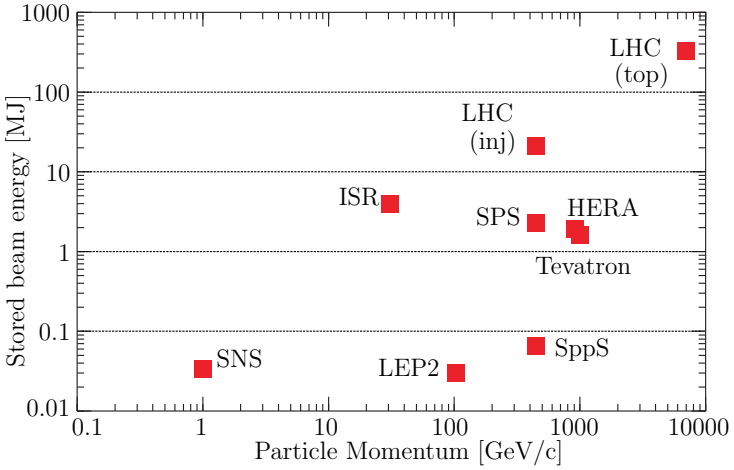

Figure 3.9: Design particle momentum and stored beam energy in different particle accelerators. Figure taken from [A+06].

3.4.1 Particle Losses in the LHC

Beam particles are subject to a wide range of physical processes that increase their betatron amplitudes or change their momenta, ultimately bringing them outside of the acceptance of the beam pipes. Important processes driving particle losses in the LHC are [Lam05]:

- Intrabeam scattering [Piw74, MB83],
- Scattering of colliding particles at the interaction point,
- Orbit instabilities or optics changes with associated resonance crossing,
- Feedback noise,
- Scattering on residual gas molecules,
- Longitudinal drifts out of the RF bucket,
- Energy loss due to synchrotron radiation,
- Abnormal losses due to hardware failure. These include losses from injection failures [S$^+$07] and asynchronous beam dump [A$^+$02b].

The particles driven to large betatron or momentum amplitudes by the mentioned processes compose a transverse and longitudinal beam halo, which is continuously repopulated during operation. The rate at which particles of the main beam are lost is quantified by the beam lifetime τ, representing the time at which the beam intensity[4] $N(t)$ has dropped to $1/e$ of its initial value N_0 [B$^+$04b]:

$$N(t) = N_0 \exp\left(-\frac{t}{\tau}\right) . \tag{3.6}$$

The instantaneous loss rate $R_L = -\frac{\mathrm{d}N(t)}{\mathrm{d}t}$ is related to the beam life time (which is in general time dependent) as follows:

$$\tau(t) = \frac{N(t)}{R_L(t)} . \tag{3.7}$$

3.4.2 Collimation Requirements and System Layout

Typical good lifetime values are of the order of hours, but operationally the lifetime can often drop below 1 h. The corresponding loss rates are in the order of some 100 kW. This value is

[4] The total number of beam particles.

orders of magnitude above the quench limits introduced above. The LHC can therefore not be operated without a collimation system, even at injection energy.

Very robust collimators are required to withstand the impact of the intense bunches with highly energetic particles. On the other hand, the required robustness implies a sufficiently low density of the material with the inevitable consequence of a reduced absorption rate for the beam particles. Therefore, the LHC collimation system is designed as a multi-stage system with different collimation stages to effectively absorb the beam halo.

The LHC collimators consist of two movable jaws which are adjusted around the beam which passes in between. An example for a collimator jaw and the assembly in a collimator tank is shown in Fig. 3.10. The different types of collimators are presented in Chap. 3.4.3.

The functionality of the LHC collimation system is schematically illustrated at the example of the betatron cleaning insertion IR7 in Fig. 3.11. Primary collimators (Target Collimator Primary, TCP) serve the purpose of intercepting the primary beam halo (particles of the main beam which are at large amplitudes). In IR7, a horizontal, a vertical and a skew TCP provide betatron cleaning in all transverse planes. The TCPs define the global aperture bottleneck and are the collimators closest to the main beam [B$^+$04b]. In order to provide enough robustness to withstand a large power load of impacting protons, the active material of the TCPs is a dedicated carbon-fiber composite (CFC) [B$^+$04b]. They can withstand a maximum power load $P_{max} = 487\,\text{kW}$ over 10 s. At the design energy of 7 TeV [A$^+$02a], this corresponds to a minimum allowed beam life time of $\tau_{\text{min}} = 720\,\text{s}$.

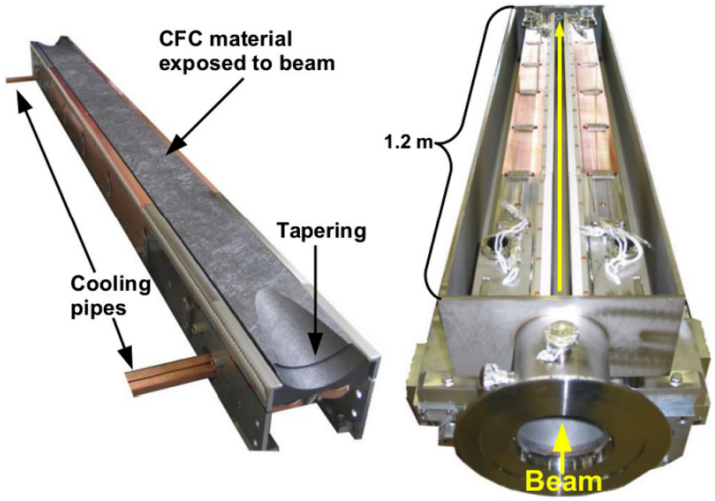

Figure 3.10: Left: Jaw of a secondary collimator. The collimators are water cooled through the copper pipes. Right: Two collimator jaws installed in a collimator tank. Courtesy of [B$^+$14d].

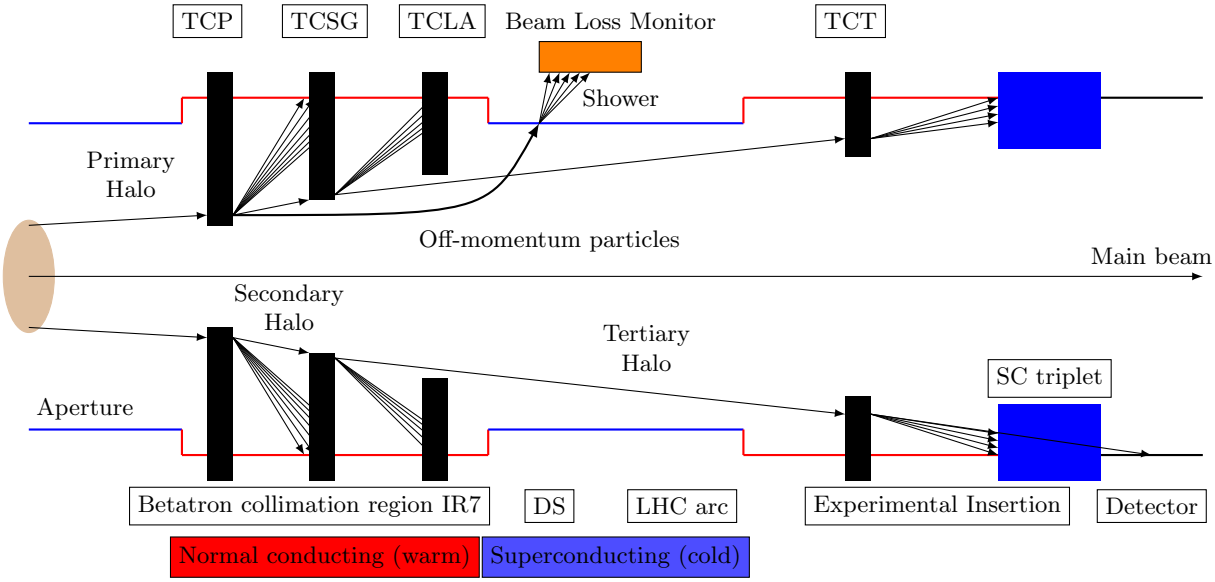

Figure 3.11: Schematic overview of the LHC multi stage collimation system. Based on [Red13].

The multi-stage approach relies upon the particle scattering to even larger amplitudes at their passage through the TCP. When a halo particle is sufficiently scattered, it is intercepted by the secondary graphite collimators (Target Collimator Secondary Graphite, TCSG).

The TCSG collimators are retracted with respect to the TCP. They should only be exposed to the secondary beam halo of particles scattered out of the TCP, which carries significantly less energy than the primary beam halo. Downstream of the TCSG collimators, shower absorbers (Target Collimator Long Absorber, TCLA) are installed. They shall protect the superconducting magnets downstream of the collimation IRs from the hadronic and electromagnetic showers generated at the TCSG collimators. They intercept also parts of the tertiary beam halo which can still leave the TCSG collimators and continue moving inside the machine.

When particles are scattered out of the TCP at an insufficient angle to be intercepted by the TCSGs, they can continue moving into the DS downstream of IR7. In the strong LHC bending dipoles, out-scattered particles can receive large dispersive offsets and intercept the magnet aperture if they have rigidities different from the main beam. Losses from this so-called collimation debris in the IR7 DS are one of the main threats for beam-induced magnet quenches.

In LHC physics operation with squeezed beams, particles of the tertiary beam halo which are not captured by the TCLA collimators are most likely absorbed in the triplet magnets where the betatron functions are extreme [R$^+$12a]. In order to avoid beam losses in the superconducting triplet magnets, tertiary collimators (abb. Target Collimator Tertiary, TCT) are installed to provide local protection. They also reduce undesired background in the experiments [B$^+$13b].

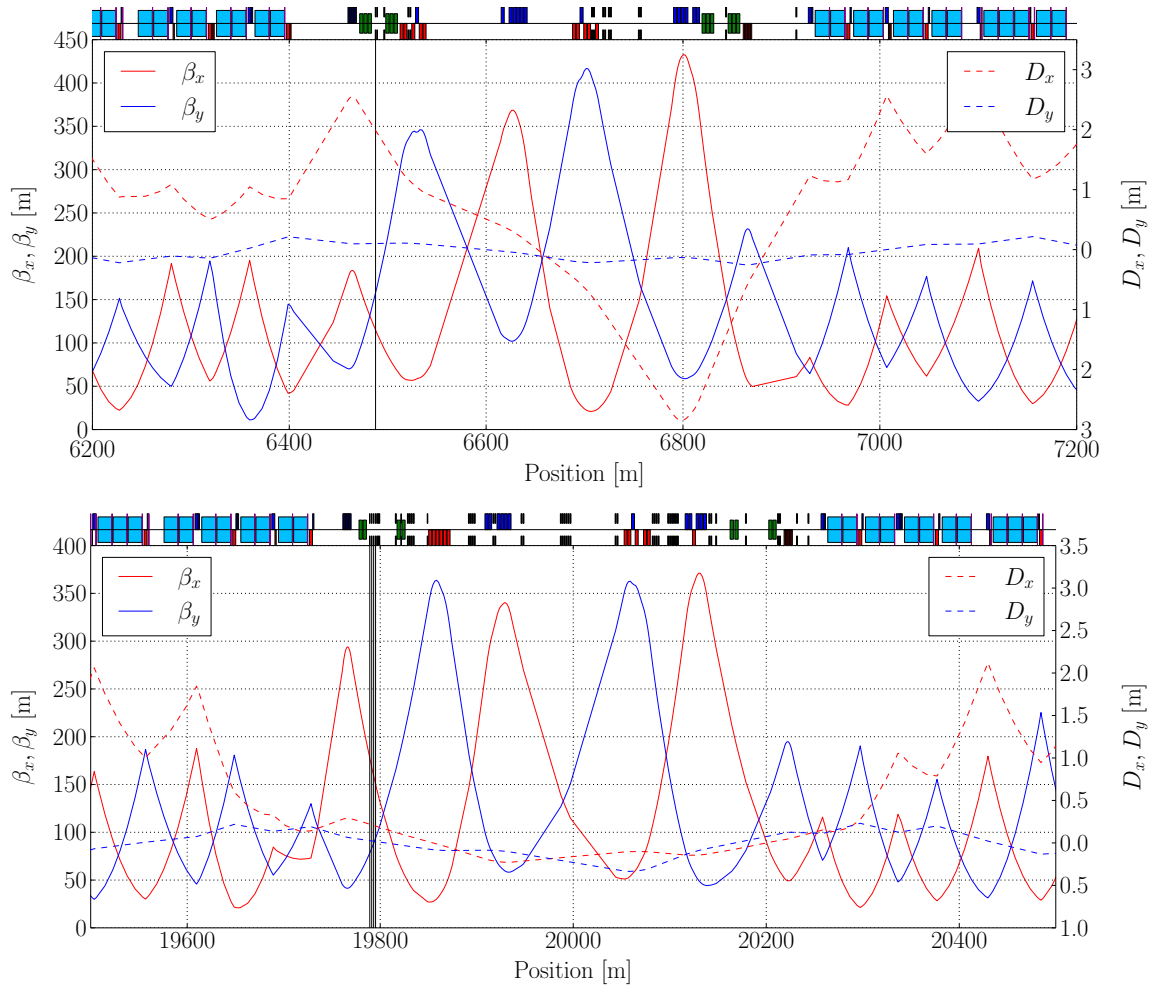

Figure 3.12: Optical functions in the two collimation insertions, IR3 (top) and IR7 (bottom). The vertical black lines represent the locations of the primary collimators

The active material of the TCT collimators is a tungsten heavy alloy, INERMET 180 [Pla16] (IT180), providing a high stopping power.

The optical functions in IR7 are optimized for small dispersion to intercept mostly particles at large betatron amplitudes. The momentum collimation region IR3 defines the global rigidity cut in the LHC and intercepts particles with rigidity offsets beyond this threshold. In this region, the optics is matched for a large horizontal dispersion function to intercept the off-momentum particles with the TCP. Contrary to the betatron cleaning, which is carried out for the horizontal, vertical and the skew plane with one dedicated primary collimator each, the principle of momentum cleaning requires a primary collimator only in the horizontal plane. The optical functions for the two LHC cleaning insertions are compared in Fig. 3.12.

3.4.3 Collimator Types

Besides the presented primary, secondary and tertiary collimators, additional collimators are installed at strategic locations throughout the ring to prevent from particle losses which are invulnerable for the collimators installed in IR3 and IR7. A list of all collimator types, which are also called families, for the present LHC is given in Table 3.6.

In the high luminosity insertions IR1 and IR5, dedicated physics debris collimators (Target collimator long, TCL) are installed to protect the machine from debris created at the collisions in the IP [Ass05]. Those particles may be scattered and/or off-momentum and would otherwise be likely to be lost in the magnets of the experimental insertion.

In case of a beam dump failure, multiple components of the LHC could be seriously damaged, in particular the dumping system, magnets downstream of IP6 or even the detector components in the experimental insertions. Therefore, IR6 is equipped with the single-jaw dump protection collimator TCDQ (Target Collimator Dump Quadruple) and the double-jaw TCSP (Target Collimator Secondary with Pick-up) collimator [Ass05]. The jaw of the TCDQ is composed of graphite. With a length of 9 m it is the longest collimator used in the LHC.

The TDI (Target Dump Injection) collimators installed in the injection insertions IR2 and IR8 provide protection against beam loss from injection failures. They are composed of graphite in a different structure than CFC. The TCLI (Target Collimator Long Injection Protection) collimators are installed downstream of the TDI to protect a larger area in phase space [B$^+$04b].

Table 3.6: Overview of the types (or families) of LHC collimators presently installed in the machine (H,V,S: horizontal, vertical, skew) [B$^+$04b].

Type	Region	Name	Plane	Material	Length [m]
Primary	IR3	TCP	H	CFC	0.6
Secondary	IR3	TCSG	H	CFC	1.0
Shower Absorbers	IR3	TCLA	H,V	IT180	1.0
Primary	IR7	TCP	H,V,S	CFC	0.6
Secondary	IR7	TCSG	H,V,S	CFC	1.0
Shower Absorbers	IR7	TCLA	H,V	IT180	1.0
Tertiary	IR1/2/5/8	TCT	H,V	IT180	1.0
Physics Debris Absorbers	IR1/5	TCL	H	Cu	1.0
Dump Protection	IR6	TCDQ	H	C	9.0
Dump Protection	IR6	TCSP	H	CFC	1.0
Injection Protection	IR2/8	TDI	V	C	4.0
Injection Protection	IR2/8	TCLI/TCLIB	V	CFC	1.0

3.4.4 Collimator Settings and Alignment

The positions of the movable collimator jaws can be individually adjusted. By convention, the collimator openings are given as the half gap between the jaws in units of the normalized RMS beam size σ. The settings in σ are identical for all collimators of a given family and can be adjusted to optimize the collimation efficiency. The settings must obey the following constraints:

- The risk of damaging the machine hardware, including collimators, must be minimized.
- The settings must ensure that the collimation hierarchy[5] is maintained even under realistic drifts of the orbit or optics [A$^+$11b]. This implies a smallest achievable retraction between the TCP and TCS collimators. In operation, this requirement led to the application of larger retractions between TCS and TCP than initially foreseen in the design phase.
- The triplet aperture must always be protected by the tertiary collimators, which imposes a constraint on the largest applicable TCT setting.
- The impedance induced by the collimators can change the tune of the individual particles, which must be taken into account for the collimator settings.
- All tungsten collimators and apertures must be sufficiently retracted from the TCDQ/TCSP to avoid damaging during an asynchronous dump [A$^+$02b].

The normalized beam size is determined using a normalized emittance of $\epsilon_N^p = 3.5\,\mu$m rad for proton beams. This value was chosen instead of the design emittance at top energy of $3.75\,\mu$m rad because the injectors could deliver a significantly better emittance than initially foreseen. This convention furthermore provides simplicity because the same reference emittance applies for the whole cycle and establishes consistency and comparability between the runs.

The collimator setting in terms of the normalized beam size also takes into account the energy dependence of the geometric emittance due to adiabatic damping. In 2015, the half gap of the primary collimator in IR7 was 1.4 mm at top energy. During the ramp, the collimators are synchronously closed follow the beam size which decreases with the beam energy.

The geometrical collimator openings in mm for heavy-ion operation are so far adopted from the respective precedent proton runs. The normalized emittance of heavy-ion beams is significantly smaller than for proton beams, mainly due to the electron cooling in LEIR. In the LHC Design Report [B$^+$04b], a heavy-ion emittance of $\epsilon_N^{\mathrm{Pb}} = 1.5\,\mu$m rad is foreseen, which yields the same geometrical emittance as for proton beams with $\epsilon_N^p = 3.5\,\mu$m rad at the same rigidity.

[5] The collimation hierarchy demands that the highest losses occur at the TCP, followed by the TCSGs etc.
[6] Settings refer to a proton energy of 6.5 TeV.
[7] For design emittance $\epsilon_N = 3.75\,\mu$m rad.

Table 3.7: LHC collimator settings applied with squeezed beams at top energy in the LHC heavy ion runs, compared to the design settings. The settings refer to the beam size of proton beams at equivalent energy with a normalized proton beam emittance of $\epsilon_N = 3.5\,\mu$m rad.

Collimator		Half gap (σ)				
Type	Region	2010	2011	2013	2015[6]	Design[7]
TCP	IR7	5.7	5.7	4.3	5.5	6.0
TCS	IR7	8.5	8.5	6.3	8.0	7.0
TCLA	IR7	17.7	17.7	8.3	14.0	10.0
TCP	IR3	12.0	12.0	12.0	15.0	15.0
TCS	IR3	15.6	15.6	15.6	18.0	18.0
TCLA	IR3	17.6	17.6	17.6	20.0	20.0
TCT	IR1/IR2/IR5	15.0	11.8	9.0	13.7	8.3
TCT	IR8	15.0	11.8	9.0	15.0	8.3
Heavy-ion energy [Z TeV]		3.5	3.5	4.0	6.37	7.0
Proton energy [TeV]		3.5	3.5	4.0	6.5	7.0

An exception is the 2015 heavy-ion run at $6.37\,Z$ TeV, in which the geometrical collimator settings of the previous proton run at 6.5 TeV were adopted. Accordingly, the assumed heavy-ion emittance was $\epsilon_N = 1.41\,\mu$m rad.

The collimator settings applied so far during heavy-ion operation with stable beams are compared to the design values in Table 3.7. These settings differ from the design settings and have been modified over the years. The margins between the TCP and TCSG collimators were chosen to be increased in order to mitigate measured hierarchy violations[8] during proton operation [B$^+$14d]. Starting from the conservative settings applied at the beginning of the LHC operation, the settings were continuously optimized and reset based on operational experience and on the results of dedicated experiments. This includes tightening of the collimator half gaps to allow for smaller β^* values [BAR15].

The reference orbit is not necessarily at the center of the beam pipe aperture. One reason are the crossing and separation bumps in the experimental IRs. Also magnet misalignments which are corrected with the orbit corrector magnets alter the reference orbit.

[8]This applies for proton beams. Based on the measured loss signals in 2011, 2013 and 2015, the cleaning hierarchy with heavy-ion beams is, however, violated. With the smaller beam intensities for heavy ions, this is not considered critical.

At the beginning of every run, all collimators are aligned around the beam center and the collimators are driven back to the found positions in all subsequent physics fills. This procedure relies upon a good reproducibiliy of the machine conditions.

Two major methods are used for the collimator alignment, the first being the beam-based alignment [V$^+$11], in which the beam edge is defined by the TCP and it is ensured that the beam fills the TCP gap by artificial beam excitation (see Chap. 5.1). The jaws of the collimator to be aligned are then moved individually towards the beam, until losses are measured with the beam loss monitors close to the collimator (see Chap. 3.4.7). The second method - in the present configuration only implemented for the TCTs - uses beam position monitors [V$^+$15] which are integrated in the collimator jaws, measuring the beam position and aligning the collimators accordingly.

3.4.5 Particle-Matter Interaction and Collision Effects

It is the interaction with the primary collimator which determines if a particle is scattered into the secondary collimators or if it receives a rigidity offset without being scattered enough and is hence absorbed in the superconducting magnets. The particle-matter interaction is therefore an important keystone in the theoretical understanding of the collimation cleaning performance.

Relativistic particles traversing matter or interacting with counter-rotating beam particles are subject to different types of physical interactions. They can be described on a microscopic scale by the interaction of the moving particle (projectile) with the atoms and/or nuclei (target) of the traversed material or counter-rotating beam particle. An important quantity in the microscopic description of such interactions is the minimum transverse distance of the projected projectile trajectory from the target position, the so-called impact parameter b, illustrated in Fig. 3.13. The types of interactions which can occur are often determined by the impact parameter with respect to the radii of the target R_T and the projectile R_P.

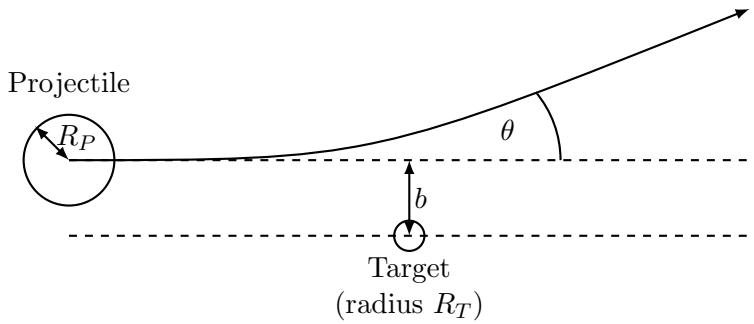

Figure 3.13: Schematic illustration of the impact parameter.

Multiple Coulomb Scattering

Coulomb scattering occurs when the projectile is deviated from its trajectory due to the interaction with the Coulomb field of the atomic nuclei of the material traversed [B+12].

The particle can be repeatedly subject to small angular Coulomb scattering and so accumulate an angular deviation significantly larger than from the individual interactions. This process, referred to as Multiple Coulomb Scattering (MCS), leads to a wide distribution of scattering angles. It can be quantified by the RMS scattering angle $\langle \Delta x'_{\mathrm{MCS}} \rangle$ which is well-described the Molière formula [B+12]

$$\langle \Delta x'_{\mathrm{MCS}} \rangle = \frac{13.6\,\mathrm{MeV}}{\beta\, c\, P}\, Z \sqrt{\frac{d}{X_0}} \left[1 + 0.038\, \ln\left(\frac{d}{X_0} \right) \right] , \tag{3.8}$$

where d is the distance the particle traversed inside the material and X_0 is the radiation length that is a characteristic quantity for the target material.

The radiation length is accessible via tabulated data or by means of the approximated formula depending on the charge Z_m, nucleon number A_m and density ρ_m of the target material [B+12]

$$X_0 = \frac{716.4\,\mathrm{g\,cm^{-2}}\, A_m}{\rho_m\, Z_m (Z_m + 1)\, \ln(287/\sqrt{Z_m})} . \tag{3.9}$$

The radiation length for the most important collimator materials is given in Table 3.8.

Energy Loss from Ionization

Particles at the passage through matter can interact inelastically with the electrons of the atoms constituting the target material. At such encounters, a fraction of the projectile's kinetic energy is disposed into the energy required to deliberate an electron from an atom of the target material.

Table 3.8: Nuclear charge number Z_m, average nuclear mass number A_m, density ρ_m and radiation length X_0 for different materials. Data taken from [Q+15].

Material	Z_m	A_m	ρ_m [g/cm^3]	X_0 [cm]
C (CFC)	6	12.01	1.67	25.57
Cu	29	63.55	8.96	1.435
W	74	183.85	19.30	0.35
Mo_2C	30	67.978	8.40	1.222

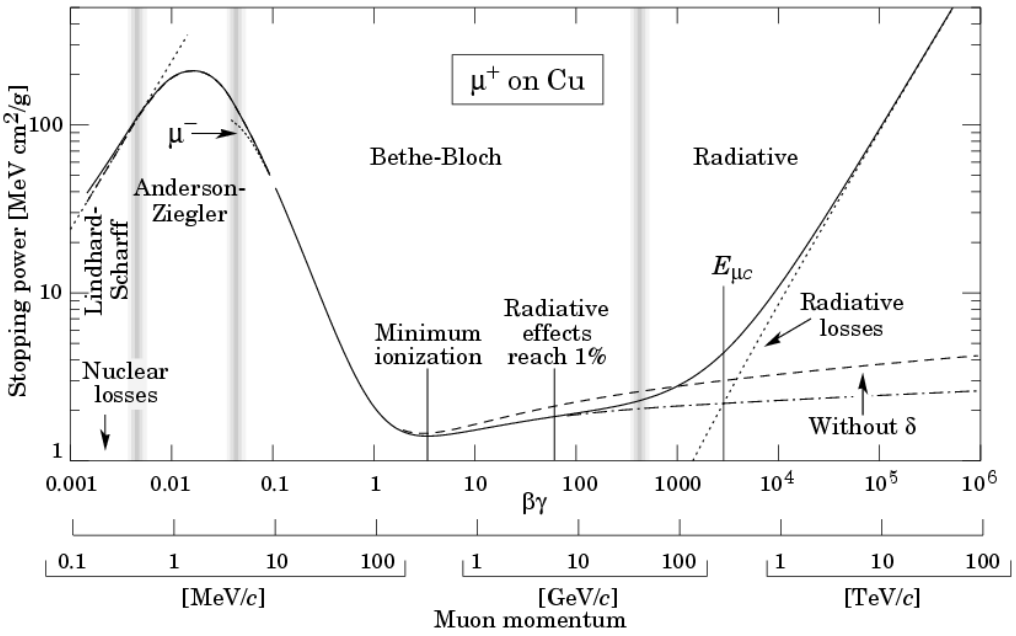

Figure 3.14: Stopping power as described by the Bethe-Bloch formula [B+12].

Quantitatively, the mean energy loss per traversed length unit (or stopping power) in the material is described by the Bethe-Bloch formula [B+12]:

$$-\frac{1}{\rho_m}\left\langle\frac{dE}{dx}\right\rangle = \frac{4\pi}{\rho\, m_e c^2}\,\frac{nq^2}{\beta^2}\left(\frac{e}{4\pi\varepsilon_0}\right)^2\left[\ln\left(\frac{2\,m_e c^2\,\beta^2}{I\,(1-\beta^2)}\right)-\beta^2\right], \tag{3.10}$$

where I is the mean excitation energy (which is tabulated for different materials), m_e is the electron rest mass, q is the particle charge, ρ_m is the density of the traversed material and n is the electron density in the material. The stopping power is shown as a function of $\beta\gamma$ of the particle in Fig. 3.14. It increases quadratically with the particle charge. Energy loss from ionization is therefore more important for $^{208}Pb^{82+}$ ions than for protons (see Table 3.11).

Electromagnetic Interactions

Electromagnetic Dissociation in Collimators

Electromagnetic dissociation (EMD) is a photo-nuclear reaction that occurs at ultraperipherical collisions of the involved nuclei ($b > R_P + R_T$). The Lorentz contracted electric fields lead to the exchange of a large number of virtual photons which can induce the nuclear excitation of one or both of the involved nuclei [B+14c]. The cross section of the EMD process scales logaritmically with the relativistic γ factor of the impacting nucleus [B+14c].

The excited nuclei dissipate the energy acquired under the emission of one or more nucleons, where the emission of neutrons has the largest cross section for heavy nuclei. The process of neutron (n) emission of $m-$th order, triggered by EMD from the interaction with the carbon of the LHC collimators, is summarized by the following reaction formula:

$$\text{EMD}m: \quad {}^{208}\text{Pb}^{82+} + {}^{12}\text{C} \rightarrow {}^{(208-m)}\text{Pb}^{82+} + {}^{12}\text{C} + m\,\text{n}\,. \tag{3.11}$$

Also higher order EMD processes with the emission neutrons and protons are possible, but have a lower cross section. Overall, the EMD process is very important to consider in the picture of heavy-ion collimation, because the residual ions have rigidities very close to the main beam. As it is demonstrated in Chap. 8.2, they can travel through the magnetic lattice of the LHC over large distances and may cause distinct losses at given LHC elements. The cross-section for photo-nuclear reactions scales proportionally with Z^2 [B$^+$14c].

Electromagnetic Dissociation in Interaction Points
EMD can also occur from the interaction of colliding particles at the IP. The reaction chain for neutron emission of $m-$th order is the following:

$$\text{EMD}m: \quad {}^{208}\text{Pb}^{82+} + {}^{208}\text{Pb}^{82+} \rightarrow {}^{208}\text{Pb}^{82+} + {}^{208-m}\text{Pb}^{82+} + m\,\text{n} \tag{3.12}$$

Again, higher order processes are possible, but the emission of a single neutron has the largest cross section. For example, the emission of one neutron and one proton is suppressed by two orders of magnitude compared to the single neutron emission [Psh16].

Bound-Free Pair Production
The photon exchanged in ultra-peripheral collisions of two ions can create a virtual pair of leptons from which the negatively charged particle may be captured by one of the interacting nuclei. This process is referred to as bound-free pair production (BFPP). Of practical relevance in terms of cross-section are BFPP processes in which electrons are captured. The BFPP process of m-th order for LHC $^{208}\text{Pb}^{82+}$ ions is summarized as follows [Ast08]:

$$\text{BFPP}m: \quad {}^{208}\text{Pb}^{82+} + {}^{208}\text{Pb}^{82+} \rightarrow {}^{208}\text{Pb}^{82+} + {}^{208}\text{Pb}^{(82-m)+} + m\,e^+ \tag{3.13}$$

The cross-section for the first order BFPP processes in which one ion captures an electron can be approximated by the formula:

$$\sigma_{\text{BFPP}} = Z_P^5\, Z_T^2\, a \log\left(\frac{\gamma_{\text{cm}}}{\gamma_0}\right), \tag{3.14}$$

Table 3.9: Cross sections and relative mass to charge ratio of interaction products for electromagnetic and photo-nuclear interactions of colliding $^{208}Pb^{82+}$ beams at $7\,Z$ TeV [Sch15].

	Unit	BFPP1	BFPP2	EMD1	EMD2	$\sum$ EMD
σ	[b]	281	0.006	96	29	226
$\chi - 1$	$[10^{-3}]$	-12.2	-24.4	4.84	9.72	-
Reference		[M$^+$01]	[ASS14]	[B$^+$09b]	[B$^+$09b]	[B$^+$09b]

where Z_P and Z_T are the charge numbers of the projectile and target, γ_{cm} is the relativistic Lorentz factor in the center of mass frame and a, γ_0 are tabulated values with a small dependence on Z_T [M$^+$01]. This equation also shows that, compared to processes at the IP, the BFPP cross section for interactions at the collimators is significantly smaller because of the quadratic dependence on Z_T and the reduced γ_{cm} for a fixed target interaction.

Compared to the fully stripped nucleus, the $^{208}Pb^{(82-m)+}$ ion has a different mass to charge ratio and is therefore subject to dispersion. Already the secondary beam generated from first order BFPP (the dominating process in $^{208}Pb^{82+}$ - $^{208}Pb^{82+}$ collisions at $7\,Z$ TeV) is outside the momentum acceptance of the LHC arcs and hence lost in the DS magnets at the end of the IR in which it is produced [B$^+$09b]. The cross sections for the most important electromagnetic interactions of $^{208}Pb^{82+}$ ions colliding at the IP at $7\,Z$ TeV are summarized together with the χ factor quantifying their mass to charge ratio in Table 3.9.

With the presented cross section and considering the design luminosity, the secondary BFPP1 beam carries a power of 26 W. With its distinct rigidity change, the secondary BFPP beam impacts the DS magnets in a very localized manner. This leads to a locally high power density in the magnet coils that may cause a quench, which was demonstrated in a dedicated BFPP quench test [S$^+$15a]. In 2015, dedicated orbit bumps were used in IR1 and IR5 to steer the secondary BFPP beam into an empty cryostat where the lost particles cannot cause a magnet quench. In the region around the ALICE experiment this solution is not applicable, such that for future operation in HL-LHC, the installation of additional collimators in the IR2 DS magnets is envisaged [B$^+$15].

Nuclear Interactions

Nuclear Interactions in Collimators

Nuclear encounters with impact parameters smaller or equal to the sum of the radii of the involved nuclei can lead to interactions over strong force. The gluon exchange implies large momentum transfers which may lead to the production of new particles or nuclear fragmentation subsequent to the nuclear excitation of one or both nuclei.

A very important nuclear process for protons interacting with the collimator material is single diffractive scattering. In this process, the proton interacts with a nucleus of the collimator material and is excited to a higher nuclear state. This excited state decays back into a proton and other particles. The momentum of the outgoing proton is reduced with respect to the proton which was initially entering the reaction [S$^+$14c].

For heavy ions, the nuclear excitation of either the target and/or the projectile and their subsequent disintegration leads to a spectrum of residual nuclei much wider than that of EMD processes [Bar09]. Typically residual ion fragments from nuclear interactions can cover the full isotope spectrum (with $A < A_0$) and therefore produce particles with rigidities far from the main beam. For the materials used in primary LHC collimators nuclear interactions occur with cross sections almost one order of magnitude above that of EMD1 (see Table 3.10). The mechanism of nuclear fragmentation of $^{208}\mathrm{Pb}^{82+}$ ions in the TCP collimator material is summarized by the following reaction formula:

$$^{208}\mathrm{Pb}^{82+} + ^{12}\mathrm{C} \rightarrow ^{A_X}\mathrm{X}^{Z_X+} + ^{A_Y}\mathrm{Y}^{Z_Y+} + ^{12}\mathrm{C} + N_n\,\mathrm{n} + N_p\,\mathrm{p} + ... \tag{3.15}$$

Here, A_X, A_Y are the nuclear mass numbers of the fragment X and Y, Z_X, Z_Y are their charge numbers and N_n, N_p are the number of produced neutrons and protons.

Table 3.10: Cross sections for EMD1 (single neutron emission) and nuclear interactions of $^{208}\mathrm{Pb}^{82+}$ ions for different fixed target materials at the 2011 LHC energy of $3.5\,Z$ TeV and its design energy $7.0\,Z$ TeV [B$^+$14c].

	σ [b] $3.5\,Z$ TeV		σ [b] $7.0\,Z$ TeV	
Target	EMD1	Nuclear	EMD1	Nuclear
C	0.471	3.24	0.498	3.26
Cu	10.16	5.09	11.05	5.11
W	63.52	6.92	68.91	6.95

Processes of fragmentation, either from EMD or nuclear interactions, cause also deviations in angle and transfer of transverse and longitudinal momentum. The created fragments hence populate not only a wide spectrum in terms of mass and charge, but also in terms of angle (which can dominate over angular scattering from MCS) and momentum. The latter leads to an additional smearing of the distribution of magnetic rigidities and hence loss locations [B$^+$14c].

Nuclear Interactions at the IP

Nuclear fragmentation processes at the IP are the main interest of the LHC experiments. At a momentum of 7 Z TeV, the total cross section for such hadronic interactions of two $^{208}Pb^{82+}$ ions is 8 b [Col95]. In terms of quench risk, debris from nuclear fragmentation of $^{208}Pb^{82+}$ ions at the IP is a negligible process compared to the secondary BFPP beam, because the cross section is significantly smaller and the broad spectrum of generated χ-values leads to a wider spread of loss locations.

For proton operation at high luminosity, physics debris from nuclear interactions can lead to significant loss rates at magnets close to the IP, which motivated the installation of the TCL collimators, because the superconducting Q5 in IR1 or IR5 could quench otherwise.

Nuclear Evaporation and Statistical Fragmentation

The residual heavy ions generated at a cascade of interactions of either nature may still be in a nuclear charge state above the ground level. Depending on the mass of the fragment, two physical processes of energy dissipation can be distinguished.

Heavy nuclei can decay into their ground state by either nuclear fission, the emission of nucleons or γ rays, a process referred to as nuclear evaporation [F$^+$03]. Proton emission from nuclear evaporation is suppressed compared to neutron emission because of the Coulomb barrier [F$^+$03].

Light residual ions are subject to fragmentation which can be statistically described by the Fermi breakup model [C$^+$12]. In this model, significant momentum can be transferred to the residual fragments.

Summary and Conclusions

Interactions of heavy ions with the collimator material can cause changes in transverse and longitudinal momentum. Furthermore, fragmentation processes produce residual particles with changed mass and charge that have large rigidity offsets with respect to the main beam. A summary of the most important processes for the study of heavy-ion interactions with collimators is given in Table 3.11. The mean free path λ for nuclear interactions and EMD describes the mean distance a particle traverses in the material before it interacts via the respective reaction channel.

Table 3.11: Characteristic quantities for the most important physical processes of protons and lead ions traversing CFC at 7 Z TeV. Data taken from [B$^+$04a] and scaled to the density of CFC.

Physics Process	Unit	Proton	$^{208}Pb^{82+}$
$-\frac{dE}{E\,\mathrm{d}x}$	$[10^{-5}\,\mathrm{m}^{-1}]$	11	917
$\langle \Delta x'_{\mathrm{MCS}} \rangle$	$[\,\mu\mathrm{rad}/\sqrt{m}]$	4.0	4.0
$\lambda_{\mathrm{nuclear}}$	[cm]	47.9	3.1
λ_{EMD}	[cm]	-	23.9

The comparison to protons clearly shows that the nuclear interaction length $\lambda_{\mathrm{nuclear}}$ for $^{208}Pb^{82+}$ ions is smaller by more than one order of magnitude compared to protons. In addition, the EMD process generates off-rigidity ion fragments.

3.4.6 Collimation Cleaning Inefficiency

Particles which are not absorbed by the TCPs, but instead out-scattered, should be captured by the TCSG collimators. This requires that they receive a sufficient transverse angular kick $\Delta x'$ at the TCP, which is mathematically expressed by the following inequality [B$^+$04a]

$$\Delta x' > \sqrt{\frac{(N_S^2 - N_P^2)\,\epsilon_N}{\gamma\,\beta_x}}\,. \tag{3.16}$$

Here, β_x is the horizontal betatron function at the TCP and N_P and N_S are the applied half gaps of the TCP and TCSG respectively. The formula assumes an ideal betatron phase advance between TCP and TCS, such that the particle amplitude at the secondary collimator is maximized. Particles which do not obey the condition defined in Eq. (3.16), may leave the collimation system and continue moving in the machine.

If, in the course of interacting with the collimator material, they have been subject to significant change of rigidity, they can to be outside of the rigidity acceptance and absorbed in the aperture of the superconducting magnets in the dispersion suppressor where the dispersion increases.

The local loss rate in the machine aperture from collimation debris is measured by means of the local cleaning inefficiency $\eta(s)$, which quantifies the cleaning performance of the collimation system. For proton losses, it is defined as the number of locally lost protons $N_{\mathrm{loc}}(s)$ in the

interval $[s, s + \Delta s]$, normalized by the number of protons lost at the collimators N_{tot} [B$^+$14d]:

$$\eta_p(s) = \frac{N_{\mathrm{loc}}(s)}{N_{\mathrm{tot}}\,\Delta s}\,. \tag{3.17}$$

This definition is valid if the momenta of the impacting particles are similar. As shown in the previous section, the collimation debris of heavy-ion beams is composed of many different isotopes which can have a large spread in momentum. To take into account the different energetic contributions from the individual particles, the cleaning inefficiency of heavy-ion beams is defined in a more generic manner. Instead of counting the number of lost ions, the total amount of locally lost heavy-ion energy E_{loc} in the interval $[s, s + \Delta s]$ is related to the highest amount of energy lost in the LHC collimators E_{max}:

$$\eta(s) = \frac{E_{\mathrm{loc}}(s)}{E_{\mathrm{max}}\,\Delta s}\,. \tag{3.18}$$

The local cleaning inefficiency allows a simple scaling of the total loss rate to the amount of locally lost energy. Note that the above definition of the cleaning inefficiency considers a particle loss as the point of interception with the aperture of the beam pipe. In measurements of the losses in the LHC, this definition is not applicable, because secondary showers created by the particles interacting with the material at the location of impact are measured. The measurement of beam losses in the LHC is presented in the next section.

3.4.7 Measurement of Losses in LHC Operation

The LHC is equipped with more than 4500 ionization chambers, the beam loss monitors (BLM) [H$^+$05, H$^+$08b], with the aim of keeping track of the particle losses throughout the ring. They are installed at the outer side of superconducting magnets, collimators and other locations. The ionization chambers are gas filled cylinders housing a structure of parallel electrodes operated with opposite voltages (see Fig. 3.15). Charged particles traversing the detector ionize the gas particles and the created ions and their electrons are captured by the electrodes, which is measured as a drop of the high voltage at which the BLMs are operated. The measured signal is proportional to the radiation dose.

The BLMs measure the secondary particle showers from the interaction of beam particles with the material of collimators or with the beam pipes and surrounding components. Given their small size, the positioning of the BLMs is essential to monitor the loss rate at strategic locations where high losses are expected. A schematic illustration of the BLM positioning around the superconducting magnets in the LHC arcs is shown in Fig. 3.16.

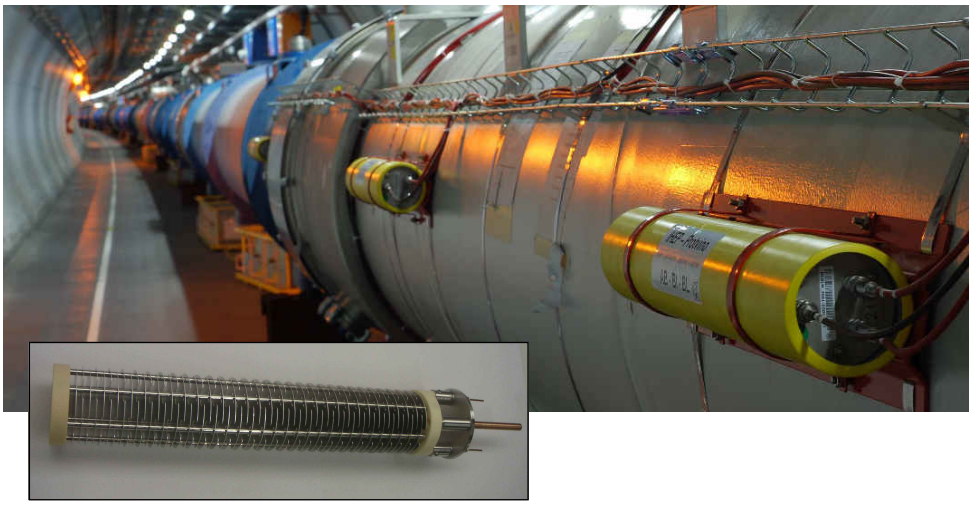

Figure 3.15: Top: Ionization chambers of the LHC BLM system, mounted at the LHC Magnets. Bottom: Inner structure of an ionization chamber. Figures taken from [BLM16].

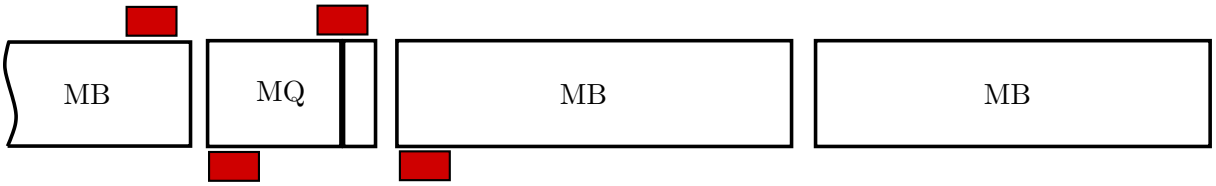

Figure 3.16: BLM positioning around a MQ magnet [Lec14].

The BLM data is continuously monitored by the LHC interlock system which triggers a beam dump if defined thresholds are exceeded [Gua05]. Both the quench limit and the intensity limit at which the physical integrity of the collimators is endangered by beam induced plastic deformations, depend on the time scale at which the losses occur [B$^+$11b, R$^+$14]. Therefore the signals of the ionization chambers are sampled over twelve different integration time scales reaching from 40 μs to 83.89 s. The different integration times are denominated running sums (RS) and reach from RS01 to RS12 (see Table 3.12). With increasing RS, the BLM thresholds are set to larger values, accounting for the larger quench limit with increasing loss duration.

It is not straight-forward to deduce the number of locally lost particles and the energy deposition in the magnet coils from measured BLM signals. One reason for this is the limited azimuthal and longitudinal coverage of the BLMs. Furthermore, at every location and for every beam loss scenario, a different response function relates the measured signal to upstream particle impacts at the beam pipe. Therefore, the BLM signals should be interpreted on a global scale to identify critical loss locations in the machine, rather than deducing quantitative information about energy deposition. The latter requires dedicated simulations, including the shower propagation from the point of primary particle impact [B$^+$09a, B$^+$14d, A$^+$15]. Such shower propagation simulations can be combined with quench limit estimates to derive operational thresholds for the BLMs.

The longitudinal distribution of losses in the LHC ring is referred to as a loss map. The constant loss monitoring in operation (physics loss map) delivers a convolution of all losses presently occurring, whatever their origin might be. The qualification of the LHC collimation system is carried out in dedicated measurements, presented in detail in Chap. 5.1.

Table 3.12: Summary of LHC BLM integration times [Z$^+$05].

Running Sum	Integration Time (ms)
1	0.04
2	0.08
3	0.32
4	0.64
5	2.56
6	10.24
7	81.92
8	655.36
9	1310.72
10	5242.88
11	20971.52

4. Simulation Tools

Important contributions to the excellent performance of the LHC came from theoretical simulations. Many tools have been developed and used to predict various physics aspects of the machine. For collimation, particularly software for particle tracking and simulations of particle-matter interaction are important. The former requires also a detailed model for optics computation, since the configuration of the magnetic lattice is crucial for the particle motion in the machine. In order to have a complete picture of the collimation efficiency, information must be exchanged between the tracking tool and the particle-matter interaction, which can be realized in different manners. In this chapter, different software tools which are important for the development of an improved heavy-ion collimation simulation tool are presented.

4.1 MAD-X

MAD-X (Methodical Accelerator Design) [MAD] is the standard tool at CERN to simulate beam dynamics and compute beam optics in particle accelerators. The software is a complete migration of MAD-8 (written in FORTRAN77) to C++ and was introduced in 2002 for the design and simulation of the LHC optics [Sch06].

The structure of the machine and the strengths of the magnets are given by the user by means of dedicated input files. A matching function provides the functionality to adjust specific variables such that defined constraints are fulfilled. An aperture model of the machine can be processed and compared with the beam position and dimensions to evaluate the available normalized aperture throughout the machine. A dedicated function produces the required optics input for SixTrack (see below).

4.2 FLUKA

FLUKA (FLuktuierende KAskade) is a fully integrated Monte-Carlo package to simulate particle transport and the interaction of particles with matter [FSFR05, B$^+$14b]. The package simulates

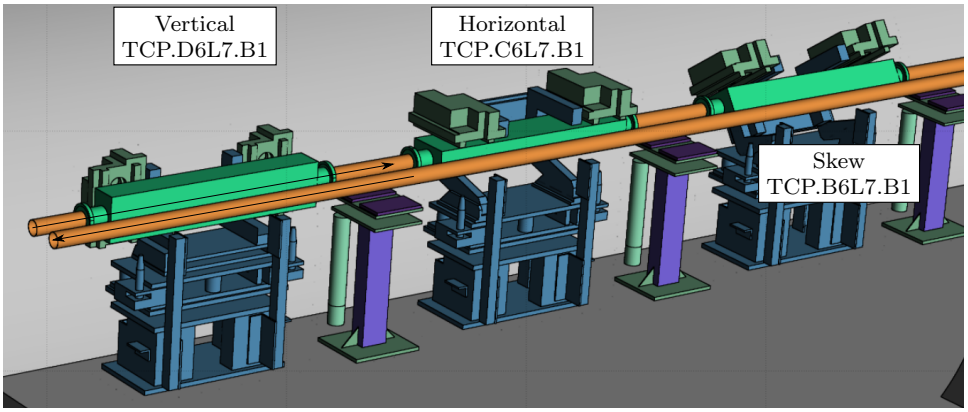

Figure 4.1: FLUKA geometry of the three primary collimators in IR7 for B1 [S+13b].

the interaction of a primary beam particle with the nuclei of the traversed material in a user-defined 3D geometry. It also simulates the particle-matter interaction of particles generated in electromagnetic or hadronic cascades. The software uses regularly updated physics models derived from experimental data and is used for a variety of applications, including particle shower simulations and energy deposition studies in the LHC.

The species, energy and direction of the incident particles are given by the user in a dedicated input file. The geometry can be defined manually with a dedicated syntax or generated from the FLUKA element database (fedb) which contains LHC elements which may be assembled [M+12]. The full geometry of the different LHC IRs is available as a FLUKA model and is regularly used to study energy deposition, activation or shower propagation for different beam loss scenarios. As an example, the geometry of three primary LHC collimators, including their supports, is shown in Fig. 4.1.

The FLUKA user input file is a sequence of command lines (called *cards*), which define the simulation setup via different available options. The required output information can be selected, post-processed and written to dedicated files via 38 different user routines that can be linked to the FLUKA executable. Each user routine consists of FORTRAN code that can be adjusted to the specific requirements of the user. The options for a pre-defined output can be set in the FLUKA input file by means of the respective card linked to the specific user routine.

4.3 SixTrack

4.3.1 Tracking in SixTrack

SixTrack [Sch94, TJ94, RD+05a, Tam14] is designed to provide symplectic (see Chap. 7.2.1) six-dimensional tracking of relativistic proton beams in high-energy synchrotrons over many turns.

Initially developed for dynamic aperture studies, the software is subject to regular updates providing new features for dedicated functions or improved physics models. The tracking algorithm is based on symplectic tracking maps derived from the accelerator Hamiltonian. Tracking maps are transformation rules for the six-dimensional particle coordinates describing the effect of the beam line element on the particle. Based on these tracking maps, the six-dimensional particle coordinates are transported element by element through the magnetic lattice of the accelerator. The symplecticity (see Chap. 7.2.1) makes SixTrack an excellent tool to provide accurate tracking over a large number of turns. The tracking is performed around the reference orbit which is known from the optics computation.

4.3.2 Collimation SixTrack

SixTrack is equipped with a collimation subroutine [RD$^+$05b, Web12] providing an integrated environment for 6D thin-lens tracking together with a Monte-Carlo module to simulate the interaction of the protons with the material of the collimation devices. For this purpose, physics models and cross-sections for different types of interactions are implemented for different collimator materials. The SixTrack particle-matter interaction simulation includes energy loss via ionization, multiple Coulomb scattering and nuclear interactions at the passage of the protons through the collimator. Both elastic and inelastic nuclear interactions are simulated, where the proton is considered to be lost when the interaction is inelastic, except in the case of single diffractive scattering. For particles having undergone single diffractive and elastic scattering, the tracking is continued when the particle has left the collimator.

In order to identify the loss distribution in the ring, the individual particle tracks are compared to a detailed model of the LHC aperture. The aperture check is first carried out at dedicated aperture markers to reduce the required computing time. Beginning from the marker, particle track is then reversely extrapolated as a straight line and the aperture check is iteratively repeated in steps of 10 cm until the loss location is identified. In the current SixTrack release version[1], this algorithm is executed on a post-processing level by means of the software `BeamLossPattern` [RARD05] (see Fig. 4.2). Given that all particle tracks have to be saved and analyzed in this approach, this method of loss detection is very time- and space-consuming.

An important recent extension of SixTrack is an online aperture check during the tracking, instead of computing the aperture losses on a post-processing level. With this algorithm, SixTrack continuously compares the particle coordinates to a detailed model of the LHC aperture while tracking. With the initial aperture check carried out at the markers, the losses are precisely localized by backwards extrapolation, equivalent to the aperture check with `BeamLossPattern`. The approach significantly reduces the required CPU time and the amount of generated data.

[1] SixTrack Version 4.5.34 from 20.04.2016.

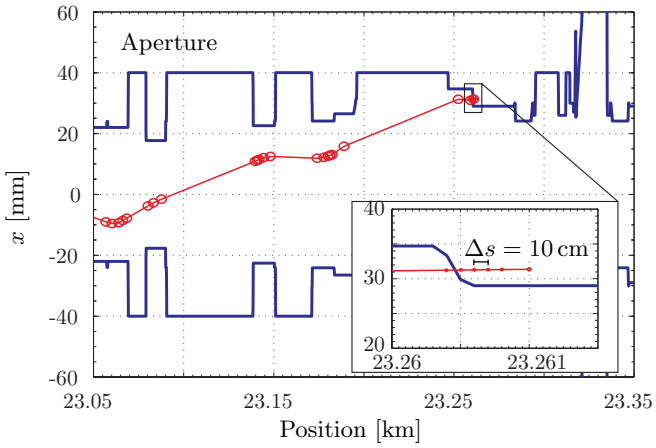

Figure 4.2: Illustration of the `BeamLossPattern` algorithm to identify aperture losses from particle tracks simulated with SixTrack. Figure taken from [RARD05].

Options and input for the execution of Collimation SixTrack are given via dedicated input files:

- `fort.2`: Defining the optical configuration of the accelerator. This file can be automatically generated from MAD-X.
- `fort.3`: Selection of options and beam settings via dedicated blocks. The most relevant options for collimation studies are the number of tracked particles, number of turns through the machine, particle energy, RF settings, collimator settings and initial distribution.
- `CollDB`: Collimator database file, containing information on the name, length and material of the different collimators.
- `allapert`: Contains detailed information about the beam pipe aperture throughout the ring.

The `COLLIMATION` block in the `fort.3` file contains information about the settings of the different collimator families. Collimator families are classified by the prefix of the collimator name and the region where the collimator is installed.

The initial particle distribution can be selected from different options. In the framework of this document, two of them are of major importance: the annular halo and the direct halo [B$^+$14d], as shown in Fig. 4.4. The annular halo is a hollow ellipse in the horizontal or vertical phase space with a normalized amplitude between N_P and $N_P+\bar{\epsilon}$, where N_P is the normalized half gap of the primary collimator and $\bar{\epsilon}$ is a small quantity. The quantity $\bar{\epsilon}$ accounts for the diffusion which is not taken into account in SixTrack, in order to save computing time [B$^+$14d]. The annular halo is typically sampled at IP1, with a Gaussian distribution in the other plane.

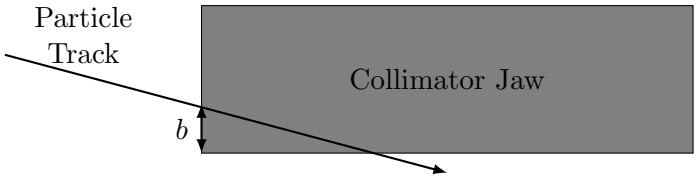

Figure 4.3: Illustration of the impact parameter b.

The particles hit the primary collimator within several turns, depending on their initial betatron phase. The selection of an appropriate value for $\bar{\epsilon}$ requires to assume the impact parameter at the collimator jaw (the transverse distance of the impacting particle from the edge of the collimator jaw, see Fig. 4.3). It is, however, altered by non-linearities in the machine from higher order fields than quadrupoles, which deform and shift the phase space ellipse [B$^+$14d]. This effect is discussed in more detail in Chap. 7.6.1. The direct halo is simulated to impact immediately at the TCP jaws, which allows for a direct control of the impact parameter and reduces the number of turns required for the tracking.

Besides these halo types which can be generated by SixTrack, the software is capable of reading an input file containing the 6D coordinates of the particle distribution to be tracked.

Collimation simulations with SixTrack are usually carried out for 200 turns with an initial sample of 6.4 million protons to gain enough statistics. In this scenario, one proton lost in the aperture leads to a cleaning inefficiency of $1.5 \times 10^{-6}\,\mathrm{m}^{-1}$ over a 10 cm bin, about one order of magnitude below the estimated quench level during the design of the LHC. Given the large amount of required space which has to be allocated for the aperture loss detection, the simulations are split into 1000 sub-simulations which are submitted to the CERN batch computing service [Dep16].

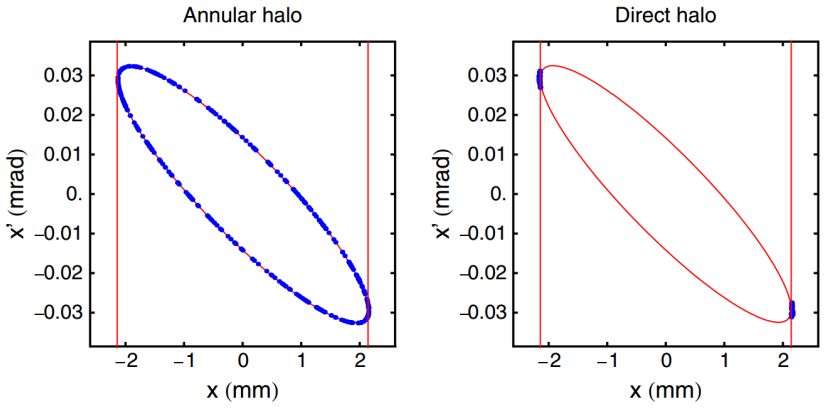

Figure 4.4: Initial distribution sampled as an annular halo (left panel) and as a direct halo (right panel). Figure courtesy of [B$^+$14d].

In the latter, they are processed in parallel, if possible. The post-processing is carried out on the virtual machine of the cluster, such that only the relevant output is saved back in the user directory and the disk space which has to be allocated is reduced by several orders of magnitude. Additional information can be obtained by a subsequent shower propagation simulation with FLUKA. This allows for the study of energy deposition in the machine hardware, in particular the superconducting magnets, including contributions from hadronic and electromagnetic showers. The input for the subsequent simulation is obtained by SixTrack, which saves the information on particles having undergone inelastic interactions in the collimators to a dedicated file. Furthermore, the shower simulations can be used to quantitatively predict the resulting BLM signals. Compared to the nominal cleaning simulations with SixTrack these simulations are extensive in terms of time and space consumption and are therefore only carried out for dedicated configurations, e.g. when experimentally measured quench limits shall be theoretically accessed.

4.4 SixTrack-FLUKA Coupling

The SixTrack-FLUKA active coupling [M$^+$13a] is a dedicated framework in which the two simulation codes SixTrack and FLUKA are run in parallel to perform beam-machine interaction studies. In particular, the framework is applied to simulate the cleaning performance of the collimation system by complementary tracking in accelerator lattices and particle-matter interaction at the collimators.

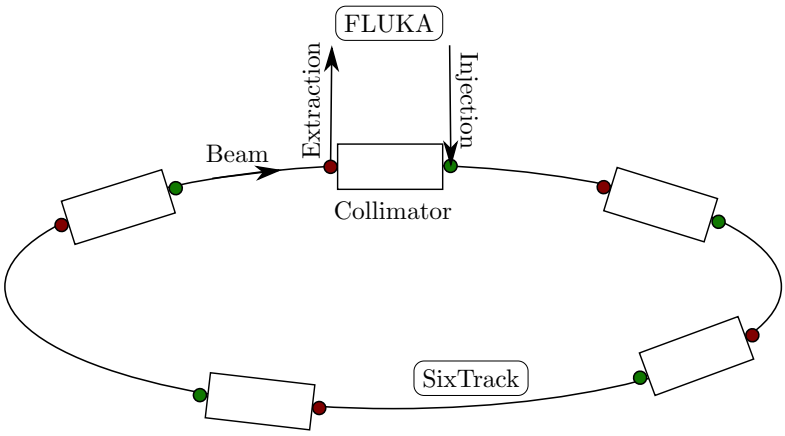

Figure 4.5: Principle of the SixTrack-FLUKA coupling. At every collimator extraction marker (red) the particle bunch is sent to FLUKA where the interaction with the collimator is simulated. The resulting distribution is then re-injected in SixTrack at the injection marker (green), from where the tracking is continued.

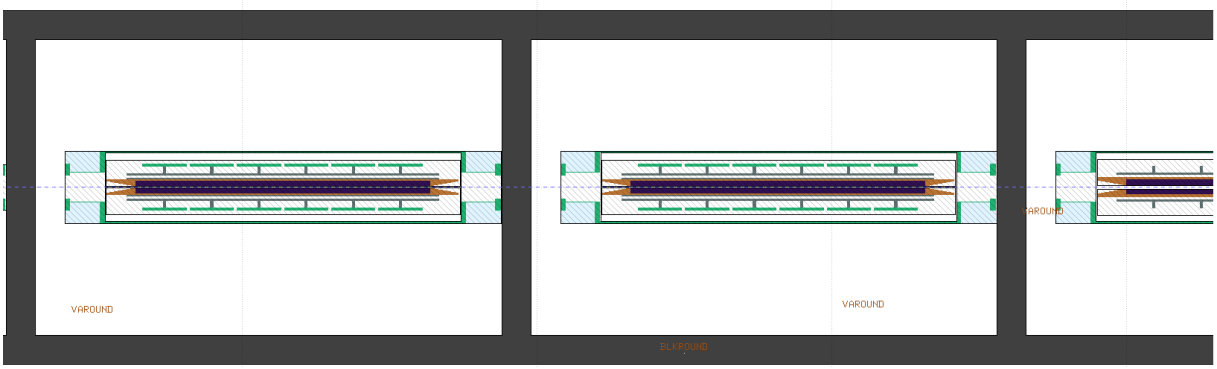

Figure 4.6: Collimator models in the FLUKA input file used for the SixTrack-FLUKA coupling.

The SixTrack-FLUKA coupling can be used as an alternative to the built-in scattering in SixTrack and instead simulate the beam-matter interaction with FLUKA. It combines the advantages of both codes with their detailed and regularly updated physics models. The backbone of the particle exchange is the use of a network port and a C library to handle TCP/IP network messages. This shortens the required simulation time compared to having to reinitialize each code after each particle exchange.

The basic principle of the SixTrack-FLUKA coupling is illustrated in Fig. 4.5. The magnetic lattice used in a regular SixTrack simulation is expanded by additional collimator extraction markers at which SixTrack sends the particle distribution to FLUKA, where the interaction with the collimator is simulated. At the end of the collimator, the distribution of residual particles is sent back to SixTrack and re-injected into the lattice at a dedicated injection marker from which the tracking is continued.

The marker locations correspond to the beginning and end of the collimator tanks. The FEDB stores detailed models of the individual collimator components for each collimator type. The settings for each collimator are loaded in a dedicated pre-processing algorithm and the FLUKA input file is populated with all the necessary collimators based on the FEDB models (see Fig. 4.6). Residual protons which are not identical to the incoming protons (e.g. those produced in nuclear interactions) are assigned to a new particle ID.

Losses at the aperture of the LHC magnets are identified by the online aperture check. The input for subsequent energy deposition simulations can be obtained in full analogy to that of SixTrack, by saving the positions of inelastic interactions in the collimator jaws. As an alternative, a `toucMap` file can be generated, which contains the first collimator impact of each proton at each turn.

4.5 ICOSIM

It was yet anticipated in the LHC design phase that the interaction of the heavy ions with the collimator material can lead to fragmentation into other isotopes, with consequences on the cleaning inefficiency. This was incorporated into a dedicated simulation software for heavy-ion collimation, called Ion Collimation Simulation (ICOSIM) [B$^+$04a, Hol08].

It is an integrated program for particle tracking with a Monte-Carlo module to simulate the interaction of heavy ions with the collimator materials. The tracking routine is split in two stages: first, the impact distribution at the TCPs is determined by a linear transformation between them. Every 100 turns, random transverse kicks are applied to the particles to simulate diffusion. When all particles have impacted the TCPs, the tracking of the residual fragments is continued based on a matrix multiplication with chromatic modeling in linear approximation, including sextupole fields in thin-lens approximation. The information about the magnetic lattice is read from MAD-X output. Along with the tracking, the particle amplitudes are compared to a simplified aperture model in which the aperture cross sections are approximated by an ellipse. Once the aperture is identified to be intercepted at the end of an element, the exact location is determined by linear extrapolation, as described in the previous section.

The Monte-Carlo module simulates the interaction of the ions with matter, including energy loss from ionization via the Bethe-Bloch equation and multiple Coulomb scattering, as well as fragmentation processes from EMD and NF [B$^+$04a]. The latter is computed using tabulated cross-section information for the two processes which was generated beforehand with FLUKA or the Pshenichnov model [B$^+$04a]. When a particle is subject to fragmentation in the collimator, the heaviest fragment is given back to the tracking routine. Momentum transfers (both transverse and longitudinal) from the fragmentation process are not taken into account [B$^+$04a]. At the time of development, these simplifications were considered to be of small importance for the simulation result, because the transverse momentum transfer from the fragmentation process and the energy loss related to it are small compared to the total energy of the ion [B$^+$04a].

5. Collimation of Heavy-Ion Beams

The LHC collimation system was designed to efficiently remove the halo of proton beams. While this purpose is well accomplished, the cleaning performance for $^{208}Pb^{82+}$ operation is measured to be significantly worse. In this chapter, the experimental findings on the heavy-ion collimation efficiency are presented and compared to simulations with ICOSIM. Despite limitations that only became apparent after the first feedback from heavy-ion operation, this code provided the state-of-the-art for heavy-ion beam collimation before the LHC was started. It is important to understand in detail its implementation and limitations before embarking for the development of a further improved simulation tool

5.1 Qualification Loss Maps

The cleaning performance of the LHC collimation system must be validated before it is operated with high intensity beams [B$^+$06]. This is done by inducing artificial beam losses at the primary collimators and measuring the collimation debris throughout the ring with the LHC BLM system. Qualification loss maps are measured with very low intensity (with a maximum of 3×10^{11} charges in the machine), compared to physics operation. The measurements take place when new optics, collimator settings or particle momenta are commissioned. High beam intensities are only allowed to be injected in the LHC if the collimation system was qualified beforehand.

To induce losses at the IR7 TCP, different strategies to increase the transverse emittance have been developed. Loss map measurements in early LHC operation have been carried out by means of optics changes that led to tune resonance crossing, inducing fast beam losses at the collimation system. Since 2012, the beam excitation is carried out using the transverse damper (ADT) [M$^+$13b] which can introduce white noise excitation such that the beam particles receive random transverse kicks, resulting in an effective increase of the transverse emittance. The excitation with the ADT is distinguished by the better controllability and can be carried out selectively for both planes of both beams with a selectable loss rate [M$^+$13b]. Loss maps measured in this approach are referred to as betatron loss maps. The full qualification of the collimation system includes also off-momentum loss maps where the primary losses are induced

at the IR3 TCP [M$^+$13b]. They shall not be further discussed in this work.
Loss maps are shown as a mapping of the BLM signals, normalized with respect to the highest measured BLM signal, as a function of the distance from IP1. A color code is applied to distinguish between losses at collimators (black), in normal conducting regions (red) and in the superconducting LHC magnets (blue).

Heavy-Ion and Proton Qualification Loss Maps measured in 2011

The horizontal B1 (B1H) betatron qualification loss maps measured in the 2011 with protons and $^{208}Pb^{82+}$ ions at $3.5\,Z$ TeV are directly compared in Fig. 5.1. The beam are squeezed in the experimental IRs with the β^* values listed in Table 3.1. The optics are identical in the full ring, except in IP2, where the injection settings with $\beta^* = 10\,\mathrm{m}$ are maintained for protons and the heavy-ion beams are squeezed to $\beta^* = 1\,\mathrm{m}$. The collimator settings are listed in Table 3.7.
In both qualification loss maps, the collimation regions IR3 and IR7 capture the largest amount of losses. The zoom to IR7 shows not only high losses at the TCP, TCSG and TCLA collimators, but also in the warm magnets in between. These loss signals are mostly induced by shower particles that are generated in the collimators. The magnets in IR7 which are close to the collimators are normal conducting, so these losses do not define a quench risk.
The measured losses at the TCP in the momentum cleaning insertion IR3 with $^{208}Pb^{82+}$ beams are two orders of magnitude above the signal measured with protons. This can be interpreted as a larger amount of off-rigid particles that is scattered out of the collimators in IR7. While for protons the measured loss signals are beyond the noise level only in regions close to collimators, the loss distribution of heavy-ion beams shows pronounced loss spikes at amplitudes up to 10^{-2} in superconducting regions across the LHC ring.
In both qualification loss maps, the highest loss signal in superconducting magnets is measured in the DS region downstream of IR7 with amplitudes of 3×10^{-4} for protons and 2×10^{-2} for $^{208}Pb^{82+}$ ions. The losses in the DS have a characteristic structure with two subsequent loss clusters DS1 and DS2 located in the cells 9 and 11. The loss clustering can be explained by the local horizontal dispersion function starting from the TCP, which is also shown in Fig. 5.1.
The loss clusters are located in regions where the local horizontal dispersion function increases, due to the strong fields in the magnetic bending dipoles downstream of IR7. The increasing dispersion guides particles with rigidity offsets into the aperture of the superconducting magnets, where they are lost. Accordingly, the outermost edge of the clusters is located at the quadrupoles in cell 9 and 11, where the dispersion functions have local maxima. Also the loss spikes in the LHC arcs (A1 to A3) that are measured with heavy-ion beams are located at positions where the dispersion function and hence the dispersive offset of off-rigid particles is maximum.

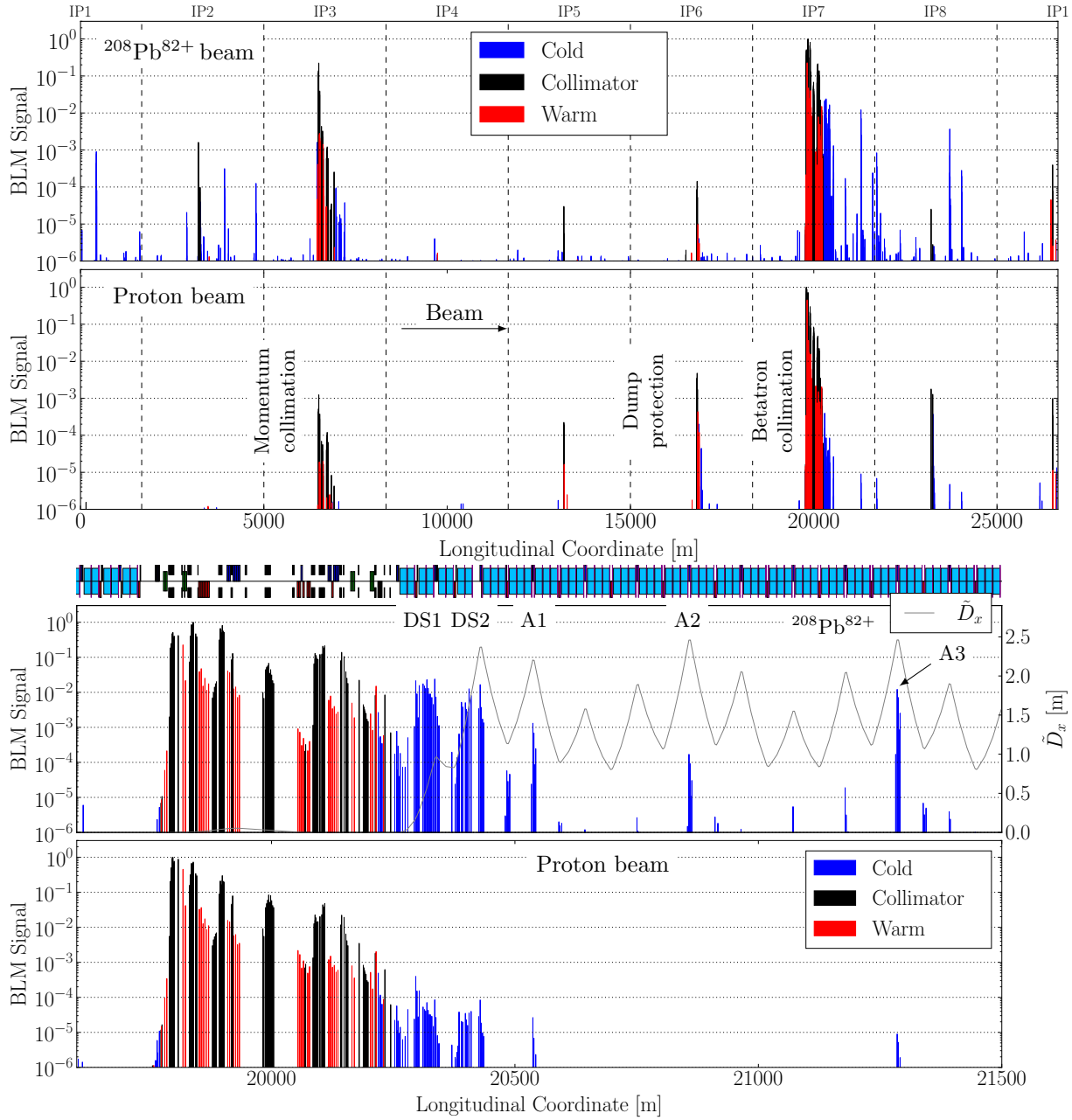

Figure 5.1: B1H qualification loss maps measured in 2011 with proton [B^+14d] and $^{208}Pb^{82+}$ beams [H^+14] at 3.5 Z TeV with identical collimator settings and optics, except in IR2. The longitudinal coordinate describes the distance from IP1. The vertical dashed lines mark the LHC octants. The BLM signals are normalized with respect to the highest measured BLM signal. Top: full LHC ring, bottom: zoom to IR7.

The IR7 DS is the superconducting region in the LHC that is exposed to the largest amount of collimation debris. The magnets in this region have the highest risk of beam-induced quenches. The comparison shows that, with heavy ions, the cleaning performance in this region is almost two orders of magnitude worse than for protons.

Conclusions

While the stored beam energies with heavy-ion beams that were foreseen in the LHC design phase[B$^+$04b] are lower by two orders of magnitude, the collimation losses in the IR7 DS are larger by the same amount. This shows that the quench risk with heavy-ion beams is comparable to that in proton operation. Therefore, the collimation system with heavy-ion beams should be studied with the same thoroughness as for proton beams.

This is particularly important, because the stored beam energy initially foreseen in the LHC design phase has already been exceeded in the 2015 heavy-ion run. If the stored beam energy is going to be further increased, the risk of beam induced quenches will increase accordingly.

It is therefore important to understand collimation losses in heavy-ion operation by means of simulation tools. With these tools, potentially critical collimation losses can be identified and possibly alleviated. Furthermore, such simulations allow studying the cleaning performance of the collimation system with different collimator settings and can hence be used to determine the settings with the best cleaning efficiency.

Collimation simulation tools must accurately predict the important loss locations in the LHC. In the next section, the heavy-ion collimation simulation tool ICOSIM is benchmarked against the B1H betatron qualification loss maps measured in the 2011 heavy-ion run.

5.2 Simulation with ICOSIM

When the first measured LHC heavy-ion loss maps became available, ICOSIM could be benchmarked against them. In the following, the loss map simulated with ICOSIM for B1H in the 2011 heavy-ion run configuration at 3.5 Z TeV is compared to the B1H betatron qualification loss map presented in the previous section. The simulation is carried out for 6×10^6 initial $^{208}Pb^{82+}$ ions starting as an annular halo in IP1. The collimator and optics settings are identical to those applied in the heavy-ion run, summarized in Table 3.1 and Table 3.7.

The measured and simulated loss maps are directly compared in Fig. 5.2 and Fig. 5.3. The simulated loss map is shown in terms of the cleaning inefficiency (see Eq. (3.18)) with a binning of 10 cm for aperture losses. It shall be emphasized that the measured and simulated loss maps cannot be compared quantitatively, because the BLMs measure particle showers, while ICOSIM directly simulates the impact location of the individual particles, as discussed in Chap. 3.4.7.

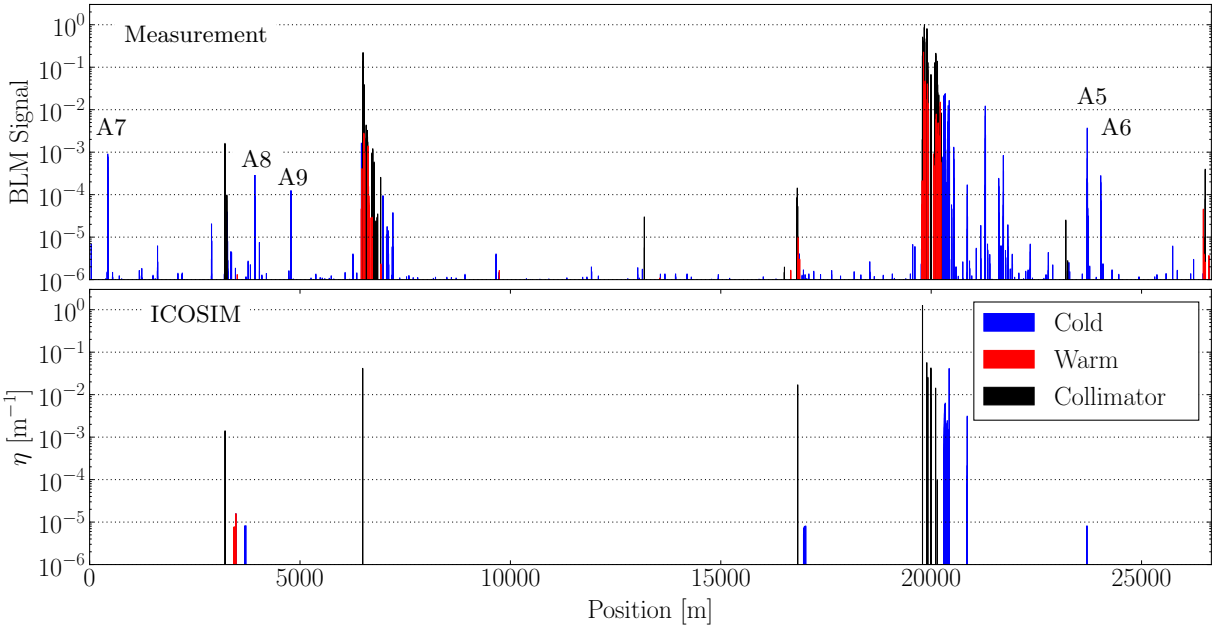

Figure 5.2: Loss map simulated with ICOSIM for 6×10^6 ions of $^{208}Pb^{82+}$ in the configuration 2011 heavy-ion run, compared to the measured BLM signal.

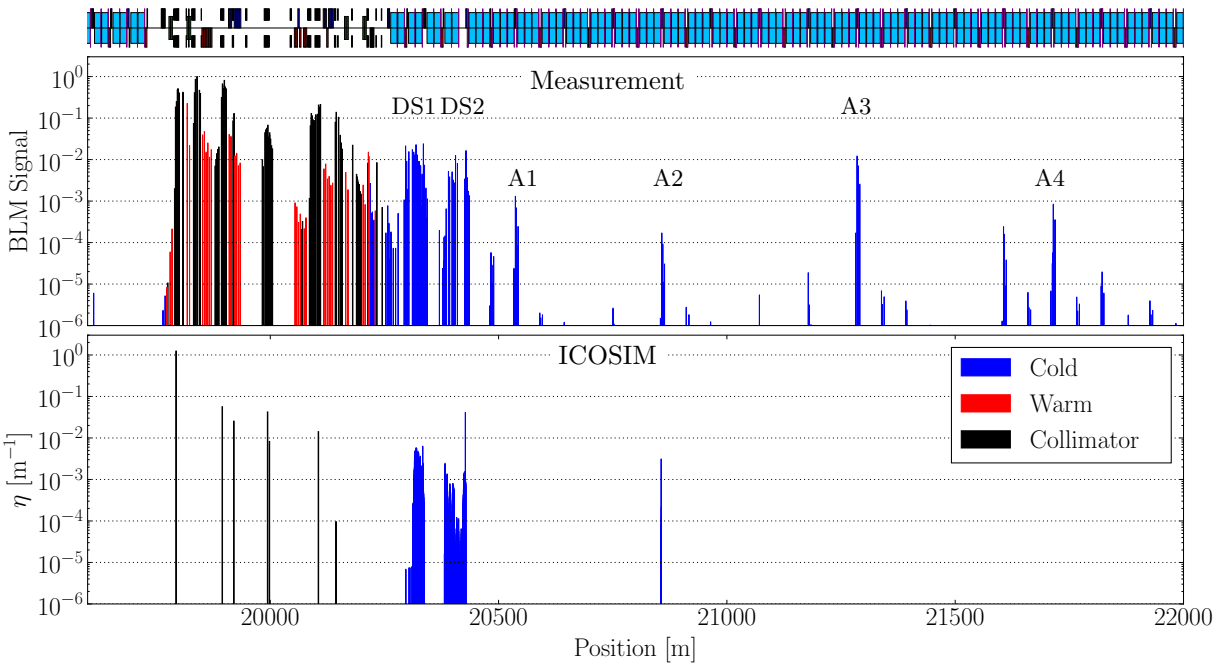

Figure 5.3: Loss map simulated with ICOSIM for 6×10^6 ions of $^{208}Pb^{82+}$ in the configuration 2011 heavy-ion run, compared to the measured BLM signal, zoomed to IR7.

The global comparison in Fig. 5.2 shows that ICOSIM simulates the dominating part of beam losses to occur in the LHC collimation system or in cold regions very close to collimators. The losses at the primary collimator in IR3 are caused by off-rigid ions scattered out of the primary collimator in IR7 with mass and charge close to the main beam (mainly $^{207}Pb^{82+}$ ions).

The measured losses in the warm elements of IR7 and IR3 are not simulated with ICOSIM. These losses are mainly caused by electromagnetic and hadronic showers generated in the collimation system. Shower propagation cannot be simulated with ICOSIM, so this discrepancy is expected. For the quench risk from collimation debris, these losses are irrelevant. Therefore, it is not necessary to model them in simulations of the collimation performance. If required, they can be be accurately simulated by detailed shower propagation studies with FLUKA. The same applies for all other simulated loss maps that are going to be presented later in this thesis.

The highest losses in superconducting LHC magnets are measured and simulated to be in the dispersion suppressor (DS1 and DS2) located in the cells 9 and 11 downstream of IR7. The simulated cleaning inefficiency in this region peaks at approximately $\eta = 10^{-2}\,\mathrm{m}^{-1}$, which is comparable to the measured loss distribution. However, the BLM signals with limited coverage cannot be compared quantitatively to the simulated loss maps. The longitudinal extension of the loss clusters in the DS do not fully match with the ones of the measured losses.

The measured loss spikes A1, A3 and A4 to A9 in the LHC arcs are not simulated with ICOSIM. Especially the A3 loss spike is measured at an amplitude almost comparable to the DS loss clusters. When higher stored beam energies should be applied, these losses could also become a quench risk. It is therefore important to accurately simulate them in a heavy-ion collimation simulation tool, which implies the requirement for an improved simulation tool.

5.3 Conclusions

The loss pattern simulated by ICOSIM shows discrepancies with respect to the measured qualification loss map. While the most critical losses immediately downstream of IR7 are well predicted, losses further downstream cannot be qualitatively reproduced. They could be of importance for LHC applications if they turn out to be a problem for uninterrupted operation or other reasons. As discussed previously, ICOSIM is equipped with a simplified tracking algorithm and uses approximations for the simulation of the ion-collimator interaction.

Based on these findings, the implementation of a new simulation software for heavy-ion collimation was initiated, which is the main development presented in this thesis. The first step in this development is to study which simplifications cause the discrepancies and then improve existing tools to overcome them. A new simulation tool to study the required improvements of the ICOSIM physics models is presented in the next chapter.

6. SixTrack with Ion-Equivalent Rigidities

The benchmarking of ICOSIM simulations against measured LHC beam loss patterns unveiled that the simulation result shows discrepancies with respect to the measurement. Possible reasons might be the simplified fragmentation algorithm in ICOSIM, which does not take into account the transverse momentum transfer and changes of the kinetic energy from the fragmentation process. Also, the simplified tracking algorithm and contributions from light ions to the measured loss patterns could be reasons for the observed discrepancies.

As a part of this thesis, the simulation tool SixTrack with Ion-Equivalent Rigidities (STIER) was developed, in order to verify or falsify these hypotheses. The aforementioned physics aspects can be individually probed with STIER. Comparisons to measurements and the ICOSIM simulation result allow for conclusions on their relevance for accurate predictions of heavy-ion loss patterns. Based on the results, the requirements for a further improved collimation simulation software are outlined. The content of this chapter has been published in part in [H$^+$14, H$^+$16b].

6.1 Efficiency of Staged Collimation for Heavy Ions

Before the new simulation tool for heavy-ion fragmentation and tracking is presented, the origin for the worse cleaning performance with heavy-ions compared to protons shall be studied.

The loss location of out-scattered particles that inevitably leave the primary collimator in IR7 depends on the type of interaction the particles have undergone. By virtue of its design, the collimation system is most efficient if the particles have been subject to small changes in rigidity, but received transverse momentum transfers large enough to scatter them into the secondary collimators. This is described by the relation defined in Eq. (3.16).

Among all superconducting LHC magnets, those in the IR7 DS are exposed to highest amount of collimation debris. It is therefore the region with the highest risk of beam-induced quenches.

Particles lost in the IR7 DS have been insufficiently scattered in the primary collimator, but have acquired rigidity offsets $1 + \delta_{\text{eff}} = (1 + \delta)/\chi$ that are outside of the rigidity acceptance of

the dispersion suppressor magnets in IR7. A rough estimate for the latter is given by

$$\delta_{\text{eff}}^{\text{max}} = \pm A_g \, \tilde{D}_x \, . \tag{6.1}$$

where A_g is the horizontal aperture in the magnet (approximately 22 mm in the IR7 DS) and $\tilde{D}_x$ is the horizontal dispersion generated locally between the TCP and the DS magnet considered. This relation is only valid in linear approximation and for particles without betatron offset. For real particles with betatron offsets, the acceptance may be reduced or enhanced, such that the expression in Eq. (6.1) is only approximate and the real value for $\delta_{\text{eff}}^{\text{max}}$ becomes a distribution, rather than a constant.

In the following, the distribution in angle and energy of residual particles created by $^{208}\text{Pb}^{82+}$ ions and protons impacting the TCP is studied by FLUKA simulations. In both cases, a particle beam with an energy of $3.5\,Z$ TeV is simulated to perpendicularly hit a carbon target of 10.3 cm thickness. This is comparable to the distance particles traverse in the material of the primary collimator with impact parameters of 3 μm at an angle of 29.1 μrad.

The resulting distribution in terms of the momentum per nucleon and the scattering angle $\Delta x'$ of all particles scattered out of the collimator material is shown for both simulations in the top and middle plots of Fig. 6.1. The horizontal lines show the minimum angular kick $\Delta x'$ required such that a particle intercepts the secondary collimator. The vertical lines show the rigidity acceptance of the MQ.11R7.B1 around the nominal beam energy of $3.5\,Z$ TeV. Assuming an aperture of $A_g = \pm 22$ mm and a local dispersion function of $\tilde{D}_x = 2.4\,\text{m}$, the rigidity acceptance yields approximately $\delta_{\text{eff}}^{\text{max}} = 9 \times 10^{-3}$. Particles not lost in this magnet are lost at locations downstream of the DS clusters. Note also that the dispersion function in this magnet is larger than in the DS1 cluster upstream, so the rigidity acceptance of the DS1 is larger.

The comparison demonstrates that the number of particles outside the rigidity acceptance of the DS magnets but inside the angular acceptance of the TCSG is significantly larger for the heavy-ion fragments than for out-scattered protons. The bottom plot of Fig. 6.1 shows the projected number of nucleons inside the angular acceptance of the TCSG collimators. For rigidities beyond $\pm\delta_{\text{eff}}^{\text{max}}$, the fraction of heavy ions (black line) is larger by up to three orders of magnitude compared to the proton distribution.

The integral of the distribution outside the rigidity acceptance in the bottom plot of Fig. 6.1 yields approximately 5.1×10^{-3} for protons and 8.6×10^{-1} for heavy ions. This difference is the origin of the larger cleaning inefficiency with $^{208}\text{Pb}^{82+}$ ions, which is two orders of magnitude above the cleaning inefficiency for proton beams. Given the drastic impact on the cleaning inefficiency, the effect of fragmentation and the motion of the ion fragments in the LHC must be accurately modeled in a simulation tool for heavy-ion collimation.

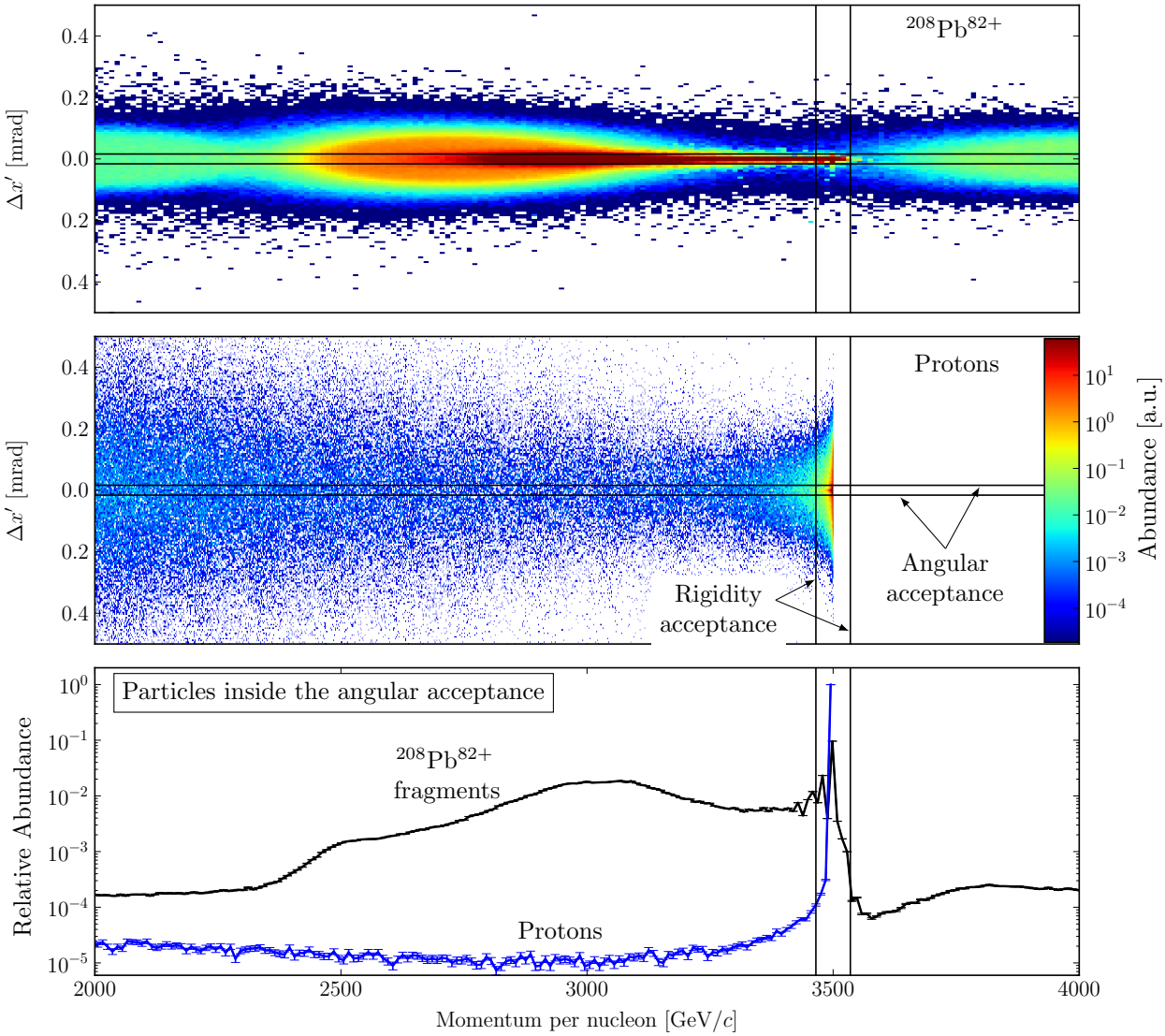

Figure 6.1: Top and middle plot: FLUKA simulated map of transverse angular kick received at the passage through a 10.3 cm thick carbon target vs particle momentum per nucleon for an initial beam of $^{208}Pb^{82+}$ ions (top) and protons (middle). The horizontal lines represent the TCSG acceptance and the vertical lines the rigidity acceptance of the MQ.11R7.B1. All data points are weighted with the total energy per bin. The bottom plot shows a projected histogram of all particles inside the TCSG acceptance as a function of the momentum per nucleon. Both histograms are weighted with the particle energy and are normalized to cover a surface of 1.

6.2 The STIER Simulation Tool

The design of the LHC collimation system foresees the TCPs in IR7 as the first collimators in the cleaning hierarchy. For every plane (H,V,S), the respective TCP should be the only collimator exposed to particles of the main beam. It is under normal circumstances the location with the highest amount of lost particles in the LHC. The pattern of collimation losses should hence be dominated by residual fragments generated from the interaction of the main beam particles with the TCP. It should hence be possible to accurately describe the loss distribution by a simulation model which takes into account only the fragmentation at the primary collimator.

Based on these assumptions, a new simulation tool for heavy-ion cleaning was established as an alternative to ICOSIM. Instead of using a simplified fragmentation model for all collimators, the approach relies upon a detailed fragmentation simulation only at the TCP. This includes taking into account all residual fragments and kicks in angle and energy from the fragmentation process. Other collimators are treated as perfect absorbers.

The resulting distribution of residual heavy-ion fragments is tracked as protons with ion-equivalent rigidities in SixTrack, starting from the TCP. The approach is referred to as SixTrack with Ion-Equivalent Rigidities (STIER). Initially developed to study the effect of the simplifications used in ICOSIM, and to determine the requirements for an improved simulation tool, STIER simulations proved to be in good agreement with the measured loss patterns. It was used in the 2015 heavy-ion run to validate the collimator settings and to develop loss mitigation strategies, which were successfully tested in operation (see Chap. 8).

STIER relies upon three consecutive simulation steps shown in Fig. 6.2. In the first step, the phase space properties of the particles impacting the collimator jaws of the TCP are determined by means of MAD-X. The angle of incidence is then used as an input for the following simulation

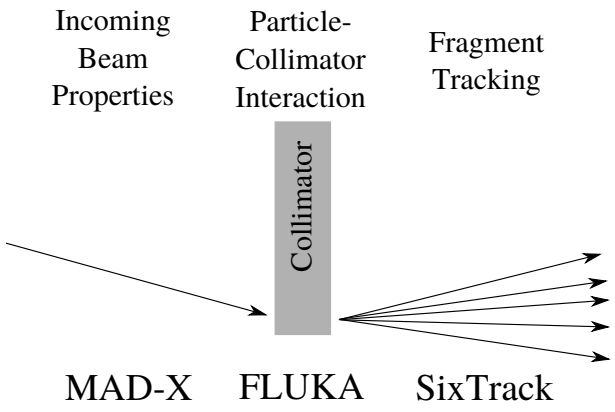

Figure 6.2: Three stages of the STIER simulation setup.

step in which the interaction of the primary heavy-ion beam with the material of the primary collimator is simulated with FLUKA. The information about the out-scattered ion fragments is then converted to input for SixTrack where the ions are tracked as protons with momenta that match the rigidities of the individual ion fragments.

In the following sub-sections, the three STIER stages are described in detail and important simulation results for every stage are summarized. Some of the results are also important for the development of a further advanced heavy-ion collimation tool described in Chap. 7.

6.2.1 Optics Calculation

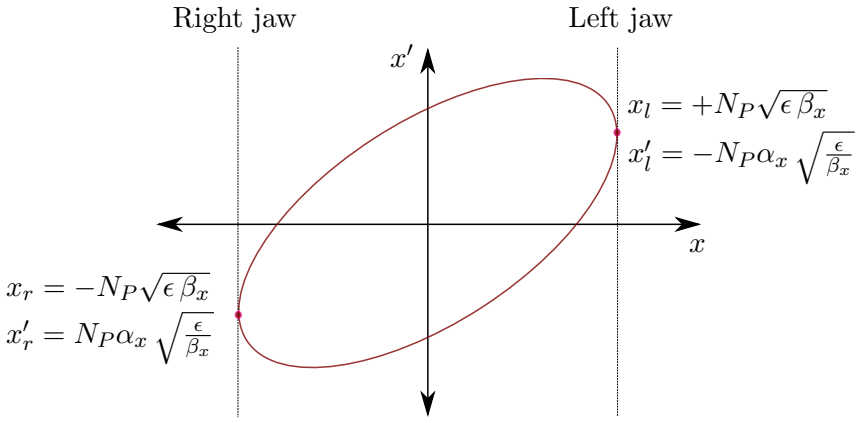

Figure 6.3: Phase space diagram of particles at a maximum normalized betatron amplitude N_P. Particles hitting the left and right jaw of the TCP have specific coordinates in phase space.

As a first step of the STIER simulation approach, the optical functions are computed with MAD-X. Particles impacting the primary collimator have specific properties in phase space, as illustrated in Fig. 6.3. The collimator jaw is assumed to be in parallel to the nominal closed orbit (i.e. it is not aligned to the divergence of the beam envelope). Furthermore, it is assumed that the diffusion is slow enough for particles to hit the TCP close to their maximum spacial amplitude. Then one can conclude from Fig. 6.3 that the particles impacting the collimator do so with a non-zero angle of incidence, if $\alpha \neq 0$. This is illustrated in Fig. 6.4.

The angle of incidence $x'_{l/r}$ at the left ($x > 0$ for B1 and vice versa for B2) and right collimator jaw is defined by the normalized half gap N_P, the geometric emittance ϵ_x and the Twiss parameters β_x, α_x at the location of the TCP as follows [Wie99]

$$x'_{l/r} = \mp N_P\,\alpha_x\sqrt{\frac{\epsilon_x}{\beta_x}}\,. \tag{6.2}$$

For LHC emittances and collimator settings, the distance the primary beam particles traverse

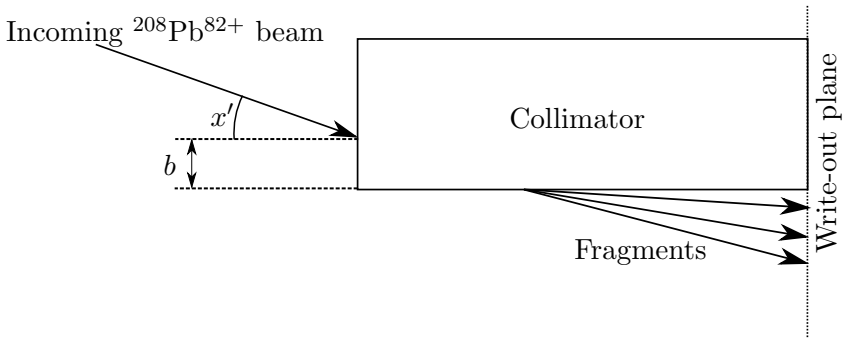

Figure 6.4: Geometry used for the FLUKA simulation of the fragmentation at the TCP.

in the collimator material scales, in good approximation, linearly with the impact parameters. They were found in SixTrack simulations for protons to be between 1 μm and 10 μm [B$^+$14d]. Assuming that the diffusion for heavy-ion beams is similar, and taking into account the angle of incidence for 3.5 Z TeV presented in Table 6.1, the traversed distances lie in the range from $\approx$ 3 cm to 30 cm. This is in the same order of magnitude as the mean free path for nuclear interactions (see Table 3.11). The fragment composition of the out-scattered heavy ions hence depends strongly on the angle of incidence and on the impact parameter.

A summary of the Twiss parameters at the TCP, the collimator opening and the resulting angles of incidence for different scenarios are shown in Table 6.1. Note that the optics in IR7 remains unchanged during the LHC cycle and for the different configurations.

Table 6.1: Summary of the parameters used to calculate the angle of incidence at the primary collimator for different LHC configurations. The Twiss parameters β_x and α_x are computed using MAD-X. The angle x' is calculated by means of Eq. (6.2).

Year	E [Z GeV]	β_x [m]	α_x [ ]	ϵ_N [μm rad]	γ [ ]	N_p [σ]	x' [rad]
2010/2011	3500	148.46	2.04	1.50	1482.8	5.7	-2.9×10^{-5}
2015	6370	148.46	2.04	1.41	2696.8	5.5	-2.1×10^{-5}
Design	7000	148.46	2.04	1.50	2964.5	5.7	-2.1×10^{-5}

6.2.2 Fragmentation Simulation

Simulation Setup

The fragmentation at the TCP is simulated with FLUKA. The primary collimator is modeled as a simple rectangular carbon cuboid of 60 cm length (see Fig. 6.4). Alternatively, the more accurately modeled collimator geometry of the FEDB can be used. Comparisons between fragmentation simulations using the two geometries have shown no significant discrepancy in the resulting spectrum of heavy-ion fragments. The density of the carbon composite is set to 1.61 g/cm^3 to account for the CFC material used for the TCPs.

Species, energy and transverse momentum of the heavy ions arriving at the end of the collimator jaw are saved to an output file. Other particles than protons or heavy ions are ignored. They are most probably lost in the warm aperture immediately downstream of the TCP. While this approximation is valid for simulations of the collimation performance, detailed shower simulations of energy deposition and radiation dose in the collimation region IR7 take them into account [B$^+$14a].

The FLUKA simulation input file is adjusted to take into account for electromagnetic dissociation, nuclear fragmentation using the DPMJET-III model [R$^+$00] and nuclear evaporation.

In the presented simulations of the 2011 cleaning performance, the primary beam is simulated as 10^7 particles of $^{208}\mathrm{Pb}^{82+}$ at an energy of $3.5\,Z$ TeV, impacting the TCP at an angle of incidence of $x'_{r,l} = \pm 2.91 \times 10^{-5}$ rad. They have been carried out for three different impact parameters: $b = 1\,\mu$m, $b = 3\,\mu$m and $b = 10\,\mu$m. The beam is simulated to impact with fixed x, x' (in contrast to a distribution in x, x') and no amplitude in y, y'. This setup is called pencil beam.

Fragment Spectrum

From the FLUKA simulations for the three impact parameters $1\,\mu$m, $3\,\mu$m and $10\,\mu$m, the isotope spectra can be derived for the different simulation cases. In Fig. 6.5, the fraction of energy carried by the different isotopes is shown for the simulation with $b = 3\,\mu$m. The fragment spectrum covers almost the full range of nuclei lighter than $^{208}\mathrm{Pb}^{82+}$, with over 3000 different fragments created.

In Fig. 6.6, the distribution of A, weighted with the particle momentum, is shown for the simulations with the three impact parameters. With an impact parameter of $b = 1\,\mu$m, the distribution is clearly dominated by heavy fragments, with masses closely to the main beam. For $b = 3\,\mu$m, the production yield of lighter ion fragments increases. For $b = 10\,\mu$m the spectrum is dominated by very light fragments such as helium nuclei, tritium, deuterium and protons. In all simulations, the main amount of energy is carried by either very light ion fragments or isotopes with A and Z close to the main beam.

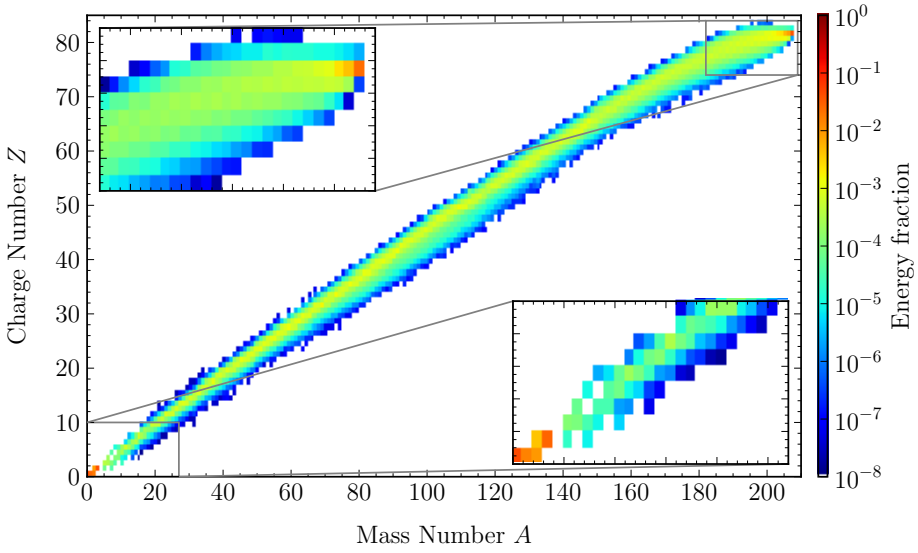

Figure 6.5: Energy fraction carried by the individual isotopes in the fragmentation of 10^7 $^{208}Pb^{82+}$ ions impacting the TCP at an impact parameter of $b = 3\,\mu$m. The data is normalized to the total energy of all ions scattered out of the collimator.

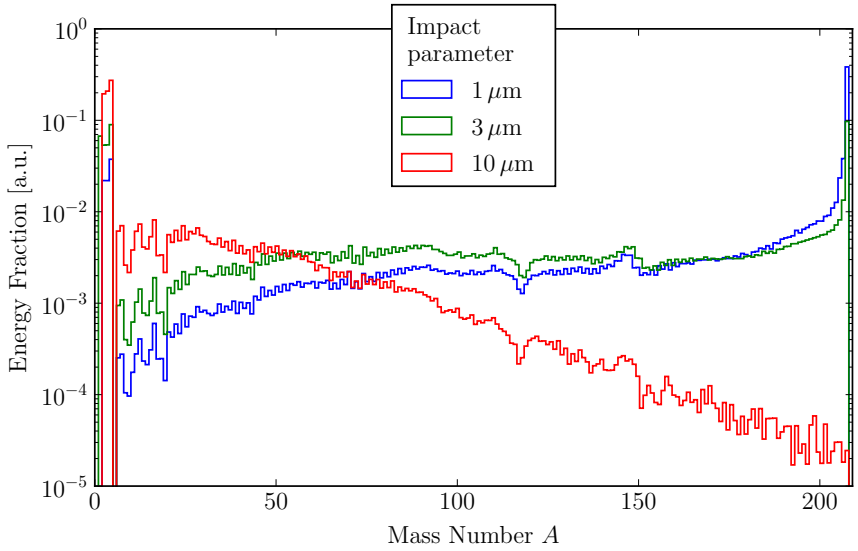

Figure 6.6: Mass numbers of ion fragments simulated by FLUKA simulated for $^{208}Pb^{82+}$ ions impacting the TCP at three different impact parameters $b = 1\,\mu$m, $b = 3\,\mu$m and $b = 10\,\mu$m. The individual contribution of each isotope is weighted with the momentum. The distributions are normalized to the total energy carried by all ions.

A detailed overview of the energy fraction carried by the most important isotopes is given for the different impact parameters in Table 6.2.

The reason for the increasing number of light ion fragments with larger impact parameters is the linear relation between the impact parameter and the distance the particles travel through the material. The probability of fragmentation increases exponentially with the traversed distance through the collimator. As shown in Table 6.2, for an impact parameter of $b = 1\,\mu$m, the amount of energy carried by protons is approximately one order of magnitude below the energy carried by out-scattered $^{208}Pb^{82+}$ ions. At $b = 10\,\mu$m, approximately 40% of the out-scattered beam energy is carried by protons and 16% by $^{4}He^{2+}$ ions, while the contribution of particles of the main beam is lower by four orders of magnitude. This demonstrates that the impact parameter is important for the isotope spectrum generated at the passage through the collimator. The impact on the resulting loss distribution is studied in the following chapters.

In ICOSIM it is assumed that the momentum per nucleon P/A of the fragments generated in NF and EMD processes is similar to the momentum per nucleon of the main beam ($\delta \approx 0$). The FLUKA simulation allows to analyze the spectrum of P/A for the out-scattered ions. This spectrum is shown for ion fragments with $A < 5$ and $A > 5$ in Fig. 6.7. The comparison shows that the heavy fragments have indeed mostly P/A values close to that of the main beam (1379.8 GeV/c). Light fragments, however, have a broad distribution in terms of mass per nucleon and some fragments have significantly larger P/A than the main beam. Parts of the Fermi-motion in the nucleus can be transferred to individual ion fragments, which can lead to a significant gain in momentum for the light fragments. The largest P/A obtained from the FLUKA simulation is approximately 1950 GeV/c, A. This broad spectrum of momenta indicates

Table 6.2: Isotopes with the largest energetic fractions scattered out of the collimator material from the initial fragmentation simulation.

	Energetic Fraction		
Isotope	$b = 1\,\mu$m	$b = 3\,\mu$m	$b = 10\,\mu$m
$^{1}H^{1+}$	4.7×10^{-2}	6.3×10^{-2}	4.0×10^{-1}
$^{2}H^{1+}$	2.1×10^{-2}	2.5×10^{-2}	1.2×10^{-1}
$^{3}H^{1+}$	1.5×10^{-2}	1.7×10^{-2}	7.4×10^{-3}
$^{3}He^{2+}$	5.8×10^{-3}	8.1×10^{-3}	4.9×10^{-3}
$^{4}He^{2+}$	3.6×10^{-2}	4.2×10^{-2}	1.6×10^{-1}
$^{205}Pb^{82+}$	7.1×10^{-3}	2.3×10^{-3}	1.1×10^{-5}
$^{206}Pb^{82+}$	1.7×10^{-2}	5.0×10^{-3}	1.4×10^{-5}
$^{207}Pb^{82+}$	3.3×10^{-2}	8.4×10^{-3}	1.0×10^{-5}
$^{208}Pb^{82+}$	3.6×10^{-1}	3.6×10^{-2}	1.4×10^{-5}

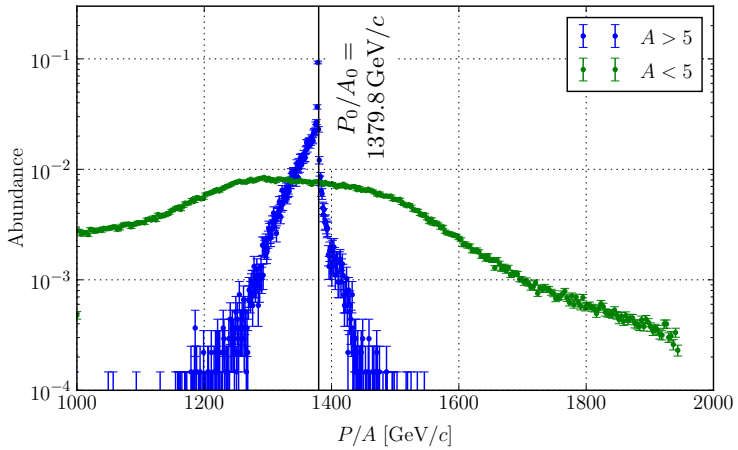

Figure 6.7: Momentum per nucleon of ion fragments with $A > 5$ (blue) and $A < 5$ (green) generated in the interaction of 10^6 ions of $^{208}\mathrm{Pb}^{82+}$ with the TCP material for an impact parameter of 3 μm. Both distributions are normalized such that the sum of all data points yields one. The vertical line shows the momentum per nucleon of the reference particle.

that an improved heavy-ion collimation tool should include the change of kinetic energy from the fragmentation process, especially if light fragments shall be included in the simulation.

6.2.3 Heavy-Ion Tracking in STIER

SixTrack is designed for the tracking of protons, so the tracking algorithm does not include effects of dispersion from a different mass to charge ratio. Following Eq. (2.13), the rigidity offset $1 + \delta_{\mathrm{eff}}$ of an ion fragment with momentum per mass offset δ and mass to charge offset χ, can be described as

$$1 + \delta_{\mathrm{eff}} = \frac{(1+\delta)}{\chi}\,. \tag{6.3}$$

If the reference particle is a proton, the applicable proton momentum to obtain the same rigidity as the heavy ion to be tracked yields:

$$P_E = P_0\,(1 + \delta_{\mathrm{eff}}) = \frac{P}{Z}\,. \tag{6.4}$$

The transverse motion of a heavy ion not matched to the magnetic lattice can therefore be accurately simulated by assigning the ion-equivalent momentum P_E to a proton. From the FLUKA simulation output, the momentum and charge of every ion fragment can be extracted and converted into proton momenta to track the heavy-ion distribution in STIER. Furthermore, the transverse positions and angles are taken into account for the initial conditions.

Losses in the aperture of the LHC magnets are identified with `BeamLossPattern`, which is also used for proton studies with SixTrack. Momenta of ions generated from the fragmentation of $^{208}Pb^{82+}$ span over two orders of magnitude. Therefore, particle losses are weighted with the total energy of the impacting nuclei, as described in Eq. (3.18).

The Monte-Carlo routine implemented in SixTrack to simulate the proton interaction with the collimators must be avoided because it is not adapted to heavy ions. In STIER, the collimators are therefore set to perfect absorbers. This approach will lead to an overestimation of the collimator losses which should be considered in the analysis of the simulated loss patterns.

Accelerating RF cavities are switched off, because the acceleration depends on the particle charge, which is not incorporated in the framework. However, it is expected that the number of turns that a heavy-ion fragment can perform in the machine without being lost is very small compared to the synchrotron period of ≈ 500 turns.

6.3 Simulation Results

6.3.1 Full Heavy-Ion Loss Map Simulations

In this section, the simulated B1H loss maps in the 2011 configuration at 3.5 Z TeV (see Table 3.1 and Table 3.7) from ICOSIM and STIER are compared to the measured B1H qualification loss map. The STIER simulation is carried out with an impact parameter of 3 μm.

To compare with ICOSIM, an additional STIER simulation with simplified out-scattering from the TCP is carried out. Angular and energetic kicks from the fragmentation simulation are not taken into account. The approach is referred to as *simplified STIER*. ICOSIM and the simplified STIER approach are not fully comparable because of the different aperture checks, different tracking routines and the losses from subsequent fragmentation processes included in ICOSIM but not in STIER. Furthermore, simplified STIER includes light ion fragments. Their contribution to the loss pattern is studied separately later-on.

The result of the ICOSIM simulation presented before in Chap. 5.2 is shown in the first row of Fig. 6.8 (zoomed to IR7) and Fig. 6.9 (full LHC ring). The measured losses are shown as a comparison to all simulations in the bottom row of these figures.

Simplified STIER

The loss map simulated with the simplified STIER approach is shown in the second row of Fig. 6.8 and Fig. 6.9. The comparison unveils that some additional loss features are visible compared to ICOSIM. This applies, for example, to the S12 losses in the arc between IR1 and IR2.

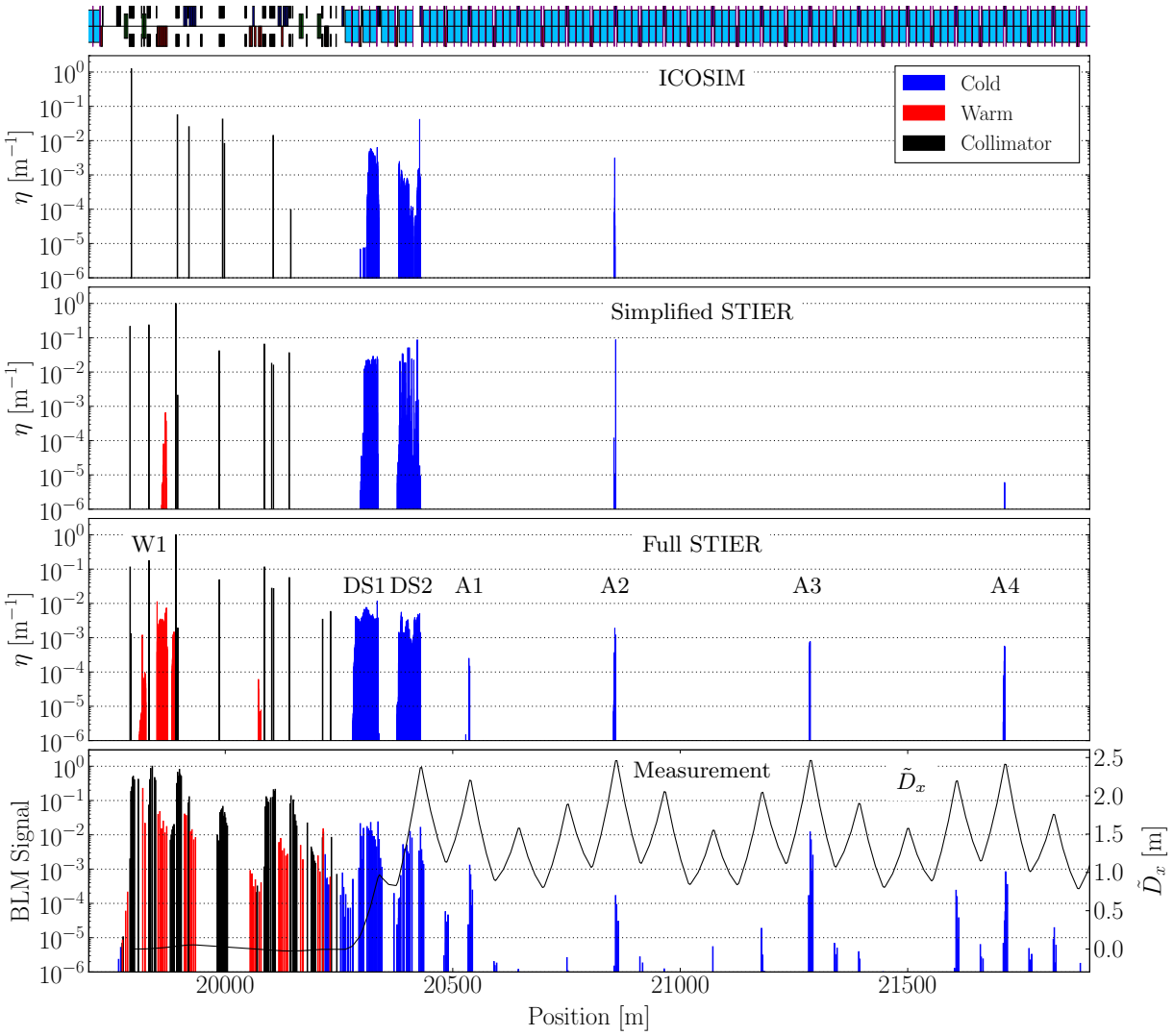

Figure 6.8: Comparison of the B1H loss map simulations using ICOSIM (top row), the simplified STIER approach (second row), a full STIER simulation (third row) and the measured B1H qualification loss maps (bottom) for the 2011 LHC heavy-ion run at 3.5 Z TeV. The bottom row also shows the locally generated dispersion function $\tilde{D}_x$ from the TCP. The STIER simulations are carried out assuming an impact parameter of $b = 3\,\mu$m.

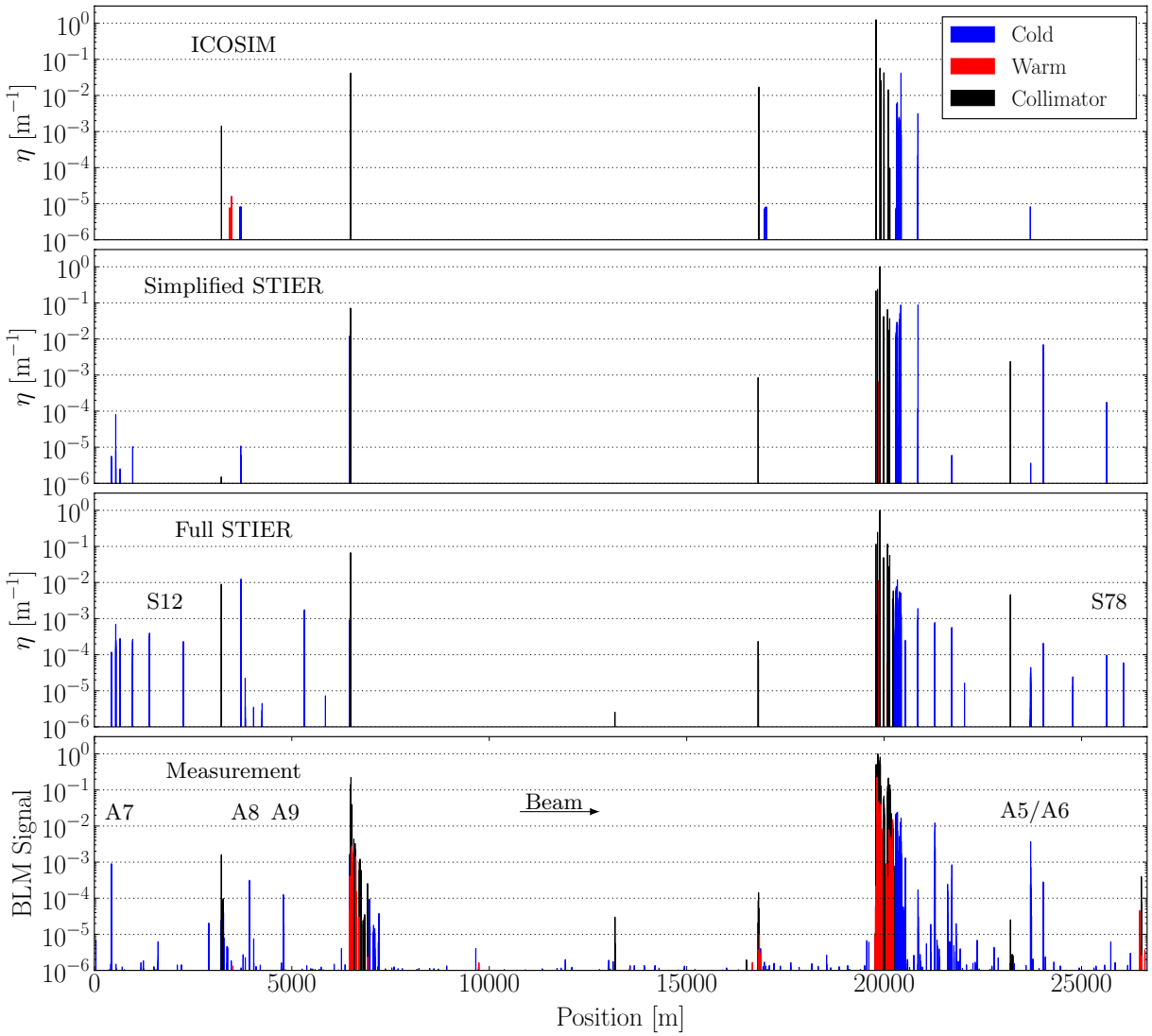

Figure 6.9: Comparison of the B1H loss map simulations using ICOSIM (top row), the simplified STIER approach (second row), a full STIER simulation (third row) and the measured B1H qualification loss maps during the 2011 LHC heavy-ion run at 3.5 Z TeV. The STIER simulations are carried out assuming an impact parameter of $b = 3\,\mu$m.

Also the A6 loss peak downstream of IR8, which is also measured with the BLMs, is visible in the simplified STIER approach, but not in ICOSIM. Further analysis shows that mainly $^{206}Pb^{82+}$ ions are lost in the A6 peak in the simplified STIER simulation. Possibly, this discrepancy can be explained by the different tracking algorithms applied in the two simulation approaches. The error from the simplified tracking in ICOSIM is further studied in Chap. 6.4.

Compared to ICOSIM, the two loss clusters in the IR7 DS (called DS1 and DS2) simulated with the simplified STIER approach are at larger amplitudes. The measured A2 loss peak in the arc downstream of IR7 is simulated in ICOSIM and the simplified STIER approach. Neither of the loss peaks A1, A3 and A4 is simulated in ICOSIM or the simplified STIER simulation. From this finding one can conclude, that STIER can indeed be used to produce loss maps comparable to ICOSIM. Both approaches show discrepancies to the measurement. Apparently the sole inclusion of light ion fragments in the simulation framework does not improve the agreement. With the full STIER simulation, it can now be studied if the agreement improves if the angles and energies of the ion fragments are taken into account.

Full STIER

The loss maps simulated with the full STIER approach are shown in the third row of Fig. 6.8 and Fig. 6.9. Compared to ICOSIM and the simplified STIER approach, it shows a significantly better agreement to the measured data. It shall again be emphasized that the simulated loss patterns should not be compared quantitatively to the measurements. The characteristic loss locations are discussed and analyzed below.

Warm Region W1

The losses in the warm region W1 are more broadly distributed than in the simplified STIER approach. The isotopes lost in the W1 region are listed, sorted by their energetic contribution to the loss cluster, in Tab. 6.3. The analysis shows that the simulated losses are mainly composed of protons and other light ions.

It shall again be emphasized that losses in warm regions simulated with STIER are not comparable to measured loss patterns in these regions. In reality, the BLM signals are caused by hadronic and electromagnetic showers starting from the collimators, which are not simulated in STIER. To define the risk of beam induced quenches, these losses are irrelevant, because all magnets in this region are normal conducting. If these losses should be understood by simulations, detailed shower propagation simulations can be carried out with FLUKA.

Table 6.3: STIER simulated contributions on the total deposited energy at the warm magnets in IR7 (W1), the two loss clusters in the IR7 DS (DS1 and DS2) and in the arcs downstream of IR7 (A1, A2, A3, A4) as shown in Fig. 6.8

W1		DS1		DS2		A1		A2		A3		A4	
Ion	(%)	Ion	(%)	Ion	(%)	Ion	(%)	Ion	(%)	Ion	(%)	Ion	(%)
$^{1}H^{1+}$	57.0	$^{3}H^{1+}$	8.6	$^{206}Pb^{82+}$	34.0	$^{204}Tl^{81+}$	61.0	$^{204}Tl^{81+}$	74.6	$^{204}Tl^{81+}$	86.6	$^{204}Tl^{81+}$	86.7
$^{3}H^{1+}$	38.0	$^{4}He^{2+}$	4.5	$^{205}Pb^{82+}$	16.2	$^{206}Pb^{82+}$	18.7	$^{206}Pb^{82+}$	10.3	$^{199}Au^{79+}$	6.7	$^{199}Au^{79+}$	7.2
$^{2}H^{1+}$	2.6	$^{2}H^{1+}$	3.2	$^{204}Pb^{82+}$	11.6	$^{199}Au^{79+}$	7.4	$^{199}Au^{79+}$	5.7	$^{206}Pb^{82+}$	2.2	$^{206}Pb^{82+}$	1.7
$^{3}He^{2+}$	1.4	$^{203}Pb^{82+}$	3.2	$^{203}Tl^{81+}$	8.7	$^{1}H^{3+}$	3.5	$^{201}Hg^{80+}$	2.3	$^{194}Ir^{77+}$	1.2	$^{202}Hg^{80+}$	1.6

Dispersion Suppressor DS1 and DS2

The two loss clusters DS1 and DS2 in the IR7 DS are accurately modeled in STIER. The isotopes with the highest energy contribution to the losses in the DS1 and DS2 are listed in Tab. 6.3. The highest fraction of the DS1 losses is caused by very light isotopes (H and He ions). The four most important isotopes compose only ≈19.5 % of the energy deposited in the DS1. The DS2 loss cluster is dominated by three different isotopes of Pb which contribute to 61.8 % of the total energy lost in this cluster. With 1227 different isotope species lost in the DS1, the deposited energy is shared between a much larger number of isotopes than at the DS2, where only 334 different isotopes are absorbed.

The distributions of the quantity χ for the isotopes lost in the regions DS1 and DS2 are graphically represented in Fig. 6.10. As expected, the aperture in the cold region DS1 captures a very broad range of mass to charge ratios. The heavy ions lost in the DS2 have mostly mass to charge ratios closer to the reference heavy-ion species.

To understand this difference, the locally generated dispersion function from the TCP to the DS1 and DS2 is shown in the bottom plot of Fig. 6.8. The dispersion increases from $\tilde{D}_x \approx 0\,\mathrm{m}$ in the warm IR7 magnets to $\tilde{D}_x \approx 1\,\mathrm{m}$ at the end of the DS1 and reaches $\tilde{D}_x = 2.4\,\mathrm{m}$ a the end of the DS2. Particles with large rigidity offsets are outside of the rigidity acceptance of the DS1 magnets and hence lost. For particles with rigidities closer to the main beam, the dispersion in the DS1 is not large enough to guide them into the magnet aperture. They continue to move further downstream and can be lost in the DS2, where the local dispersion function is higher and hence the rigidity acceptance is smaller.

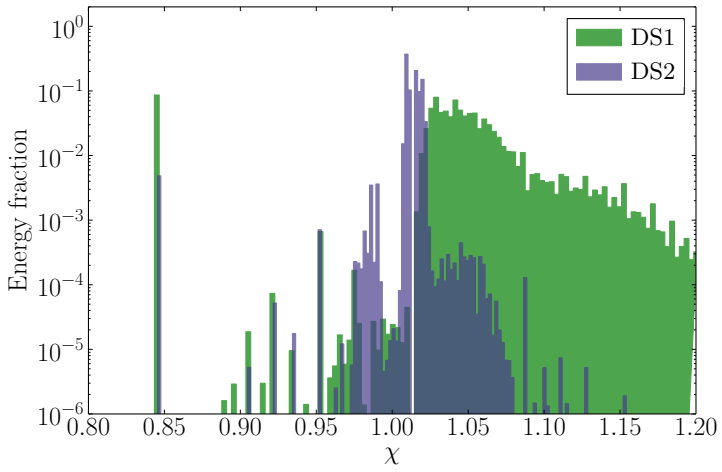

Figure 6.10: Momentum weighted abundance of χ for fragments lost in the DS1 and DS2 clusters. The abundances are normalized by the total momentum of all particles lost in the DS1 or DS2. The data is extracted from the full STIER simulation with $b = 3\,\mu$m.

Arc Losses A1 to A4

The comparison between the simplified and the full STIER simulation shows that the three measured loss spikes A1, A3 and A4 become visible when the angles and energies of the fragments are included. The isotope composition at these locations is very similar (see Tab. 6.3). This can be explained by the fact that the local dispersion function at all of these loss locations is similar. The individual starting conditions at the TCP (starting angle and collimator jaw) can partly add or subtract to dispersive effects. Therefore, the loss location of particles of the same species is different, if the starting angle and energy is taken into account.

This statement is supported by the fact that, except $^{1}\mathrm{H}^{3+}$, all isotopes lost in A1 to A4 are also included in the ICOSIM simulation but the loss spikes are not simulated. The study underlines that it is crucial to incorporate angular and energetic shifts by fragmentation, to accurately simulate heavy-ion beam loss patterns. This should be considered for future simulations.

Losses Downstream of A4

Further downstream, the A5/A6 loss peaks between IR8 and IR7 and the A7 peak between IR1 and IR2 are both simulated and measured. At some locations, STIER predicts losses which are not measured. This applies to the loss peaks S78 in the arc between IR7 and IR8 and S12 in the arc between IR1 and IR2. On the contrary, the A8/A9 loss peaks between IR2 and IR3 are measured, but not simulated by STIER. Instead, two distinct loss peaks at other locations between IR2 and IR3 are simulated. The losses at the IR8 TCT are overestimated in the simulation, while STIER does not predict the losses measured at the IR1 TCT.

These remaining discrepancies could arise from small aperture displacements or orbit fluctuations in the real machine. An analysis of the particle trajectories at the corresponding loss locations shows that aperture or orbit displacements as small as $\approx 300\,\mu$m are sufficient to shift the loss location of the impacting ions.

As it is discussed in more detail in Chap. 10.1.2, the measured magnet aperture varies by some hundred μm. Also, the closed orbit which is commissioned at the beginning of a LHC run can have offsets in this order of magnitude [Red16]. In addition, orbit drifts in the order of $50\,\mu$m can be observed during one fill or between different fills [Wen16] within one run. The combination of these effects can possibly result in the observed discrepancies between the STIER simulation and the measurement.

Another reason for losses which are measured but not simulated could be fragments which are generated in secondary collimator interactions after the passage of the TCP. This can be studied with a simulation tool that includes subsequent fragmentation. Such a tool is presented in Chap. 7.

6.3.2 Dependence on the starting Collimator Jaw

STIER can be used to study the loss behavior of isotopes starting at the individual collimator jaws. So far, all STIER results assume the same amount of ions impacting on the two TCP jaws. In reality the beam halo can impact the two collimator jaws asymmetrically, because the collimator jaw alignment and the reference orbit can only be accurate to some μm. Furthermore, non-linear magnetic fields can tilt or shift the phase space ellipse (see Chap. 7.6.1).

In Fig. 6.11, the loss map is shown, as simulated with STIER with the same settings as above, for particles starting at the left and right collimator jaw separately. A different behavior of the losses can be expected because the betatron motion and the dispersive offset can add or subtract, depending on the starting conditions of the ion.
From the obtained loss maps it can be seen that the simulation result for the particles starting at the right collimator jaw is in much better agreement with the measured data than the simulation of particles starting at the left jaw. The largest fraction of the loss peaks between IR8 and IR1 as well as between IR1 and IR2, which are not observed in the measurement but visible in STIER, is composed of particles starting at the left jaw. However, still one intense peak between IR2 and IR3 is visible in the simulation for the right jaw, which is not observed in the measurement.

In conclusion, the loss patters simulated for particles starting from the individual collimator jaws are different. The separate study of the loss distribution for fragments starting from the individual TCP jaws shall turn out to be very useful to mitigate losses in the 2015 heavy-ion run, as described in Chap. 8.2.

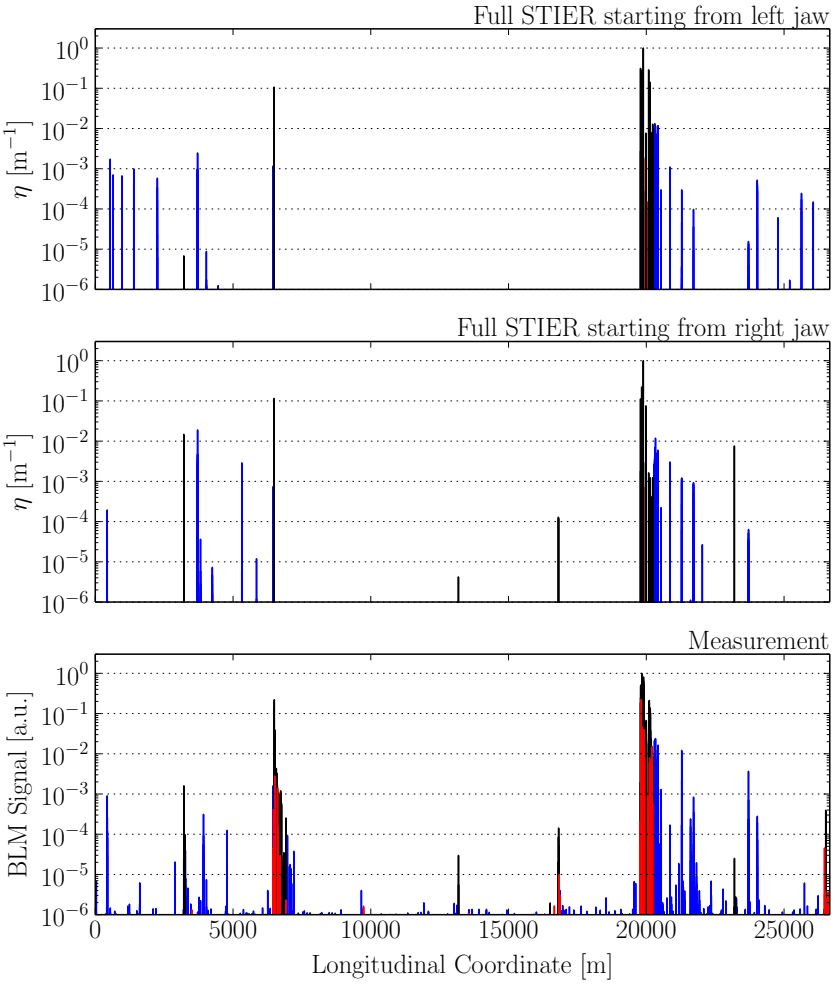

Figure 6.11: STIER simulations in the 2011 configuration with $^{208}Pb^{82+}$ beams at 3.5 Z TeV starting at the left and right collimator jaw, shown in comparison to the measured loss map. The simulations are carried out considering an impact parameter of 3 μm.

6.3.3 Simulations with different Impact Parameters

In the real machine, the impact parameter b of the ions hitting the collimators may vary. For the STIER simulations presented so far, an impact parameter of 3 μm was assumed, based on previous proton studies. As shown in Chap. 6.2.2, the production yield for very light fragments increases with increasing impact parameter. The difference in the fragment spectrum will lead to a change in the simulated loss maps, which is studied in this section.

The loss maps simulated with the full STIER approach for the three different impact parameters $1\,\mu$m, $3\,\mu$m and $10\,\mu$m are compared in Fig. 6.12 and Fig. 6.13. The loss patterns are qualitatively similar but the loss peak amplitudes differ quantitatively.

For the smallest studied impact parameter of $1\,\mu$m, the highest losses occur at the primary collimator in IR7. The main contribution of these losses arises from $^{208}\mathrm{Pb}^{82+}$ ions that were not fragmented but scattered at small angles in the TCP. They circulate inside the machine for one or multiple turns until they are intercepted again by the primary collimator. In reality, these ions are again subject to fragmentation and scattering inside of the TCP, which is not considered in STIER. In the latter, they are assumed to be absorbed in the TCP.

The losses at the DS region peak at $\eta = 10^{-3}$, which is smaller than in the other simulations, due to the large amount of $^{208}\mathrm{Pb}^{82+}$ ions surviving the initial passage through the TCP. The remaining losses in the aperture and the other collimators are located at elements which are also subject to losses for the other impact parameters, but the loss amplitudes are smaller.

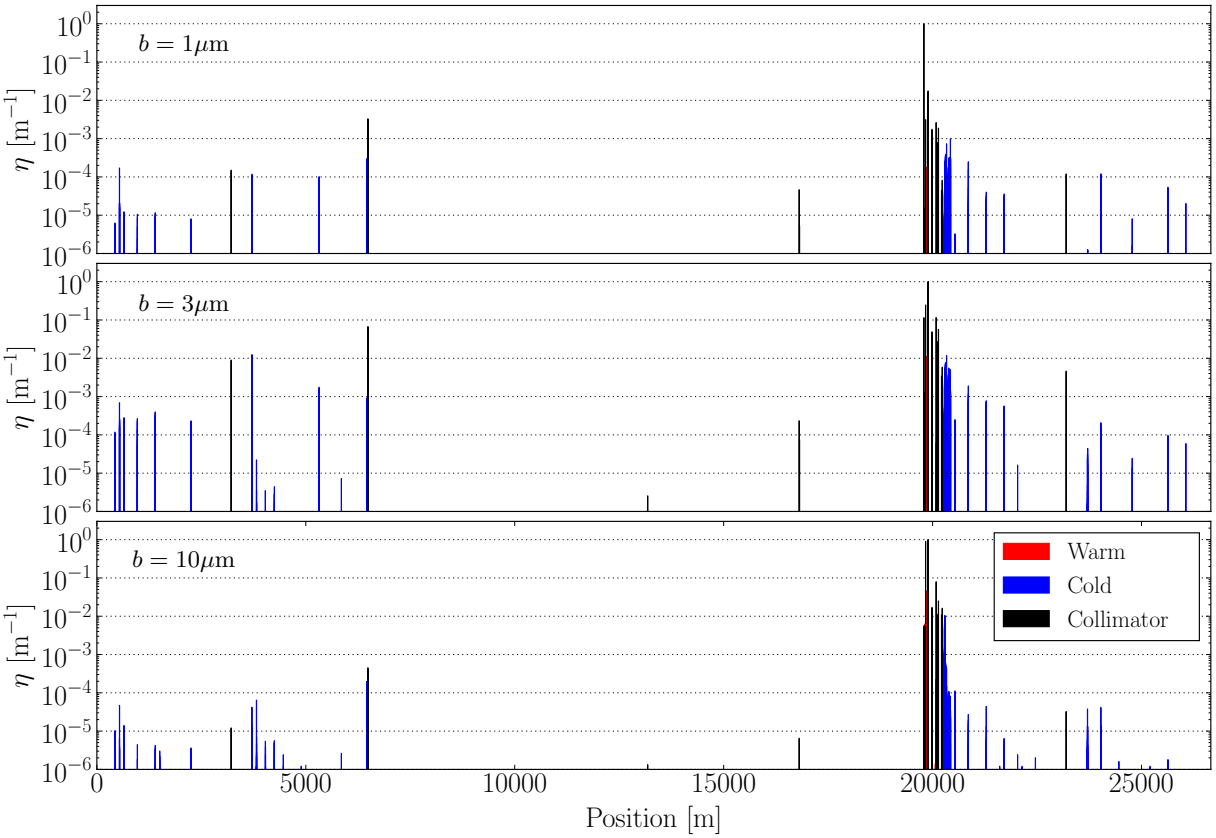

Figure 6.12: B1H loss maps for the 2011 configuration with $^{208}\mathrm{Pb}^{82+}$ beams at $3.5\,Z$ TeV simulated with the full STIER approach for the impact parameters $b = 1\,\mu$m, $b = 3\,\mu$m, $b = 10\,\mu$m.

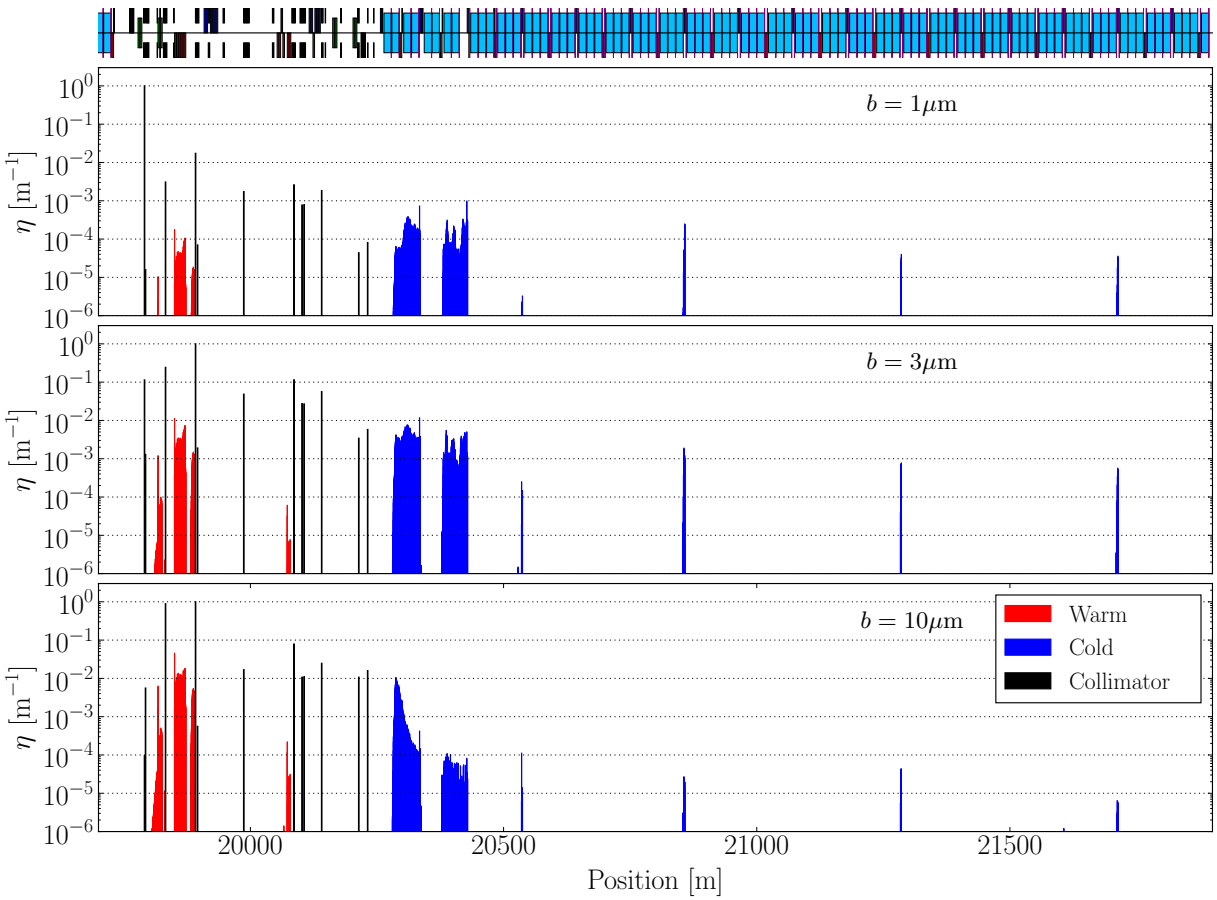

Figure 6.13: B1H loss maps zoomed to IR7 for the 2011 configuration with $^{208}\mathrm{Pb}^{82+}$ beams at $3.5\,Z$ TeV simulated with the full STIER approach for the impact parameters $b = 1\,\mu$m, $b = 3\,\mu$m, $b = 10\,\mu$m.

For the study cases with $b = 3\,\mu$m and $b = 10\,\mu$m, the highest losses are visible at a secondary collimator. The losses in the IR7 DS clusters peak at $\eta = 10^{-2}$ for $b = 3\,\mu$m. For $b = 10\,\mu$m the peak loss in the cold LHC regions is simulated in the DS1, while the peak loss in the DS2 is smaller by two orders of magnitude. This indicates that the residual ion fragments generated with $b = 10\,\mu$m have larger rigidity offsets and are mostly lost closer to the TCP than in the other simulated scenarios. The A1 to A4 loss spikes are significantly lower for the simulation with $b = 10\,\mu$m than with $b = 3\,\mu$m. As it was discussed in the previous section, these losses are mainly composed of heavy nuclei with masses close to $^{208}\mathrm{Pb}^{82+}$. These are significantly less abundant when the larger impact parameter is applied.

In conclusion, the choice of impact parameter is very important to accurately simulate the cleaning inefficiency of heavy-ion beams. For the smallest impact parameter, the losses at the TCP and hence the cleaning performance are overestimated, because ion fragmentation at subsequent turns is not included. This should be better modeled with an improved tool taking into account multiple fragmentation, presented in Chap. 7.

6.3.4 Loss Distribution of individual Isotopes

STIER allows studying of the distribution of losses for the individual isotopes. With the previous studies it became apparent that the measured loss pattern may be affected by light ion fragments not only in the warm regions just downstream of the collimators, but also in the superconducting magnets. In Fig. 6.14, the loss maps for five different isotopes are compared. Three heavy nuclei ($^{207}\mathrm{Pb}^{82+}$, $^{204}\mathrm{Tl}^{81+}$ and $^{206}\mathrm{Pb}^{82+}$) are studied, because they are relevant for important loss spikes simulated. In addition, two very light fragments (protons and $^{4}\mathrm{He}^{2+}$) are simulated to study their loss distribution. The loss peaks are normalized by the total number of ions of the respective species lost in the ring.

The top plot shows the loss pattern for the isotope $^{207}\mathrm{Pb}^{82+}$ with $\chi = 1.0048$. This isotope is generated via EMD with a relatively high cross section and has a small offset in rigidity compared to the main beam. It can hence travel in the machine over long distances. As expected, the losses are globally distributed, showing that the isotope is within the momentum acceptance of the arcs. The losses are mainly localized at collimators. Some losses are visible at the secondary collimators in IR7. The dominating part is simulated to be lost at the TCP in IR3, which is set to a momentum cut of 2×10^{-3}. Furthermore, losses are simulated at the TCTs in IR2 and IR8. It shall be shown later that for a different particle momentum and different optics, a significantly larger fraction of this isotope is lost at the TCT in IR2 (see Chap. 8.2).

The isotope $^{204}\mathrm{Tl}^{81+}$ with $\chi = 1.0072$ is the dominant species lost at the A1 loss peak. The global distribution for this isotope also shows a defined peak at the horizontal TCT in IR8 and significant losses in superconducting magnets from IR7 to IR2.

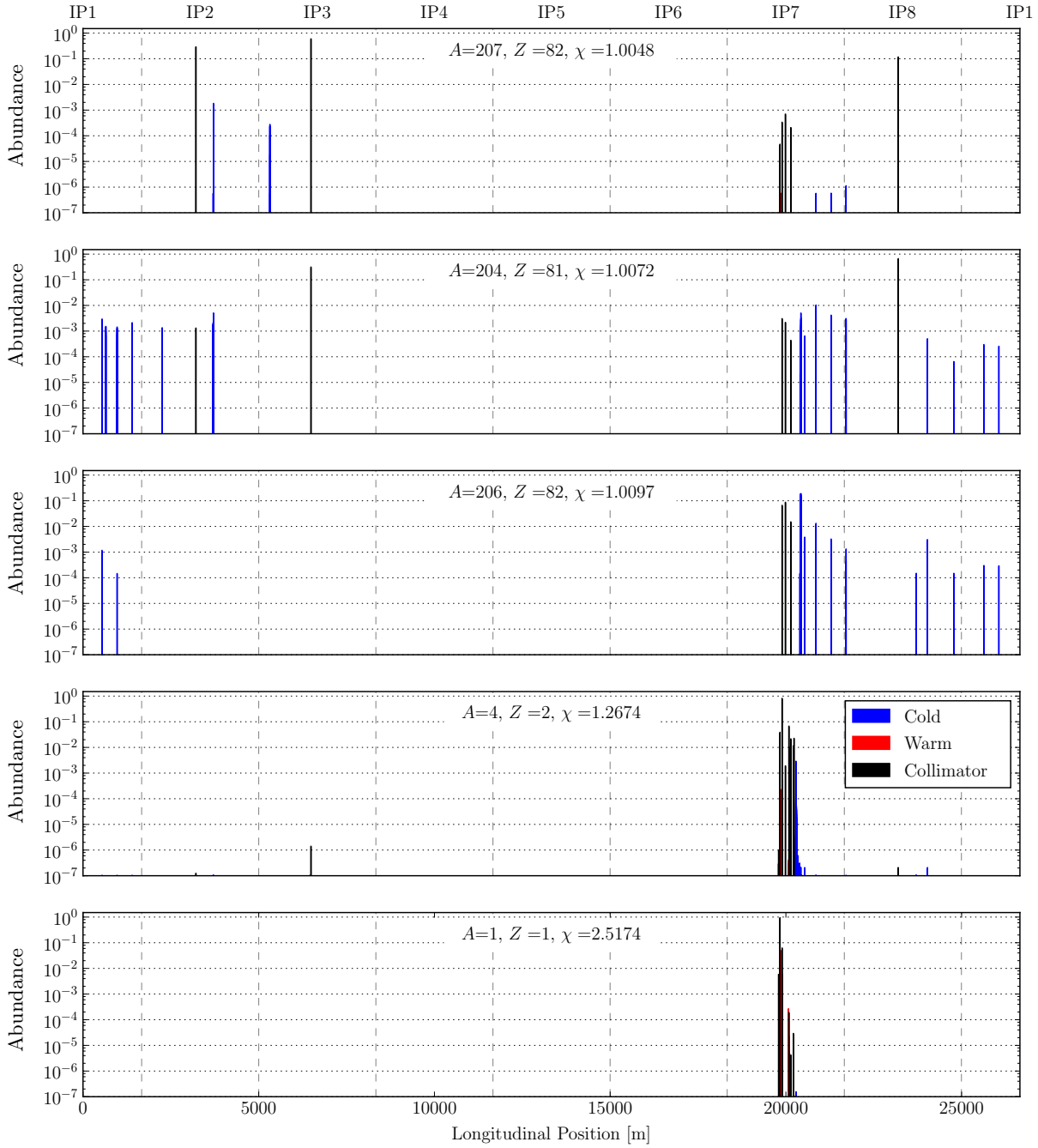

Figure 6.14: STIER simulated loss locations of the isotopes $^{207}Pb^{82+}$, $^{204}Tl^{81+}$, $^{206}Pb^{82+}$, $^{4}He^{2+}$, $^{1}H^{1+}$ (from top to bottom) in the 2011 heavy-ion configuration at 3.5 Z TeV. The vertical axis describes the number of lost particles normalized by the total number of particles of this species.

The fragments of the isotope $^{206}Pb^{82+}$ with $\chi = 1.0097$ are absorbed in the LHC aperture before they can reach the TCP in IR3. This isotope is generated via second order EMD or two first order EMD processes and dominates the losses in the DS2. Most of these ion fragments are lost in the latter, followed by the IR7 TCSGs and the arc region between IR7 and IR8.

In the domain of very large rigidity offsets, the losses are mostly localized in IR7 as shown on the example of $^{4}He^{2+}$ and $^{1}H^{1+}$. Both of them are produced with high abundances when $^{208}Pb^{82+}$ interacts with the primary collimator. All protons are lost in the IR7 collimation system, so they are not contributing to the losses in cold regions. Small fractions of the isotope $^{4}He^{2+}$ are also lost in the IR7 DS.

6.4 Chromatic Tracking in ICOSIM and SixTrack

ICOSIM tracks off-rigidity heavy ions by means of matrix multiplication with chromatic effects modeled in linear order. This approximation is valid for small rigidity offsets and becomes less accurate when δ_{eff} increases. SixTrack uses tracking maps derived from the accelerator Hamiltonian and does not truncate the contributions of dispersion (see Chap. 7).

To study the accuracy and importance of the chromatic modeling, tracking simulations of off-rigid isotopes are carried out with identical optics and initial conditions in STIER and ICOSIM. The isotopes $^{8}Li^{3+}$ (with $\delta_{\text{eff}} = 0.054$) and $^{207}Pb^{82+}$ (with $\delta_{\text{eff}} = -0.005$) were selected to study the tracking accuracy with different rigidity offsets. Assuming that the chromatic modeling in STIER is more accurate to that of ICOSIM, the comparison allows to quantify the tracking error implied by the linear truncation of the equation of motion in the ICOSIM implementation.

Both tracking simulations start at the edge of the right jaw of the horizontal TCP in IR7 with a

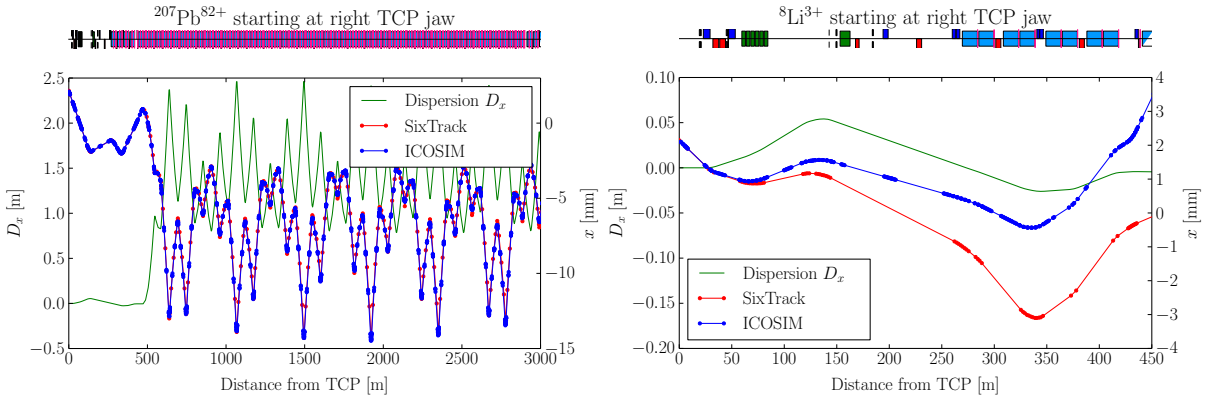

Figure 6.15: Comparison of the simulated tracks with ICOSIM and STIER for the two isotopes $^{8}Li^{3+}$ (left) and $^{207}Pb^{82+}$ (right) with identical starting conditions at the right jaw of the IR7 horizontal TCP. Note the different scales applied in the two plots.

starting angle identical to the angle of incidence at the collimator derived from the phase space parameters. The simulated tracks are compared in Fig. 6.15. For the isotope $^{207}Pb^{82+}$, the tracks simulated with STIER and ICOSIM are similar. At a distance of 2 km from the TCP, the horizontal positions simulated with the two codes differ by 200 μm.

For the isotope $^{8}Li^{3+}$, the horizontal position differs by 3 mm after a longitudinal distance of 450 m. This demonstrates the drastic impact of the linear approximation on the simulated track for particles with large rigidity offsets. In spite of the fact that these ions are lost closely to the TCP, the error on the simulated track may cause a large shift in their simulated loss position.

As demonstrated previously, particles with large rigidity offsets are created in the collimators. Therefore, a heavy-ion collimation simulation tool should rather use a tracking algorithm that is similar to SixTrack.

6.5 Summary and Conclusions

The STIER simulation tool was developed to assess the importance of the different approximations used in ICOSIM. The latter is implemented with a simplified fragmentation simulation where changes in angle and energy from the fragmentation process are not included. It was studied whether the accuracy can be increased by a more detailed fragmentation simulation only at the TCP. STIER cleaning simulations are based on combining FLUKA for an accurate fragmentation simulation and SixTrack where the heavy-ion fragments are tracked as protons with ion-equivalent rigidities.

The application of STIER to the 2011 heavy-ion run demonstrated that the tool can reproduce the measured loss patterns with an unprecedented accuracy. The studies have demonstrated that it is crucial to include the angle and energy of the particles that are scattered out of the TCP into the tracking simulation.

Given the good agreement with the measured data, it appears to be a valid approximation of simulating the fragmentation only in the TCP. Therefore, shortly after its introduction in 2014, STIER became the standard simulation tool for LHC heavy-ion collimation simulations at the LHC. It was used directly in machine studies during the 2015 heavy-ion operation at 6.37 Z TeV (see Chap. 8).

Nevertheless, the comparison of the loss maps with different impact parameters shows that the cleaning simulations can be further improved if also collimator interactions after the first TCP passage are included in the simulation setup. This functionality is provided by the successor of STIER, which is presented in the next chapter.

7. Heavy-Ion SixTrack

The STIER simulation tool shows a good agreement with the measured data. In order to further improve the agreement between simulation and measurement, the interaction of the heavy ions with all LHC collimators (not only with the TCP) should be included in the simulation setup. A possible solution to provide this functionality is the usage of the SixTrack-FLUKA active coupling. Using this framework also for heavy ions requires to store information about A and Z in SixTrack.
In this chapter, the new tracking tool heavy-ion SixTrack (hiSixTrack) is presented as one of the major results of this thesis. The physics models implemented in its tracking routine are based on symplectic tracking maps derived from a new Hamiltonian for multi-isotopic particle beams. In a second step, hiSixTrack is coupled to FLUKA to allow for fragmentation simulations at all collimators. The tracking and the fragmentation routine are individually benchmarked against STIER and the main version of FLUKA.

7.1 Requirements and Implementation Strategy

The following list summarizes the implementation tasks to be carried out in order to make the new tracking software heavy-ion SixTrack (hiSixTrack) operational.

- SixTrack assumes all particles to be protons. hiSixTrack shall provide additional arrays storing information about the particle rest mass m, nuclear charge number Z, and nuclear mass number A. For LHC studies it is reasonable to assume fully stripped ions (all electrons removed), such that the particle charge equals the nuclear charge. If required, an adequate extension to define the particle charge differently could be implemented.
- The reference species must be defined in a designated input option, preferably given in the `fort.3` file. Furthermore, the particle species of the initial bunch to be tracked must be read from an initial distribution file. This allows to track particles different from the reference species, starting from arbitrary positions in the machine.

- The tracking maps must be modified to accurately account for the magnetic rigidity of the particle, taking into account the mass to charge ratio with respect to the reference particle. Instead of using effective proton momenta as in STIER, the tracking maps should be implemented such that each particle carries its correct physical momentum.
- The algorithm which stores the information about particle losses must be changed to store also A and Z of the lost ion. This will allow studying the loss locations of individual isotopes and analyzing the isotope composition of losses.

7.2 Theoretical Description of Multi-Isotope Tracking

Particle tracking in SixTrack is performed on the basis of tracking maps for each beam line element. They define a transformation of the six-dimensional particle coordinates by the electromagnetic field of the beam line element.
Tracking maps for multi-isotopic particle beams can be derived from an appropriate Hamiltonian which incorporates information about the particle mass and charge with respect to the reference species. As a part of this thesis, a consistent mathematical framework for the derivation of heavy-ion tracking maps is introduced. It is based on a generalized Hamiltonian that is also applicable for particles different from the reference species. The derivation of this Hamiltonian follows the same approach as for the mono-isotopic Hamiltonian. In addition it takes into account the mathematical description of the magnetic rigidities treated in Chap. 2.1.2. Once derived, the multi-isotopic Hamiltonian is applied to vector potentials specific to the LHC beam line elements, to derive the corresponding tracking maps for multi-isotopic particle beams. Some contents of this section were published in [HBDM16].

7.2.1 Hamiltonian Formalism of Particle Motion

Consider a physical system described by the generalized position coordinates $\mathbf{q}$ and the canonical conjugate momentum $\mathbf{p}$. The individual components of $\mathbf{q}$ and $\mathbf{p}$ are called q_i and p_i, where $i = 1, 2, ..., N$. The generalized velocities are defined as $\dot{\boldsymbol{q}} = (\dot{x}, \dot{y}, \dot{z})$, where $\dot{q}_i = \frac{dq_i}{dt}$ and the time t is the independent variable. The time evolution of the coordinates obeys Hamilton's equation of motion and can hence be described by the Hamiltonian formalism. The set of canonical coordinates can be written as a $2\,N$-dimensional vector:

$$\mathbf{x} = (q_1, p_1, q_2, p_2, ..., p_N, q_N)^T . \tag{7.1}$$

To describe the particle motion in the magnets of a particle accelerator, the coordinates of the reference frame defined in Chap. 2.1.1 can be used as generalized coordinates.

The position parameter $s(t)$ increases monotonically and smoothly in time, so that Hamilton's equations can also be expressed using s as the independent variable [FLS65, Ree03]

$$\frac{\mathrm{d}q_i}{\mathrm{d}s} = \frac{\partial H}{\partial p_i}\,, \qquad \frac{\mathrm{d}p_i}{\mathrm{d}s} = -\frac{\partial H}{\partial q_i} \qquad i = 1, 2, ..., N\,. \tag{7.2}$$

Here, $H = H(p_i, q_i, s)$ is the Hamiltonian with the independent variable s. Using the vector notation introduced in Eq. (7.1), Hamilton's equations can be expressed in the simple manner

$$\frac{\mathrm{d}\mathbf{x}}{\mathrm{d}s} = \mathbf{S}\,\frac{\partial H}{\partial \mathbf{x}}\,, \qquad \text{with} \qquad \left(\frac{\partial H}{\partial \mathbf{x}}\right)_i = \frac{\partial H}{\partial x_i}\,, \qquad \text{and} \qquad i = 1, 2, ..., 2\,N. \tag{7.3}$$

The rearranging matrix $\mathbf{S}$ is the so-called *symplectic matrix*

$$\mathbf{S} = \begin{pmatrix} \mathbf{s} & \mathbf{0} & \cdots & \mathbf{0} \\ \mathbf{0} & \mathbf{s} & & \mathbf{0} \\ \vdots & & \ddots & \vdots \\ \mathbf{0} & \dots & \mathbf{0} & \mathbf{s} \end{pmatrix}, \qquad \text{with} \qquad \mathbf{s} = \begin{pmatrix} 0 & 1 \\ -1 & 0 \end{pmatrix} \quad \text{and} \quad \mathbf{0} = \begin{pmatrix} 0 & 0 \\ 0 & 0 \end{pmatrix}. \tag{7.4}$$

The particular shape of this matrix is determined by the specific ordering used for $\mathbf{x}$ and the representation of Hamilton's equations in Eq. (7.3) is referred to as their *symplectic form*. The set of canonical coordinates and momenta is often transformed by a mapping $\mathcal{T}$

$$\mathcal{T}: \quad \mathbf{x} = (q_1, p_1, q_2, p_2, ..., q_N, p_N)^T \quad \rightarrow \quad \mathbf{X} = (Q_1, P_1, Q_2, P_2, ..., Q_N, P_N)^T\,. \tag{7.5}$$

The transformation $\mathcal{T}$ is called canonical or symplectic if the new set of variables $\mathbf{X}$ is also obeying Hamilton's equations with respect to a transformed Hamiltonian $\mathcal{K}(Q_i, P_i, s)$

$$\frac{\mathrm{d}Q_i}{\mathrm{d}s} = \frac{\partial \mathcal{K}}{\partial P_i} \qquad \text{and} \qquad \frac{\mathrm{d}P_i}{\mathrm{d}s} = -\frac{\partial \mathcal{K}}{\partial Q_i} \qquad \text{with} \qquad i = 1, 2, ..., N\,. \tag{7.6}$$

This new Hamiltonian can be derived through a generating function. The Jacobian matrix $\mathcal{J}$ of the transformation $\mathcal{T}$ is defined by [RS95]

$$\mathcal{J}_{ij} = \left(\frac{\partial \mathbf{X}}{\partial \mathbf{x}}\right)_{i,j} = \frac{\partial X_i}{\partial x_j}\,, \qquad \text{with} \qquad i, j = 1, 2, ...2\,N\,. \tag{7.7}$$

The Jacobian matrix can be used to test the canonicality of a transformation or mapping.

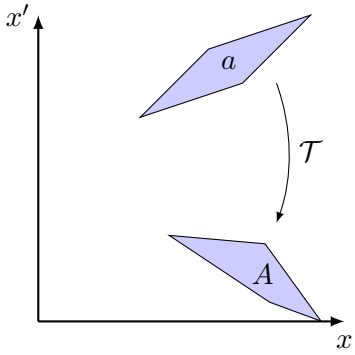

Figure 7.1: Illustration of symplecticity: the transformation $\mathcal{T}$ is symplectic if the phase space volume a occupied by a particle ensemble is conserved, such that $a = A$.

One can show that a given transformation is symplectic (or canonical) if the Jacobian matrix obeys the *symplectic condition* [RS95]:

$$\mathcal{J}^T \mathbf{S} \mathcal{J} = \mathbf{S} \,. \tag{7.8}$$

Symplecticity corresponds to a conservation of phase space volume throughout the transformation [Wol14], as illustrated in Fig. 7.1.

A particle moving in the accelerator lattice has three degrees of freedom $i = 1, 2, 3$. The dynamical behavior is thus described by a set of six coordinates. The generalized position coordinates are defined as $\boldsymbol{q} = (x, y, z)$ and their canonical conjugates, the generalized momenta as $\boldsymbol{p} = (p_x, p_y, p_z)$.

7.2.2 The Accelerator Hamiltonian for Multi-Isotopic Ion Beams

Literature [Rip85, BRS87, RS95, HRS95, Wol14] has so far discussed the accelerator Hamiltonian and the resulting equations of motion in the mono-isotopic scenario. This is valid if particles of the same species as reference particle should be tracked. In heavy-ion collimation studies, a large fraction of energy is carried by isotopes different from the reference species. Therefore, a more generic Hamiltonian should be used which incorporates the mass and charge ratio with respect to the reference particle.

A new Hamiltonian which fulfills these requirements was developed as a part of this thesis. The derivation shall be presented below. It shall be used later-on in this chapter to derive the tracking maps for the different beam line elements. These tracking maps are implemented in the new heavy-ion tracking tool hiSixTrack.

The derivation of the generalized multi-isotopic accelerator Hamiltonian follows the same approach as the mono-isotopic derivation presented in [Rip85, BRS87, Pro95]. If not indicated differently, the basic definitions used in the following are taken from these references. Fundamental differences are introduced with the normalization of the dynamic variables and the redefinition of δ, to be in line with Eq. (2.10).

In the following derivation, the rest mass of the considered particle is given as m, the charge as q and nuclear mass number as Z, while the equivalent quantities for the reference particle are given as m_0, q_0, A_0. Eventual ambiguities between the particle charge q and generalized position coordinate $\boldsymbol{q}$ shall be ruled out by using the vector notation for the latter, or q_i when referring to one particular coordinate.

The Multi-Isotopic Hamiltonian in a Straight Coordinate System

The generic Hamiltonian H is given by[1] [Rip85]

$$H(\boldsymbol{p}, \boldsymbol{q}, t) = p_i \dot{q}_i - \mathcal{L}(\boldsymbol{q}, \dot{\boldsymbol{q}}, t)\,, \tag{7.9}$$

where $\mathcal{L}$ is the Lagrangian of the particle and $\dot{q}_i = \frac{\mathrm{d}q_i}{\mathrm{d}t}$. The Lagrangian of an arbitrary particle with mass m and charge q moving in an electromagnetic field, defined by the magnetic vector potential $\boldsymbol{A}$ and the electric (scalar) potential ϕ, is given by

$$\mathcal{L}(\boldsymbol{q}, \dot{\boldsymbol{q}}, t) = -\frac{mc^2}{\gamma} - q\,\phi + q\,\dot{\boldsymbol{q}}\boldsymbol{A}\,. \tag{7.10}$$

The quantity γ is the relativistic Lorentz factor, which is a function of the velocity vector $\dot{\boldsymbol{q}}$. The canonical momentum is then defined by Hamilton's variation principle

$$p_i = \frac{\partial \mathcal{L}}{\partial \dot{q}_i} = m\,\dot{q}_i\,\gamma + q\,A_i\,. \tag{7.11}$$

Combining the Eqs. (7.9) and (7.10) yields for the Hamiltonian

$$H(\boldsymbol{p}, \boldsymbol{q}, t) = \sqrt{(\boldsymbol{p} - q\boldsymbol{A})^2\,c^2 + m^2c^4} + q\,\phi\,. \tag{7.12}$$

The Hamiltonian represents the total energy of the particle. It is advantageous to transform the independent variable from t to $s(t)$, which is valid because $s(t)$ is a bijection. The new dynamic variables can be obtained by comparing the action functional S before and after the transformation. Following the Euler-Lagrange equations, the temporal evolution of the canonical

[1] Note that the Einstein notation is used.

coordinates is such that the action functional is minimized. The action functional is given by the expression

$$S = \int_{t_0}^{t_1} \mathcal{L}(\boldsymbol{q}, \dot{\boldsymbol{q}}, t)\,\mathrm{d}t\,. \tag{7.13}$$

With the relation defined in Eq. (7.9), the action functional yields

$$S = \int_{t_0}^{t_1} (p_x\dot{x} + p_y\dot{y} + p_z\dot{z} - H)\,\mathrm{d}t\,, \tag{7.14}$$

for the set of canonical coordinates

$$(x, p_x), (y, p_y), (z, p_z)\,. \tag{7.15}$$

After the transformation of the independent variable t to the path length s, the action functional is given by

$$S = \int_{s_0}^{s_1} (p_x x' + p_y y' - Ht' + p_z)\,\mathrm{d}s\,, \tag{7.16}$$

where $q_i' = \frac{\mathrm{d}q_i}{\mathrm{d}s}$. The direct comparison of the original and the transformed action functional shows that the new set of canonical coordinates is given by

$$(x, p_x), (y, p_y), (-t, H)\,. \tag{7.17}$$

The transformed Hamiltonian $\tilde{H}$ yields

$$\tilde{H} = -p_z\,. \tag{7.18}$$

Taking into account that H represents the full ion energy E and elementary transformations of Eq. (7.12), the new Hamiltonian is given by

$$\tilde{H} = -p_z = -\sqrt{\frac{(E - q\phi)^2}{c^2} - m^2c^2 - (p_x - qA_x)^2 - (p_y - qA_y)^2} - qA_z\,. \tag{7.19}$$

The total particle energy E in the square root is a very large quantity. The Hamiltonian should be expandable to allow for the analytic treatment of complex vector potentials. This requires the dynamic variables in the square root to be small.

The following substitution of p_i, A_i, $\tilde{H}$ and E serves the purpose of obtaining small dynamic variables in the square root, while maintaining the validity of Hamilton's equations

$$\begin{aligned} p_i \to \tilde{p}_i &= \frac{p_i}{P_0}\frac{m_0}{m}\,, \qquad & \tilde{H} \to \bar{H} &= \frac{\tilde{H}}{P_0}\frac{m_0}{m}\,, \\ qA_i \to \chi a_i &= \chi\frac{q_0 A_i}{P_0}\,, \qquad & E \to \tilde{E} &= \frac{E}{P_0}\frac{m_0}{m}\,. \end{aligned} \tag{7.20}$$

This is a different definition than usually given in literature, where the quantities are typically normalized by P_0 or E_0 (see e.g. [Rip85]). The definition introduced above also takes into account the mass of the particle relative to the mass of the reference particle. This definition shall allow an elegant shape of the tracking maps introduced below. Note the normalized vector potential a_i which is defined equally as in derivations of the mono-isotopic Hamiltonian [Rip85]. This allows using the same vector potentials already introduced for the derivation of the mono-isotopic tracking maps.

Expressed in terms of the new coordinates, and assuming that a gauge can be found such that $\phi = 0$, the transformed Hamiltonian after applying the set of substitutions is given by

$$\bar{H} = -\sqrt{\frac{m_0^2}{m^2}\left(\frac{E^2 - m^2c^4}{P_0^2c^2}\right) - (\tilde{p}_x - \chi a_x)^2 - (\tilde{p}_y - \chi a_y)^2} - \chi a_z\,. \tag{7.21}$$

Using the relativistic energy-momentum relation and Eq. (2.10), this can be simplified to

$$\bar{H} = -\sqrt{(1+\delta)^2 - (\tilde{p}_x - \chi a_x)^2 - (\tilde{p}_y - \chi a_y)^2} - \chi a_z\,. \tag{7.22}$$

This equation is similar to the standard expression used in literature [Rip85]. It should, however, be kept in mind that the quantities $\tilde{p}_i$, $\bar{H}$ and δ are defined differently. Furthermore, instead of the particle charge q, the normalized vector potential is multiplied by χ.

To describe also the longitudinal particle motion (e.g. the synchrotron motion) by small quantities, another transformation is required

$$(x, \tilde{p}_x), (y, \tilde{p}_y), (-t, \tilde{E}) \to (X, P_x), (Y, P_y), (\sigma, p_\sigma)\,. \tag{7.23}$$

This transformation can be provided using the following generating function of second order

$$F_2 = xP_x + yP_y + (s - \beta_0 ct)\left(p_\sigma + \frac{E_0}{\beta_0 P_0 c}\right)\,. \tag{7.24}$$

The transformed variables Q_i, P_i and the new Hamiltonian K follow from the following relations [HRS95]

$$\tilde{p}_i = \frac{\partial F_2}{\partial q_i} \qquad Q_i = \frac{\partial F_2}{\partial P_i} \qquad K = \bar{H} + \frac{\partial F_2}{\partial s} = \bar{H} + p_\sigma \,. \tag{7.25}$$

The transformed coordinates are then related to the initial coordinates as

$$X = x \,, \qquad Y = y \,, \qquad \sigma = s - \beta_0 c t \,, \tag{7.26}$$

$$P_x = \tilde{p}_x \,, \qquad P_y = \tilde{p}_y \,, \qquad p_\sigma = \frac{\frac{m_0}{m} E - E_0}{\beta_0 P_0 c} \,. \tag{7.27}$$

The new Hamiltonian yields

$$K = p_\sigma - \sqrt{(1+\delta)^2 - (P_x - \chi a_x)^2 - (P_y - \chi a_y)^2} - \chi a_z \,. \tag{7.28}$$

The new longitudinal coordinate σ describes the difference in arrival time with respect to the reference particle. The quantity p_σ is the canonical conjugate of σ. After a last transformation for convenience $P_i \to p_i$, $K \to H$, the final generic accelerator Hamiltonian is written as

$$H = p_\sigma - \sqrt{(1+\delta)^2 - (p_x - \chi a_x)^2 - (p_y - \chi a_y)^2} - \chi a_z \,. \tag{7.29}$$

This Hamiltonian describes the particle motion in a straight coordinate system.

The Multi-Isotopic Hamiltonian in a Curved Coordinate System

In a curved coordinate system, the derivation of the Hamiltonian is identical, but the coordinates are canonically transformed as follows

$$(x, y, z) \to (X, Y, S) \,, \tag{7.30}$$

$$(p_x, p_y, p_z) \to (p_X, p_Y, p_S) \,, \tag{7.31}$$

$$(A_x, A_y, A_z) \to (A_X, A_Y, A_S) \,, \tag{7.32}$$

where X, Y, S are the position coordinates in the curved reference frame, as illustrated in Fig. 7.2. The full derivation is shown in Appendix A.4 and is discussed in detail in [Wol14]. Assuming a horizontal bending, the position coordinates in the old and new coordinate system are related

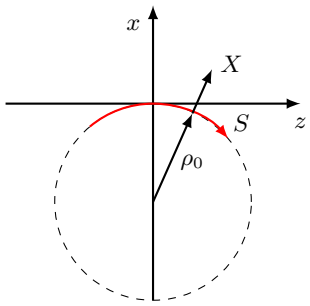

Figure 7.2: Transformation of the straight coordinate system (x, y, z) into the curvilinear system (X, Y, S). Based on [Wol14].

as follows

$$\begin{aligned} x &= (\rho_0 + X)\,\cos\left(h_x\,S\right) - \rho_0\,, \\ y &= Y, \\ z &= (\rho_0 + X)\,\sin\left(h_x\,S\right)\,, \end{aligned} \tag{7.33}$$

with the well-known curvature $h_x = \frac{1}{\rho_0}$ of the reference frame. From the generating function in Eq. (A.10), the transformation of the momentum coordinates can be shown to be

$$\begin{aligned} P_X &= p_x\,\cos\left(h_x\,S\right) + p_z \sin\left(h_x\,S\right)\,, \\ P_Y &= p_y\,, \\ P_S &= p_z\,\left(1 + h_x\,X\right)\cos\left(h_x\,S\right) - p_x\,\left(1 + h_x\,X\right)\sin\left(h_x\,S\right)\,. \end{aligned} \tag{7.34}$$

Finally, the transformed vector potentials are given as

$$\begin{aligned} A_X &= A_x\,\cos\left(h_x\,S\right) - A_z\,\sin\left(h_x\,S\right)\,, \\ A_Y &= A_y\,, \\ A_S &= A_z\,\cos\left(h_x\,S\right) + A_x\,\sin\left(h_x\,S\right)\,. \end{aligned} \tag{7.35}$$

Again, for convenience, a redefinition of the symbols used for the position coordinates is applied to have consistency in the tracking maps defined below $(X, Y, S) \rightarrow (x, y, s)$. The physical meaning of these quantities should be kept in mind when tracking maps are derived in curved coordinate systems. The final Hamiltonian after this transformation is given by [F+13]

$$H = p_\sigma - (1 + h_x(s)\,x)\,\left(\sqrt{(1+\delta)^2 - (p_x - \chi a_x(s))^2 - (p_y - \chi a_y(s))^2} + \chi a_s(s)\right)\,. \tag{7.36}$$

For the case of a straight coordinate system with $h_x = 0$, the quantities described in the curved reference frame converge into those derived for the straight coordinate system.

In the mono-isotopic limit of $m \to m_0$ and $q \to q_0$, which implies $\chi \to 1$, all derived equations converge to the standard expressions derived from the mono-isotopic Hamiltonian [RS95].

Expansion

The Hamiltonian presented in Eq. (7.36) is exact, thus without the usage of approximations. Depending on the complexity of the electromagnetic field of the beam-line element and the corresponding boundary conditions it can be useful to expand the square root in $\frac{(p_x-\chi a_x)^2+(p_y-\chi a_y)^2}{(1+\delta)^2}$. By virtue of the normalization applied in Eq. (7.20), this is a small quantity, such that the second order Taylor expansion delivers a good approximation of the physical problem:

$$H \approx p_\sigma - (1 + h_x(s)x) \left[(1+\delta) \left(1 - \frac{1}{2} \frac{(p_x - \chi a_x(s))^2 + (p_y - \chi a_y(s))^2}{(1+\delta)^2} \right) + \chi a_s(s) \right] . \tag{7.37}$$

The accuracy of tracking maps derived from the expanded Hamiltonian is studied for the example of a drift space in the mono-isotopic case in [F+13]. It shows that the tracking maps derived from the exact and expanded Hamiltonian are in very good agreement if p_x and p_y are small. Significant differences arise only for values of p_x and p_y which are so large that the particle would be lost in the magnet aperture after only a few mm.

7.3 Tracking Maps for Beam-Line Elements

In this section, the tracking maps for various types of individual beam line elements (such as drift space, dipole, quadrupole and RF cavity) are derived, based on the Hamiltonian for multi-isotopic particle beams introduced before. They are the baseline for the implementation of hiSixTrack, which was the main aim of this thesis project.

For the dipole and the quadrupole, also the thick lens tracking maps are presented, although the implementation in hiSixTrack performs thin lens tracking. All implemented tracking maps, except for the drift space, are derived from the expanded multi-isotopic accelerator Hamiltonian in thin lens approximation.

The symplecticity of the tracking maps for the different beam line elements is demonstrated by means of the Jacobian matrix in Appendix A.1. The technical implementation in hiSixTrack is presented in Appendix A.5.4.

7.3.1 Drift Space

Exact Hamiltonian

A drift space is defined by the absence of electromagnetic fields, thus the vector potential is zero in all directions. With regard to Eq. (7.36), the Hamiltonian is then given by

$$H = p_\sigma - \sqrt{(1+\delta)^2 - p_x^2 - p_y^2}\,. \tag{7.38}$$

Taking into account that δ is a function of p_σ with the derivative $\frac{\partial \delta}{\partial p_\sigma} = \frac{\beta_0}{\beta}$, the equations of motion derived from this Hamiltonian are

$$x' = \frac{dx}{ds} = \frac{\partial H}{\partial p_x} = \frac{p_x}{\sqrt{(1+\delta)^2 - p_x^2 - p_y^2}}\,, \qquad p_x' = -\frac{\partial H}{\partial x} = 0\,, \tag{7.39}$$

$$y' = \frac{dy}{ds} = \frac{\partial H}{\partial p_y} = \frac{p_y}{\sqrt{(1+\delta)^2 - p_x^2 - p_y^2}}\,, \qquad p_y' = -\frac{\partial H}{\partial y} = 0\,, \tag{7.40}$$

$$\sigma' = \frac{d\sigma}{ds} = \frac{\partial H}{\partial p_\sigma} = \left(1 - \frac{\beta_0}{\beta_z}\right)\,, \qquad p_\sigma' = -\frac{\partial H}{\partial \sigma} = 0\,, \tag{7.41}$$

where β_z is defined as

$$\beta_z = \beta\,\frac{\sqrt{(1+\delta)^2 - p_x^2 - p_y^2}}{1+\delta}\,. \tag{7.42}$$

Starting from the equations of motion, the transformation of the initial set of coordinates $(\mathbf{q}^I, \mathbf{p}^I)$ at the beginning of the drift space is related to their final coordinates $(\mathbf{q}^F, \mathbf{p}^F)$ by the following set of equations

$$x^F = x^I + \frac{p_x^I}{\sqrt{(1+\delta)^2 - p_x^2 - p_y^2}}\,L\,, \qquad p_x^F = p_x^I\,, \tag{7.43}$$

$$y^F = y^I + \frac{p_y^I}{\sqrt{(1+\delta)^2 - p_x^2 - p_y^2}}\,L\,, \qquad p_y^F = p_y^I\,, \tag{7.44}$$

$$\sigma^F = \sigma^I + \left(1 - \frac{\beta_0}{\beta_z}\right)\,L\,, \qquad p_\sigma^F = p_\sigma^I\,, \tag{7.45}$$

where, L denotes the length of the drift space. This type of mapping is referred to as a tracking map.

Expanded Hamiltonian

Combining Eq. (7.37) and Eq. (7.38) results into the expanded Hamiltonian

$$H \approx p_\sigma - \delta + \frac{1}{2}\,\frac{p_x^2 + p_y^2}{(1+\delta)}\,. \tag{7.46}$$

Hamilton's equations of motion are then

$$x' = \frac{dx}{ds} = \frac{\partial H}{\partial p_x} = \frac{p_x}{(1+\delta)}\,, \qquad p'_x = -\frac{\partial H}{\partial x} = 0\,, \tag{7.47}$$

$$y' = \frac{dy}{ds} = \frac{\partial H}{\partial p_y} = \frac{p_y}{(1+\delta)}\,, \qquad p'_y = -\frac{\partial H}{\partial y} = 0\,, \tag{7.48}$$

$$\sigma' = \frac{d\sigma}{ds} = \frac{\partial H}{\partial p_\sigma} = 1 - \frac{\beta_0}{\beta}\left(1 + \frac{1}{2}\,\frac{p_x^2 + p_y^2}{(1+\delta)^2}\right)\,, \qquad p'_\sigma = -\frac{\partial H}{\partial \sigma} = 0\,. \tag{7.49}$$

Note the different definition of x' with respect to the exact Hamiltonian. The resulting tracking map for the drift space from the expanded Hamiltonian yields

$$x^F = x^I + \frac{p_x^I}{1+\delta}\,L\,, \qquad p_x^F = p_x^I\,, \tag{7.50}$$

$$y^F = y^I + \frac{p_y^I}{1+\delta}\,L\,, \qquad p_y^F = p_y^I\,, \tag{7.51}$$

$$\sigma^F = \sigma^I - L\,\frac{\beta_0}{\beta}\left(1 + \frac{1}{2}\,\frac{(p_x^I)^2 + (p_y^I)^2}{(1+\delta)^2}\right)\,, \qquad p_\sigma^F = p_\sigma^I\,. \tag{7.52}$$

The direct comparison of x' for the expanded and the exact drift space shows that they agree if p_x and p_y are small quantities. Since 2013, the exact Hamiltonian is implemented in SixTrack.

The modification of tracking maps for the drift space is not necessary for hiSixTrack, because the key quantity β_0/β is defined in SixTrack as follows

$$\frac{\beta_0}{\beta} = \frac{E}{p\,c}\,\frac{p_0\,c}{E}\,. \tag{7.53}$$

When the correct energy and momentum are assigned to the heavy ions, this expression is also valid in the multi-isotopic case.

7.3.2 Dipole

For simplicity, parts of the following derivations are only considered for a horizontal bending (x direction), but they are also valid for vertical bending by permuting x and y. The uniform

magnetic field in a horizontal bending dipole can be described by the vector potential [Wol14]

$$A_x = 0\,, \qquad A_y = 0\,, \qquad A_s = -B_y x \left(1 - \frac{h_x x}{2(1+h_x x)}\right). \tag{7.54}$$

Ideally, the vertical magnetic field B_y is matched to the reference momentum and charge such that the bending radius of the reference particle yields $\rho_0 = h_x^{-1}$. In reality, the magnet strength may differ from the reference, such that the ideal particle is bent with the radius $\rho^i = k_0^{-1}$ and

$$B_y = \frac{P_0 k_0}{q_0}\,. \tag{7.55}$$

Combining Eq. (7.36) and Eq. (7.54) delivers the following Hamiltonian

$$H = p_\sigma - (1+h_x x)\, p_z + \chi\, k_0 \left(x + \frac{h_x x^2}{2}\right), \tag{7.56}$$

with

$$p_z = \sqrt{(1+\delta)^2 - p_x^2 - p_y^2}\,. \tag{7.57}$$

Omitting non-linear and constant terms delivers for the expanded Hamiltonian

$$H \approx p_\sigma - \delta - (h_x x)(1+\delta) + \frac{1}{2}\frac{p_x^2 + p_y^2}{(1+\delta)} + \chi\, k_0 \left(x + \frac{h_x x^2}{2}\right). \tag{7.58}$$

Thick Dipole

The following derivation is done assuming a sector magnet or a dipole with straight edges. With the expanded Hamiltonian and considering that δ is a function of p_σ with the derivative $\frac{\mathrm{d}\delta}{\mathrm{d}p_\sigma} = \frac{\beta_0}{\beta}$, the equations of motion become

$$x' = \frac{\partial H}{\partial p_x} = \frac{p_x}{1+\delta}\,, \qquad p_x' = -\frac{\partial H}{\partial x} = h_x\,(1+\delta) - \chi\, k_0\,(1+h_x x)\,, \tag{7.59}$$

$$y' = \frac{\partial H}{\partial p_y} = \frac{p_y}{1+\delta}\,, \qquad p_y' = -\frac{\partial H}{\partial y} = 0, \tag{7.60}$$

$$\sigma' = \frac{\partial H}{\partial p_\sigma} = 1 - \frac{\beta_0}{\beta}\left(1 + h_x x + \frac{1}{2}\frac{p_x^2 + p_y^2}{(1+\delta)^2}\right), \qquad p_\sigma' = -\frac{\partial H}{\partial \sigma} = 0\,, \tag{7.61}$$

where $q_i' = \frac{\mathrm{d}q_i}{\mathrm{d}s}$. In the vertical direction, the dipole acts like a drift space.

Starting from Eq. (7.59), the horizontal motion can be described by the differential equation

$$x''(s) + \frac{\chi\, h_x\, k_0}{(1+\delta)}\, x = \frac{h_x\, \delta}{(1+\delta)} + \frac{h_x - \chi\, k_0}{(1+\delta)}\,. \tag{7.62}$$

The homogeneous part of the equation describes an oscillation with frequency $\omega_x = \sqrt{\frac{\chi\, h_x\, k_0}{1+\delta}}$. Note that the inhomogeneous part of the differential equation Eq. (7.62) represents the dispersion in the magnet. Compared to the corresponding mono-isotopic equation presented in [HRS95], an additional term $\frac{h_x - \chi\, k_0}{(1+\delta)}$ appears, which takes into account the isotopic dispersion and a mismatched magnetic field. If the magnetic field is perfectly matched for the reference momentum ($h_x = k_0$), this term vanishes for particles of the reference species.

The differential equation Eq. (7.62) can be solved by a superposition of sine and cosine functions. The quantities x^F and y^F can be subsequently used to derive p_x^F and p_y^F by integrating Eq. (7.59) and Eq. (7.60). For convenience, the following quantities are introduced

$$S_x = \sin \omega_x L\,, \qquad C_x = \cos \omega_x L\,, \tag{7.63}$$

$$\omega_x^2 = \frac{\chi\, h_x\, k_0}{1+\delta}\,, \qquad \Omega_x = \frac{1+\delta}{k_0\, \chi} - \frac{1}{h_x}\,. \tag{7.64}$$

The resulting tracking map for the transverse coordinates is then given by

$$x^F = x^I\, C_x + p_x^I\, \omega_x^{-1} \frac{S_x}{(1+\delta)} + \Omega_x\, (1 - C_x)\,, \tag{7.65}$$

$$p_x^F = -x^I\, \omega_x\, (1+\delta)\, S_x + p_x^I\, C_x + (1+\delta)\, \Omega_x\, \omega_x\, S_x\,, \tag{7.66}$$

$$y^F = y^I + (y')^I\, L, \tag{7.67}$$

$$p_y^F = p_y^I\,. \tag{7.68}$$

The longitudinal coordinates can be derived by integrating Eq. (7.61) after replacing x, y, p_x and p_y by the transformed quantities. The resulting expression is identical to that derived for the mono-isotopic case in [DMFF15], with re-defined quantities in Eq. (7.63) and Eq. (7.64).

Thin Dipole

Thick lens tracking is very demanding in terms of time and computing power. Also, the exact motion of the particle inside the magnet is often not required and the global tracking through a large accelerator like the LHC can be well approximated by thin lenses. The tracking routine used in hiSixTrack and in SixTrack for collimation studies is based on thin lens tracking, so the derivation of thin lens tracking maps is of particular interest.

The Hamiltonian in Eq. (7.58) can be decomposed into the expanded Hamiltonian H_D of a drift space, defined in Eq. (7.46), and the contribution from electromagnetic fields H_L as follows

$$H = H_D - h_x\, x\,(1+\delta) + \chi\, k_0 \left(x + \frac{h_x\, x^2}{2}\right) = H_D + H_L\,. \tag{7.69}$$

In the thin lens approximation, this Hamiltonian is changed to [HRS95]

$$H = H_D + \bar{\delta}(s - s_0)\, L\, H_L\,, \tag{7.70}$$

where $\bar{\delta}(s - s_0)$ is the Dirac δ distribution which is non-zero only at the center s_0 of the magnet [Dir58]. Starting from this Hamiltonian, the equations of motion are given by

$$x' = \frac{p_x}{(1+\delta)}\,, \tag{7.71}$$

$$p_x' = L\,\bar{\delta}(s - s_0)\,\left[h_x(1+\delta) - \chi\, k_0\,(1 + h_x\, x)\right]\,, \tag{7.72}$$

$$y' = \frac{p_y}{(1+\delta)}\,, \tag{7.73}$$

$$p_y' = 0\,, \tag{7.74}$$

$$\sigma' = 1 - \frac{\beta_0}{\beta} - \frac{\beta_0}{\beta}\,\left[\frac{1}{2}\left(x'^2 + y'^2\right)\right] - \frac{\beta_0}{\beta}\, h_x\, x\,(1+\delta)\,\bar{\delta}(s - s_0)\, L\,, \tag{7.75}$$

$$p_\sigma' = 0\,. \tag{7.76}$$

The solution of the differential equations in the thin lens approximation are obtained by integrating over s, in the range from $s - \epsilon$ to $s + \epsilon$ in the limit of $\epsilon \to 0$. The tracking map for x with the equation of motion given in Eq. (7.71) is obtained as follows

$$x^F - x^I = \lim_{\epsilon \to 0}\left[\int_{s_0-\epsilon}^{s_0+\epsilon} \frac{p_x}{(1+\delta)}\,\mathrm{d}s\right] = 0\,. \tag{7.77}$$

Applying the same approach for the remaining quantities, the transformation rules for the dipole in thin lens approximation are given by

$$x^F = x^I\,, \qquad p_x^F = p_x^I + L\left[h_x\,(1+\delta) - k_0\,\chi\,(1 + h_x\, x^I)\right]\,, \tag{7.78}$$

$$y^F = y^I\,, \qquad p_y^F = p_y^I\,, \tag{7.79}$$

$$\sigma^F = \sigma^I - \frac{\beta_0}{\beta}\, h_x\, x^I\, L\,, \qquad p_\sigma^F = p_\sigma^I\,. \tag{7.80}$$

The change in p_x hence depends on the initial horizontal offset x^I.

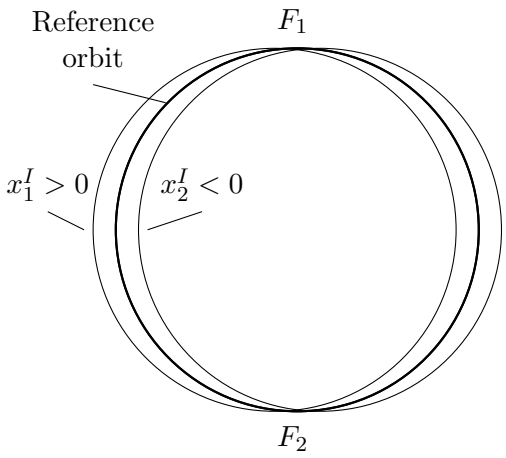

Figure 7.3: Weak focusing in a transverse magnetic dipole field. Two particles starting with different inital offsets x_1^I and x_2^I are focused on two distinct focal points F_1 and F_2.

Two particles with the same set of χ and δ hence receive a different change in transverse momentum if they pass the dipole at two different initial offsets x_1^I and x_2^I. The difference in the transverse momentum transfer is such that both particles are ultimately focused to a defined focal point, as illustrated in Fig. 7.3. This effect is known as weak focusing [Wol14].

The effect of dispersion is taken into account by the dependence on δ and χ. The dispersive offset from chromatic offsets (chromatic dispersion) is which is a pure function of the particle velocity and hence δ. The dispersive offset from the different mass to charge ratio (isotopic dispersion) is described by χ. Chromatic and isotopic dispersion can compensate or enhance each other.

For $x = 0$, the change in x' is given as

$$(x')^F = (x')^I + h_x\, L - \frac{\chi}{1+\delta}\, k_0\, L\,. \tag{7.81}$$

This shows that, in addition to the nominal bending $h_x\, L$, the particle receives a change of x' that is proportional to $\frac{\chi}{1+\delta}$, well known from Eq. (2.9). This shows that the generic Hamiltonian delivers the expected dynamics and correctly accounts for the isotopic dispersion.

7.3.3 Thin Transverse Kicker Magnet

Transverse kicker magnets are used in accelerators as the LHC to control the beam orbit. Technically they are identical to bending magnets, with the exception that $h_x = 0$, so the reference trajectory in these magnets is not bent. The Hamiltonian for a transverse kicker magnet in thin

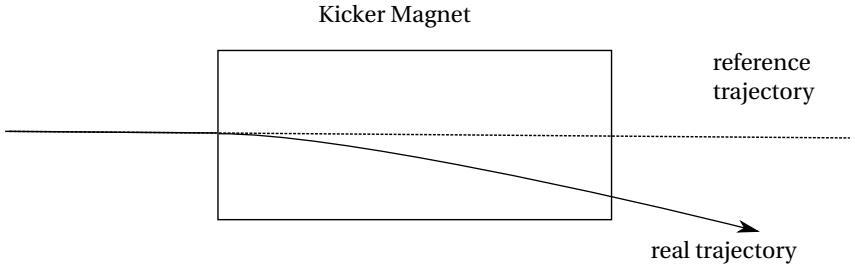

Figure 7.4: Schematics of a transverse kicker magnet. Kicker magnets are dipole magnets where the reference trajectory is not bent, thus $h_x = 0$.

lens approximation is given by

$$H = H_D + \chi\, k_0\, L\, \bar{\delta}(s - s_0)\,. \tag{7.82}$$

The resulting equations of motion lead to the following transport map

$$p_x^F = p_x^I - k_0\, \chi\, L\,, \tag{7.83}$$
$$p_y^F = p_y^I\,, \tag{7.84}$$
$$p_\sigma^F = p_\sigma^I\,. \tag{7.85}$$

Taking into account that $x' = \frac{p_x}{(1+\delta)}$, the transformation of x' yields

$$(x')^F = (x')^I - k_0\, L\, \frac{\chi}{(1+\delta)}\,. \tag{7.86}$$

As expected from Eq. (2.9), the change in x' is proportional to $\frac{\chi}{1+\delta}$.

7.3.4 Quadrupole

The vector potential of a horizontal or vertical quadrupole magnet is given by [RS95]

$$A_x = 0\,, \qquad A_y = 0\,, \qquad A_z = -\frac{1}{2}\, g\,(y^2 - x^2)\,. \tag{7.87}$$

Expressed in the normalized coordinates, the longitudinal vector potential becomes

$$a_z = -\frac{1}{2}\frac{q_0}{P_0} g\,(y^2 - x^2) = -\frac{1}{2}\, k\,(y^2 - x^2)\,. \tag{7.88}$$

The quantity g is the quadrupole gradient introduced in Chap. 2.2.1, and $k = \frac{q_0}{P_0} g$ is the normalized quadrupole gradient which has the unit $[k] = \mathrm{m}^{-2}$. The optics of a machine in a

certain configuration is defined by a full set of k_i with $i = 1, ..., N_q$, where N_q is the number of quadrupoles in the machine. Thanks to the definition of the normalized quadrupole gradient (see Eq. (2.17)), the machine optics can be described by identical values valid for different energies, even if in reality the magnet currents are ramped with increasing beam energy.

The reference trajectory passes through the center of the quadrupole, where no magnetic field is present and is hence straight with $h_x = 0$. The exact Hamiltonian of a quadrupole yields

$$H = p_\sigma - \sqrt{(1+\delta)^2 - p_x^2 - p_y^2} + \frac{1}{2}\, k\, \chi\, (x^2 - y^2)\,. \tag{7.89}$$

Thick quadrupole

The expanded Hamiltonian for the quadrupole is then given by

$$H = p_\sigma + \frac{1}{2}\frac{p_x^2 + p_y^2}{(1+\delta)} + \frac{1}{2}\,\chi\, k\, (x^2 - y^2) - \delta\,. \tag{7.90}$$

Hamilton's equations deliver the following equations of motion

$$x' = \frac{\partial H}{\partial p_x} = \frac{p_x}{(1+\delta)}\,, \qquad p_x' = -\frac{\partial H}{\partial x} = -\chi\, k\, x\,, \tag{7.91}$$

$$y' = \frac{\partial H}{\partial p_y} = \frac{p_y}{(1+\delta)}\,, \qquad p_y' = -\frac{\partial H}{\partial y} = \quad \chi\, k\, y\,, \tag{7.92}$$

$$\sigma' = \frac{\partial H}{\partial p_\sigma} = 1 - \frac{\beta_0}{\beta}\left[1 + \frac{1}{2}\frac{p_x^2 + p_y^2}{(1+\delta)^2}\right], \qquad p_\sigma' = -\frac{\partial H}{\partial \sigma} = \quad 0\,. \tag{7.93}$$

To facilitate the solution of the equations of motion, the quantity ω is defined as

$$\omega^2 = \frac{|\chi\, k|}{(1+\delta)}\,. \tag{7.94}$$

Using these relations, the transverse motion can be described by two differential equations of the same type

$$x'' + \omega^2 x = 0\,, \tag{7.95}$$

$$y'' - \omega^2 y = 0\,. \tag{7.96}$$

The transverse transport map is the general solution of the two differential equations

$$x^F = C_x x^I + S_x \frac{p_x^I}{(1+\delta)}\,, \qquad p_x^F = C_x p_x^I - S_x\,\omega^2 x^I\,(1+\delta)\,, \tag{7.97}$$

$$y^F = C_y y^I + S_y \frac{p_y^I}{(1+\delta)}\,, \qquad p_y^F = C_y p_y^I + S_y\,\omega^2 y^I\,(1+\delta)\,. \tag{7.98}$$

The quantities C_u and S_u are defined as follows

$$C_x = \begin{cases} \cos(\omega L) & \text{if} \quad \chi\,k > 0 \\ \cosh(\omega L) & \text{if} \quad \chi\,k < 0 \end{cases}, \qquad S_x = \begin{cases} \omega^{-1}\sin(\omega L) & \text{if} \quad \chi\,k > 0 \\ \omega^{-1}\sinh(\omega L) & \text{if} \quad \chi\,k < 0 \end{cases}, \tag{7.99}$$

$$C_y = \begin{cases} \cosh(\omega L) & \text{if} \quad \chi\,k > 0 \\ \cos(\omega L) & \text{if} \quad \chi\,k < 0 \end{cases}, \qquad S_y = \begin{cases} \omega^{-1}\sinh(\omega L) & \text{if} \quad \chi\,k > 0 \\ \omega^{-1}\sin(\omega L) & \text{if} \quad \chi\,k < 0 \end{cases}. \tag{7.100}$$

The longitudinal coordinates are identical to those derived in [DMFF15].

Thin Quadrupole

Following the Eqs. (7.70) and (7.90), the following Hamiltonian can be derived to describe the quadrupole in thin lens approximation

$$H = H_D + \frac{1}{2}\,\bar{\delta}(s - s_0)\,L\,\chi\,k\,(x^2 - y^2)\,. \tag{7.101}$$

The corresponding transfer map for the kick by a thin-lens quadrupole yields

$$x^F = x^I\,, \qquad p_x^F = p_x^I \;\; - \chi\,k\,L\,x^I\,, \tag{7.102}$$

$$y^F = y^I\,, \qquad p_y^F = p_y^I \;\; + \chi\,k\,L\,y^I\,, \tag{7.103}$$

$$\sigma^F = \sigma^I\,, \qquad p_\sigma^F = p_\sigma^I\,. \tag{7.104}$$

This transfer map corresponds to a focusing lens in horizontal and a defocusing lens in vertical direction (if $\chi\,k > 0$ and vice versa for $\chi\,k < 0$). The transformation of x' and y' is given as

$$(x')^F = (x')^I - k\,L\,x^I\,\frac{\chi}{1+\delta}\,, \tag{7.105}$$

$$(y')^F = (y')^I + k\,L\,y^I\,\frac{\chi}{1+\delta}\,. \tag{7.106}$$

The focal length for the different isotopes is proportional to $\frac{\chi}{(1+\delta)}$, in line with the expectation.

7.3.5 Thin Multipole

Higher order magnetic fields are described in a more generic way by[2] [Wol14]

$$B_y + iB_x = \sum_{n=1}^{\infty}(b_n + ia_n)\left(\frac{x+iy}{r_0}\right)^{n-1} . \tag{7.107}$$

In this context, n is the multipole order, b_n, a_n are the multipole coefficients which describe the field orientation for the contribution of each multipole order [Wol14] and the quantity r_0 is a reference radius. The well-known dipole and quadrupole fields described in the previous sections correspond to the multipole orders $n_D = 1$ and $n_Q = 2$. In a perfect multipole of the order n, all remaining multipole coefficients yield zero.

The magnetic field described in Eq. (7.107) corresponds to the following vector potential

$$A_x = 0\,, \qquad A_y = 0\,, \qquad A_z = -\mathrm{Re}\sum_{n=1}^{\infty}(b_n + ia_n)\frac{(x+iy)^n}{n\,r_0^{n-1}}\,. \tag{7.108}$$

Inserting this vector potential the Hamiltonian in thin lens approximation yields

$$H = H_D - \frac{q_0}{P_0}\,\chi\,L\,\bar{\delta}(s-s_0)\,\mathrm{Re}\left[\sum_{n=1}^{\infty}(b_n + i\,a_n)\,\frac{(x+i\,y)^n}{n\,r_0^{n-1}}\right] . \tag{7.109}$$

The resulting tracking map for the thin multipole kick is

$$x^F = x^I\,, \qquad p_x^F = p_x^I \;- \chi\,L\,\mathrm{Re}\left[\sum_{n=1}^{\infty}(k_n + i\,\hat{k}_n)\,(x+i\,y)^{n-1}\right] , \tag{7.110}$$

$$y^F = y^I\,, \qquad p_y^F = p_y^I \;- \chi\,L\,\mathrm{Re}\left[\sum_{n=1}^{\infty} i(k_n + i\,\hat{k}_n)\,(x+i\,y)^{n-1}\right] , \tag{7.111}$$

$$\sigma^F = \sigma^I\,, \qquad p_\sigma^F = p_\sigma^I\,, \tag{7.112}$$

where k_n and $\hat{k}_n$ are defined as

$$k_n = \frac{q_0}{P_0}\,\frac{a_n}{r_0^{n-1}} \quad \text{and} \quad \hat{k}_n = \frac{q_0}{P_0}\,\frac{b_n}{r_0^{n-1}}\,. \tag{7.113}$$

These transformations are very demanding in terms of computing time. SixTrack therefore calculates multipole fields of higher order than quadrupoles using a Horner scheme (see Chap. 7.4.1).

[2] In some references, e.g. in [Wie99], the multipole field is defined as $B_y + i\,B_x = \sum_n \frac{(b_n + i\,a_n)}{n!}\left(\frac{x+i\,y}{r_0}\right)^{n-1}$. The multipole coefficients are defined differently than here, but the underlying physics remains unchanged.

7.3.6 Accelerating RF Cavity

The energy gain ΔE a particle receives at the position s inside an accelerating cavity operated in the lowest order mode can be approximated by

$$\frac{\mathrm{d}\Delta E}{\mathrm{d}s} = q\,V(s)\,\sin\left(2\pi\,\frac{h}{C}\,\sigma + \phi\right)\,, \tag{7.114}$$

where $V(s)$ is the longitudinal electric field, h is the harmonic number, ϕ is the phase and C is the circumference of the accelerator. The dependence of V on s complicates the solution of the equations of motion and is therefore not explicitly considered in the magnetic vector potential. Rather, the electric field is averaged over the length of the cavity which is summarized in the mean electric field U [Wol14]

$$U = \frac{1}{L}\int_{-L/2}^{L/2} V(s)\,\mathrm{d}s\,. \tag{7.115}$$

This approximation leads to the following vector potential for a cavity [RS95]

$$A_x = A_y = 0 \qquad A_s = -\frac{1}{\beta_0 c}\,\frac{C}{2\pi\,h}\,U\,\cos\left(\frac{2\pi\,h}{C}\,\sigma + \phi\right)\,. \tag{7.116}$$

The resulting expanded Hamiltonian for a thin cavity is then given by

$$H = H_D + \chi\,q_0\,\frac{1}{\beta_0^2}\,\frac{U}{E_0}\,\frac{C}{2\pi\,h}\,\cos\left(\frac{2\pi\,h}{C}\,\sigma + \phi\right)\,L\,\bar{\delta}(s - s_0)\,. \tag{7.117}$$

From this Hamiltonian, the transfer map can be deduced as

$$x^F = x^I\,, \qquad p_x^F = p_x^I\,, \tag{7.118}$$

$$y^F = y^I\,, \qquad p_y^F = p_y^I\,, \tag{7.119}$$

$$\sigma^F = \sigma^I\,, \qquad p_\sigma^F = p_\sigma^I + \chi\,q_0\,\frac{1}{\beta_0^2}\,\frac{U}{E_0}\,L\,\sin\left(\frac{2\pi\,h}{C}\,\sigma + \phi\right)\,. \tag{7.120}$$

The change in p_σ is, as expected, proportional to $q\,\frac{m_0}{m}$. Using the relation between p_σ and E, the energy transfer from the accelerating RF cavity of length L corresponds to the expression given in Eq. (7.114) and yields

$$\Delta E = q\,U\,L\,\sin\left(\frac{2\pi\,h}{C} + \phi\right)\,. \tag{7.121}$$

This transformation is implemented in hiSixTrack.

7.4 Multi-Isotope Tracking in hiSixTrack

The new heavy-ion tracking tool hiSixTrack, which was developed for this thesis, is based on the multi-isotopic symplectic tracking maps derived in the previous chapter. In contrast to the STIER approach, hiSixTrack tracks the heavy ions with their correct physical properties instead of tracking protons with ion-equivalent rigidities. This generic approach required extensive changes of the physics implemented in SixTrack.

In this section, the changes introduced in hiSixTrack are discussed qualitatively and individual features are benchmarked against other simulation tools. A more detailed technical overview, including examples of source code, is given in Appendix A.5.

7.4.1 Implementation of hiSixTrack

With respect to SixTrack, the new tool hiSixTrack must provide additional arrays containing information about the particle mass, charge number and nucleon number to keep track of the ion species and apply the correct physics models. Also new arrays storing information about χ and auxiliary quantities derived from it are introduced.

The definition of χ requires to load and store information about the reference species. To define the latter, a dedicated `HION` block is introduced in the `fort.3` file. In this block, the nuclear charge number, mass number and physical particle mass (in GeV/c^2) are given by the user.

In the standard version of SixTrack, the quantity δ is defined as the relative momentum offset. In hiSixTrack, the definition is changed to obey the multi-isotopic definition given in Eq. (2.10):

$$\delta = \frac{P - P_0}{P_0} \qquad \rightarrow \qquad \delta = \frac{P\frac{m_0}{m} - P_0}{P_0} \,. \tag{7.122}$$

With the new definition of δ and the information on χ available, the SixTrack tracking maps were modified following the thin lens tracking maps derived from the generalized Hamiltonian, presented in the previous chapter. Magnetic elements in SixTrack and hiSixTrack are implemented up to 20th order. However, for higher order fields than quadrupoles, the transformation is not calculated over the multipole equations presented in Chap. 7.3.5. Instead, the magnetic field acting on the particle is determined by several geometric transformations ultimately followed by the tracking map of a quadrupole (Horner Scheme) [Sch94].

Instead of the transverse canonical momenta p_x and p_y, SixTrack and hiSixTrack compute the evolution of x', y'. As an example, the tracking map for a thin-lens quadrupole is modified in hiSixTrack to obey Eq. (7.102) and Eq. (7.103):

$$(x')^F = (x')^I + \frac{k\,L}{1+\delta}\,x^I \qquad \rightarrow \qquad (x')^F = (x')^I + \frac{\chi\,k\,L}{1+\delta}\,x^I\,. \tag{7.123}$$

Further details on the implementation are given in Appendix A.5.4. The new tracking routine for multi-isotopic heavy-ion tracking was extensively tested and benchmarked. The results of these tests are presented in the following sections.

7.4.2 Benchmarking of Ion Tracking in hiSixTrack

hiSixTrack provides symplectic tracking with multipole contributions to the same order as STIER. Hence, both simulation tools should simulate identical particle tracks when RF cavities and scattering in collimators are not included. In this section, the hiSixTrack tracking routine is benchmarked for all relevant scenarios against the tracking in STIER. All simulation cases to study the accuracy of the implementation of hiSixTrack are listed in Table 7.1.
All simulations assume the reference isotope to be $^{208}\mathrm{Pb}^{82+}$. Collimators and RF cavities are not included in the simulations.

Betatron Motion without Dispersion

The betatron motion in hiSixTrack is benchmarked against STIER by comparing the tracks of on-momentum particles ($\delta = 0$) of the respective reference species ($\chi = 1$) with identical starting conditions in IP1. The simulations with hiSixTrack and STIER are carried out for 100 particles starting with identical initial coordinates. The starting conditions are randomly sampled on the surface of a horizontal annular halo at $5.7\,\sigma$, which corresponds to the half gap of the primary collimator in the 2011 heavy-ion run. As an example, the betatron motion simulated with hiSixTrack and STIER for ten of these particles is shown in Fig. 7.5.

Table 7.1: Simulation cases to benchmark hiSixTrack against STIER.

δ	χ	Description
0	1	On-momentum tracking of particles of the reference species
0	$\neq 1$	On-momentum tracking of isotopes different from the reference species
$\neq 0$	1	Off-momentum tracking of the reference ion species
$\neq 0$	$\neq 1$	Off-momentum tracking of particles different from the reference species

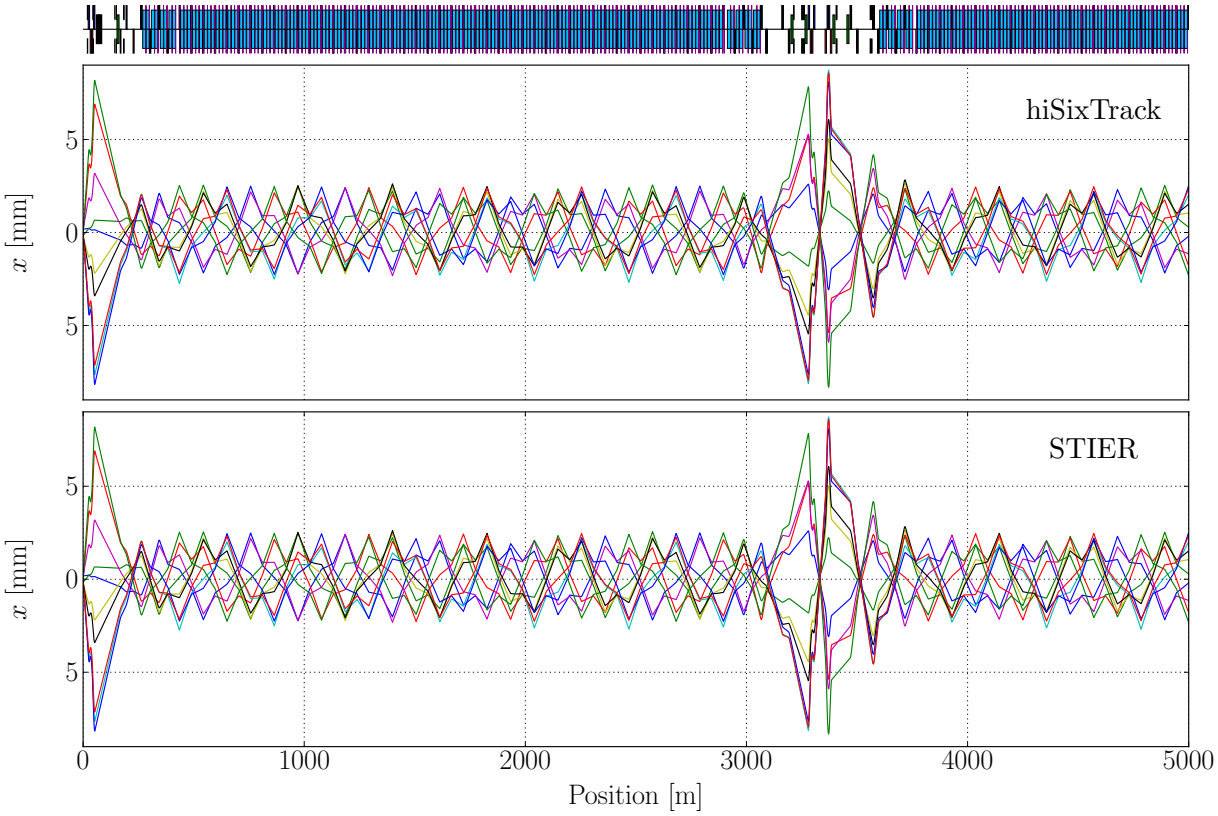

Figure 7.5: Horizontal particle tracks, simulated with hiSixTrack (top) and STIER (bottom), for on-momentum particles of the reference species. All particles start from IP1 on the surface of an horizontal annular halo at an amplitude of $5.7\,\sigma$.

The tracking is performed over 10^6 turns through the magnetic lattice of the LHC for a particle energy of $3.5\,Z$ TeV. The optical settings correspond to the configuration of the 2011 heavy-ion run with crossing and separation bumps switched on in all experimental IRs, except for IR1.

The comparison shows that the tracks simulated with STIER and hiSixTrack are identical within the precision of the floating point numbers (15 significant digits) for all study cases. This does not imply that particles can be tracked with such a precision. Rather, it demonstrates that the numeric reproducibiliy is maintained in hiSixTrack.

Additional tests in which the particles started at different betatron amplitudes delivered the same result.

Tracking of different Isotopes without chromatic Dispersion

In this set of simulations, the modeling of isotopic dispersion in hiSixTrack is benchmarked against STIER. Particles of different isotopes are tracked without initial betatron amplitude or offset in momentum per mass. The optical lattice used for the simulation is matched to $^{208}\mathrm{Pb}^{82+}$ and corresponds to the configuration of the 2011 heavy-ion run. Crossing and separation bumps are applied in all IRs, except IP1.

Six different isotopes were chosen to be tracked, to cover a broad spectrum of χ values. They are listed in Table 7.2. The tracks simulated with hiSixTrack and STIER are illustrated in Fig. 7.6. The particle tracks of all isotopes except for $^{207}\mathrm{Pb}^{82+}$ and $^{207}\mathrm{Tl}^{81+}$ were simulated for less than one turn through the LHC, because the dispersive offset becomes too large (SixTrack stops the particle tracking when amplitudes of 1 m are reached). For the same reason, the isotope $^{207}\mathrm{Pb}^{82+}$ can only be tracked over 100 turns. For $^{207}\mathrm{Tl}^{81+}$, the tracking is performed over 10^6 turns.

Also in this study case, the tracks simulated with both tools fully agree within the numeric precision. The tracking maps implemented in hiSixTrack hence deliver the same tracking behavior as the tracking with SixTrack with ion-equivalent rigidities.

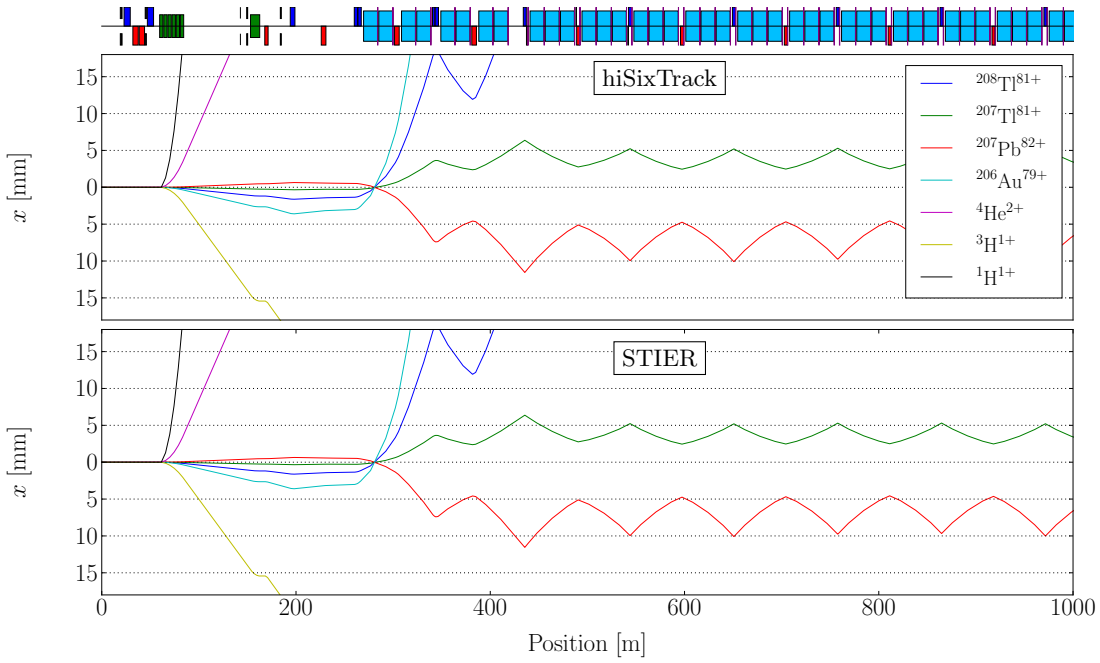

Figure 7.6: Heavy-ion tracks for different on-momentum ($\delta = 0$) isotopes unmatched to the magnetic lattice ($\chi \neq 1$) starting with the same initial conditions in IP1, simulated with hiSixTrack (top) and STIER (bottom).

Table 7.2: Isotopes used for the benchmarking of the heavy-ion tracking. Values for χ and δ_{eff} are computed with respect to the reference isotope $^{208}\text{Pb}^{82+}$. The masses correspond to the fully stripped ions and are extracted from FLUKA. The rest mass of $^{208}\text{Pb}^{82+}$ is 193.688 GeV/c^2.

Element	A	Z	m [GeV/c^2]	χ	δ_{eff}
H	1	1	0.938	2.51744	-0.6030
H	3	1	2.809	0.84090	0.1892
He	4	2	3.727	1.26740	-0.2110
Au	206	79	191.833	0.97273	0.0280
Pb	207	82	192.755	1.00484	-0.0048
Tl	207	81	191.823	0.99741	0.0026
Tl	208	81	193.693	0.98778	0.0124

Tracking of the Reference Species with Momentum Offset

The chromatic tracking without isotopic dispersion is probed by tracking 100 particles with small momentum offsets over 10^6 turns through the machine. The LHC configuration used is the optics of the 2011 heavy-ion run. Crossing and separation bums are switched on, except for IP1. All particles start without betatron offset in IP1, with momentum offsets randomly sampled with a RMS width of 1×10^{-4}.

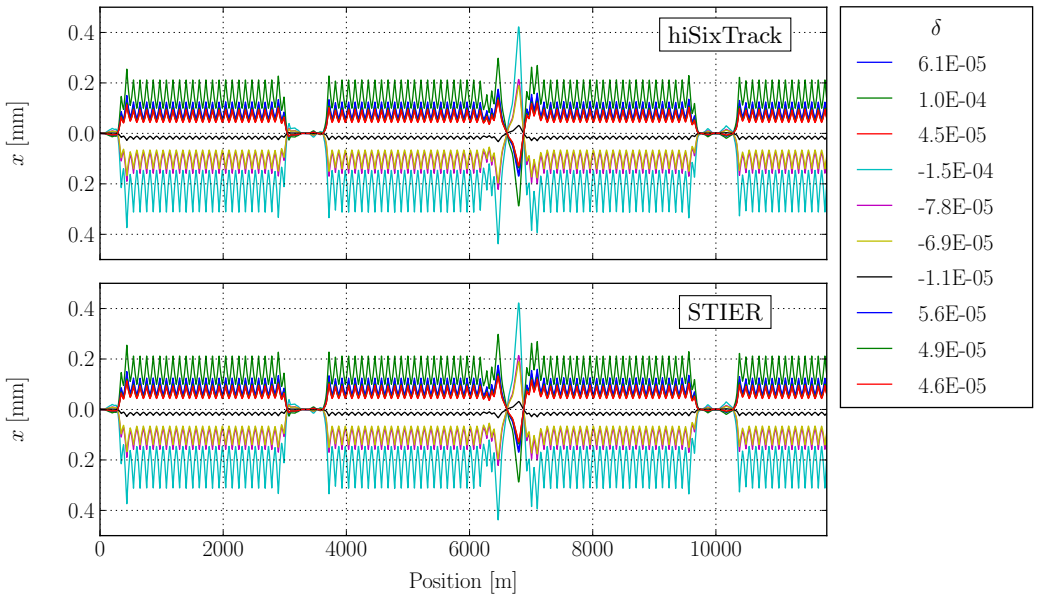

Figure 7.7: Particle tracks of ten $^{208}\text{Pb}^{82+}$ ions with different δ, simulated with hiSixTrack (top) and STIER (bottom).

The tracks of ten off-momentum particles of $^{208}Pb^{82+}$ simulated with hiSixTrack and STIER are shown in Fig. 7.7. The chosen range of momentum offsets correspond to the LHC design value of the RMS momentum spread [B+04b]and is sufficiently small to stay within the acceptance of the machine over many turns. For all study cases, the comparison with STIER shows a full agreement within the numeric precision. Studies with larger momentum offsets have confirmed this result.

Unmatched Isotope with Momentum Offset

In a last set of tracking benchmarking simulations, particles of a species unmatched to the magnetic lattice are tracked with an additional offset in δ. As an example, Fig. 7.8 shows the simulated track of a $^{207}Tl^{81+}$ ion ($\chi = 0.9974$) starting from IP1 in a LHC lattice matched for $^{208}Pb^{82+}$ with $\delta \neq 0$ and an initial betatron offset. The particular isotope was chosen because the mass to charge ratio is close to that of $^{208}Pb^{82+}$. This allows to track the isotope over a large number of turns through the LHC.

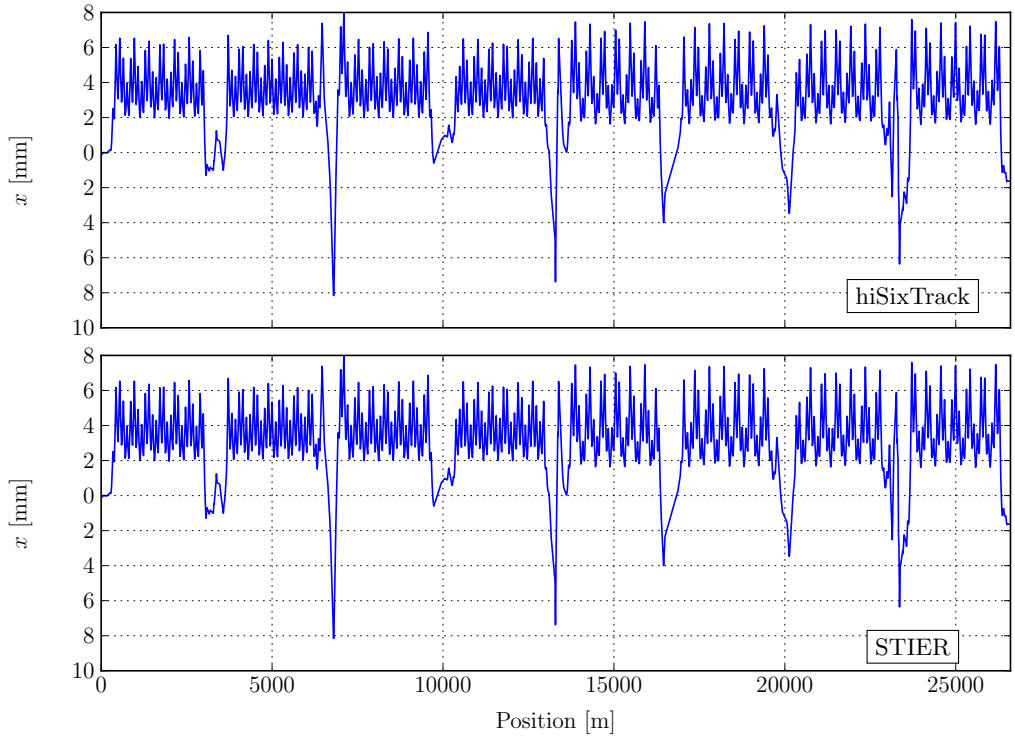

Figure 7.8: Horizontal motion of $^{207}Tl^{81+}$ with momentum offset $\delta \neq 0$ starting from IP1 simulated with hiSixTrack (top) and STIER (bottom).

The study is conducted for 100 particles of $^{207}Tl^{81+}$ which is tracked through the LHC lattice in the 2011 heavy-ion run configuration for 10^6 turns. Every particle is associated to a chromatic offset in the range $-5 \times 10^{-4} < \delta < 5 \times 10^{-4}$. The starting conditions in x, x', y and y' are randomly sampled as a Gaussian distribution in IP1. The comparison between hiSixTrack and STIER shows a full agreement within the numeric precision.
The study was repeated also for $^{207}Pb^{82+}$ ions, $^{206}Pb^{82+}$ ions and $^{204}Tl^{81+}$ ions. Within the limited number of turns these isotopes could be tracked (because of the large dispersive offsets they received after a few turns), the tracks simulated with hiSixTrack and STIER are identical.

Symplecticity

The software hiSixTrack was developed with the aim of providing a symplectic tracking tool for heavy-ion beams of different particle species. Two methods can be used to study the symplecticity of the tracking algorithm:

- The analytic demonstration of the tracking map symplecticity for the individual beam line elements. In this approach, the Jacobian matrix is derived for the individual tracking maps and it is verified if it obeys Eq. (7.8). This approach is applied in Appendix A.1, where it is shown that the derived tracking maps are indeed symplectic.

- The global symplecticity of the implementation can be probed by tracking multiple particles over a large number of turns. The phase space volume which is populated by the distribution should remain constant.

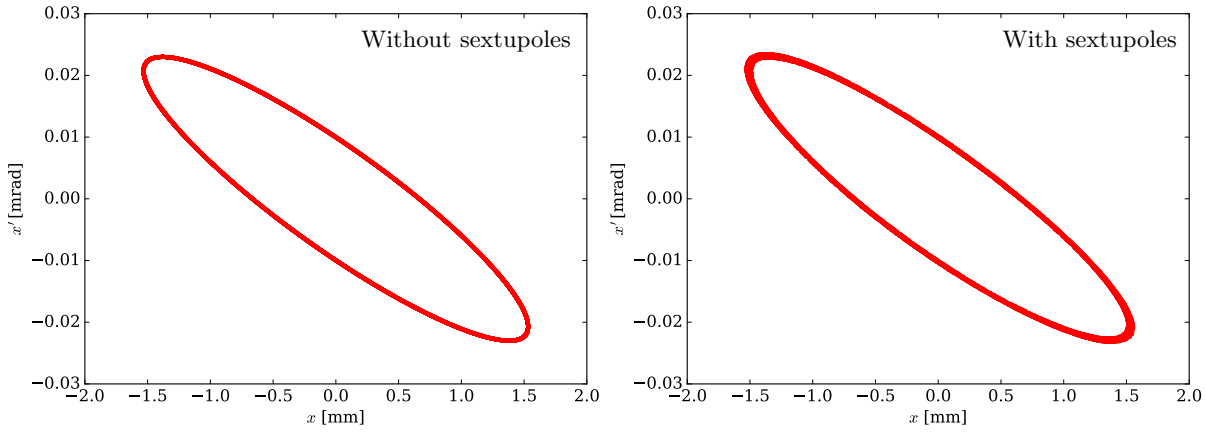

Figure 7.9: Phase space of an initial annular beam halo at $5.5\,\sigma$ at the location of the TCP.C6L7.B1 over 10^6 turns. Left panel: without sextupole fields. Right panel: with sextupole fields. For both study cases 1000 particles were tracked with hiSixTrack.

For the study of the global symplecticity, a bunch of on-momentum particles of the reference species is sampled as an annular halo in the horizontal phase space in IP1. The tracking is performed over 10^6 turns. Two different simulations are carried out, with and without sextupoles. The study was conducted for the LHC configuration of the 2011 heavy-ion run at $3.5\,Z$ TeV and the 2015 heavy-ion run at $6.37\,Z$ TeV. In every turn, the particle coordinates are saved at the location of the TCP.C6L7.B1.

The simulation result for the 2015 heavy-ion run (with an initial annular halo sampled at $5.5\,\sigma$, corresponding to the TCP half gap) is shown in Fig. 7.9. For the simulation without sextupole fields, the phase space ellipse is of the same shape and orientation for all turns. The phase space volume is hence conserved. For the simulation with sextupole fields included, the phase space ellipse is slightly shifted from turn to turn, but the phase space volume enclosed by the bunch of particles remains constant. The same applies for the simulation in the LHC configuration applied in 2011. The study hence confirms the symplecticity of hiSixTrack.

Conclusions

The benchmarking of the hiSixTrack tracking algorithm has reproduced the simulation results of the reference program STIER. It can therefore be assumed that the tracking in hiSixTrack is as accurate and trustworthy as the tracking in STIER. To simulate the cleaning performance of the LHC collimation system, it is required to transfer the six-dimensional particle coordinates and the particle mass and charge at every collimator to a software simulating the particle-matter interaction. At the end of each collimator, the out-scattered fragments have to be transferred back to hiSixTrack. This is accomplished by means of a coupling of hiSixTrack with FLUKA, which is described in the next section.

7.5 The hiSixTrack-FLUKA Coupling

With the native heavy-ion tracking established in hiSixTrack, the active coupling with FLUKA for fragmentation simulations and subsequent fragment tracking becomes possible. The implementation of the hiSixTrack-FLUKA coupling is one of the major outcomes of this thesis.
The application of the coupling for heavy-ion beams requires to adapt the algorithms for particle exchange and to produce additional output data to accurately account for heavy-ion beam losses. The newly established framework is referred to as the hiSixTrack-FLUKA coupling. In this section, the essential modifications and their testing are qualitatively described. More details on the implementation are given in Appendix A.6.

7.5.1 Definition of the Heavy-Ion Species

The algorithm to load the initial distribution in the SixTrack-FLUKA coupling was already prepared, though not completely set up, for the eventual sampling of the particle species. The general structure of input therefore includes by default not only the six-dimensional particle coordinates, but also A, Z, m of the particle to be tracked.
In the proton coupling between SixTrack and FLUKA, the subroutine initializing the particle properties from the external input file ignores this information. For heavy-ion applications, this algorithm is adjusted to populate the new arrays introduced in hiSixTrack with information about the particle species. This modification allows to load an initial bunch of user-defined ions to perform the tracking in hiSixTrack.
Note that the mass of both reference particle and tracked particle must coincide with their associated masses in FLUKA. If this is not respected, FLUKA refuses their exchange between the codes, to provide consistency.

7.5.2 Heavy-Ion Exchange between hiSixTrack and FLUKA

Particle Selection

In the nominal framework of the SixTrack-FLUKA coupling for protons, it is sufficient to send the six-dimensional particle to FLUKA and back. A transfer of information defining the particle type is not required for proton studies. For the implementation of the hiSixTrack-FLUKA coupling, the inclusion of the particle species (defined by A, Z) and mass m is important to ensure the use of the correct physics models in both FLUKA and hiSixTrack. Every initial and residual particle is identified in SixTrack by its unique particle ID. The hiSixTrack-FLUKA coupling assigns the new particle ID automatically to a residual heavy-ion fragment that is scattered out of a collimator and sent back to hiSixTrack.

The particles sent back to hiSixTrack are filtered by means of their FLUKA particle ID, which classifies them into different particle categories. For the heavy-ion coupling, the selection of protons is replaced by heavy ions (describing all fully stripped ions heavier than $^4He^{2+}$), deuterons, tritium, $^3He^{2+}$ and $^4He^{2+}$. Protons are by default not sent back to hiSixTrack, but if needed this feature can be activated in the corresponding FLUKA subroutine `fluscw.f`.

The tracking tool hiSixTrack can in principle compute the trajectory of all other charged particles (protons, pions, Δ-baryons, ...) which may be generated in the collimators. Most of these particles have, however, very large rigidity offsets with respect to the main beam. They are most likely absorbed in the warm regions closely downstream of the collimator at which they are produced. This was demonstrated for the residual protons tracked in STIER (see Fig. 6.14). The losses in these regions are not important to quantify the quench risk in the superconducting LHC magnets. It should be kept in mind that the losses in the warm regions of IR7 and IR3 are not comparable between cleaning simulations and measurements. On the other hand, including these particles in the simulations would significantly increase the simulation time, as explained in the next section.

Working Memory and Particles per Job

The simulations with the hiSixTrack-FLUKA coupling are very space and time consuming, due to the large number of different fragments produced. The definition of dynamic arrays is not possible in FORTRAN77, such that all arrays containing information about the particle distribution must be statically allocated. This implies an upper boundary on the number of tracked particles, depending on the available working memory.

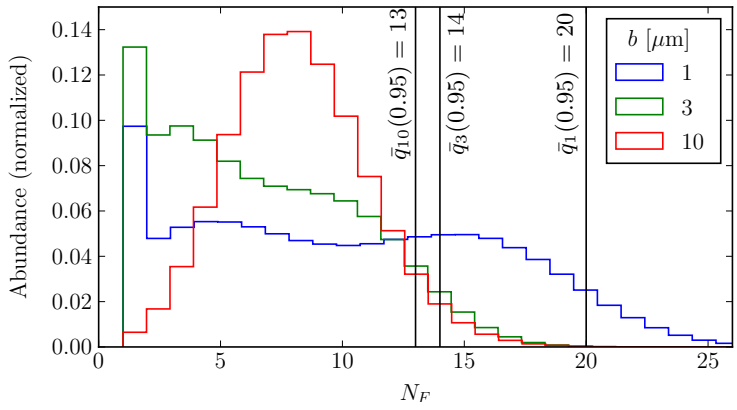

Figure 7.10: Relative abundance of the number of fragments N_F, generated at the first passage through the TCP for $^{208}Pb^{82+}$ beams at $7\,Z$ TeV with different impact parameters. The black vertical lines indicate the 95% quantiles. Only ions heavier than protons are included.

The total number of particles which can be tracked in one simulation with the hiSixTrack-FLUKA coupling is limited to 2000 (number of different particle IDs) due to the 2GB memory limitation of the CERN batch system. This number includes both the primary beam particles and their residual fragments.

Simulations with the hiSixTrack-FLUKA coupling (without including out-scattered protons) for 10^6 ions of $^{208}\mathrm{Pb}^{82+}$ at $7\,Z\,\mathrm{TeV}$ have been carried out to quantify the number of residual fragments N_F generated per initial ion impacting the TCP material. Three different impact parameters $1\,\mu$m, $3\,\mu$m and $10\,\mu$m are studied.

The resulting distribution of N_F per passing ion is shown for the three simulation cases in Fig. 7.10. Furthermore, the 95% quantile $\bar{q}_b(0.95)$ is shown for each case. The latter indicates the limit at which 95% of the ions traversing the TCP will produce less residual fragments than $\bar{q}_b(0.95)$. They lie between $N_F = 13$ and 20 for the different impact parameters.

If 95% of the simulations with the hiSixTrack-FLUKA coupling shall be executed without exceeding the size of the static arrays (which would cause the simulation to interrupt and deliver no output), the number of initial particles of the main beam should not be larger than

$$n_{\mathrm{max}}^{\mathrm{main}} = \frac{2000}{1 + \bar{q}_b(0.95)}\,. \tag{7.124}$$

With the inclusion of protons, the maximum number of initial beam particles per job would decrease accordingly. To achieve the same number of events, the number of jobs would have to be increased. Simulations with protons included show that the number of residual fragments sent back to hiSixTrack increases by a factor of three. Their inclusion would hence lead to a three times longer simulation time for a full simulation with the hiSixTrack-FLUKA coupling. The simulation time for a cleaning simulation with 6×10^6 initial $^{208}\mathrm{Pb}^{82+}$ particles is approximately 24 h. The inclusion of protons would require two additional days, without delivering additional information about losses in superconducting magnets. It is therefore reasonable to exclude protons from the simulation.

Benchmarking and Application of the Particle Exchange

To illustrate the interplay between tracking and fragmentation simulation in the hiSixTrack-FLUKA coupling, the particle tracks of primary ions and their residual fragments generated in the TCP are shown in Fig. 7.11. The simulation is carried out for four initial particles of the main $^{208}\mathrm{Pb}^{82+}$ beam impacting the primary collimator. The figure shows how most of the residual light ion fragments are lost in the TCSGs downstream of the TCP. Some of them are intercepted by the magnet aperture of the quadrupole downstream of the TCP and few are moving further to the TCLA collimators or even to the DS magnets.

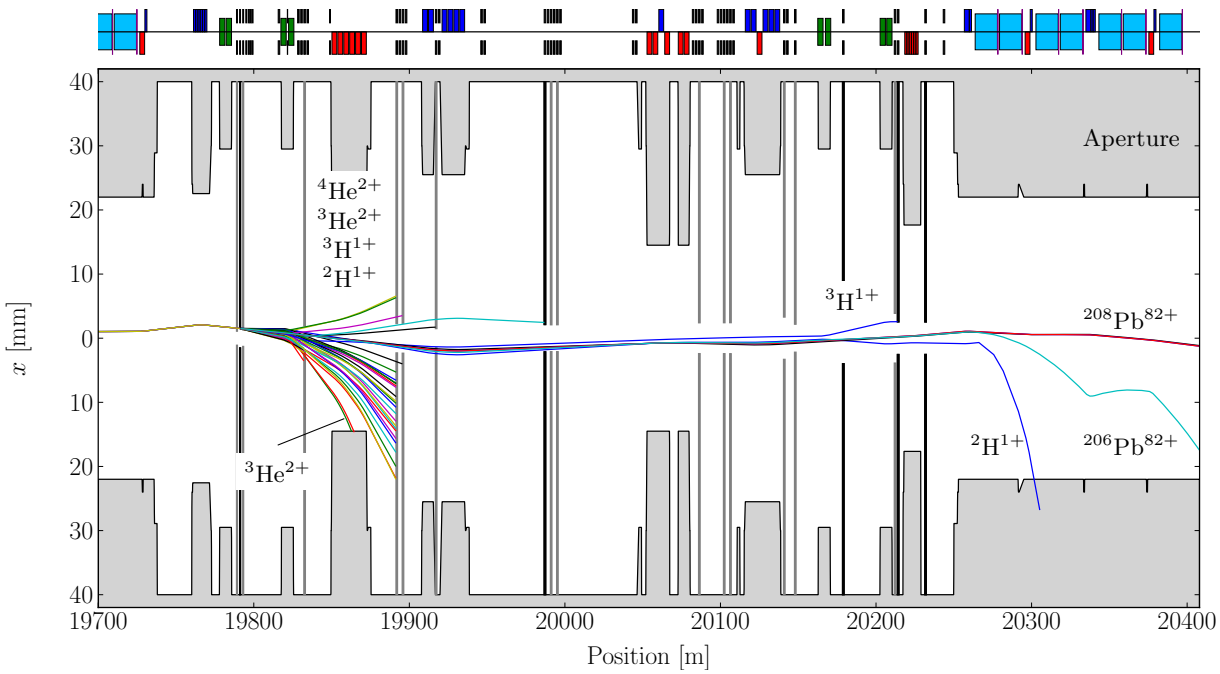

Figure 7.11: Fragmentation of four $^{208}Pb^{82+}$ ions at the TCP and the subsequent motion of their residual fragments, as simulated with the hiSixTrack-FLUKA coupling. Horizontal collimators are shown as black bars, skew collimators are shown as gray bars.

The particle exchange between hiSixTrack and FLUKA was extensively tested to ensure that the correct particle species and 6D coordinates are transferred between the codes. The tests carried out with 1 million particles demonstrated the preservation of the full numeric precision of all particle coordinates and it confirmed that the information on the heavy-ion species is accurately transferred between the two codes.

7.5.3 Benchmarking of the Fragmentation Simulation

The accuracy of the fragmentation simulation is studied by a comparison of the heavy-ion spectrum coming out of the primary collimator between FLUKA and the hiSixTrack-FLUKA coupling. The geometry used in FLUKA is identical to the setup used for the STIER simulations. In the FLUKA simulation, the impacting beam consists of 10^6 on-momentum particles of the isotope $^{208}Pb^{82+}$ with a momentum of $7\,Z$ TeV/c. The impact parameter is selected to be 1 μm. In the hiSixTrack-FLUKA coupling, a primary distribution of 10^6 particles without momentum offset is sampled, which impacts the TCP at an impact parameter between 0.95 μm and 1.05 μm. In both methods, the nuclear evaporation model of FLUKA is switched on, the material is set to graphite with the density of CFC.

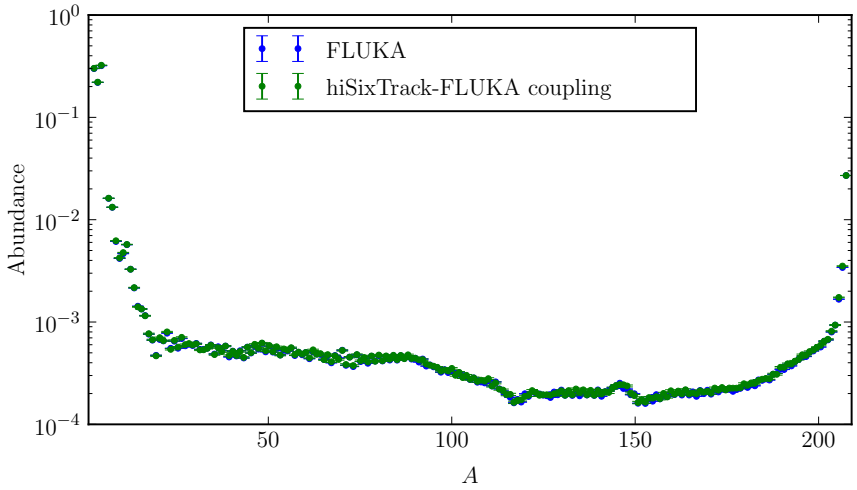

Figure 7.12: Normalized abundance of nuclear mass numbers A of fragments leaving the TCP for an initial $^{208}Pb^{82+}$ beam at 7 Z TeV as simulated with FLUKA and with the hiSixTrack-FLUKA coupling. The sampled statistics is 10^6 particles in both simulation.

The spectrum of nuclear mass numbers simulated with the two approaches is shown in Fig. 7.12. Both histograms show the normalized abundance of A. Overall, the two fragment spectra show an excellent agreement within the error bars. The rate of surviving $^{208}Pb^{82+}$ ions and of produced light fragments agrees within 0.5% in both approaches. The fragmentation simulation in the hiSixTrack-FLUKA coupling is thus equivalent to the standard FLUKA simulation.

7.5.4 Accounting for Collimator Losses

The proton implementation of SixTrack and the SixTrack-FLUKA coupling consider particles to be lost in a collimator if they undergo inelastic nuclear interactions which are not single diffractive. In the framework of the hiSixTrack-FLUKA coupling, the underlying physical processes are different, such that collimator losses have to be taken into account differently.

The loss scaling in the hiSixTrack-FLUKA coupling is based on the comparison of the total energy of all particles entering each collimator to the total energy of the residual particles scattered out of it. The coupling framework is modified to integrate the total ion energy every time the particle bunch is sent to FLUKA and when it is sent back from FLUKA to hiSixTrack. The difference in energy is then considered as the energy lost at this collimator. This information is written to the dedicated output file `fort.208`.

Given that only heavy ions are selected to be sent back to hiSixTrack, the energy of other particles coming out of the collimator is neglected in this approach. The collimator losses derived as mentioned would be hence overestimated. Therefore, the FLUKA subroutines are modified

to save information of all particles scattered out of the collimator, which are not sent back to hiSixTrack, into a dedicated correction file, called `fort.66`. The collimator losses derived from the `fort.208` are then reduced by the amount of energy of these particles.
In practice, the simulated collimator losses at the TCP are reduced by approximately 20% if the correction factor is taken into account. More information on the implementation and the structure of the `fort.208` and `fort.66` files is given in Appendix A.6.2 and Appendix A.6.3.

7.5.5 Simulation Output

The hiSixTrack-FLUKA coupling is adapted to provide additional information about the lost isotopes via new output files and by the modification of output files already implemented before. A brief summary of new output files and modifications on existing files is given below.

- `fort.999`: default output file from the online aperture check; modified to also save information on A, Z, m of the impacting particle.
- `fort.208`: stores information on collimator losses. This includes the number of nucleons and total particle energy lost at each collimator, without providing information about the individual particles lost.
- `fort.209`: relates the collimator losses to individual particles. For every particle lost at a collimator the collimator ID is saved. This allows relating the collimator losses to the individual isotopes.
- `fort.822`: Ion fragments produced at the collimator. Every residual ion produced at any collimator is listed with its particle ID, the parent particle ID, the ID of the collimator at which it is produced and its mass, charge and energy.
- `fort.66`: Contains information about particles that are scattered out of the collimator, but not sent back to hiSixTrack. The information is used to correct the collimator losses.

7.6 Loss Map Simulation with the hiSixTrack-FLUKA coupling

To validate the accuracy of full cleaning simulations with the hiSixTrack-FLUKA coupling, the simulation result is compared to the STIER simulation and the measured loss pattern in the 2011 heavy-ion run. This comparison also allows evaluating the change of the simulated loss pattern from the inclusion of secondary fragmentation. Thanks to the implementation of the RF cavities, hiSixTrack is the first tracking tool providing six-dimensional heavy-ion tracking. Therefore, the simulated loss patterns are also compared with and without RF cavities.

7.6.1 Initial Distribution

Cleaning simulations with the hiSixTrack-FLUKA coupling can in principle be initiated similarly to proton simulations with SixTrack. If non-linear magnetic elements such as sextupoles are present in the machine, the phase space ellipse is slightly shifted and tilted which can enlarge the impact parameter and lead to non-symmetric impacts on the two collimator jaws (see Fig. 7.13). This should not be confused with a lack of symplecticity, because the volume enclosed by the ensemble of beam particles remains constant. For protons, this behavior is acceptable because the scattering in the collimator is not strongly dependent on the impact parameter [B$^+$14d]. As discussed in earlier chapters, for heavy ions the spectrum of out-scattered ion fragments changes drastically with the impact parameter, such that in cleaning simulations it must be better controlled than in the proton case.

A preliminary approach to control the impact parameter at the primary collimators is used for the cleaning simulations with the hiSixTrack-FLUKA coupling presented in this thesis. In an initial high statistics simulation over one LHC turn, the impact coordinates on the collimator jaws of the respective TCP (depending on the beam and the transverse direction) are determined. Based on this simulation result, the initial conditions can be associated to impact parameters and the impacting jaw. Finally, the initial coordinates resulting in impacts at the desired jaw with the chosen impact parameter can be sampled.

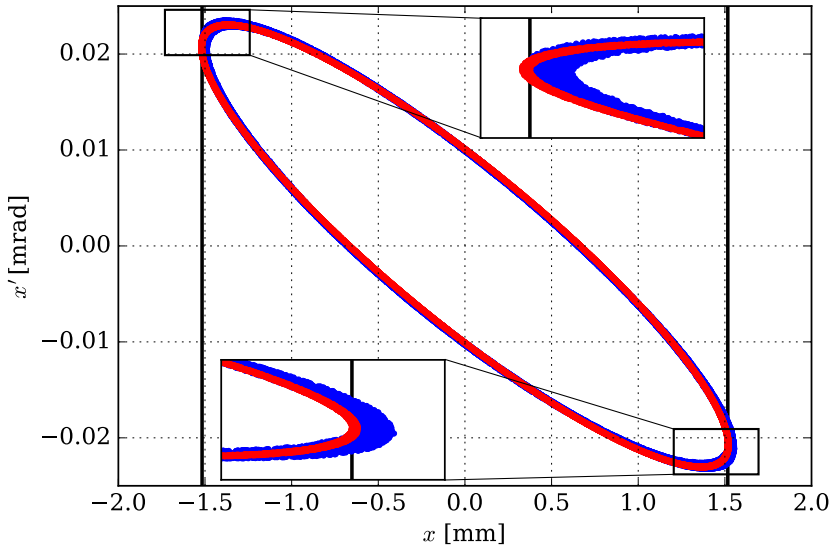

Figure 7.13: Phase space distribution of an annular halo of on-momentum particles at the TCP location over ten subsequent turns with sextupoles (blue) and without sextupoles (red). The vertical black lines indicate the TCP jaw edges.

In terms of computing time, the initial simulation and the subsequent sampling of the initial distribution file requires less than one hour if it is distributed over 1000 jobs. This is negligible compared to the total simulation time for a full cleaning simulation with the hiSixTrack-FLUKA coupling, which is approximately 24 h for 6.0×10^6 particles. The loss maps presented in the following sections are generated with this approach.

Future developments should take into account more sophisticated approaches to control the impact parameters. One option would be to implement the possibility of using pencil beams for heavy ions. This functionality is already available for protons [BMR14]. In this case, the particle distribution is sampled directly at the surface of the collimator which allows for a much better controllability of the impact parameter.

7.6.2 Loss Map Simulation

In this section, the full cleaning simulation with the hiSixTrack-FLUKA coupling is compared to the STIER simulation result presented in Chap. 6.3 and in addition benchmarked against the measured data of the 2011 heavy-ion run. The simulation is carried out for B1H with 6.0×10^6 initial $^{208}Pb^{82+}$ ions which start at IP1 and are intercepted by the TCP on the first turn in the machine. The chosen TCP impact parameter is continuously distributed between $1\,\mu$m and $10\,\mu$m. This comparison was also presented in [H$^+$16c].

Benchmarking against STIER and Measured Loss Patterns

The loss maps are shown in Fig. 7.14 (full LHC), Fig. 7.15 (zoom to IR7) and Fig. 7.16 (zoom to IR3). The global comparison shows that the simulation with the hiSixTrack-FLUKA coupling is in even better agreement with the measured data than STIER. Most remarkably, the improvement is visible for the losses downstream of the momentum collimation region IR3. The losses from residual fragments generated in the IR3 collimators become visible with the hiSixTrack-FLUKA coupling, while they were not simulated in STIER.

The comparison shows that the general shape of the collimator losses in IR7 is different between the two simulation tools. In neither of the simulations, the losses in the warm magnets of IR7 are accurately simulated. This discrepancy is expected, because the propagation of electromagnetic and hadronic particle showers from the collimators is not simulated in STIER and the hiSixTrack-FLUKA coupling.

Compared to STIER, the hiSixTrack-FLUKA coupling simulates a different ratio of losses at the primary collimator and the TCSG collimators immediately downstream. The difference can be explained by to two effects: first, the TCP losses in STIER are uniquely originating from out-scattered $^{208}Pb^{82+}$ ions surviving one or multiple turns and then impact on the TCP again.

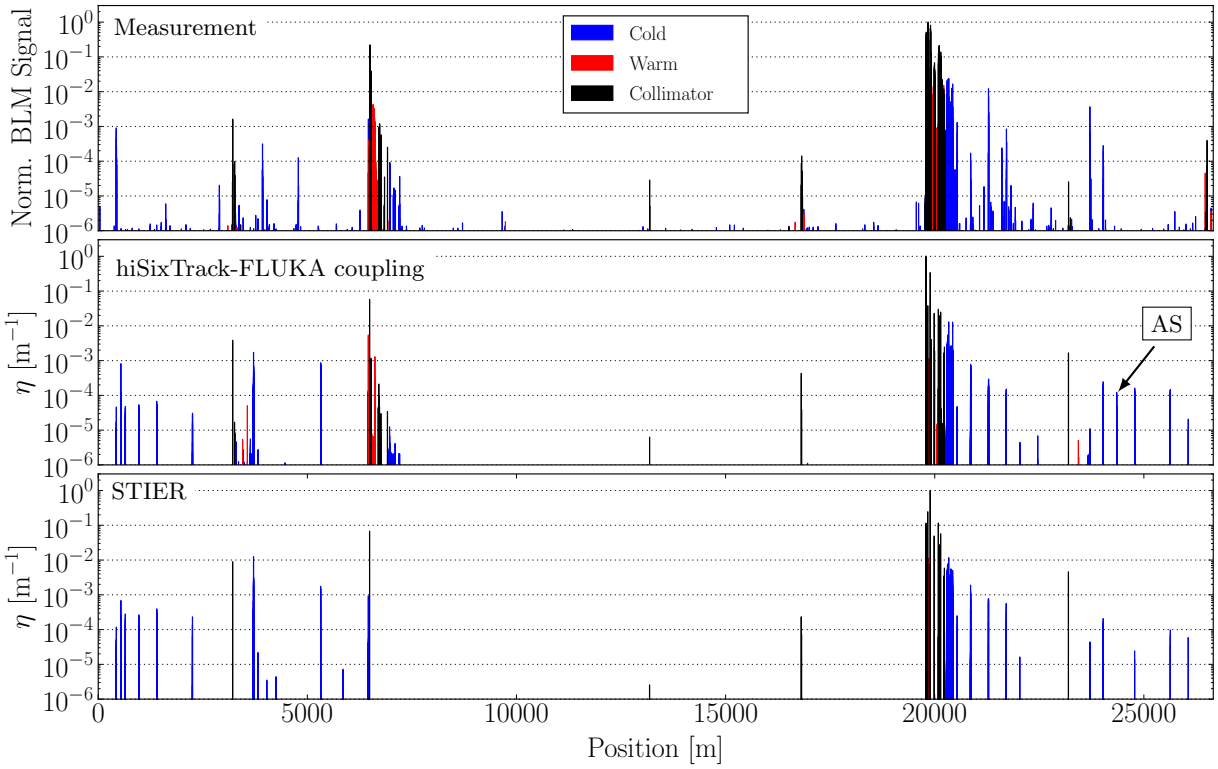

Figure 7.14: B1H betatron loss maps measured in the 2011 heavy-ion run compared to simulations with the hiSixTrack-FLUKA coupling and STIER.

The energy lost in the TCP at the initial passage is not included in STIER, which results in a reduced simulated TCP loss signal, assuming that only few fragments re-impact the TCP in a subsequent turn. Secondly, the STIER simulation includes protons, which are mostly lost at the TCSG collimators and therefore change the loss ratio between TCP and TCSG in favor of the TCSG. This assumption is supported by the outcome of low statistics simulations with the hiSixTrack-FLUKA coupling including protons.

Both tools simulate the losses in the DS clusters and the arc clusters A1 to A4 in good agreement with the measured data. The amplitudes of the individual loss spikes are different in the two simulations. This can be explained by the different impact parameter and residual particles emitted from collimators downstream of the TCP.

For the losses in the LHC arcs between IR7 and IR1, between IR1 and IR2 and between IR2 and IR3, the hiSixTrack-FLUKA coupling predicts loss peaks mostly at the same locations as STIER. A detailed comparison between STIER and the measured loss pattern was already discussed in Chap. 6.3. With the hiSixTrack-FLUKA coupling, one loss peak AS (see Fig. 7.14) is simulated, which is not simulated with STIER. This is further analyzed in the next section.

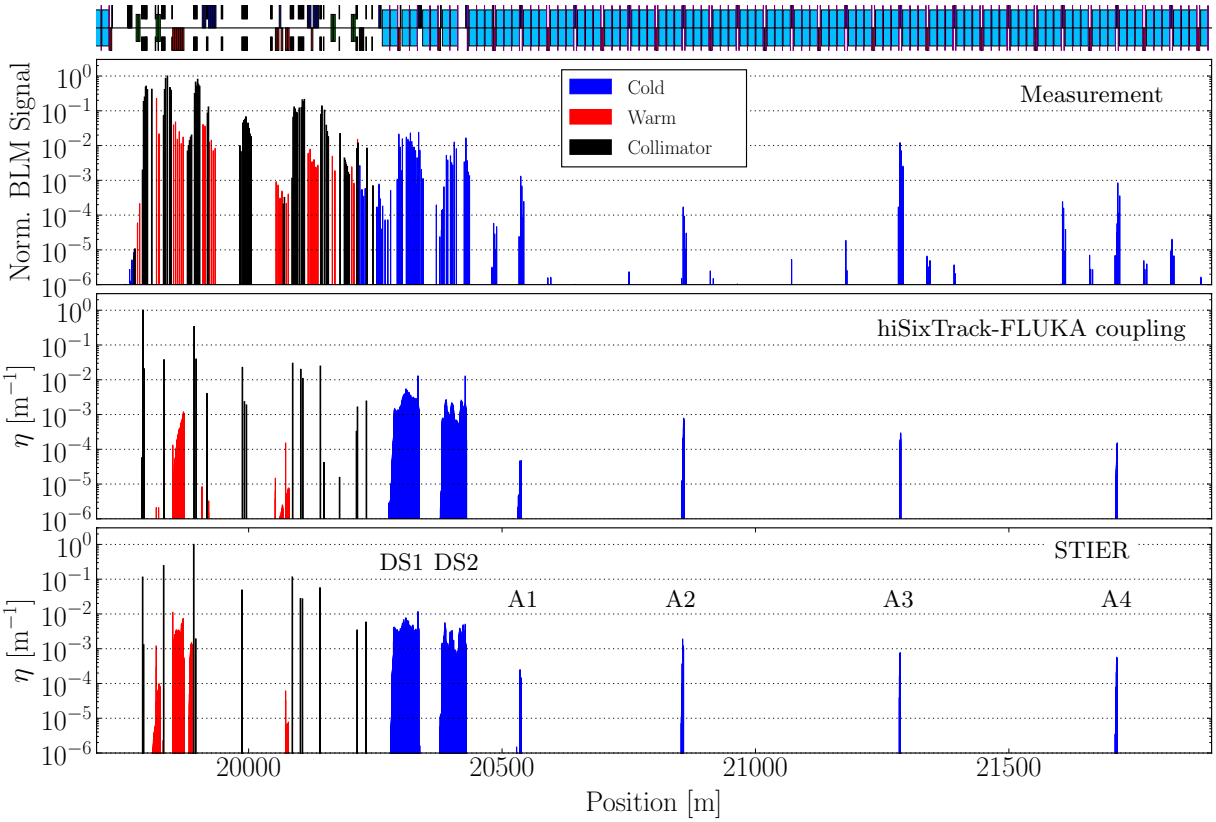

Figure 7.15: B1H betatron loss maps measured in the 2011 heavy-ion run compared to simulations with the hiSixTrack-FLUKA coupling and STIER, zoomed to IR7.

Small loss peaks from single particles are simulated in STIER that are not visible in the hiSixTrack-FLUKA coupling. Finally, in IR3 and the regions downstream of the TCTs in IR8 and IR2, the hiSixTrack-FLUKA coupling simulates losses from particles generated in interactions with these collimators.

From the similarity of the global loss distribution to STIER, one can conclude that the loss distribution simulated with the hiSixTrack-FLUKA coupling is dominated by particles starting from the IR7 TCP. This finding is in line with the assumption under which the STIER tool was developed and supports the accuracy of the loss maps simulated with it. The contribution of fragments generated in other collimators or at interactions with the TCP in subsequent turns is studied in the next chapter.

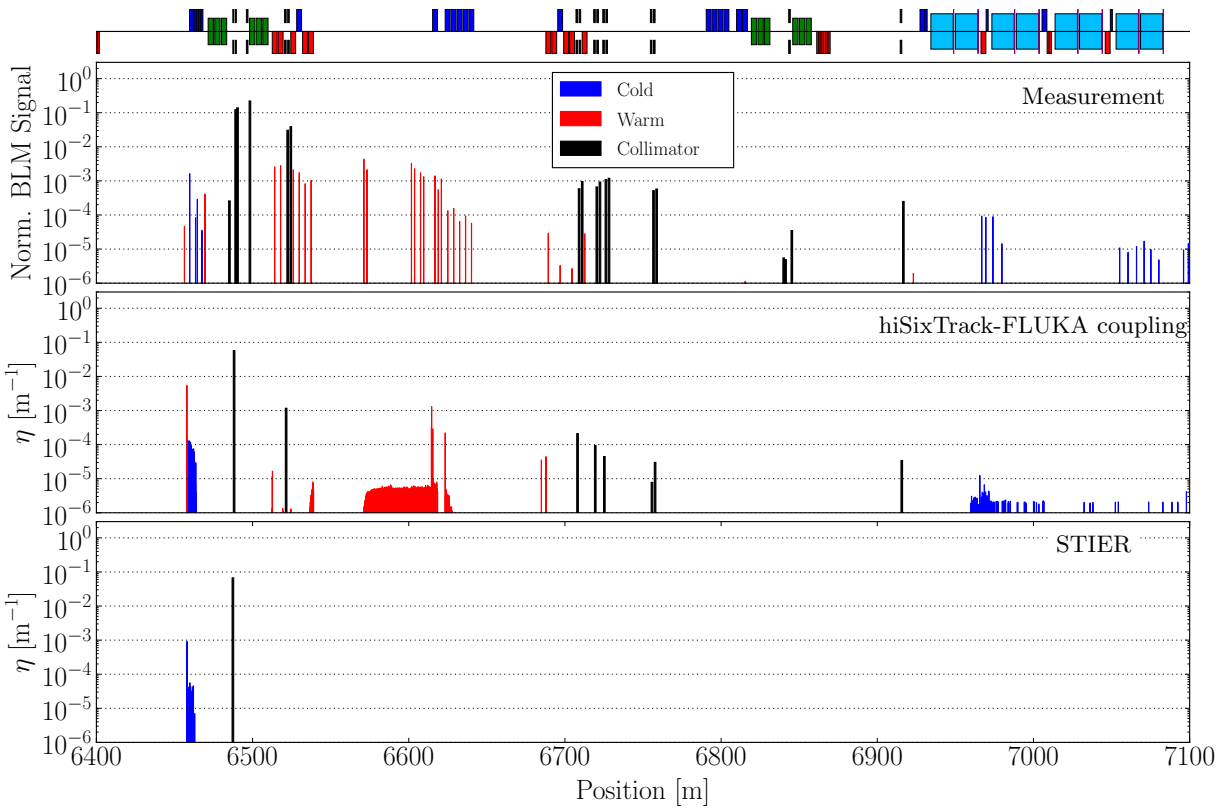

Figure 7.16: Comparison of the measured loss map in the 2011 heavy-ion run to simulations with STIER and hiSixTrack, zoomed to IR3.

Contribution of Secondary Collimator Interactions

In the following, the interactions which are undergone with collimators after the first interaction with the TCP are referred to as secondary interactions. With the hiSixTrack-FLUKA coupling, the cleaning inefficiency in the 2011 LHC heavy-ion run was simulated including the contribution of secondary interaction. In order to quantify their contribution to the individual simulated loss peaks, the integrated cleaning inefficiency η^{int} is taken into account. It is defined as the sum of the cleaning inefficiency in the region of interest (between s_0 and s_1), multiplied by the bin size Δs used for the aperture check

$$\eta^{int} = \Delta s \sum_{s=s_0}^{s_1} \eta(s)\,. \tag{7.125}$$

The integrated cleaning inefficiency caused by particles generated in secondary interactions η^{int}_{sec} can then be related to the total integrated cleaning inefficiency η^{int}_{tot} in the region of interest.

Table 7.3: Energy fraction of ion fragments generated in secondary interactions in collimators with respect to the total integrated energy lost in different LHC regions, as simulated with the hiSixTrack-FLUKA coupling.

	DS1	DS2	A1	A2	A3	A4	Global
$\eta_{sec}^{int}/\eta_{tot}^{int}$	5×10^{-3}	3×10^{-3}	3×10^{-2}	1×10^{-4}	6×10^{-4}	$1\times^{-3}$	8×10^{-3}

In Table 7.3, the ratio $\eta_{sec}^{int}/\eta_{tot}^{int}$ derived from the simulation with the hiSixTrack-FLUKA coupling is listed for the two IR7 DS loss clusters (DS1 and DS2) and the four arc clusters A1 to A4 downstream of IR7. Furthermore, the contribution of fragments created in secondary interactions to aperture losses throughout the ring (global contribution) is given.

The simulation data shows that in these regions only minor contributions to all loss peaks arise from these secondary fragmentation processes. The highest contribution in the specific simulation case is reached at the A1 cluster where approximately 3% of the losses are caused by them. On a global scale, approximately 0.8% of aperture losses arise from these ions.

In the arc region between IR7 and IR8, the hiSixTrack-FLUKA coupling simulates an additional loss peak compared to STIER. This loss peak is called AS in the following (see Fig. 7.14). Further analysis shows that mainly particles of the species $^{206}Pb^{82+}$ generated at the TCP are lost at AS. All of the studied particles are generated at secondary interactions of $^{208}Pb^{82+}$ with the TCP, which were out-scattered in a previous turn. The scattered $^{208}Pb^{82+}$ ions have lost some of their initial momentum, due to ionization loss, and impact the TCP again with different angle and impact parameter than the particles of the primary halo. The residual $^{206}Pb^{82+}$ ions generated at the second interaction at the TCP have considerably different starting conditions than those generated during the primary fragmentation which leads to a different loss location.

Evidently, the loss peak cannot be simulated with STIER because secondary fragmentation at the TCP is not included in the simulation framework.

In conclusion, ions generated from fragmentation at subsequent collimator interactions may lead to additional features of the simulated loss pattern. Compared to the losses from the primary TCP interaction, however, their contribution is small. Around 0.8% of the global aperture losses simulated with the hiSixTrack-FLUKA coupling arise from particles generated in secondary fragmentation processes. Note that this conclusion might change for other study cases at different particle momenta, with other heavy-ion species or collimator settings.

Accelerating Cavities

Both ICOSIM and STIER do not include accelerating cavities in the simulation framework. With the hiSixTrack-FLUKA coupling, the simulated loss maps can be compared with and without RF cavities. The comparison for the simulation of the 2011 heavy-ion run with 6.0×10^6 initial $^{208}Pb^{82+}$ ions starting from IP1 is shown in Fig. 7.17. For both cases, the TCP impact parameter is $b = 3\,\mu$m.

The simulated loss patterns are qualitatively in good agreement with small differences in the amplitudes of the individual loss peaks. The slight differences in terms of loss amplitudes originate from the fact that the accelerating cavity changes the energy of the particles on their way to the TCP. Therefore, the initial distribution impacting the TCP is not identical in the two simulation approaches. Furthermore, the accelerating cavity changes the energy of ions which are scattered out of the TCP and re-impact again after several turns. This changed energy also leads to slight differences in the local cleaning inefficiency.

In conclusion, the assumption that the accelerating cavities are of minor importance for the loss map simulations is valid. The period length of the synchrotron oscillation is approximately 500 turns, while in the presented simulations all particles are lost within 20 to 30 turns.

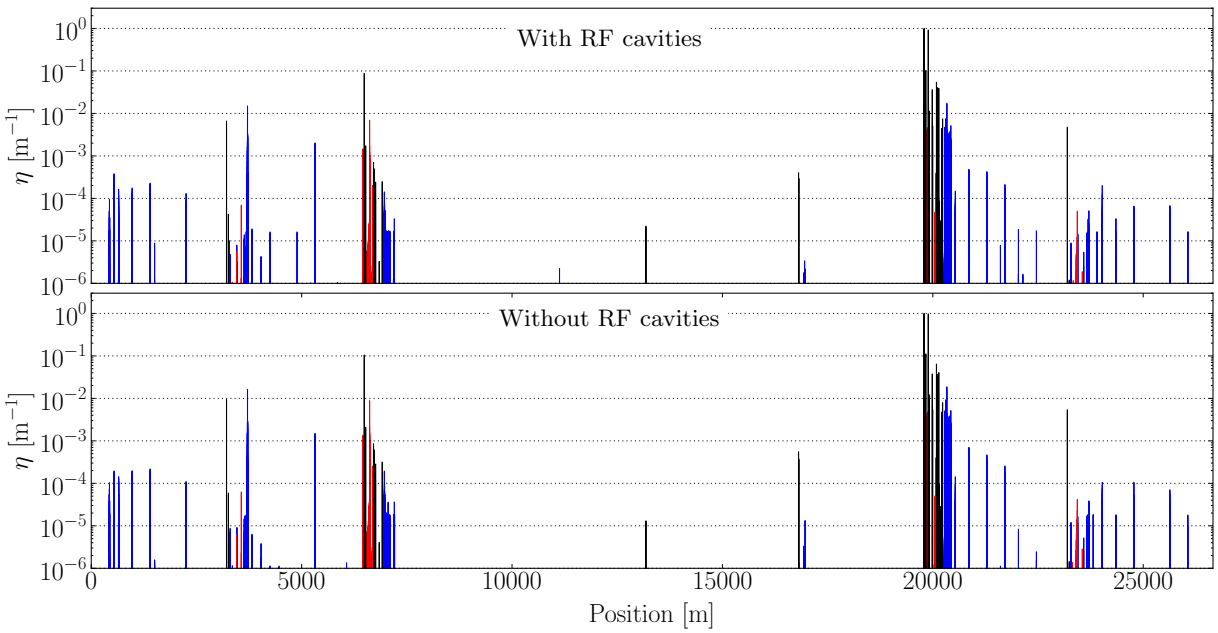

Figure 7.17: Betatron loss maps simulated with the hiSixTrack-FLUKA coupling for B1H in the configuration of the 2011 heavy-ion run at $3.5\,Z$ TeV with RF cavities (top panel) and without RF cavities (bottom panel).

Limitations

The loss patterns simulated with the hiSixTrack-FLUKA coupling still show discrepancies with respect to the measured loss pattern. Again, some loss peaks measured with the BLMs are not reproduced by the simulation, and simulated loss peaks were not measured.

Given the qualitative agreement between STIER and the hiSixTrack-FLUKA coupling for most of the loss peaks in cold regions, the origin of the discrepancies may be the same. For simulations in the configuration of the 2015 heavy-ion run at $6.37\,Z$ TeV, discrepancies between simulation and measurements are also observed at the A2 and A3 loss peaks. These differences are studied in the context of possible variations of the closed orbit and displacements of the magnet aperture in Chap. 10.

7.7 Summary and Conclusions

In this chapter, the heavy-ion tracking tool hiSixTrack and its coupling to FLUKA were introduced. Changes with respect to SixTrack include the introduction of new arrays storing information about A, Z, m and χ of the tracked heavy ion. The symplectic tracking maps used in hiSixTrack are derived from a new generalized Hamiltonian that can describe also the dynamics of particles of other species than the main beam. Hence, hiSixTrack is capable to track heavy ions together with their fragments and accurately compute effects of dispersion from their mass and charge. The tracking algorithm was benchmarked against STIER for different study cases. The implementation of hiSixTrack is soon going to be merged with the main branch and hence be included in the SixTrack main release version.

The coupling of hiSixTrack to FLUKA is a modified version of the proton coupling and allows to exchange heavy ions of any species between the two codes. The fragmentation in the hiSixTrack-FLUKA coupling was benchmarked against FLUKA. Furthermore, the loss maps simulated with the hiSixTrack-FLUKA coupling were compared to the STIER simulation and measured data from the LHC. The agreement of the hiSixTrack-FLUKA coupling with the measured data is better than that of STIER, because subsequent fragmentation processes are included.

With both STIER and the hiSixTrack-FLUKA coupling, new simulation tools are available to study heavy-ion collimation. In the next chapter, STIER is used for the preparation of the LHC heavy-ion operation in 2015 and to develop strategies for loss alleviation in that run. The hiSixTrack-FLUKA coupling is used to study the cleaning inefficiency of HL-LHC including potential upgrades which could possibly reduce the quench risk from collimation losses. It is also studied how the collimation system performs with other heavy ions than $^{208}\mathrm{Pb}^{82+}$.

8. Applications of Heavy-Ion Collimation Simulations

In this chapter, the new simulation tools are applied to different LHC and HL-LHC configurations. STIER[1] simulations are presented, which were used to validate the collimator settings for the 2015 heavy-ion run. Furthermore, STIER is used to probe alternative optics with additional orbit bumps in IR7 for their potential of loss reduction. Finally, it is presented how STIER simulations were used in the 2015 heavy-ion run to reduce the loss rate at the IR2 TCT.

Another application presented in this chapter is the study of the cleaning performance in HL-LHC. The simulations are carried out with the hiSixTrack-FLUKA coupling. Prospective collimation system upgrades are simulated, to estimate their potential for loss reduction. Finally, the cleaning performance in the HL-LHC configuration is studied with heavy ions different than $^{208}\mathrm{Pb}^{82+}$ which could possibly be stored in the LHC.

8.1 Preparation of the LHC Heavy-Ion Operation in 2015

During the operation with $^{208}\mathrm{Pb}^{82+}$ beams in late 2015, the LHC reached particle momenta of 6.37 Z TeV and stored a beam energy of approximately 9.5 MJ [J$^+$16b]. The latter corresponds to more than twice the design value [B$^+$04b]. While the number of injected bunches ($n_B = 426$) was still below the design value of $n_B^d = 518$, the excellent injector performance led to a significant increase of the bunch intensity to (2.2 ± 0.3) ions per bunch [J$^+$16b]. In combination with the small emittance of ϵ_N =(1.50±0.15) μm rad achieved, these improvements enabled luminosities surpassing the design value by a factor of 3.6 [J$^+$16b]. The β^*-value of 0.8 m applied in ATLAS, CMS and ALICE was slightly above the design value of 0.5 m [B$^+$04b].

The stored beam energy was highly challenging for the LHC collimation system. Occasionally, the amount of collimation debris measured with the BLMs in the IR7 DS exceeded the allowed thresholds and triggered protection dumps. Furthermore, losses at the tertiary collimators produced a perturbing background in the experiments, especially in ALICE (see Chap. 8.2).

[1] At the time the studies were conducted, the hiSixTrack-FLUKA coupling was not yet available.

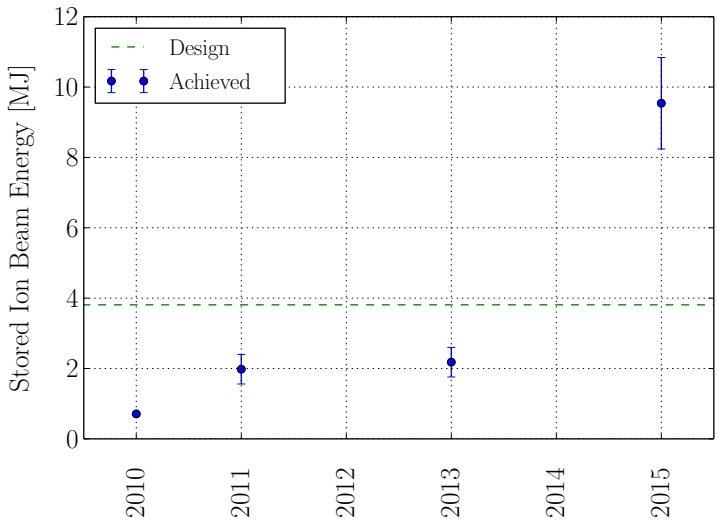

Figure 8.1: Stored heavy-ion beam energy in the past LHC heavy-ion runs. The error bars are derived from the uncertainty of the measured bunch intensity.

Alongside the physics program, which was accomplished with great success and unprecedented integrated luminosities collected [J$^+$16b], several machine experiments were carried out with the LHC. These included two quench tests. In one of these experiments, a main dipole was quenched with the secondary BFPP beams generated in IP5 [S$^+$15a]. At the last day of heavy-ion operation, a collimation quench test was carried out with collimation debris generated at the primary collimator in IR7. This experiment is described in detail in Chap. 9.

In this section, cleaning simulations carried out for the preparation and optimization of the collimation system in the 2015 configuration are presented.

8.1.1 Validation of Collimator Settings

In preparation of the 2015 heavy-ion run, STIER was used to estimate the expected cleaning performance and to study possible strategies to reduce the cleaning inefficiency in the IR7 DS magnets. This includes the study of different collimator settings, in particular different retractions of the TCSG collimators. The study serves the purpose of validating the collimation system and give estimates about the expected loss reduction with tighter settings.

With the geometrical collimator settings taken from the precedent proton operation (see Table 3.7), the TCSG collimators are retracted by $\Delta N_{S,P} = 2.5\,\sigma$ with respect to the primary collimators. STIER is employed to simulate the cleaning inefficiency for the reference settings and in addition with smaller retractions of $2.0\,\sigma, 1.5\,\sigma$ and $1.0\,\sigma$.

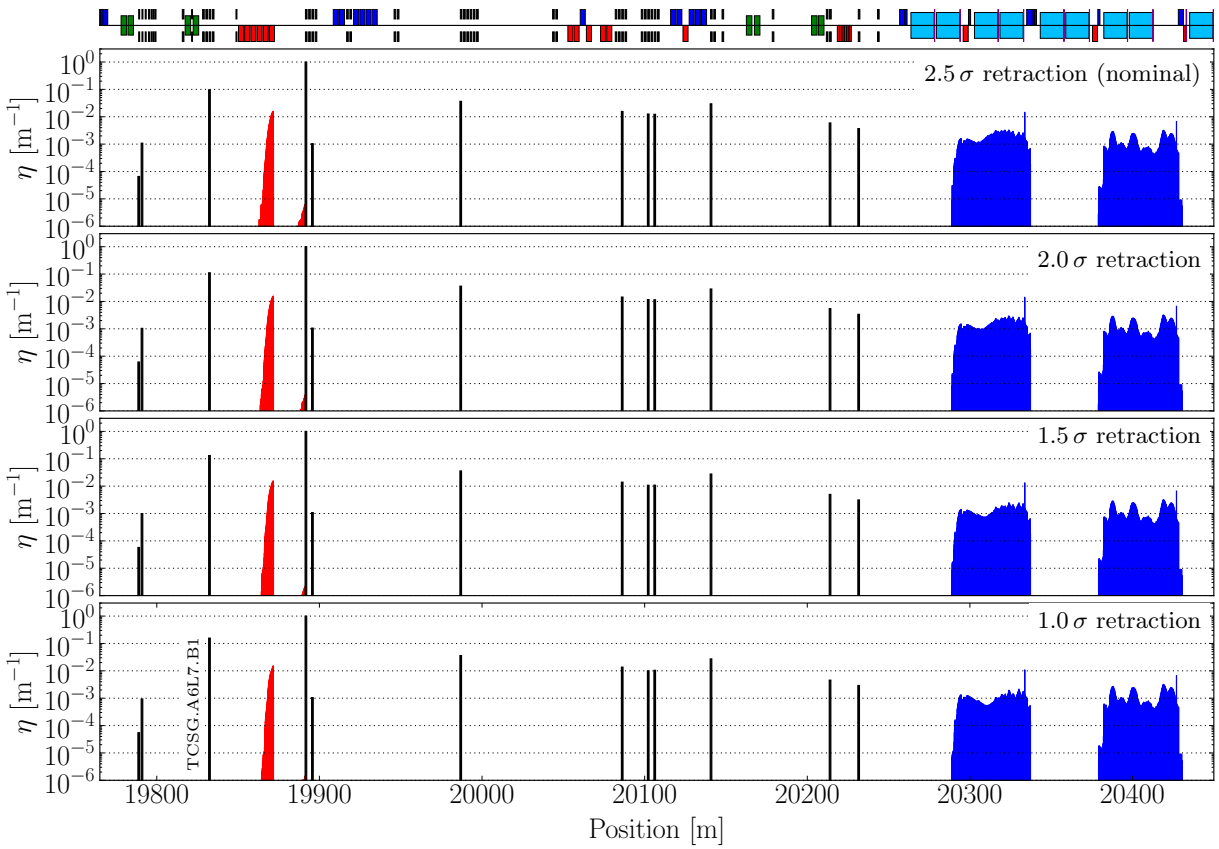

Figure 8.2: IR7 view of the STIER simulated loss maps for $^{208}Pb^{82+}$ ions at 6.37 TeV in the configuration of the 2015 heavy-ion run for different retractions of the TCSG collimators with respect to the primary collimators.

In the fragmentation simulation, the $^{208}Pb^{82+}$ beam is simulated to impact the carbon target in the same geometry already used for the simulations presented in Chap. 6. The impact parameter in these simulations is set to $b = 2\,\mu$m. With an initial sample of 6×10^6 heavy ions impacting the TCP jaw, the fragment distribution obtained from FLUKA is processed into initial coordinates in B1H for STIER. The simulation is carried out for both jaws individually to disentangle the losses arising from particles starting at each jaw. This approach turned out to be very useful for the analysis and mitigation of the losses at the TCT in IR2, as discussed in Chap. 8.2. For the four simulations with different TCSG retractions, the same sample of initial coordinates is used, so the obtained loss patterns are quantitatively comparable.

The loss maps simulated with STIER are shown zoomed to IR7 in Fig. 8.2 and for the full ring in Fig. 8.4. With the smaller TCSG half gap, additional losses occur only at the first secondary collimator (TCSG.A6L7.B1) downstream of the TCP. For the tightest setting studied, the losses at this collimator are increased by 60% with respect to the nominal case.

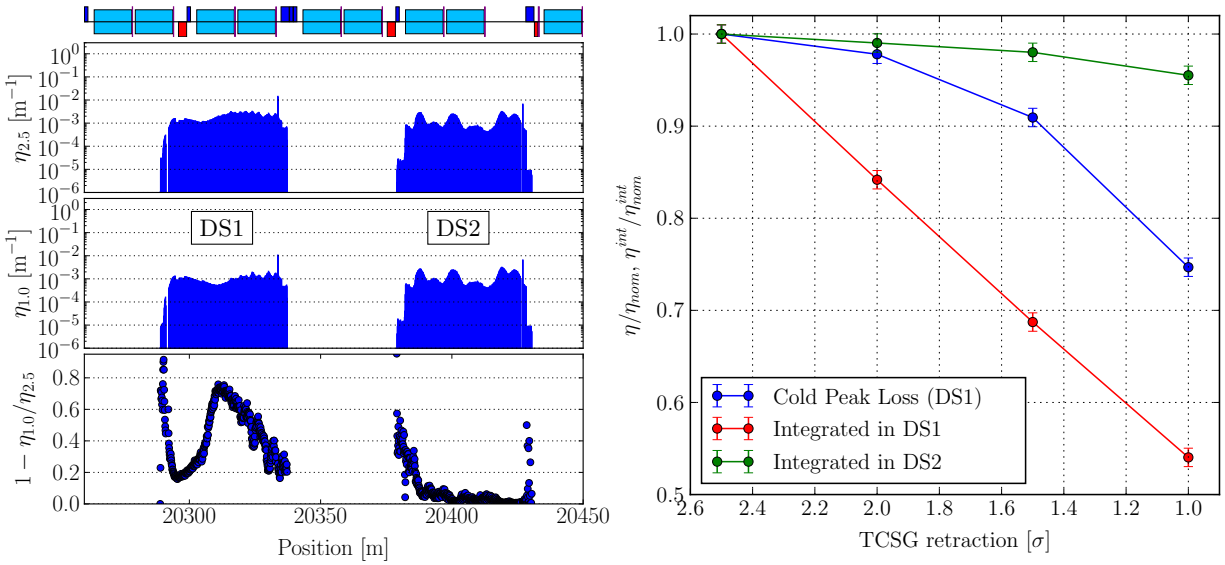

Figure 8.3: Left: Cleaning inefficiency in the dispersion suppressor loss clusters with nominal TCSG retraction (top panel) and with a TCSG retraction of $1.0\,\sigma$ (middle panel). Left bottom panel: loss reduction with $1.0\,\sigma$ retraction compared to the nominal retraction. Right: Evolution of the highest cleaning inefficiency and the integrated losses in DS1 and DS2 as a function of the applied TCSG retraction. The error bars correspond to the statistical errors.

The loss pattern simulated with STIER is similar in all studied cases. For the losses in the IR7 DS, slight differences in the loss pattern are visible for the different scenarios. The simulated cleaning performance with nominal retraction is quantitatively compared to the simulation result with the tightest settings in Fig. 8.3. Also, selected numeric key quantities as a measure of the cleaning performance evolution with decreasing TCSG retraction are listed in Table 8.1.

Table 8.1: STIER simulation results quantifying the cleaning performance as a function of the applied TCSG retraction $\Delta N_{S,P}$ for the 2015 heavy-ion run. The quantity η_{cold}^{max} is the highest cleaning inefficiency in cold LHC regions. The uncertainties correspond to the statistical errors.

$\Delta N_{S,P}$ $[\sigma]$	η_{cold}^{max} $[10^{-2}/\mathrm{m}]$	η_{DS1}^{int} $[10^{-2}]$	η_{DS2}^{int} $[10^{-2}]$
2.5	1.44 ± 0.01	8.1 ± 0.1	5.5 ± 0.1
2.0	1.41 ± 0.01	6.8 ± 0.1	5.5 ± 0.1
1.5	1.31 ± 0.01	5.6 ± 0.1	5.4 ± 0.1
1.0	1.07 ± 0.01	4.4 ± 0.1	5.3 ± 0.1

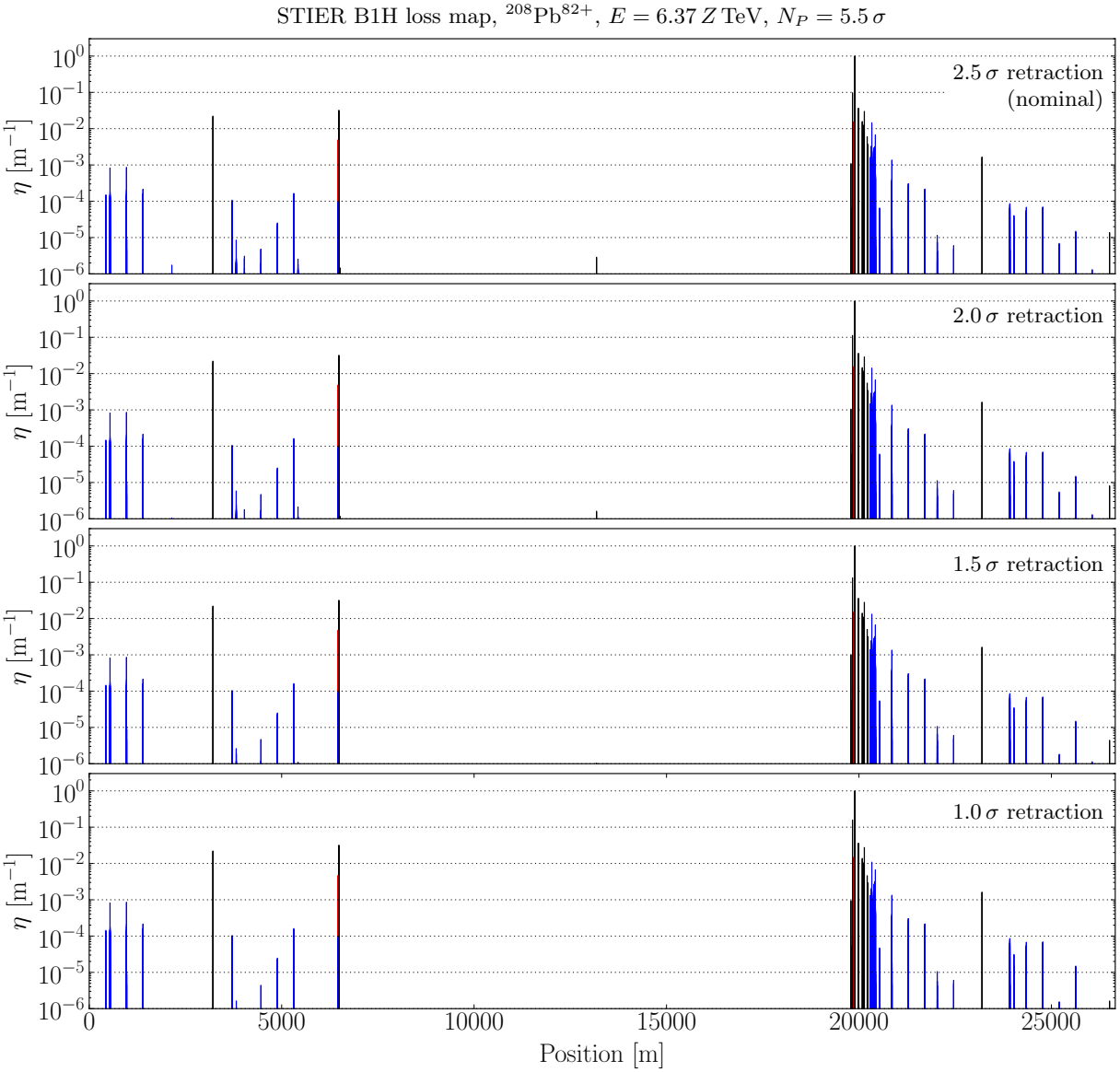

Figure 8.4: STIER simulated loss maps in the 2015 configuration with $^{208}Pb^{82+}$ beams at 6.37 Z TeV for different retractions of the TCSG collimators.

The comparison shows that, with tighter setting, the TCSG captures particularly ion fragments which are lost in the first DS loss cluster otherwise. In terms of integrated losses η^{int}, a reduction of almost 50% is simulated in the DS1, if the smallest retraction is applied. For the DS2, the integrated losses are only reduced by 4%. The peak loss in the superconducting LHC regions is found in the DS1 for all simulations, and is predicted to be reduced by approximately 25% with the tightest setting. The loss distribution in the remaining LHC ring is not changed significantly. An analysis of the loss pattern in IR2 is presented in Chap. 8.2.

In conclusion, the analysis shows that a small reduction of the DS losses could be achieved by varying the TCSG settings. One remaining uncertainty are particles generated in secondary collimator interactions, which could still be lost in the DS1. Given the low potential for loss reduction, the nominal retraction was maintained for the 2015 heavy-ion run.

8.1.2 Orbit Bumps in the IR7 Dispersion Suppressor

The loss location of off-rigid particles which are lost due to magnetic dispersion can be modified by means of dedicated orbit changes. In the 2015 heavy-ion run, the BFPP losses in IR1 and IR5 were shifted into an empty connection cryostat between two superconducting magnets. This reduced the amount of energy lost in the coils of the superconducting magnets and hence also the risk of magnet quench [B$^+$09b, J$^+$16a].

Such shifts of the loss position can be achieved if the theoretical particle trajectory (simulated without aperture restrictions) is beating with the dispersion function and the projected penetration depth (PPD) d_p in the aperture is not too large. The latter is the difference between the dimension of the aperture and the maximum amplitude a particle would reach at the dispersive peak downstream of the loss location (which is at a quadrupole center), as illustrated in Fig. 8.5.

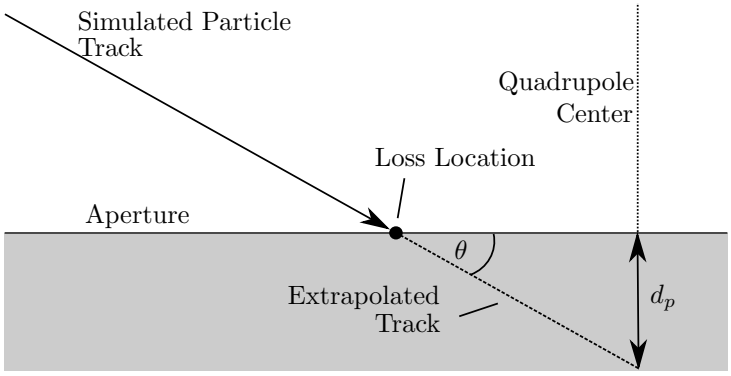

Figure 8.5: Projected penetration depth from the extrapolated particle track in the aperture.

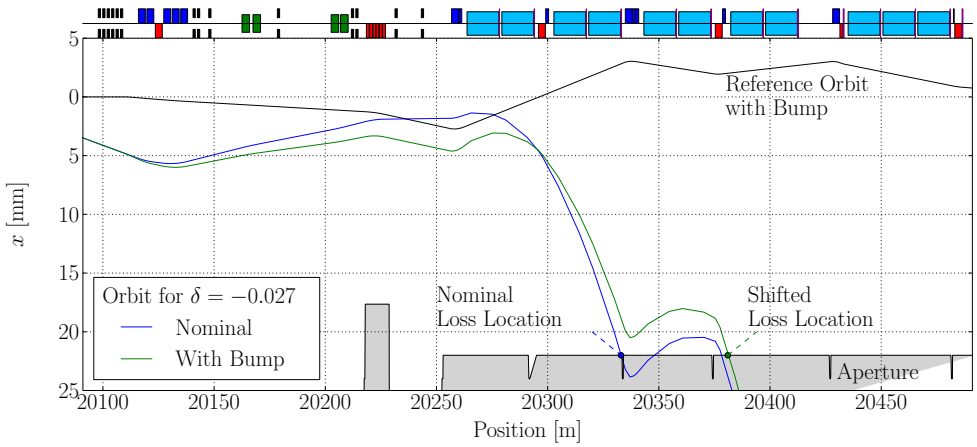

Figure 8.6: Loss location shift of an off-rigid particle by a compensating orbit bump.

As shown in Fig. 8.6, the loss location can be altered towards a dispersive peak further downstream, if d_p is small enough to be compensated by a moderate orbit bump in the opposite direction. Additional bumps in the machine reduce the normalized aperture at the bump location and introduce additional dispersion in the machine, which must be taken into account and limits the achievable bump amplitude. The peak amplitude of the 2015 BFPP bump is 3 mm.

The potential reduction of collimation losses by compensating bumps is limited by the asymmetry of the loss distribution in x. The maximum relative reduction of the cleaning inefficiency $\Delta\bar{\eta}_{max}$ as a function of the cleaning inefficiency from particles impacting on the right side of the beam pipe η_R and those impacting at the left side η_L is given by

$$\Delta\bar{\eta}_{max} = \frac{\eta_R}{\eta_L + \eta_R}\,, \tag{8.1}$$

assuming that more particles impact the right side of the beam pipe. In case of a full asymmetry of the losses, they can in theory be fully shifted by a dedicated bump if this does not increase the loss rate at the other side of the beam pipe.

PPD Estimates

The possibility of collimation loss mitigation with orbit bumps in the IR7 DS can be explored from the STIER simulation data already produced for the study presented in the previous section. The analysis of this data shows that approximately 75% of the collimation debris lost in the DS1 impacts the beam pipe aperture on the left hand side ($x > 0$). In the DS2, this fraction is even 97%. This finding is in line with the asymmetry in χ observed for the fragments scattered out of the primary collimator (see Fig. 8.7).

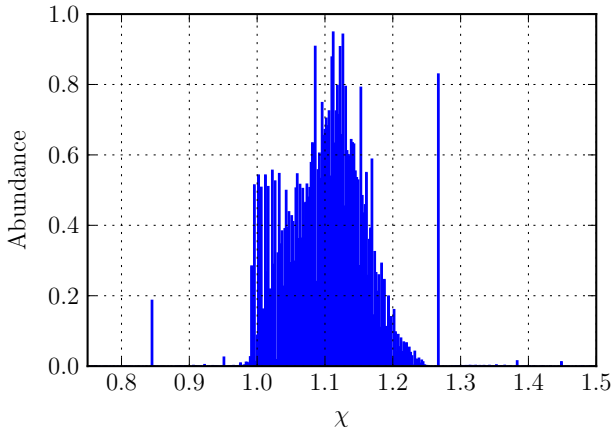

Figure 8.7: Distribution in χ of the particles scattered out of the primary collimator, simulated with FLUKA for a primary beam of $^{208}\mathrm{Pb}^{82+}$ ions at 6.37 ZTeV.

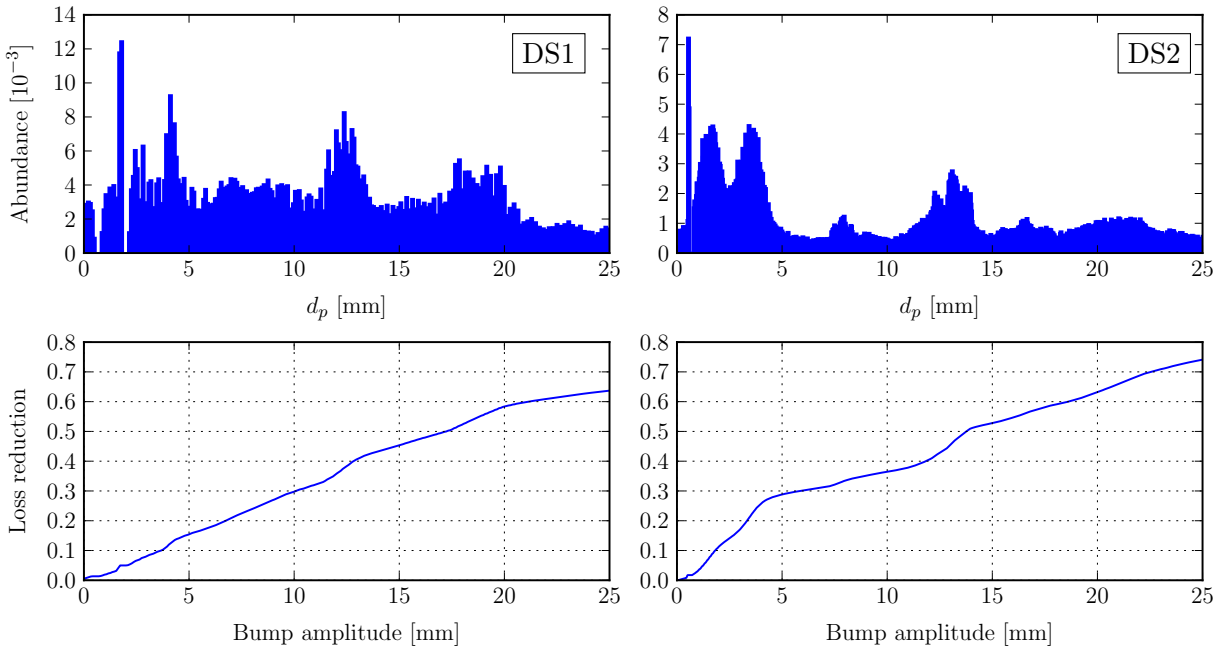

Figure 8.8: Top row: Histogram of the projected penetration depth of the different isotopes impacting the left side of the beam pipe in DS1 and DS2, weighted with the ion momentum. Both histograms are normalized by the total momentum of the impacting ions. Bottom row: Potential loss reduction as a function of the bump amplitude applied at each loss region.

The possible loss reduction by an orbit bump can be studied by means of the PPD of the isotopes impacting at the location of the two DS clusters. The quantity d_p is derived from the STIER simulation data by a linear extrapolation of the particle trajectory. The extrapolation is based on information on the longitudinal distance between impact location and quadrupole center (in which the betatron function and dispersion are maximum) and the impacting angle at the aperture. This method allows to relate a target loss reduction to the required bump amplitude at the loss location.

The distribution of the projected penetration depth of particles impacting the left hand side of the DS magnets is shown for the DS loss clusters in Fig. 8.8. Both clusters show a broad distribution of d_p reaching to values up to more than 25 mm. In the bottom panel of Fig. 8.8, the integrated losses are shown as a function of the projected penetration depth. This can be interpreted as the reachable loss reduction with respect to a given bump amplitude. Both integrated loss curves are calculated with respect to the highest achievable loss reduction, determined from the loss asymmetry. The contribution of each impacting particle is weighted with its momentum.

The bump amplitude required to alleviate 50% of the losses yields approximately 17 mm in the DS1 and 14 mm in the DS2. Both of them are significantly too large to be applied in operation (the horizontal beam pipe aperture is only 22 mm). Applicable bump amplitudes are rather in the order of a few mm. Assuming a maximum bump amplitude of 3 mm, the reachable loss reduction yields only 6% in the DS1 and 14% in the DS2.

STIER Simulation with Orbit Bump

The conclusion of the previous sub-section is supported by the outcome of a dedicated STIER simulation in which an additional horizontal bump in positive direction is applied. The bump has a maximum amplitude of 3 mm in the DS2 cluster (see Fig. 8.9). Apart from the bump, the configuration is identical to the reference STIER simulation of the 2015 heavy-ion run. Also the initial distribution of fragments is identical to that used for the previous studies.

The simulated loss map is compared to the STIER simulation with nominal optics settings in Fig. 8.9. The bump amplitude in the region of the DS1 cluster is small, so the loss pattern is very similar to the nominal one. The shape of the loss pattern in the DS2 cluster is changed, but the peak amplitude is not significantly reduced. The change of the loss distribution can be explained by the fact that the loss location of the individual isotopes is shifted to the right. This is especially true for the losses at the right bound of the DS2, which are shifted into the first loss peak of the LHC arc region (A1) which results in an increased loss signal at this location. The integrated losses in the DS2 are reduced by approximately 13%. Note that the bump is not at its maximum amplitude over the full length of the DS2 cluster.

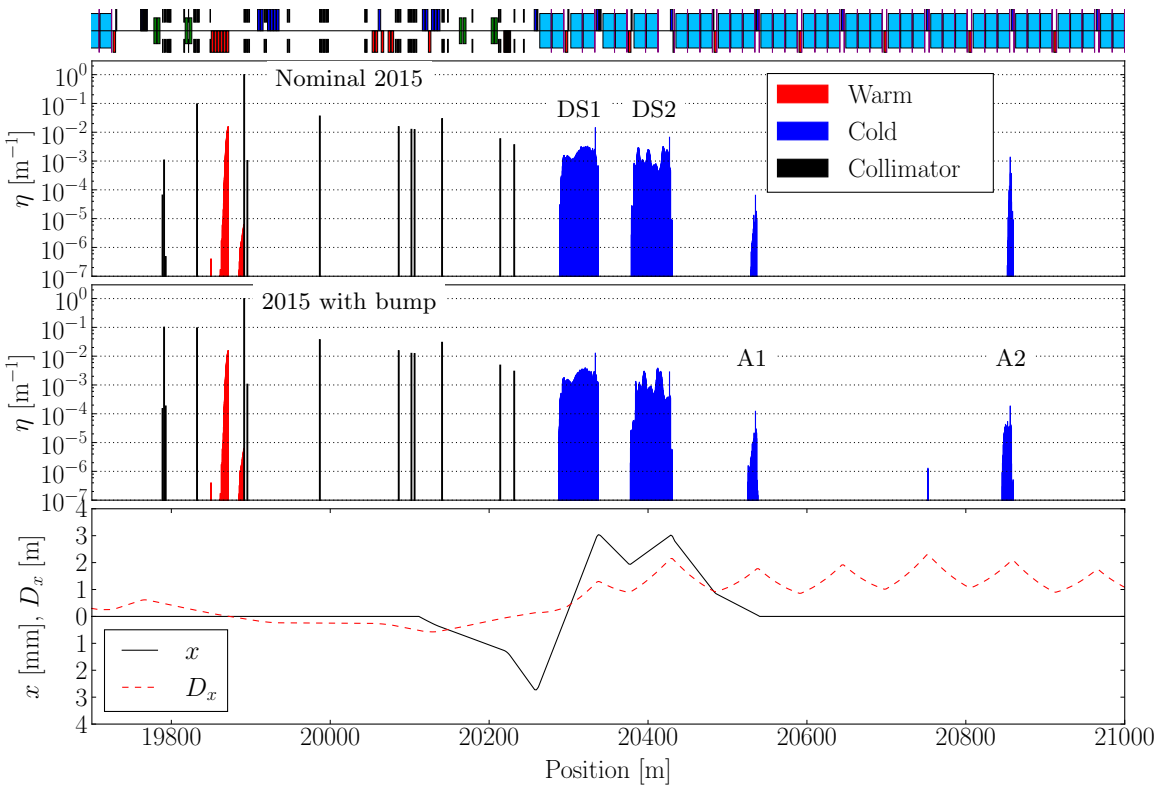

Figure 8.9: Top row: nominal STIER simulated cleaning inefficiency in the 2015 heavy-ion configuration. Middle row: STIER simulation with an additional orbit bump at a maximum amplitude of $x_b = +3$ mm at the DS2. Bottom row: beam orbit and periodic dispersion function (the local dispersion function from the TCP is similar) with the applied bump.

The loss reduction derived from the STIER simulation with altered reference orbit is in excellent agreement with that derived from the PPD distribution. This demonstrates that the latter can be used to accurately predict the reduction of losses from orbit or aperture shifts. This method is used in Chap. 10.1 to study discrepancies between measured and simulated losses.

Conclusions

In conclusion, the analysis of the projected penetration depth shows that the alleviation of the DS losses would require very large bump amplitudes, which are not compatible with safe operation of the LHC. Also the shift of losses towards the connection cryostat, as it is done for the BFPP losses, is not possible within the available margins of bump amplitudes, because the rigidity offset of the impacting particles is too large. On the contrary, the loss reduction that is achievable with reasonable bump amplitudes is not sufficiently beneficial to justify the additional effort of integrating it into the operational configuration.

8.2 Suppression of Losses at the IR2 TCT

In the commissioning phase of the 2015 heavy-ion run, also measured qualification loss maps became available. The global B1H betatron qualification loss map with squeezed beams is shown in the top panel of Fig. 8.10. The relative BLM signal in the IR7 DS reaches values of $\mathcal{B}_{\mathrm{DS}} \approx 10^{-2}$, comparable to the 2011 heavy-ion run. Again, individual loss spikes are located in the arc regions over the complete ring. Compared to the operation in 2011, some of them are at different locations. A very high loss signal was measured at the horizontal tertiary collimator for B1 in IR2 (TCTHP.4L2.B1). In the following, this collimator is referred to as TCT2. The normalized BLM signal[2] at this location yields

$$\mathcal{B}_{\mathrm{TCT2}} = (6.6 \pm 0.5) \times 10^{-2} \,. \tag{8.2}$$

The uncertainty is estimated from variations of the measured $\mathcal{B}_{\mathrm{TCT2}}$ in different measurement campaigns. It corresponds to the difference between the largest and the smallest $\mathcal{B}_{\mathrm{TCT2}}$ measured.The high collimation losses at the TCT2 were present during physics operation as a regular background also without additional beam excitation. The secondary showers created from the particles impacting the TCT2 caused a radiation background and hence distorted the operation of the ALICE experiment. The STIER simulation output was consulted to understand these losses and work out possible strategies to reduce them.

8.2.1 Situation and Analysis

Considering that the losses occur at the horizontal TCT for B1, the STIER simulation presented in Chap. 8.1.1 can be taken as a reference for the analysis. The global loss map simulated with STIER is shown, disentangled for the particles starting at the left and the right TCP jaw, in the middle and bottom panel of Fig. 8.10. With the TCT2 losses clearly visible in both simulations, the comparison unveils that the larger fraction originates from the left TCP jaw. The fragments starting from the left jaw cause 20 times more losses than those starting from the right jaw.
The quantitative analysis summarized in Table 8.2 shows that the isotope $^{207}\mathrm{Pb}^{82+}$ starting at the left TCP jaw is clearly dominating over all other isotopes lost at the TCT2. Approximately 92.5% of the total simulated TCT2 signal (by combining the simulations for the individual jaws) is caused by this single isotope. Note, however, that the production rate of this isotope and therefore also the loss composition at the TCT2 depends crucially on the impact parameter at the TCP, which is 2 μm in this simulation. The presented quantitative comparison is therefore only valid for this impact parameter.

[2]Measured with the BLMTI.04L2.B1E10_TCTPH.4L2.B1.

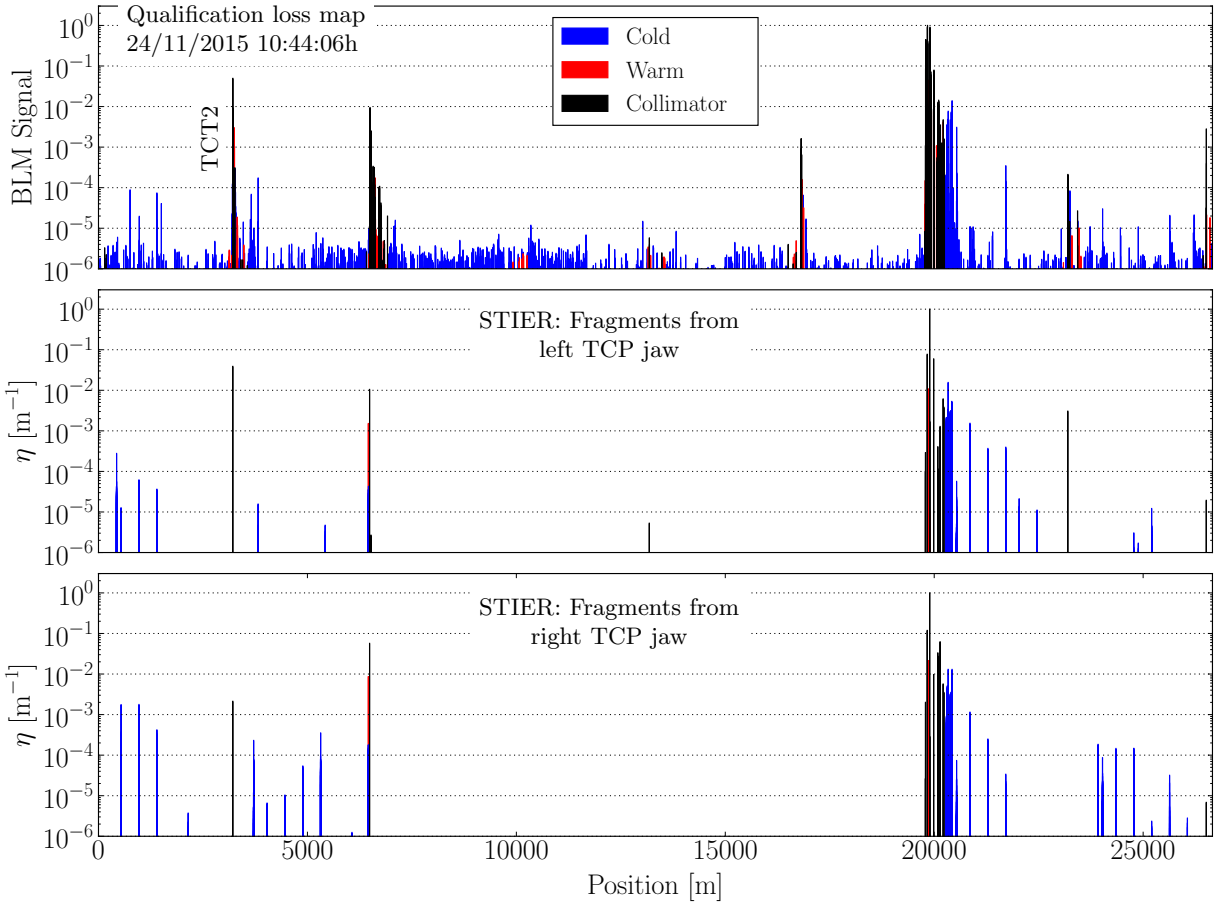

Figure 8.10: Top panel: B1H qualification loss map measured in the 2015 heavy-ion run. Middle and bottom panel: STIER simulation result of the $^{208}Pb^{82+}$ cleaning inefficiency for B1H in the configuration of the 2015 heavy-ion run at 6.37 Z TeV. The simulation result is shown for particles starting at the left and at the right horizontal TCP jaw separately. Both simulations are carried out with 6×10^6 initial $^{208}Pb^{82+}$ particles.

Table 8.2: Loss composition at the TCT2 simulated with STIER for B1H in the 2015 configuration using a TCP impact parameter of 2 μm. The energy fraction is calculated from the number of particles of each isotope, weighted with the particle momenta.

Isotope (A,Z)	TCP jaw	Fraction (%)
$^{207}Pb^{82+}$	left	92.5
$^{204}Tl^{81+}$	right	3.6
$^{202}Hg^{80+}$	left	2.2
$^{199}Au^{79+}$	right	0.3

A better understanding of the situation can be obtained from the horizontal trajectory of the secondary $^{207}Pb^{82+}$ beam which is generated by EMD in the TCP. The simulated horizontal track of this isotope starting from the left TCP jaw is shown with the machine aperture and the collimators in Fig. 8.11. The secondary beam of this isotope is not intercepted by the TCSG collimators in IR7 or the IR7 DS magnet aperture. It passes the edge of the right TCTH.4L8.B1 (TCT8) jaw at a small distance. Finally, it impacts the left jaw of the TCT2 with an impact parameter of several mm. STIER predicts the secondary $^{207}Pb^{82+}$ beam starting from the other TCP jaw to be intercepted by the momentum collimators in IR3.

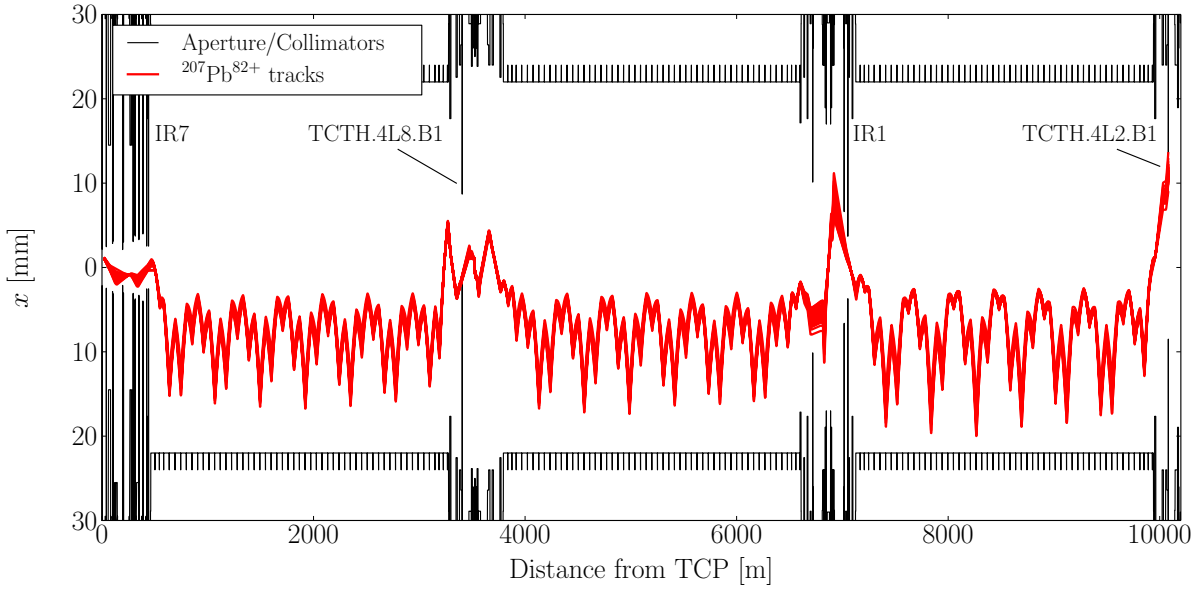

Figure 8.11: Simulated track of the secondary $^{207}Pb^{82+}$ beam starting at the left jaw of the horizontal TCP in IR7, which is lost at the TCT2.

8.2.2 Mitigation Strategies and their Application in the LHC

Based on the findings presented above, two different mitigation strategies have been worked out and tested with a $^{208}Pb^{82+}$ beam in the LHC during the 2015 heavy-ion run.

Retraction of the left TCP jaw

The asymmetry in the origin of the TCT2 losses can be exploited if asymmetric collimator settings are applied for the TCP. Given that the majority of losses is caused by particles starting from the left TCP jaw, a significant reduction of these losses can be expected if the latter is retracted. The primary losses in this case are shifted to the right TCP jaw. According to STIER, the TCT2 losses should be reduced by approximately 94.7% at full retraction of the left TCP jaw. This corresponds to a reduction of the measured BLM signal from $\mathcal{B}_{\mathrm{TCT2}} = (6.6 \pm 0.5) \times 10^{-2}$ to $\mathcal{B}_{\mathrm{TCT2}} = (3.5 \pm 0.3) \times 10^{-3}$. Note that in this study it is only possible to make quantitative predictions because the initial BLM signal is known and scaled with the reduction factor calculated with STIER. Also, the predicted reduction can only be accurate if the impact parameter in the real machine is similar to that used for the STIER simulation.

The experimental validation was conducted the 07.12.2015 with low intensity beams circulating in the LHC at 6.37 Z TeV with squeezed optics. To probe the hypothesized loss reduction, the left TCP jaw was retracted in steps and the ADT was used to induce the primary losses at the TCP at every step. The individual loss maps measured at every step are shown in Fig. A.2. The measured signal at the TCT2 is shown as a function of the left TCP jaw position in Fig. 8.12.

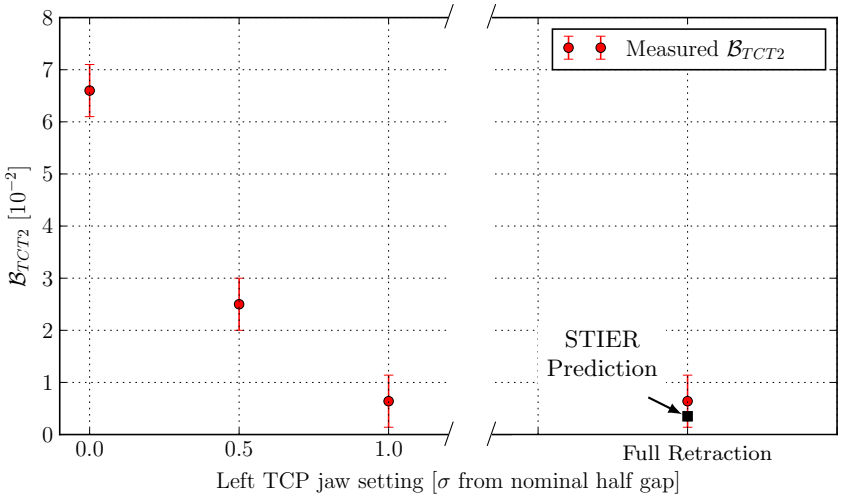

Figure 8.12: Measured BLM Signal (integration time 1.3 s) at the TCT2 for different settings of the left TCP jaw, compared to the prediction by the STIER simulation.

During the experiment, the loss signal indeed decreased with increasing retraction of the left TCP jaw and yielded $\mathcal{B}_{\mathrm{TCT2}} = (6 \pm 5) \times 10^{-3}$ at the most extreme scenario of a full retraction. This result is in excellent agreement with the prediction made by STIER. As a consistency check, the same experiment was repeated with with the left TCP jaw in place and the right TCP jaw retracted. As expected, no loss reduction was achieved in this configuration.

Tightening the TCT in IR8

The horizontal track shows that the secondary ion beam passes the horizontal TCT8 at a very small distance in x. In a second experiment, this prediction was studied by closing the TCT8 in steps. The measured loss maps for the individual steps are shown in Fig. A.1 in the Appendix. STIER can be used to derive the expected loss signal at the TCT2 as a function of the TCT8 half gap. This requires information about the horizontal distribution of the $^{207}\mathrm{Pb}^{82+}$ particles at the TCT8, to determine which fraction is intercepted with different TCT8 settings.

The horizontal betatron function of the secondary $^{207}\mathrm{Pb}^{82+}$ beam is calculated taking into account the offset in rigidity with respect to the main beam[3]. Assuming that the emittance is not significantly different from that of the main beam, the RMS size of the secondary beam is derived. The particle distribution is then modeled as a Gaussian, horizontally centered at the simulated $^{207}\mathrm{Pb}^{82+}$ particle track predicted by STIER.

[3]The betatron function is rigidity-dependent.

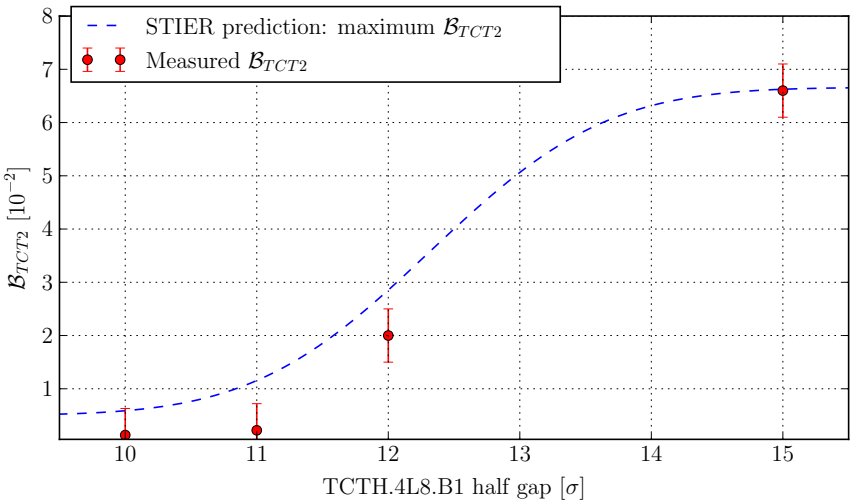

Figure 8.13: Normalized BLM signal (RS09) at the TCT2 as a function of the TCT8 half gap. The blue line shows the predicted upper boundary of the cleaning inefficiency simulated with STIER. This is achieved by taking the BLM signal at the nominal TCT8 setting as a reference and re-scaling it with the relative loss reduction predicted by STIER.

With this model, the fraction of the secondary $^{207}Pb^{82+}$ beam that is intercepted by the TCT8 is determined and converted into the expected loss reduction at the TCT2. The studied isotope is not the only one lost at the TCT2, hence the predicted reduction of the secondary $^{207}Pb^{82+}$ beam intensity must be scaled with its contribution to the TCT2 losses (which is 92.5%). Furthermore, the remaining isotopes may also be intercepted by the TCT8 which would also reduce the TCT2 loss signal. This is not taken into account in the presented approach. The result therefore indicates only an upper boundary of the expected TCT2 signal.

In Fig. 8.13, the measured TCT2 signals are shown as a function of the TCT8 half gap, together with the upper boundary predicted by STIER. The measured and predicted loss reduction is again in an excellent agreement. This result demonstrates that STIER can indeed be used to accurately predict particle tracks of heavy ions in the LHC.

8.2.3 Conclusions

Both mitigation strategies derived from the STIER simulation data have been proven to be effective and the predicted loss levels are quantitatively supported by the measured BLM signals. This result underlines the importance of heavy-ion collimation simulation tools, which are essential to understand loss mechanisms and measured loss patterns. They provide indispensable input to optimize the collimation system if the stored beam energy shall be further increased.

After the successful test, the application of asymmetric TCP settings in regular heavy-ion operation was discussed, to reduce the background at the ALICE experiment. The decision was taken to accept the TCT2 losses and maintain the nominal collimator configuration because of the time which would have been required for a re-commissioning of the new configuration. Also, the beam lifetime improved later in the run, so that the amount of losses at the TCT2 was reduced. However, the strategy of asymmetric TCP settings could be used in future heavy-ion runs to mitigate losses in similar situations.

8.3 High Luminosity LHC

With the High Luminosity LHC (HL-LHC) upgrade, a significant increase of the stored heavy-ion beam energy is envisaged, as explained in Chap. 3.2.7. Already in the 2015 heavy-ion run, the target bunch intensity for LIU has been exceeded. Upcoming upgrades of the LHC injectors will possibly lead to a further increase.

An inevitable consequence of the higher stored beam energy is the larger amount of collimation debris which is lost in the DS magnets. Also for proton beams, the collimation losses in the DS become a serious issue with the envisaged intensities. Therefore, the installation of additional collimators (TCLD) in the IR7 DS is foreseen for HL-LHC. Simulations for proton beams indicate a significant improvement of the cleaning inefficiency with this upgrade [BMR14].

This chapter is dedicated to simulations of the cleaning inefficiency of heavy-ion beams in the HL-LHC configuration with and without TCLD collimators. The outcome of the presented studies is going to be used to define the requirements on the collimation system upgrades for future heavy-ion operation.

8.3.1 Collimation System Upgrades for HL-LHC

The safe and uninterrupted operation with the proton intensities foreseen for HL-LHC requires several upgrades of the LHC collimation system. The upgrade schedule includes the installation of new collimators and the replacement of the active material of some existing collimators. Here, only the most essential modifications are summarized. A detailed overview is given in [M$^+$16b].

The increased luminosities in IR1 and IR5 are going to increase the amount of collision debris. To protect the surrounding magnets from this debris, these IRs are going to be equipped with additional TCLX collimators. Although Q4 and Q5 magnets in IR1/IR5 are envisaged to be replaced by quadrupoles with larger geometric aperture, they might still intercept high beam losses [GMBR16]. To protect their aperture, another set of two tertiary collimators per beam is envisaged to be installed in cell 5, in addition to those currently installed in cell 4. This could also reduce the background to the experiment. It is also under study to change the TCT material from IT180 to a composite material, copper-diamond [Q$^+$16], for better robustness.

In IR7, the changes include new active materials for the TCSGs with lower impedance but same robustness as the CFC presently used. To mitigate the potentially critical losses in the DS region of IR7 (for both protons and heavy ions), the installation of additional local collimators is planned. The DS1 and DS2 loss clusters are located in the cells 9 and 11 downstream of IR7. Therefore, the proposal foresees two new horizontal collimators to be installed upstream of them in the cells 8 and 10 [W$^+$08, BMR14].

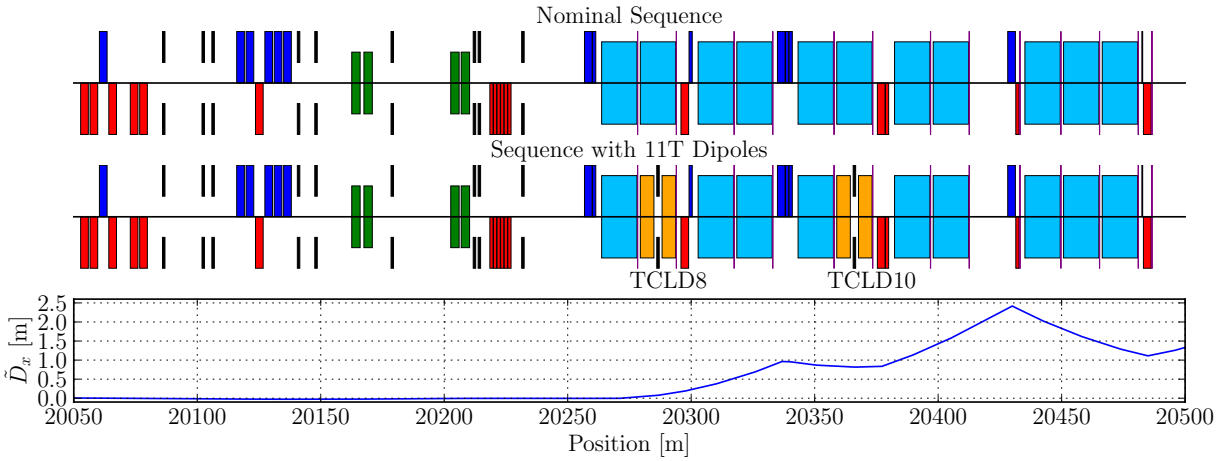

Figure 8.14: LHC beam line sequence in IR7 for B1. Top panel: Nominal sequence. Middle panel: sequence with the main dipoles in cell 8 and cell 10 replaced by two 11 T dipoles and the TCLD collimators in between. Bottom panel: local hor. dispersion function from the TCP.

The required space would be made available by replacing a nominal main dipole by two stronger and shorter dipoles than can provide a maximum magnetic field strength of 11 T.

The new collimator, called TCLD[4], could be installed in between the new dipoles. This is illustrated in Fig. 8.14. To provide a large stopping power, the present layout foresees tungsten as the active material of the TCLD collimators. SixTrack simulations predict a significant improvement of the proton cleaning inefficiency when the TCLD collimators are installed [BMR14].

Especially the construction of the stronger dipole magnets requires significant financial resources. Present cost estimates assume approximately 10 million CHF for the installation of one TCLD [Red16]. It is also not yet clear how many of them can be manufactured by the time their installation is foreseen [Red16]. For these reasons, a solution is preferred in which only one TCLD per beam is required (installed in cell 8).

The heavy-ion cleaning inefficiency in the HL-LHC configuration with and without TCLD collimators is studied by means of the hiSixTrack-FLUKA coupling. The presented simulations are therefore carried out for three cases to compare the limiting cleaning inefficiency and evaluate the risk of quenches for the three following scenarios:

- 0 TCLDs: reference simulation for the present layout without TCLD collimators,
- 1 TCLD: layout with an additional TCLD collimator in cell 8 (TCLD8),
- 2 TCLDs: TCLD collimators are installed in cell 8 and cell 10 (TCLD10).

[4]Target Collimator Long Dispersion Suppressor.

It is also envisaged to install TCLD collimators in the DS of IR2, to intercept the secondary beams generated from BFPP [M$^+$16b]. In this IR, they can be installed in the empty connection cryostat in cell 10, which makes the installation of 11 T dipoles unnecessary. In the following simulations the IR2 TCLDs are not included, because their half gap is going to be in the order of $30\,\sigma$. The influence on collimation cleaning simulations should therefore be small [Mer16].

8.3.2 Cleaning Simulations without TCLD Collimators in IR7

Table 8.3: Collimator half gaps in σ envisaged for HL-LHC.

IR7		IR3		IR1/2/5/8/6	
TCP	5.7	TCP	15.0	TCT	10.9
TCSG	7.7	TCSG	18.0	TCL	12.0
TCLA	10.0	TCLA	20.0	TCDQ	9.0
				TCSP	8.5

The cleaning simulations with the hiSixTrack-FLUKA coupling are carried out for the different planes (B1H, B2H, B1V, B2V) with different impact parameters to find the scenario with the largest cleaning inefficiency. For this scenario the cleaning inefficiency is then studied for different possible half gaps of the TCLD collimators.

All simulations are carried out with the HL-LHC heavy-ion optics V.1.2 with $\beta^* = 0.48\,\text{m}$ in IP1/IP5, $\beta^* = 0.5\,\text{m}$ in IP2 and $\beta^* = 3.0\,\text{m}$ in IP8. The collimator settings are summarized in Table 8.3. The upgrades of the collimator material are not incorporated in the simulation. The materials used in the presented studies are hence the standard materials stored in the FEDB. However, studies with protons show that the influence of the new materials on the cleaning inefficiency is small [Q$^+$16]. Future simulations are envisaged to also study the effect of the changed materials on the heavy-ion cleaning inefficiency.

Quench Risk and Cleaning Inefficiency

The main motivation for the validation studies for the 2015 heavy-ion operation was to reduce the amount of losses in the DS clusters to reduce the risk of protection dumps by the BLM system. The cleaning performance of the LHC collimation system was quantified mostly by means of the peak cleaning inefficiency in the superconducting LHC magnets and by the integrated cleaning inefficiency in the DS loss clusters. For HL-LHC, the stored beam energies are significantly larger and the heavy-ion program is seriously endangered by the risk of beam-induced quenches.

To quantify the risk of quench, the maximum average cleaning inefficiency is considered. It takes into account, that in reality also showers from particles lost upstream contribute to the energy deposition in the magnet coils. The average cleaning inefficiency η^{avg} is defined as the average $\eta(s)$ in a given interval $[s_0, s_1]$. For the presented analyses, the average cleaning inefficiency is calculated in the DS loss clusters in intervals of 7.2 m length, roughly half the length of a LHC main dipole. Since the loss distribution in the DS clusters is inhomogeneous and η^{avg} depends on the starting point s_0, all possible intervals are scanned in steps of 0.1 m and the respective maximum average cleaning inefficiency in the two DS clusters is defined as η^{avg}_{DS1} and η^{avg}_{DS2}. In the following, the global maximum average cleaning inefficiency in the superconducting LHC regions η^{avg}_{max} is considered to quantify the risk of quench.

Evidently, this is an approximation and a better modeling of the quench risk could be obtained if the energy deposition in the superconducting coils would be simulated. This requires additional studies with FLUKA, and is planned for the future.

Selection of Beam and Plane

In a first set of simulations, the most critical loss plane is identified. For this purpose simulations are carried out with identical settings without TCLDs for both beams of both planes. All simulations are carried out with $6{\times}10^6$ particles of $^{208}\mathrm{Pb}^{82+}$. The resulting loss maps are shown for IR7 in Fig. A.3 in the Appendix. The most important key parameters η^{max}_{cold} and η^{avg}_{max} deduced from the simulations of the cleaning inefficiency are summarized in Fig. 8.15. The analysis shows that the largest cleaning inefficiency is simulated in B1H in terms of both key parameters. For the following studies the simulations are therefore carried out for B1H.

Impact Parameters

In another set of cleaning simulations, the impact parameter associated to the largest cleaning inefficiency for B1H shall be identified. Seven different simulations are carried out using $6{\times}10^6$ initial $^{208}\mathrm{Pb}^{82+}$ ions with impact parameters of 0.1 μm, 0.33 μm, 1.0 μm, 3.3 μm, 10.0 μm, 33.3 μm and 100 μm. The key parameters derived from these simulations are summarized in Fig. 8.16. The figure also shows the distance d, which the particles traverse in the collimator material as a function of the impact parameter, assuming an impact angle of 2.1×10^{-2} mrad.

The comparison shows that the average cleaning inefficiency in the two IR7 DS clusters increases from $b = 0.1\,\mu$m to 3.3 μm and then decreases by two orders of magnitude for when the impact parameter is increased to 10.0 μm. From 10 μm to 33 μm, the cleaning inefficiency decreases slightly and remains constant when increasing the impact parameter to 100 μm.

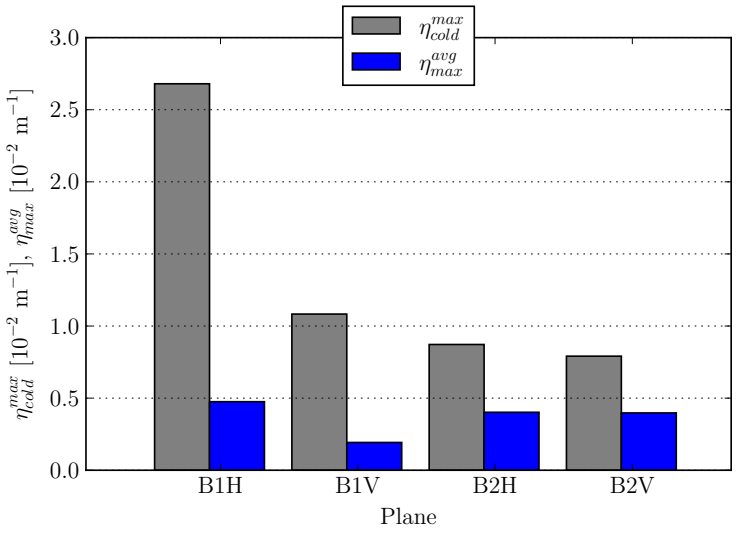

Figure 8.15: Maximum peak cleaning inefficiency η^{max}_{cold}, and maximum average cleaning inefficiency η^{avg}_{max} in the different planes simulated with the hiSixTrack-FLUKA coupling in the HL-LHC configuration at 7 Z TeV for ^{208}Pb^{82+} beams.

As shown in Fig. 8.16, the particles traverse the full length of the collimator jaw if the impact parameter is larger than 12 μm. Therefore, the fragmentation spectrum and hence the cleaning inefficiency does not change significantly from 33.3 μm to 100.0 μm.

The average cleaning inefficiency simulated for the DS1 is similar to that of the DS2 for impact parameters $b \leq 1\,\mu$m. For larger impact parameters, the losses in the DS1 become significantly

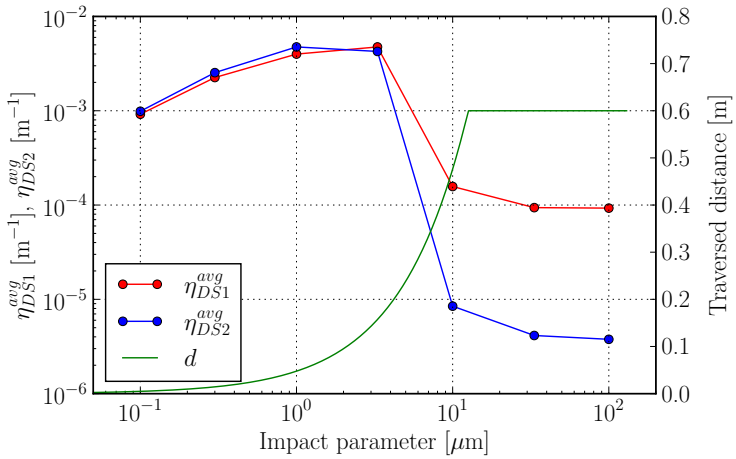

Figure 8.16: Average cleaning inefficiency in the DS1 and DS2 cluster for B1H with different impact parameters, derived from cleaning simulations with the hiSixTrack-FLUKA coupling in the HL-LHC configuration with ^{208}Pb^{82+} ions at 7 Z TeV.

larger than in the DS2. As discussed in Chap. 6.2.2, heavy nuclei with mass and charge close to the main beam that could be lost in the DS2, are mostly fragmented into other isotopes when larger impact parameters are applied. Hence, with larger impact parameters the rigidity offset of the fragments increases. In consequence the dispersion in the DS1 is sufficient to guide them into the magnet aperture and remove them from the beam before they reach the DS2.

To understand why the cleaning performance for an impact parameter of 0.1 μm is better than for 1.0 μm, a dedicated simulation was conducted. Possible effects of the phase space space shift with the associated increase of the impact parameter (this was discussed in Chap. 7.6.1) shall be ruled out by switching off the sextupole magnets. The simulation unveils that the cleaning inefficiency for $b = 1.0\,\mu$m is still worse than for 0.1 μm, also without sextupoles.

The distribution of impact parameters at the TCP for impacts at turns subsequent to the first interaction with the TCP is shown in Fig. 8.17. This means that only ions are studied which have already passed through the TCP material at least once, but have been scattered out without fragmenting. In the following description, the impact parameter at the first TCP interaction is referred to as primary impact parameter. For impacts at subsequent turns, the denotation secondary impact parameter is used.

For secondary impact parameters smaller than 120 μm, higher abundances are visible for the simulation with a primary impact parameter of 0.1 μm. For those larger than 120 μm, the opposite applies. This might come from the lower momentum offset particles receive from

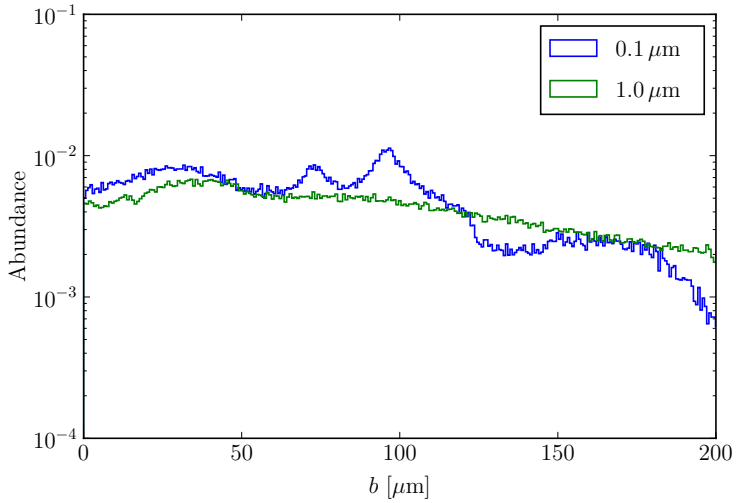

Figure 8.17: Impact parameters at the TCP at turns subsequent to the first interaction with the TCP for $b = 0.1\,\mu$m and 1 μm. All particles arriving at the TCP in a subsequent turn are $^{208}Pb^{82+}$ ions. Both distributions are weighted with the particle momenta and normalized with respect to the total momentum of all particles.

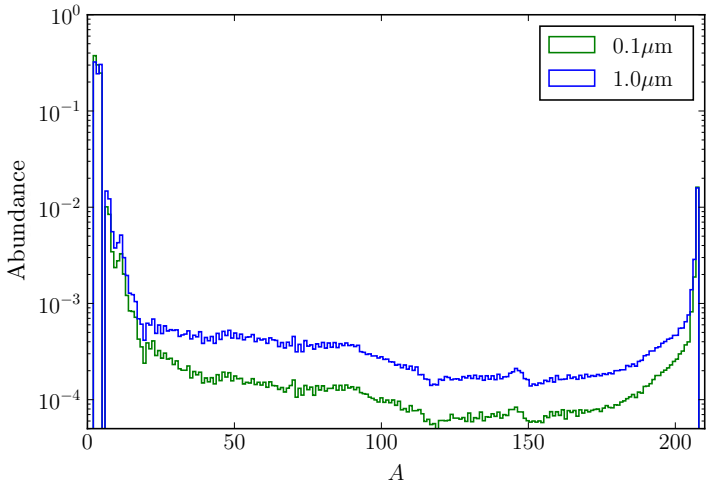

Figure 8.18: Abundance of the nuclear mass number for fragments created at the first passage of one million $^{208}Pb^{82+}$ ions through the TCP with $b = 1\,\mu$m and $b = 0.1\,\mu$m. Both distributions are normalized by the total number of particles.

ionization losses during the first passage with a primary impact parameter of $0.1\,\mu$m, because the distance traversed in the collimator is smaller. These particles arrive at a subsequent turn with a smaller dispersive offset, than those with a primary impact parameter of $1.0\,\mu$m. However, the integral is quantitatively similar for both study cases. The worse cleaning inefficiency for $1\,\mu$m must therefore be related to the interaction with the TCP at the primary passage.

The distribution of nuclear mass numbers for the heavy-ion fragments generated at the first TCP passage is shown in Fig. 8.18. The comparison shows that the number of fragments with intermediate mass numbers is significantly higher for $1\,\mu$m than for $0.1\,\mu$m. The origin of this difference is the distance the particles traverse in the TCP material, which is ten times larger for an impact parameter of $1\,\mu$m than for $0.1\,\mu$m. In total, the production rate for particles with rigidity offsets beyond 5% is higher by a factor of approximately two for the simulation with $b = 1\,\mu$m. This corresponds to the difference of the average cleaning inefficiency in the DS which is observed between the simulations with $0.1\,\mu$m and $1\,\mu$m. It is hence the difference in fragmentation at the first TCP passage which leads to the larger cleaning inefficiency at $1\,\mu$m.

8.3.3 Cleaning Simulations with TCLD Collimators in IR7

In this section, the improvement of the cleaning inefficiency from TCLD collimators in IR7 is studied. Particular emphasis is given to the question if a significant improvement can be obtained from the installation of only one TCLD per beam in IR7. If the TCLD was to be installed in cell 8 (TCLD8), the main loss reduction is expected in the DS1 loss cluster, where

the dispersion is comparable to that at the TCLD8. The locally generated dispersion from the TCP is smaller at the DS1 than at the DS2 (see Fig. 8.14). Particles lost in the DS1 are those with larger rigidity offsets compared to those lost in the DS2 (this was discussed in Chap. 6.10). Therefore, it is possible that the particles lost in the DS2 loss cluster are not intercepted by the TCLD8. The worst case scenario in terms of the maximum average cleaning inefficiency at the DS2 is the simulation with $b = 1\,\mu$m. This is hence the baseline for the following simulations.

Cleaning Performance with one TCLD

Present estimates assume TCLD half gaps between $10\,\sigma$ and $15\,\sigma$. The following studies are carried out with half gaps of $10\,\sigma$, $12\,\sigma$ and $15\,\sigma$. These should be regarded as tentative. The applicability of the settings also depends on constraints imposed by the risk of asynchronous beam dump and the settings of the momentum collimators in IR3. An initial distribution of 6.0×10^6 ions of $^{208}\mathrm{Pb}^{82+}$ is used in every simulation. The loss maps simulated with the hiSixTrack-FLUKA coupling with the TCLD8 collimator set to these half gaps are shown in Fig. 8.19 and Fig. 8.20. The key parameters quantifying the cleaning inefficiency in the DS1 and DS2 are compared in Fig. 8.21, Fig. 8.25 and Table 8.4.

Global Loss Distribution

The global loss distribution, shown in Fig. 8.19, is very similar for all study cases. For all TCLD settings, the loss peaks are at the same location. Some loss spikes, which are visible in the simulation without TCLDs, are suppressed when the TCLD is set to $12\,\sigma$ or $15\,\sigma$. However, the global cleaning inefficiency is not significantly improved with one TCLD collimator.

In neither of the study cases, particles are lost at the TCT2. Instead, a loss spike (C2) in the superconducting magnets upstream of IP2 is simulated. Further analysis shows that these losses are mainly caused by $^{207}\mathrm{Pb}^{82}$ starting from the left TCP jaw. The different optics and collimator settings compared to the 2015 heavy-ion run have shifted the losses from the TCT2 into the arc region upstream. According to the results of the study presented in Chap. 8.2, this loss peak could be suppressed by applying asymmetric TCP settings.

Overview of IR7

In regions upstream of the TCLD8, the loss maps with either TCLD setting are nearly identical. Downstream of the TCLD8, the loss maps show significant differences compared to the nominal simulation. The DS1 loss cluster is not completely removed, but secondary fragments generated in the TCLD8 are still lost in this region. This finding is new compared to studies conducted with STIER without secondary fragmentation [H$^+$15].

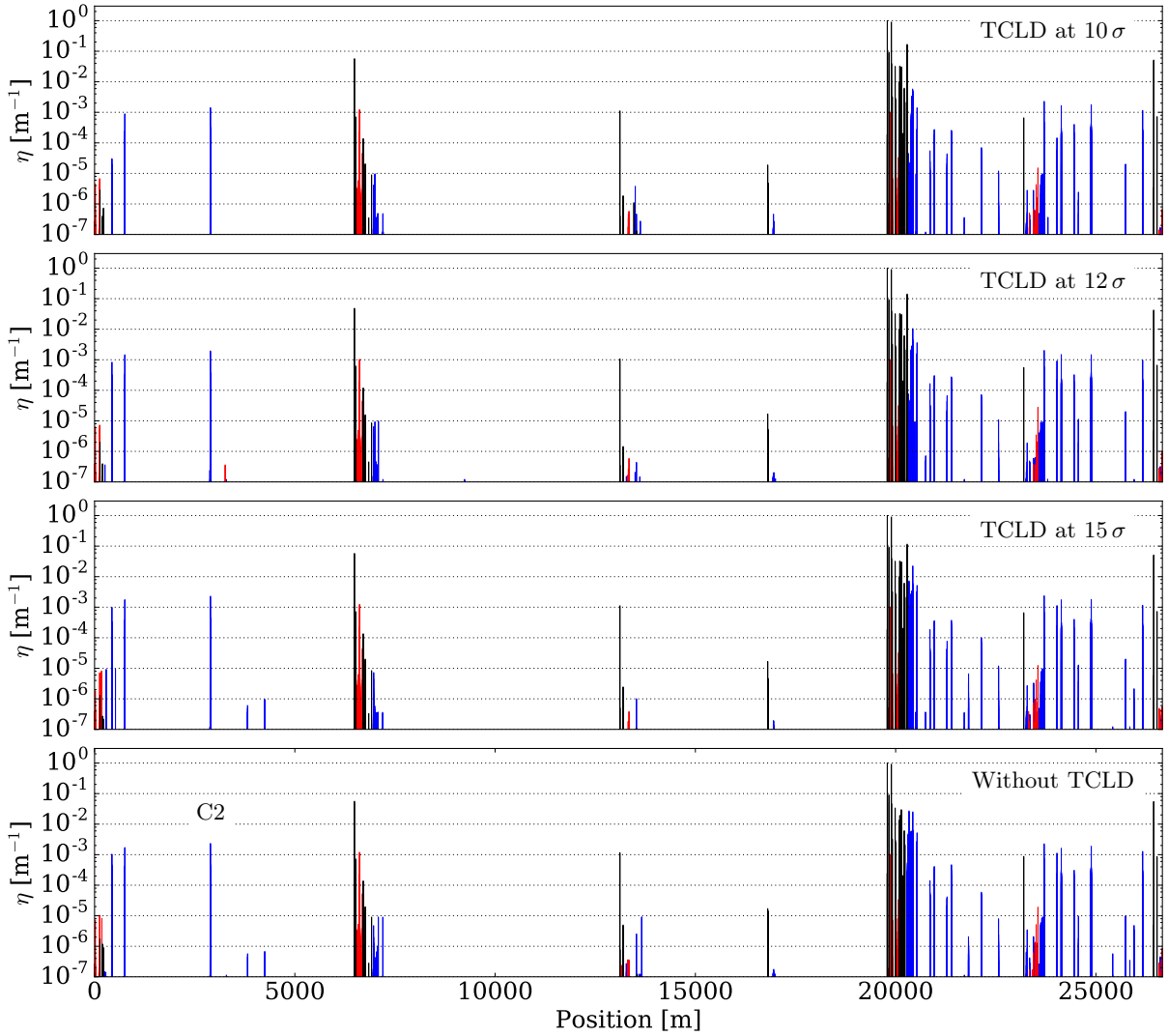

Figure 8.19: B1H loss maps simulated for the HL-LHC configuration with $^{208}Pb^{82+}$ ions at $7\,Z$ TeV and one TCLD collimator in cell 8 of IR7. The four panels show the loss maps simulated with three different settings of the TCLD collimators (three top panels) and without TCLD collimator (bottom panel).

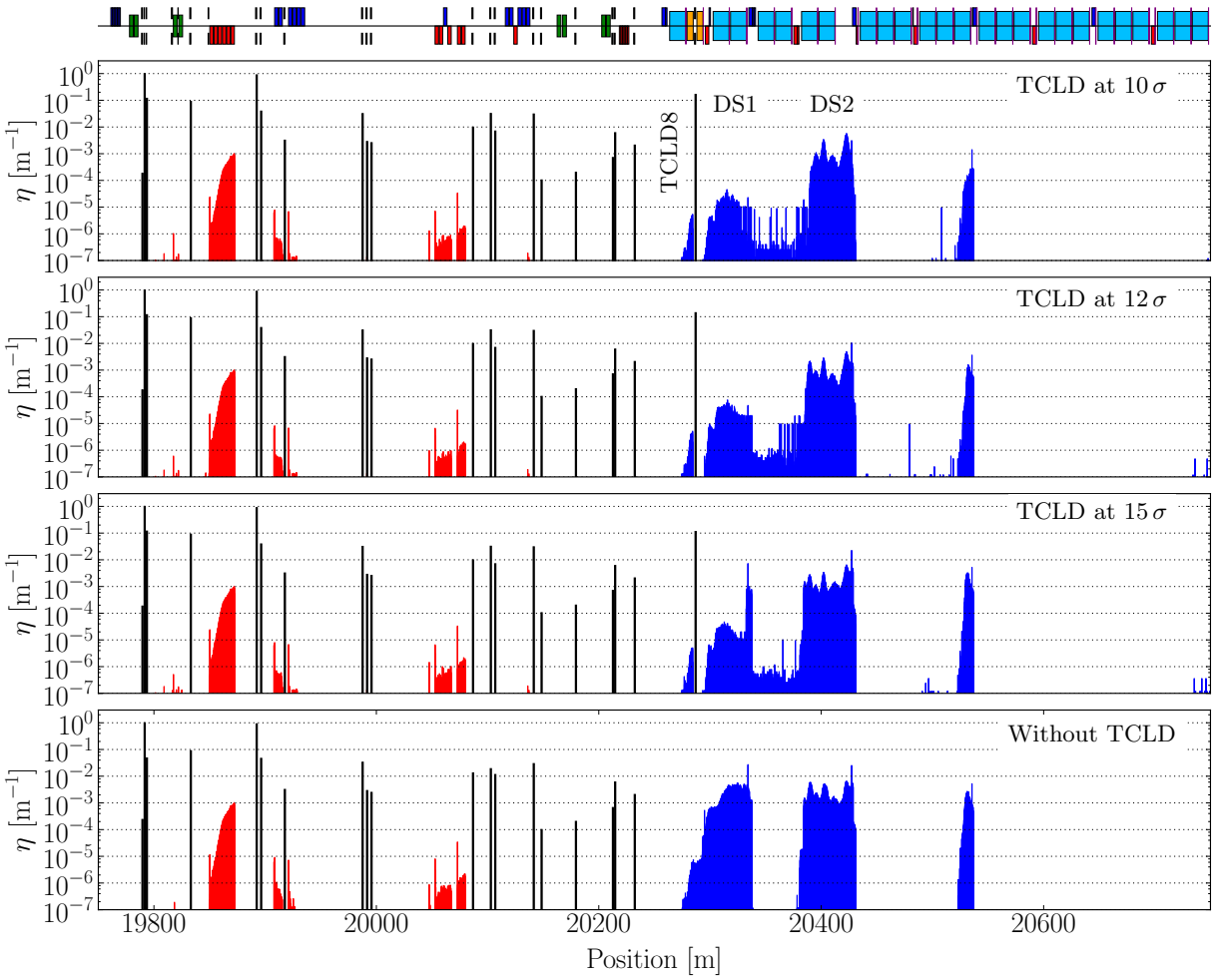

Figure 8.20: B1H loss maps zoomed to IR7, simulated for the HL-LHC configuration with $^{208}Pb^{82+}$ ions at $7\,Z$ TeV and one TCLD collimator in cell 8 of IR7. The four panels show the loss maps simulated with three different settings of the TCLD collimators (three top panels) and without TCLD collimator (bottom panel).

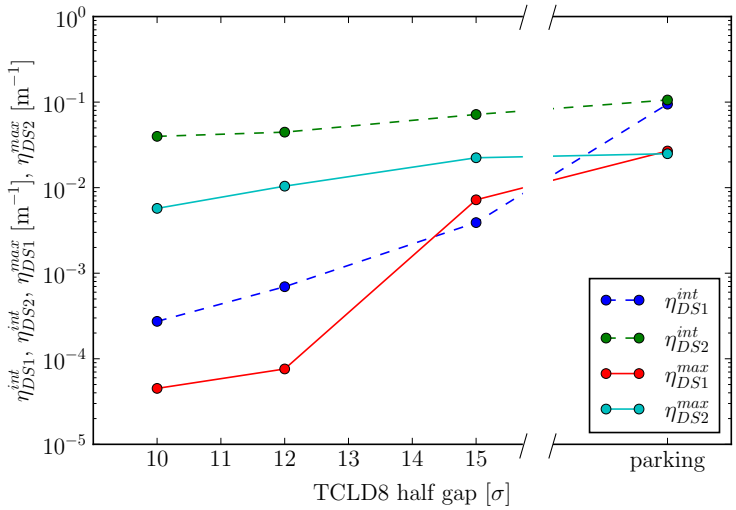

Figure 8.21: Peak and integrated cleaning inefficiency in the DS1 and DS2 with one TCLD in cell 8 for $^{208}Pb^{82+}$ ions at 7 Z TeV in the HL-LHC configuration (B1H). Parking corresponds to a fully retracted TCLD.

Losses in the DS1

With the most relaxed setting of 15 σ, the peak cleaning inefficiency η^{max}_{DS1} in the DS1 is reduced by approximately 73% compared to the simulation without TCLD. For the tighter settings, η^{max}_{DS1} is even reduced by more than two orders of magnitude. The integrated losses η^{int}_{DS1} in the DS1 are reduced by approximately 95% with the most relaxed TCLD setting and by more than two orders of magnitude for a half gap of 10 σ.

Losses in the DS2

Shape and amplitude of the DS2 loss cluster are not significantly changed by the TCLD8 collimator, regardless of the half gap applied. Compared to the simulation without TCLD, the peak loss η^{max}_{DS2} in the DS2 is only reduced by approximately 12% for the most relaxed TCLD8 setting. With the tightest half gaps applied, the maximum cleaning inefficiency in the DS2 can be reduced by approximately 77%. The integrated losses in the DS2 are reduced by approximately 35% with the most relaxed setting and by approximately 63% with the tightest setting.

Maximum average cleaning inefficiency

In the simulation of the nominal HL-LHC without TCLD, the maximum average cleaning inefficiency η^{avg}_{max} is found in the DS1. With the TCLD8 installed, the losses in the DS1 are reduced and the highest average cleaning inefficiency is simulated to be in the DS2 cluster. The possible improvement in terms of quench risk is the ratio of the maximum average cleaning inefficiency

η^{avg}_{max} with and $\eta^{avg}_{max,nominal}$ in the nominal HL-LHC configuration without TCLD collimator. As shown in Fig. 8.25, the reduction achieved yields approximately 11% for the most relaxed setting and approximately 45% for the tightest setting.

Cleaning Performance with two TCLDs

In this section, the previous study is repeated with a second TCLD installed in cell 10 (TCLD10). Also here, the cleaning inefficiency is studied for the three different TCLD settings.

The evolution of the peak, integrated and maximum average cleaning inefficiency as a function of the TCLD setting is shown in Fig. 8.22. Furthermore, the numeric values are given in Table 8.4. The simulated loss maps are shown in Fig. 8.23 and Fig. 8.24.

Global Loss Distribution

The comparison illustrated in Fig. 8.23 shows that on a global scale, the losses can be significantly reduced by the installation of the second TCLD collimator. For the tightest TCLD setting applied, the peak cleaning inefficiency in cold LHC regions is in the order of $\eta^{max} \approx 3\times10^{-5}\,\mathrm{m}^{-1}$. The location exposed to the highest amount of losses is the DS1 cluster in the IR7 DS. Apparently, the installation of the second TCLD collimator removes a large fraction of the off-rigid ion fragments from the beam, which liberates the complete ring from most of the collimation losses.

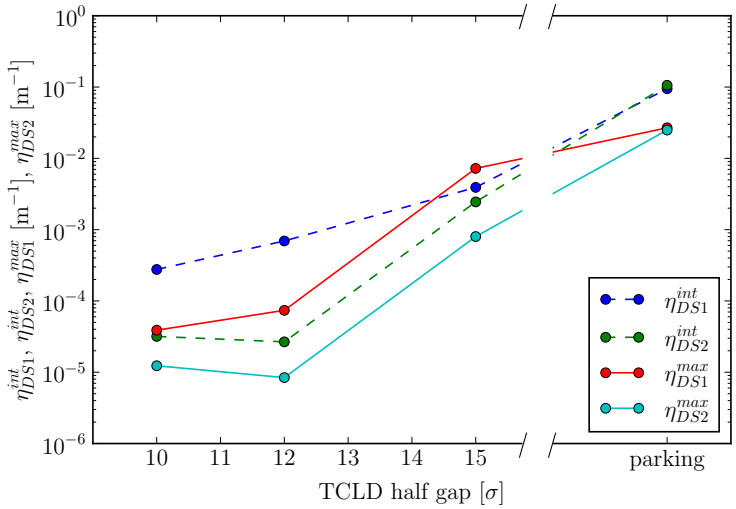

Figure 8.22: Peak and integrated cleaning inefficiency in the DS1 and DS2 with TCLDs in cell 8 and cell 10 for $^{208}\mathrm{Pb}^{82+}$ ions at $7\,Z\,$TeV in the HL-LHC configuration (B1H). Parking corresponds to a fully retracted TCLD.

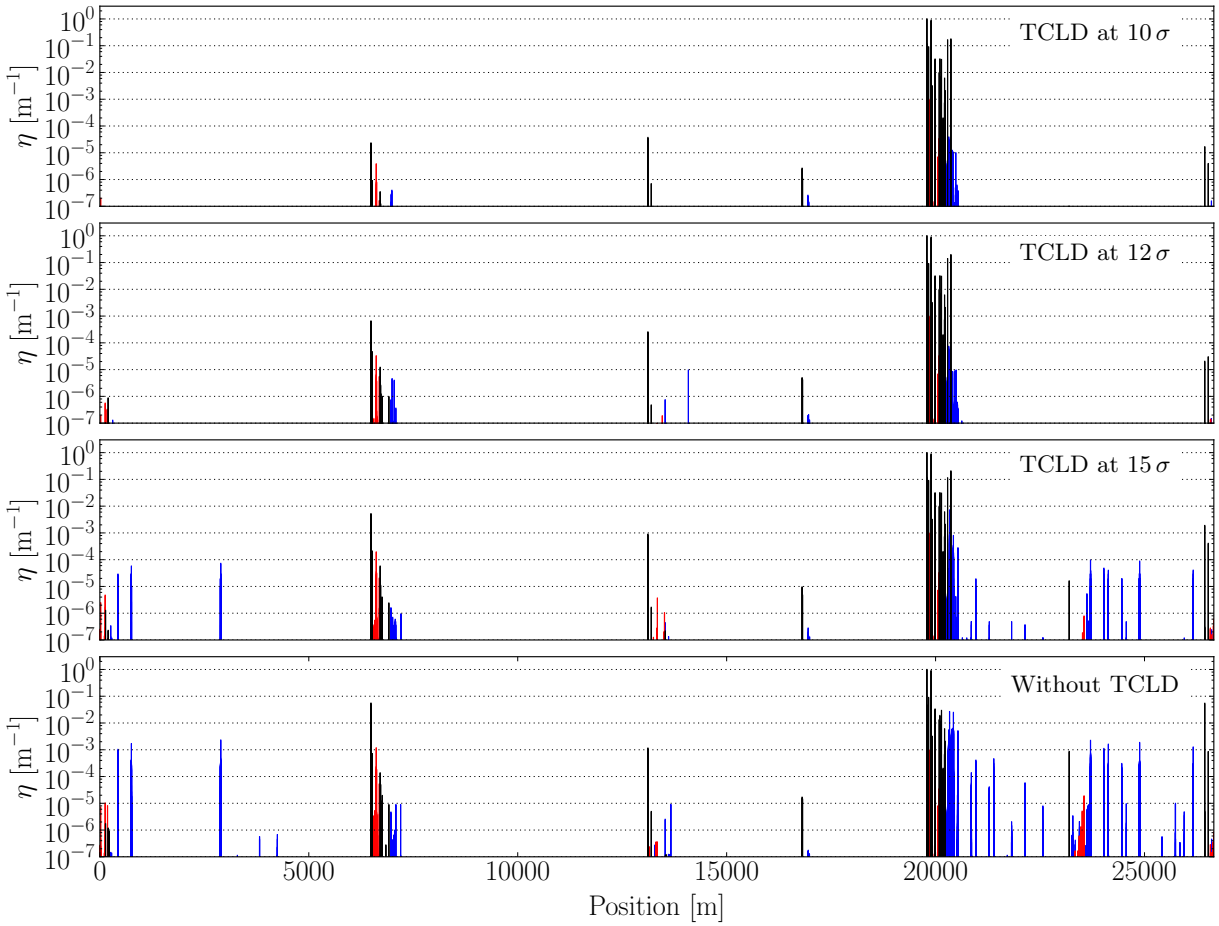

Figure 8.23: B1H loss maps (full LHC ring) simulated for the HL-LHC configuration with $^{208}Pb^{82+}$ ions at 7 Z TeV and two TCLD collimators in cell 8 and cell 10 of IR7. The four panels show the loss maps simulated with three different settings of the TCLD collimators (three top panels) and without TCLD collimator (bottom panel).

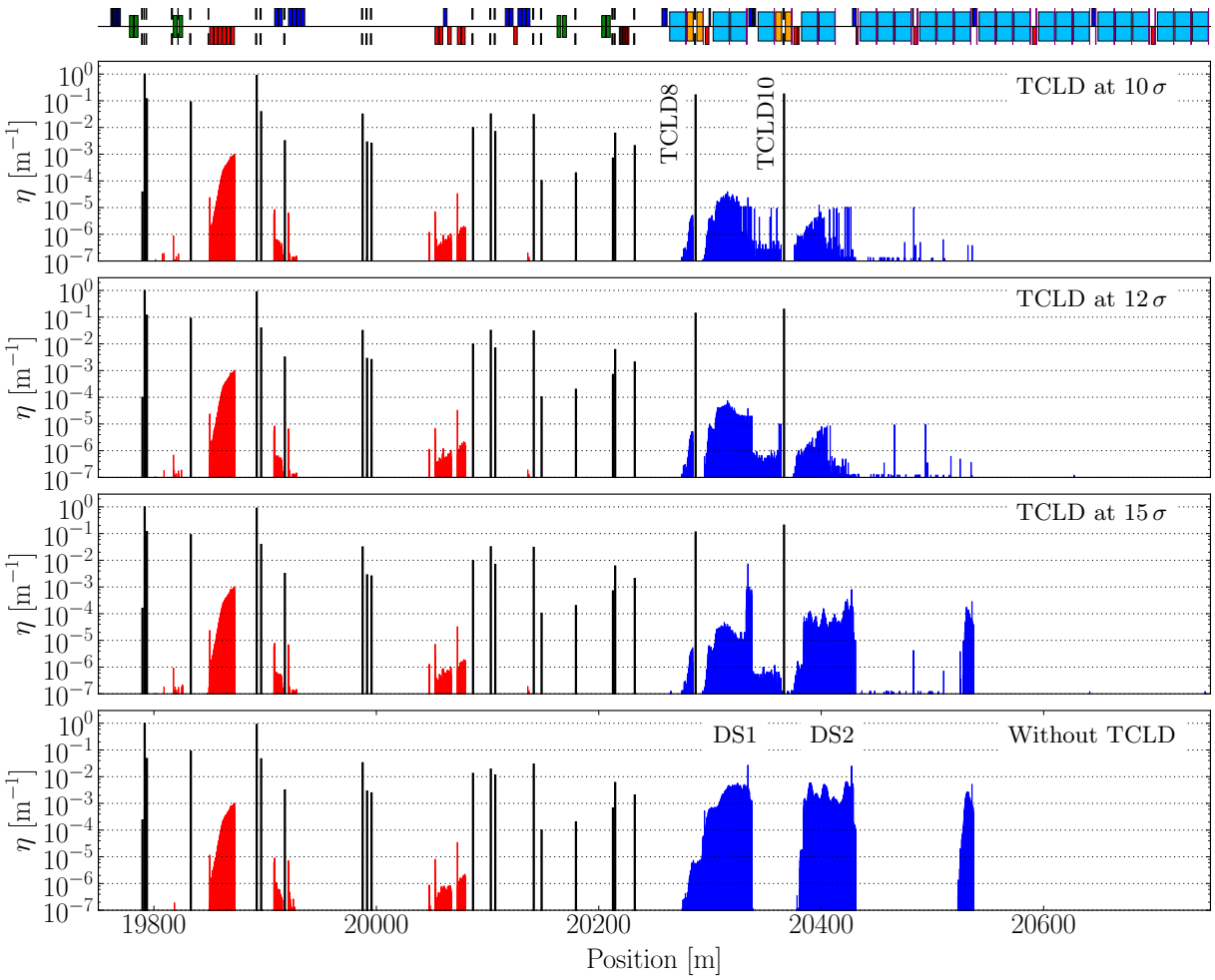

Figure 8.24: B1H loss maps (zoomed to IR7) simulated for the HL-LHC configuration with $^{208}Pb^{82+}$ ions at 7 Z TeV and two TCLD collimators (installed in cell 8 and cell 10) per beam in IR7. The four panels show the loss maps simulated with three different settings of the TCLD collimators (three top panels) and without TCLD collimator (bottom).

Losses in the DS1

Only slight differences arise compared to the simulation with one TCLD. In the latter, very few $^{208}Pb^{82+}$ particles re-impact at the TCP in a subsequent turn, which slightly changes the loss pattern in IR7, including the DS1. These out-scattered particles are now intercepted by the TCLD10. Nevertheless, their contribution is very small and the DS1 losses remain almost unchanged with respect to the previous simulation. In all studied scenarios, the globally largest amount of collimation losses in superconducting magnets is simulated in the DS1.

Losses in the DS2

The losses in the DS2 are significantly reduced when the second TCLD collimator is installed. Already with the most relaxed TCLD setting of $15\,\sigma$, the maximum cleaning inefficiency in the DS2 is reduced by almost three orders of magnitude. For tighter TCLD settings, the integrated and peak losses in the DS2 cluster increase, because more particles which would be lost in other regions are intercepted by the TCLD10 and hence more debris is produced in it. This finding is in line with the fact that the global losses are significantly reduced when TCLDs are installed in IR7. In the STIER simulations of the same scenario, presented in [H+15], this information was inaccessible because secondary fragmentation is not included in STIER.

Maximum average cleaning inefficiency

With two TCLDs at the most relaxed setting of $15\,\sigma$, the maximum average cleaning inefficiency is reduced by approximately 79% compared to the nominal HL-LHC simulation without TCLDs. In this scenario, the limiting losses are measured at the DS1. With tighter settings, the quench risk can be reduced by more than two orders of magnitude. The maximum average cleaning inefficiency with a TCLD half gap of $10\,\sigma$ is only 3×10^{-3} of the nominal value without TCLDs. The direct comparison to the study case with one TCLD in Fig. 8.25 shows that the maximum average cleaning inefficiency can be significantly reduced by the installation of a second TCLD per beam. This reflects directly in the achievable stored beam energy, as it shall be discussed in Chap. 9.3. With two TCLD collimators per beam, intensity limitations by the risk of quenches from collimation losses can be abolished.

Table 8.4: Cleaning inefficiency in the DS1 and DS2 clusters with different TCLD half gaps. The quantities η_{DS1}^{max} and η_{DS2}^{max} correspond to the maximum average cleaning inefficiency simulated in the DS1 and DS2 respectively.

Study	Setting [σ]	η_{DS1}^{max} [m^{-1}]	η_{DS2}^{max} [m^{-1}]	η_{DS1}^{int}	η_{DS2}^{int}	η_{DS1}^{avg} [m^{-1}]	η_{DS2}^{avg} [m^{-1}]
No TCLD	-	2.7×10^{-2}	2.5×10^{-2}	9.5×10^{-2}	1.1×10^{-1}	4.0×10^{-3}	4.7×10^{-3}
1 TCLD	15	7.2×10^{-3}	2.2×10^{-2}	3.9×10^{-3}	7.2×10^{-2}	1.0×10^{-3}	4.2×10^{-3}
1 TCLD	12	7.5×10^{-5}	1.0×10^{-2}	7.0×10^{-4}	4.5×10^{-2}	3.6×10^{-5}	2.7×10^{-3}
1 TCLD	10	4.2×10^{-5}	5.7×10^{-3}	2.7×10^{-4}	4.0×10^{-2}	1.5×10^{-5}	2.6×10^{-3}
2 TCLDs	15	7.2×10^{-3}	8.0×10^{-4}	3.9×10^{-3}	2.5×10^{-3}	1.0×10^{-3}	1.4×10^{-4}
2 TCLDs	12	7.5×10^{-5}	8.4×10^{-6}	7.0×10^{-4}	2.7×10^{-5}	3.6×10^{-5}	1.5×10^{-6}
2 TCLDs	10	4.2×10^{-5}	1.2×10^{-5}	2.7×10^{-4}	3.2×10^{-5}	1.5×10^{-5}	2.5×10^{-6}

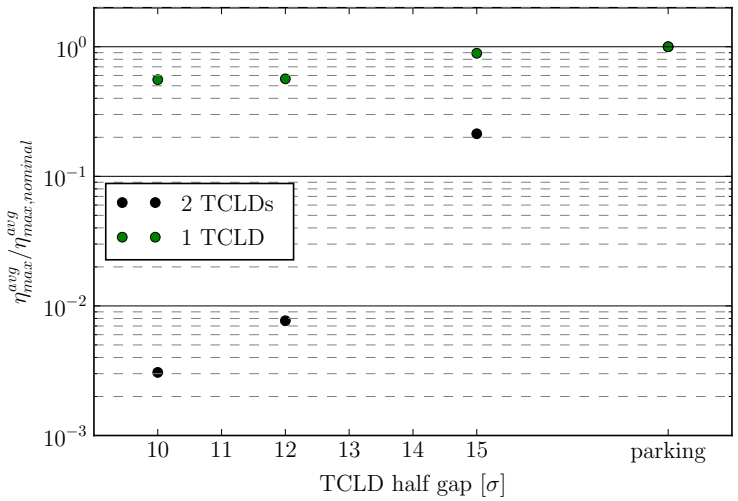

Figure 8.25: Maximum average cleaning inefficiency in the DS1 and DS2 with one and two TCLDs for $^{208}Pb^{82+}$ ions at $7\,Z$ TeV in the HL-LHC configuration (B1H). Parking corresponds to a fully retracted TCLD.

8.3.4 Conclusions

The simulations with the hiSixTrack-FLUKA coupling for the HL-LHC configuration with $^{208}Pb^{82+}$ beams at $7\,Z$ TeV have shown that the cleaning performance can be improved if one or two TCLDs are installed in IR7. A complete overview of the cleaning inefficiency in the superconducting magnets is given for the different settings of the TCLDs in Table 8.4.

The simulations indicate that the potential for improvement with only one TCLD collimator per beam is rather limited. The maximum average losses in the cold LHC regions can be reduced by less than 50% even if the smallest studied TCLD half gap of $10\,\sigma$ is applied. A significant improvement can be expected with the installation of two TCLD collimators. With the most relaxed collimator setting, the maximum average losses in the DS magnets are reduced by 80%. With a setting of $12\,\sigma$, the losses in superconducting regions are reduced by almost two orders of magnitude. In this configuration, the risk of quench from collimation debris becomes irrelevant for operation and other constraints (e.g. collimator damage or the injector performance) limit the achievable beam intensity. Furthermore, the simulations show that the installation of the second TCLD provides a global loss protection. This means that possibly critical losses also in regions downstream of IR7 can be mitigated by the second TCLD collimator. This should also be considered in the discussion of the collimation system upgrades for HL-LHC.

To derive the allowed stored beam energy from these simulations, experimental input about the quench limit in operational conditions in required. This is discussed in detail in Chap. 9.

8.4 Operation with Ar and Xe Ions

The LHC injectors are capable of providing different heavy-ion species than $^{208}Pb^{82+}$. Presently these lighter heavy ions are only used for fixed target experiments with beams extracted from the SPS. The NA61/Shine experiment has so far received $^{40}Ar^{18+}$ ions for fixed target experiments and $^{129}Xe^{54+}$ ions are scheduled for future operation [M$^+$16a, Scr15, Man14].

At the time of writing, LHC operation with these ions is not envisaged, but some of the LHC experiments have shown interest in colliding other heavy-ion species than $^{208}Pb^{82+}$. The reason for this interest is that, compared to $^{208}Pb^{82+}$, bunches with higher intensities could be delivered to the LHC and hence the achievable luminosity could be higher [M$^+$16a]. To study possible limitations from the LHC collimation system, an exploratory study of the cleaning performance with the ions $^{40}Ar^{18+}$ and $^{129}Xe^{54+}$ is conducted with the hiSixTrack-FLUKA coupling.

8.4.1 Simulation Setup

The cleaning simulations are carried out for B1H in the HL-LHC configuration without TCLDs at $7\,Z$ TeV. The optics and collimator settings are identical to those used for the simulations with $^{208}Pb^{82+}$ beams and are listed in Table 8.3. In all simulations, a primary beam of 6.0×10^6 ions is assumed to impact the TCP at $b = 1\,\mu$m.

8.4.2 Simulation Result

The loss maps simulated for the different heavy-ion species are compared in Fig. 8.26 (zoom to IR7) and Fig. 8.27 (full LHC ring). Peak, integrated and maximum average cleaning inefficiency in the DS clusters are summarized for all study cases in in Table 8.5.

The global distribution of loss peaks is qualitatively similar for all study cases. Shape and amplitude of the losses in the DS clusters are slightly different. Among the simulated scenarios, the largest peak loss in the IR7 DS is simulated with $^{129}Xe^{54+}$ ions. However, the comparison of the integrated cleaning inefficiency shows that the sum of η^{int}_{DS1} and η^{int}_{DS2} is almost the same as

Table 8.5: Cleaning inefficiency for different isotopes in the HL-LHC configuration.

Isotope	η^{max}_{cold} [10^{-2} m^{-1}]	η^{int}_{DS1} [10^{-2}]	η^{int}_{DS2} [10^{-2}]	η^{avg}_{DS1} [10^{-3} m^{-1}]	η^{avg}_{DS2} [10^{-3} m^{-1}]
$^{208}Pb^{82+}$	2.7	9.5	10.6	4.0	4.7
$^{129}Xe^{54+}$	3.5	12.0	8.3	4.8	4.3
$^{40}Ar^{18+}$	2.5	11.1	4.6	4.6	1.9

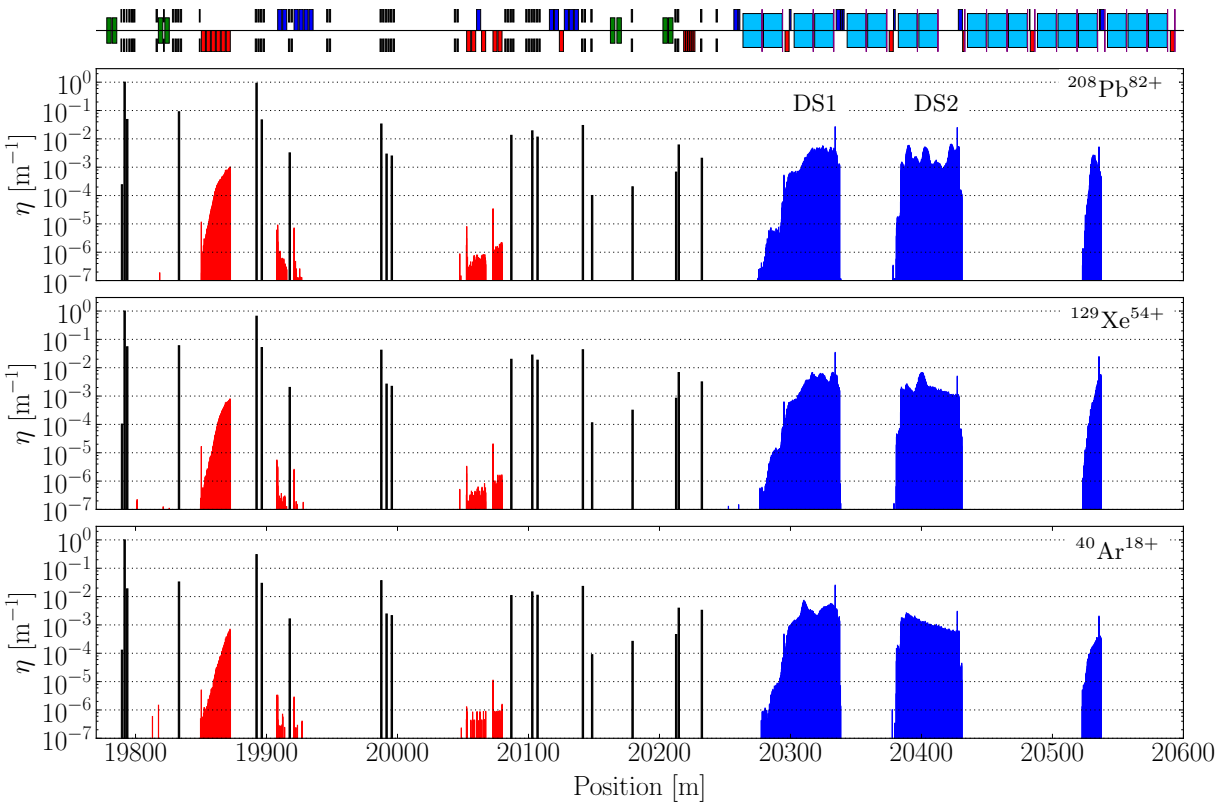

Figure 8.26: Loss maps zoomed to IR7 simulated with the hiSixTrack-FLUKA coupling for the HL-LHC configuration at 7 Z TeV with $^{208}Pb^{82+}$ ions, $^{129}Xe^{54+}$ ions and $^{40}Ar^{18+}$ ions.

for $^{208}Pb^{82+}$ ions. The amount of losses in the DS is hence similar, but the collimation debris is distributed differently. Also the maximum average cleaning inefficiency for $^{129}Xe^{54+}$ is slightly higher than for $^{208}Pb^{82+}$, while for $^{40}Ar^{18+}$ it is slightly lower.

A remarkable difference observed between the different simulation scenarios is the ratio of the losses in the DS1 and DS2. For the simulation with $^{208}Pb^{82+}$ ions, the peak, integrated and maximum average losses are similar in the DS1 and DS2, with slightly more losses in the DS2.

With the lighter ions, the losses in the DS1 cluster become dominating. For $^{129}Xe^{54+}$, the integrated losses in the DS1 are approximately higher by 44% compared to the DS2. In the simulation with $^{40}Ar^{18+}$ ions, they are more than twice as high as in the DS2.

As discussed in Chap. 6.3.1, the probability that a residual heavy-ion fragment is lost at the DS1 instead of the DS2 location increases with the rigidity offset. As a consequence of the quantization of nucleons in the nuclei, the nuclear loss of the same amount of protons or neutrons results in a larger rigidity offset with respect to the main beam. In Table 8.6, the χ-values of particles generated from EMD1 and EMD2 are summarized for the different reference isotopes.

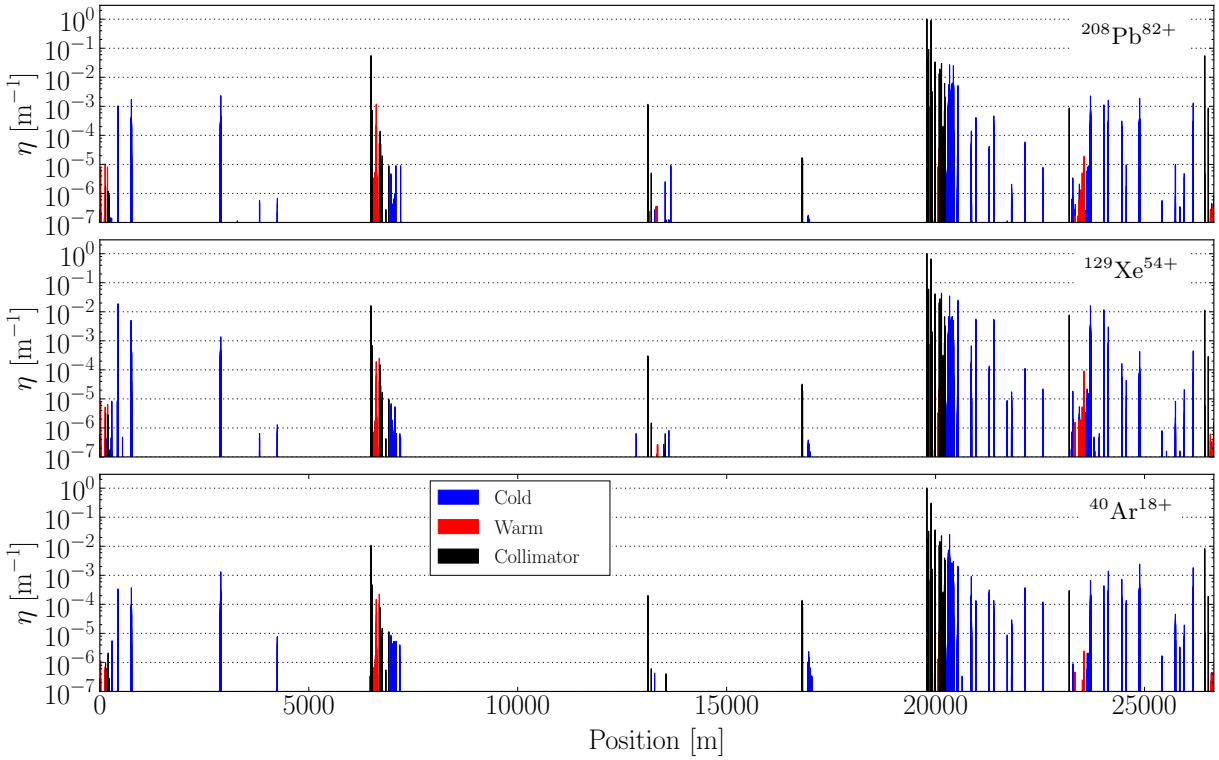

Figure 8.27: Full ring loss maps simulated with the hiSixTrack-FLUKA coupling for the HL-LHC configuration at 7 Z TeV with $^{208}Pb^{82+}$ ions, $^{129}Xe^{54+}$ ions and $^{40}Ar^{18+}$ ions.

Table 8.6: Rigidity offset (expressed in terms of χ, assuming that $\delta = 0$) of fragments generated by EMD1 and EMD2 for different reference isotopes.

Ref. species	χ_{EMD1}	χ_{EMD2}
$^{208}\mathrm{Pb}^{82+}$	1.0048	1.0097
$^{129}\mathrm{Xe}^{54+}$	1.0078	1.0157
$^{40}\mathrm{Ar}^{18+}$	1.0256	1.0527

The comparison shows that the rigidity offset associated to particles created in EMD processes is significantly increasing with decreasing mass of the main beam.

8.4.3 Summary

In summary, the simulation with the hiSixTrack-FLUKA coupling shows that the loss pattern and the cleaning inefficiency for the studied heavy-ion species is comparable to that of $^{208}\mathrm{Pb}^{82+}$. Therefore, the same limitations in terms of stored beam energy apply similarly for the other ion species. On the other hand, especially for the scenario $^{40}\mathrm{Ar}^{18+}$ beams, already today higher bunch intensities are available than those which may be reachable for $^{208}\mathrm{Pb}^{82+}$ ions in HL-LHC [M+16a]. Compared to $^{208}\mathrm{Pb}^{82+}$ beams, the higher bunch intensity could increase the achievable luminosity, even if the allowed total stored beam energy would be similar.

Furthermore, the charge to mass ratio and therefore the relativistic γ of $^{40}\mathrm{Ar}^{18+}$ is higher than that for $^{208}\mathrm{Pb}^{82+}$ at the same rigidity. Assuming that the normalized emittance with Ar and Xe is the same as for $^{208}\mathrm{Pb}^{82+}$ beams, this leads to a further increase of the luminosity.

To study potential limitations of the allowed stored beam energy with $^{208}\mathrm{Pb}^{82+}$, $^{40}\mathrm{Ar}^{18+}$ and $^{129}\mathrm{Xe}^{54+}$ beams, it is required to have experimental input about the quench limit. This is further studied in Chap. 9.3.

8.5 Summary and Conclusions

The new heavy-ion collimation simulation tools STIER and the hiSixTrack-FLUKA coupling were applied to study the cleaning performance in different configurations of the LHC and HL-LHC. In the 2015 heavy-ion run, STIER was used to validate the collimation system and probe different strategies to reduce the IR7 DS losses. It was also used to derive mitigation strategies for losses at the tertiary collimator in IR2, which were successfully tested in the LHC.

The hiSixTrack-FLUKA coupling was used for exploratory studies of the cleaning performance in HL-LHC. The simulations with TCLD collimators delivered new evidence which is going to be essential in the discussion of the required collimation system upgrades for HL-LHC. Furthermore, the cleaning inefficiency with other heavy-ion species than $^{208}Pb^{82+}$ was explored.

These applications demonstrate the importance of heavy-ion collimation simulation tools. They are not only required to ensure safe and uninterrupted LHC operation, they also define the requirements for future upgrades which are often related to substantial budgetary decisions.

In order to relate these findings to tangible intensity and hence luminosity limitations for the operation in the LHC, the quench limit of the IR7 DS magnets must be known. For this purpose, a dedicated heavy-ion collimation quench experiment was carried out at the end of the heavy-ion operation in 2015. This quench test and the resulting implications on the permitted stored beam energy in HL-LHC are presented in the next chapter.

9. Heavy-Ion Collimation Quench Test in 2015

To exploit the full potential of the LHC and achieve the highest possible (integrated) luminosity, the beam intensity has to be pushed to the maximum which is compatible with safe and uninterrupted operation. One of the limiting factors for the maximum stored beam energy is the possible quench of the superconducting DS magnets downstream of IR7 from collimation debris. As shown in Chap. 3.3.3, the quench limit of the LHC magnets is difficult to estimate and subject to large uncertainties. It also depends on the loss scenario, which reflects in the fact that the BLM thresholds are set with respect to the expected quench limit for UFO events [B$^+$11a]. Unidentified Falling Objects (UFOs) are dust particles with size in the order of some μm falling from the top of the beam pipe. The beam particles interact with the UFOs which leads to secondary showers that can possibly quench the superconducting magnets [B$^+$11a].

The quench limit for other loss scenarios, such as the impact of collimation debris on the superconducting magnets can be experimentally accessed with beam in operational conditions. In such measurements, very high losses are produced at the primary collimator with the aim to quench the IR7 DS magnets with the collimation debris in a controlled manner.

Several collimation quench tests have been carried out in the past to get experimental input for quench limit studies [A$^+$11a, A$^+$12, R$^+$12c, S$^+$14a, S$^+$16]. The most important key parameters of this and previous tests are summarized in Table 9.1.

Table 9.1: Key parameters of collimation quench tests carried out at the LHC.

Year	Energy [Z GeV]	Particle	Method	$P_{\max}$ [kW]	τ_L [s]	Quench	Ref.
2011	3.5	p	tune	500	1	No	[A$^+$11a]
2013	4.0	p	ADT	1050	5-10	No	[S$^+$14a]
2015	6.5	p	ADT	585	4	No	[S$^+$16]
2011	3.5	^{208}Pb^{82+}	tune	151	0.075	No	[A$^+$12]
2015	6.37	^{208}Pb^{82+}	ADT	15	14	Yes	[S$^+$16]

Quench test experiments are complemented by simulations of the experimental setup. Combined with simulations from the hiSixTrack-FLUKA coupling, the gathered information can be used to define upgrade requirements for the LHC collimation system. Detailed shower propagation and energy deposition studies with FLUKA allow for interrelating the measured BLM signal to the energy deposited in the magnet coils [S$^+$15b].

While the quench tests in early operation used tune resonance crossing methods, which induce very fast losses at the primary collimator, the tests from 2013 and later could make use of the ADT. This led to a much better control of the losses and enabled a significant increase of the loss duration to probe the quench limit with steady state losses.

In this chapter, the design, realization and analysis of the 2015 heavy-ion collimation quench test are presented. It was the first collimation quench test in which a magnet quench was achieved. The content of this chapter was partly published in [H$^+$16a].

9.1 Preparation of the Experiment

The preparation of the test includes to determine the beam parameters, target loss rates and machine modifications required for the successful realization of the experiment. The quench limit in the DS magnets downstream of IR7 is probed with collimation debris which is lost immediately after its generation in the primary collimators. Therefore, the quench limit in operational conditions can be tested with un-squeezed beams in the IRs (flat top at 6.37 Z TeV). Accordingly the collimator settings correspond to the operational settings in the collision mode, except for the TCTs and physics debris collimators (see Table 9.2).

The beam and plane to be used for the test can be freely chosen, whereas preference should be given to the horizontal plane in which the DS losses are typically higher. The decision was taken to use the horizontal plane of B2 (B2H) for the test to potentially benefit from synergies with the precedent proton quench test which was also carried out in this plane [S$^+$16].

Table 9.2: Collimator settings in σ applied in the 2015 heavy-ion collimation quench test.

IR7		IR3		IR1/2/5/8/6	
TCP	5.5	TCP	15.0	TCT	37.0
TCSG	8.0	TCSG	18.0	TCL	out
TCLA	14.0	TCLA	20.0	TCDQ	9.1

9.1.1 Target Beam Loss Rate

The target beam loss rate at the primary collimator is an important measure that must be defined before the experiment is carried out. It determines the number of bunches that must be excited simultaneously and hence has direct implications on the filling scheme.

As explained before, the quench limit is related to many uncertainties. The decision of the target loss rate was therefore based on the operational BLM thresholds. The latter are set to 1.5 times the assumed quench limit for UFO events, which is taken as a baseline. The qualification loss map for B2H measured at flat top in the 2015 heavy-ion run is shown in Fig. 9.1. The highest BLM signal at the superconducting LHC magnets is measured at the BLMQI.09L7.B2I10_MQ which monitors the losses at the quadrupole in cell 9 left of IP7. The relative measured BLM Signal with 1.3 s integration time (RS09) at this BLM is

$$\mathcal{B}^{\mathrm{lm}}_{\mathrm{MQ9L7}} = (1.6 \pm 0.4) \times 10^{-2}\,. \tag{9.1}$$

The uncertainty is estimated by variations in the peak cleaning inefficiency between different loss map measurements. From the measured loss signal $\mathcal{B}^{\mathrm{lm}}_{\mathrm{MQ9L7}}$ and the operational BLM threshold for RS09, the expected BLM signal at quench $\mathcal{B}^{\mathrm{q}}_{\mathrm{MQ9L7}}$ can be extrapolated

$$\frac{\mathcal{B}^{\mathrm{q}}_{\mathrm{MQ9L7}}}{\mathcal{B}^{\mathrm{lm}}_{\mathrm{MQ9L7}}} = (1.13 \pm 0.29) \times 10^{2}\,. \tag{9.2}$$

During the measurement of the qualification loss map, an intensity drop equivalent to a peak primary beam loss of $P_l = 123\,\mathrm{W}$ was measured with the beam current transformers (BCT) [B$^+$10].

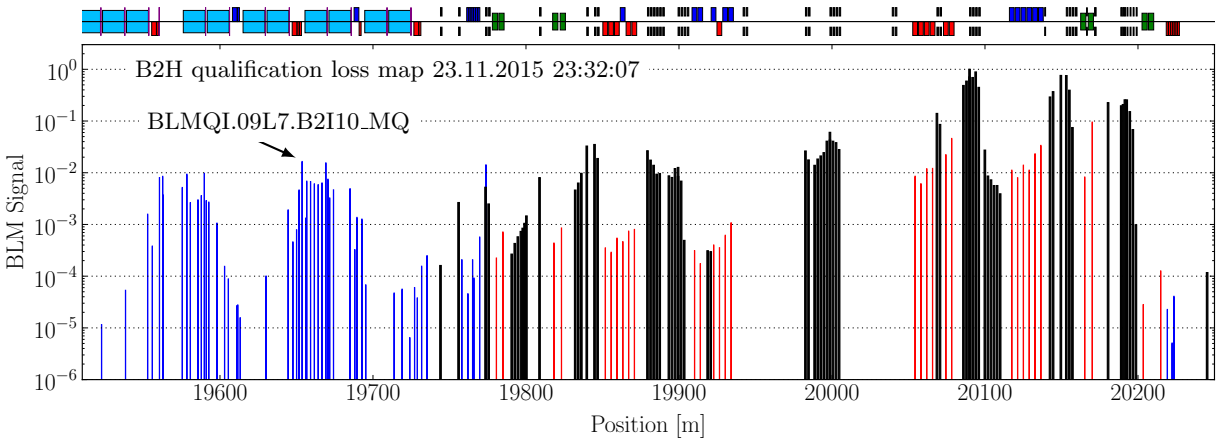

Figure 9.1: B2H qualification loss map with $^{208}\mathrm{Pb}^{82+}$ ions at 6.37 Z TeV used for the preparation of the heavy-ion collimation quench test.

The quantity P_l can be scaled with the ratio given in Eq. (9.2) to obtain a BLM signal equivalent to the assumed quench limit for UFO events yields

$$P_q^T = \frac{\mathcal{B}^{\mathrm{q}}_{\mathrm{MQ9L7}}}{\mathcal{B}^{\mathrm{lm}}_{\mathrm{MQ9L7}}} P_l = (13.9 \pm 3.6)\,\mathrm{kW}\,. \tag{9.3}$$

This number should not be considered to be the expected quench limit. Rather, it should be regarded in the context of the beam loss mechanism which is different from the UFO scenario to which the BLM threshold is adjusted. Even for the UFO event, the quench limit is uncertain.

However, P_q^T is an important measure and was the first step in the cascade of envisaged target loss rates, because it can give important information about the accuracy of the setting of operational BLM thresholds. In case a quench would not be achieved with a loss rate of P_q^T, it was envisaged to increase the loss rate in steps to narrow down the real quench limit.

The upper boundary for the achievable loss rate is given by the power load that the primary collimators can resist without being damaged. They are designed to withstand continuous proton losses of 487 kW [A$^+$02a]. The analysis of the 2013 proton collimation quench test demonstrated that their physical integrity is not endangered by losses up to 1 MW [S$^+$14b].

The dominating process of energy deposition in the collimator is different for protons and heavy ions. The power deposited by an impacting proton and $^{208}\mathrm{Pb}^{82+}$ ion at $7\,Z$ TeV along the primary collimator is shown in Fig. 21.7 in [B$^+$04b]. The charge dependence of the Bethe-Bloch formula indicates that the energy deposited by the $^{208}\mathrm{Pb}^{82+}$ ions is, in a narrow region around the track of the impacting ion, more driven by ionization losses than for protons. The peak energy deposited from $^{208}\mathrm{Pb}^{82+}$ ions at this energy is approximately $57\,\mathrm{GeV/cm^3/charge}$. For protons it is approximately $6.5\,\mathrm{GeV/cm^3/charge}$, mainly due to hadronic showers produced during the passage through the collimator. To protect against surface damage from ionization losses, the peak loss rate at the primary collimator was conservatively limited to 100 kW, leaving enough margin to significantly outreach the power load derived in Eq. (9.3).

From the envisaged peak power load, the number of bunches required for the experiment can be deduced. Conservatively assuming that one ion bunch carries 10^{10} charges with an energy of 6.37 TeV per charge, the energy per bunch yields E_B =10 kJ. The LHC beam position monitors (BPM) [B$^+$99] require sufficiently populated bunches to accurately measure their position. Therefore, the LHC interlock system triggers a beam dump if the bunch intensity of a circulating bunch is below 30% of its nominal value. With this constraint included, on can derive the required number of bunches n_B^P to continuously induce a primary power load of 1 kW over 10 s

$$n_B^P = 1.4\,\mathrm{bunches/kW}\,. \tag{9.4}$$

From the qualification loss map and the associated loss rate, the expected BLM signals at a peak loss rate of 100 kW can be estimated for the full ring. This data is used to derive the increase of BLM thresholds required to permit the target loss rate during the experiment without triggering a protection beam dump. In the preparation phase of the experiment, the required modifications on the BLM thresholds (mainly the BLMs in IR7) were prepared and presented in [Kal15].

9.1.2 Experimental Schedule

From the quantity n_B^P, the required number of bunches to achieve a given loss rate can be deduced. The chosen approach of a stepwise loss rate increase reflects in the filling schedule that was foreseen for the experiment, as shown in Table 9.3.

An initial fill at injection energy was foreseen to set up the ADT. The control software of the latter is designed for the excitation of single bunches and had to be adjusted for an enlarged window covering the many bunches required to achieve the target loss rate. Also the time profile of the losses had to be modified to obtain continuous losses at a constant level over some seconds. More details on the ADT modifications are given in [H^+16a].

In the second fill, four bunch trains of 24 bunches as well as 8 individual bunches were foreseen to be accelerated to top energy for a first quench attempt with a peak loss rate around 13.5 kW. This approximately corresponds to the loss rate required to reach the BLM signal equivalent to the assumed quench limit for UFO events. The individual bunches should allow for a first testing of the ADT excitation at top energy with small intensities, without the risk of outreaching the envisaged loss rate. The four bunch trains carry enough particles to allow multiple attempts at a peak loss rate of approximately 13.5 kW. In the case a quench would not be achieved, two optional fills were foreseen to increase the loss rate to 50 kW and 100 kW respectively.

Table 9.3: Fills foreseen for the heavy-ion collimation quench experiment.

Fill	Bunches	E [Z TeV]	P_{max}[kW]
1	8	0.45	≈ 0.1
2	8 + 4×24	6.37	13.5
3	8×24	6.37	50
4	8×24	6.37	100

9.2 Results

9.2.1 Analysis

The heavy-ion collimation quench test was carried out the 13.12.2015 from 17:00h and ended with the quench at 22:08 h (LHC fill numbers 4722 & 4723).

The filling scheme and the envisaged peak loss rates were slightly modified during the experiment, due to unforeseen LHC downtime which significantly reduced the time available for the test. After the set up of the ADT in the first fill, the machine was filled with 12 bunch trains of 24 bunches and 2 single bunches which were accelerated to 6.37 Z TeV.

At the first excitation of 6 bunch trains, the MBB.9L7 quenched at loss rate of approximately

$$P_q \approx (15 \pm 1)\,\mathrm{kW}. \tag{9.5}$$

The beam was subsequently dumped by the quench protection system [DDPM08] (QPS). The intensity and energy evolution throughout the experiment is shown in Fig. 9.2. Furthermore, the evolution of the beam intensity, the power loss derived from it and the BLM signal at the quench location is shown in Fig. 9.3.

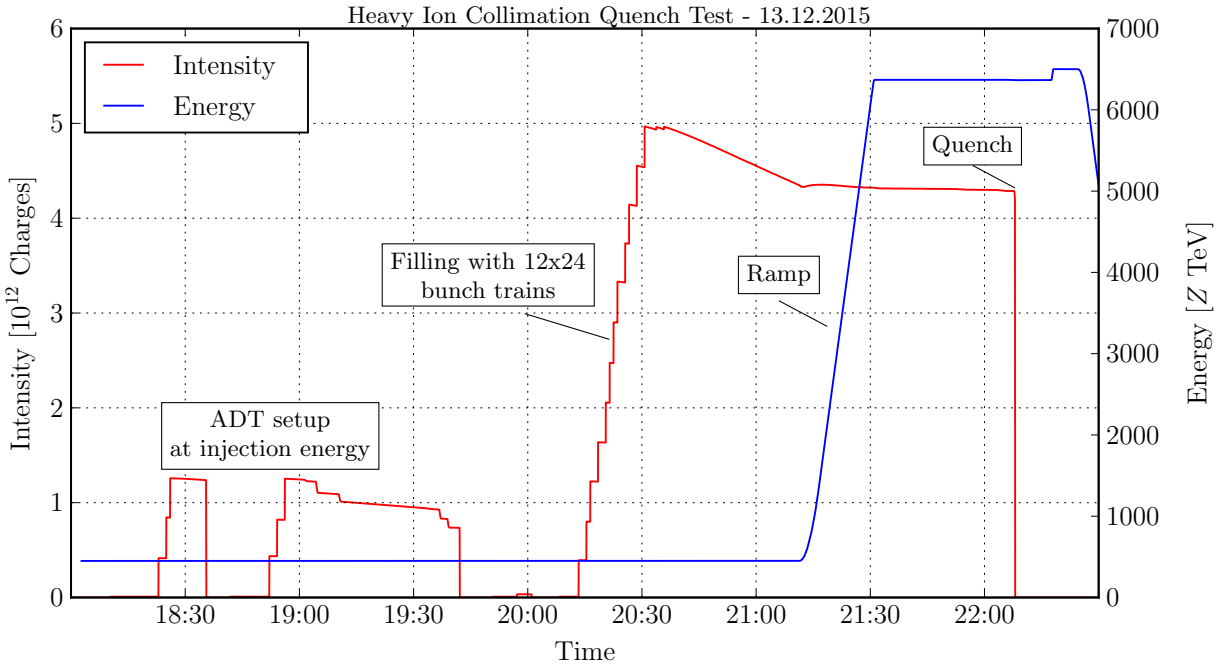

Figure 9.2: Intensity and particle energy evolution during the quench test.

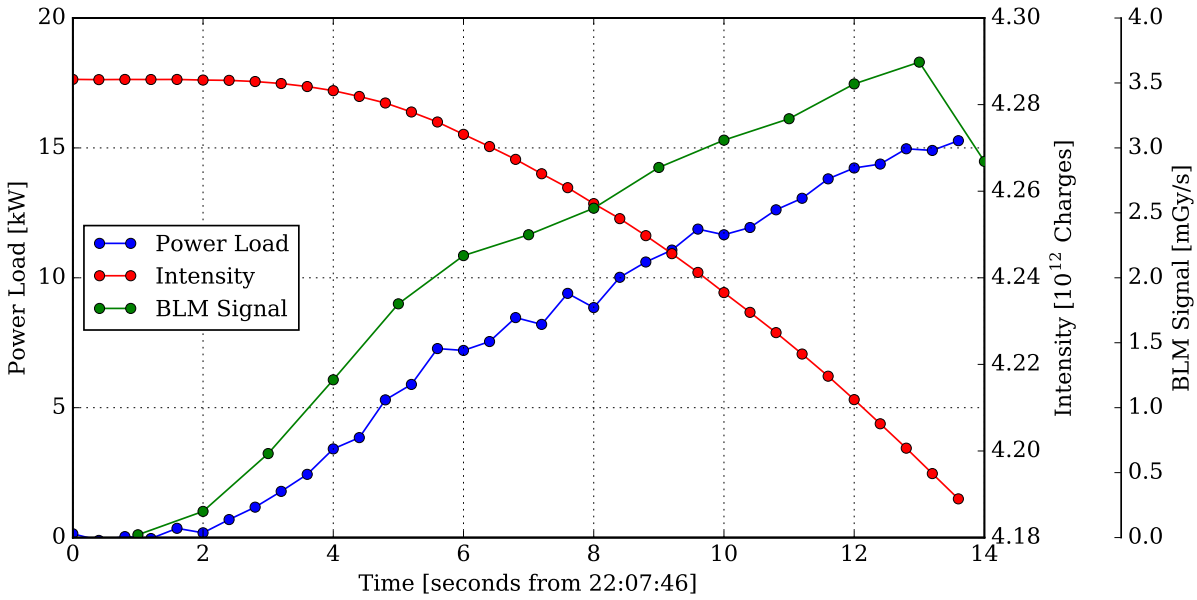

Figure 9.3: Power load on the TCP, intensity evolution and measured BLM signal (BLMEI.09L7.B2I30, RS09) during the final beam excitation in which the quench was achieved at the main dipole MBB.9L7.

The uncertainty on the peak power loss is estimated based upon the fluctuations visible in the increasing power load evolution. The loss rate increased continuously over approximately 14 s when the peak power load was achieved and the quench occurred. In lack of better estimates, the measurement result can be used to scale the permitted stored beam energy in the LHC on the basis of the minimum beam lifetime.

Considering the design value of $\tau_{\mathrm{DS}} = 12\,\mathrm{min}$ for the minimum beam life time, and taking into account that the quench occurred with a loss rate of P_q at the TCP, the maximum stored beam energy in the studied configuration yields

$$E_s^{\mathrm{max,QT}}(6.37\,Z\,\mathrm{TeV}) = P_q\,\tau = (10.8 \pm 0.8)\,\mathrm{MJ}\,. \tag{9.6}$$

This value is very close to the stored beam energy achieved in the 2015 heavy-ion run and therefore imposes a serious limitation for the achievable luminosity in future operation. Note that the derived intensity limit is only valid for $6.37\,Z\,\mathrm{TeV}$, because the quench limit for higher magnetic fields is expected to be lower. In Chap. 9.3, intensity limitations for $7\,Z\,\mathrm{TeV}$ are derived on the basis of the HL-LHC cleaning simulations presented in Chap. 8.3.

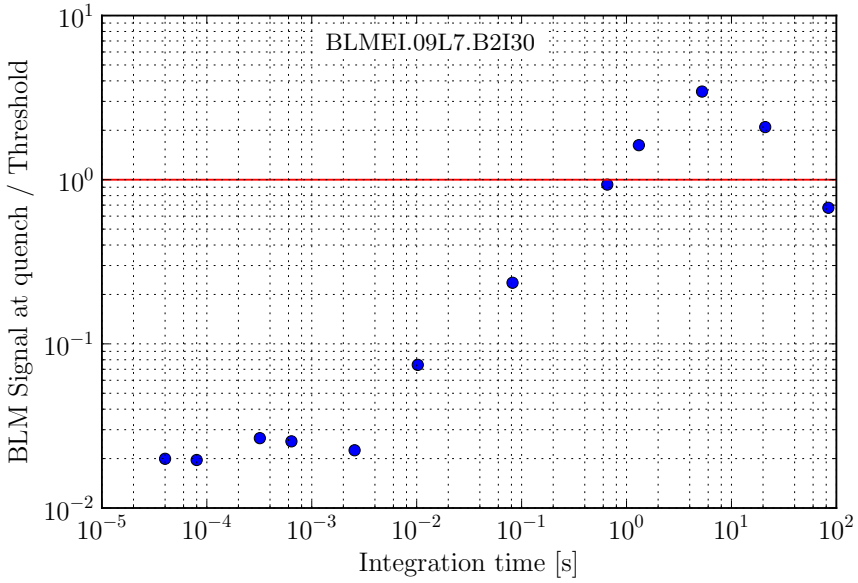

Figure 9.4: BLM Signals at quench for different running sums. The maximum exceed is obtained for RS10 where the signal was measured to be at 350% of the operational threshold.

An important outcome of the experiment are the measured BLM signals at quench with respect to the operational BLM thresholds. The measured data is going to be used to adjust the BLM thresholds for future operation. The BLM signals at the BLMEI.09L7.B2I30 at the moment of the quench are shown, normalized to the present operational BLM thresholds, in Fig. 9.4. The highest signal is measured for RS10 with 350% of the applied threshold. For RS09 and RS11, the thresholds were exceeded by 60% and 110% respectively [H$^+$16a].

From the measured cleaning inefficiency at the MBB.9L7 and the known peak power loss at the TCP, a rough estimate of the peak power deposited in the latter can be extracted as:

$$P_{\mathrm{MBB}} = \eta_Q \, P_q = (330 \pm 30)\,\mathrm{W}. \tag{9.7}$$

This value should be regarded with caution, knowing that the energy deposited is related to the BLM signals via a response function which is unknown. Better estimates for the power deposited can be obtained with a detailed shower deposition study carried out with FLUKA. The basis for this is a cleaning simulation with the hiSixTrack-FLUKA coupling in which the `toucMap` input is generated. This simulation is presented in the next section.

9.2.2 Simulations

Further information from the experiment can be gathered if the cleaning performance in the quench test configuration is simulated with the hiSixTrack-FLUKA coupling. The simulated cleaning performance can be combined with the measured quench limit to extrapolate the maximum stored beam energy also for the LHC configurations studied in Chap. 8.3 and Chap. 8.4. Furthermore, the simulation output can be used to perform a subsequent FLUKA shower propagation and energy deposition study to derive the power deposition in the superconducting magnet coils.

Cleaning Simulation with the hiSixTrack-FLUKA Coupling

Simulation Setup and Referene Loss Maps

The cleaning simulation with the hiSixTrack-FLUKA coupling is carried out in the B2H plane with 6.0×10^6 initial $^{208}Pb^{82+}$ ions at an energy of $6.37\,Z$ TeV, starting from IP1. The simulated optics and collimator settings are identical to the settings applied in the measurement, listed in Chap. 9.2. The impact parameter at the TCP.C6R7.B2 was set to values between 0.5 μm and 2.0 μm on both collimator jaws. The simulated loss pattern is compared to the loss map measured during the quench test in Fig. 9.5 (full ring) and Fig. 9.6 (zoom to IR7).

For comparison, also two measured B2H qualification loss maps are shown. One of them is the loss map measured at flat top (FT), already used for the quench test preparation in Chap. 9.1.1. The second loss map was measured at the end of squeeze (EoS). It was chosen for the comparison, because the background signal is significantly lower. From IR7 to IR5, the optics is identical, so the measured loss maps should be comparable in between.

Global Loss Distribution

The loss map simulated with the hiSixTrack-FLUKA coupling shows a good overall agreement with the measured loss maps. As explained in Chap. 5.2, the simulated losses in the warm magnets of IR7 are not comparable to the measured BLM signals. The dominating losses in IR7, IR6 and IR3 are well modeled in the simulation and also the loss peak C5 (see Fig. 9.5) in the cold region downstream of IR5 is accurately predicted.

Remarkable differences are visible in the arcs between IR5 and IR6 (called C56) as well as between IR6 and IR7 (C67). The C56 loss peaks are only visible in the loss map measured during the quench test, while they are neither simulated nor measured in either of the qualification loss maps. In the EoS loss map, their amplitude should be above the noise level.

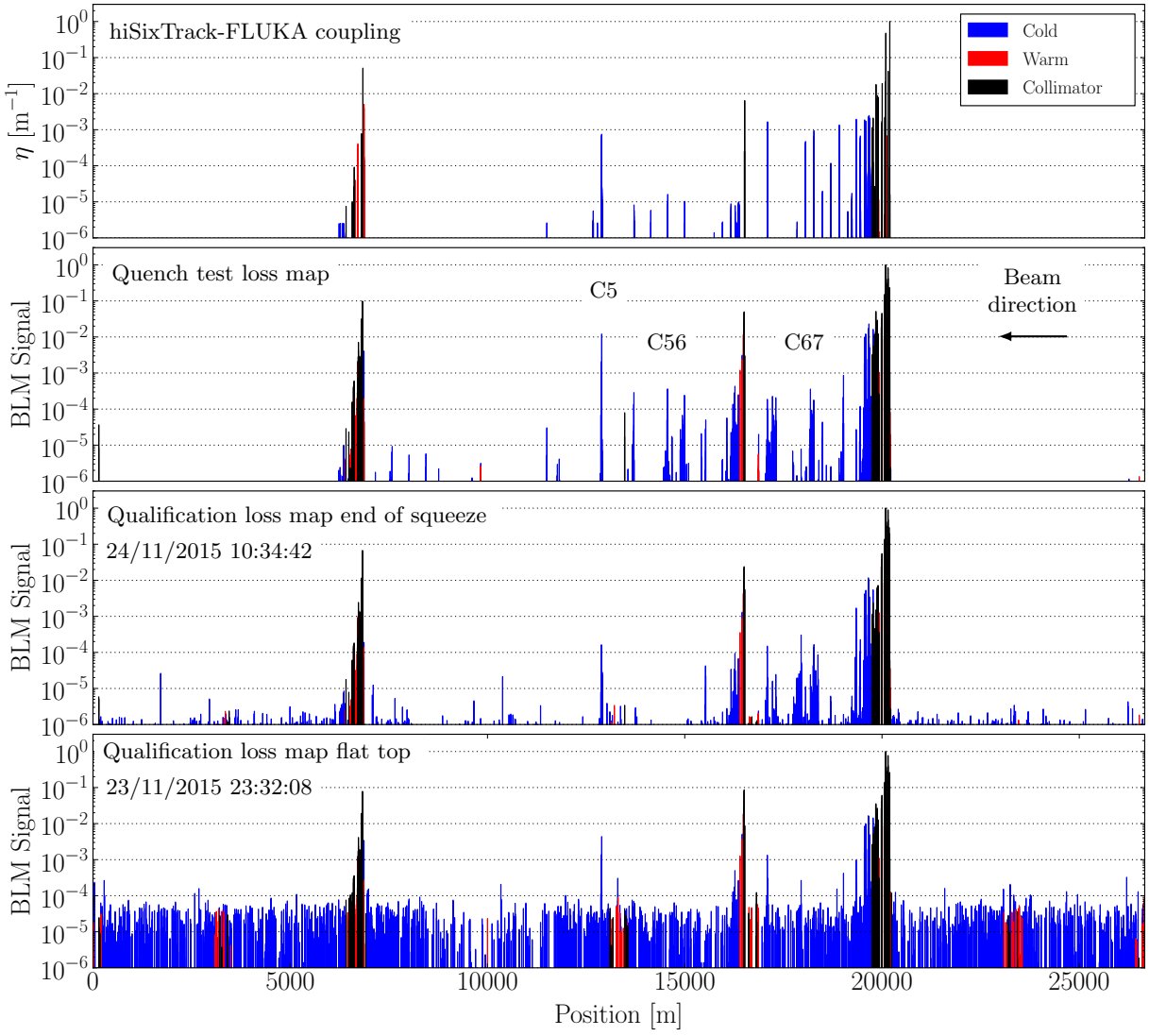

Figure 9.5: Measured and simulated B2H loss maps for the B2H collimation quench test.

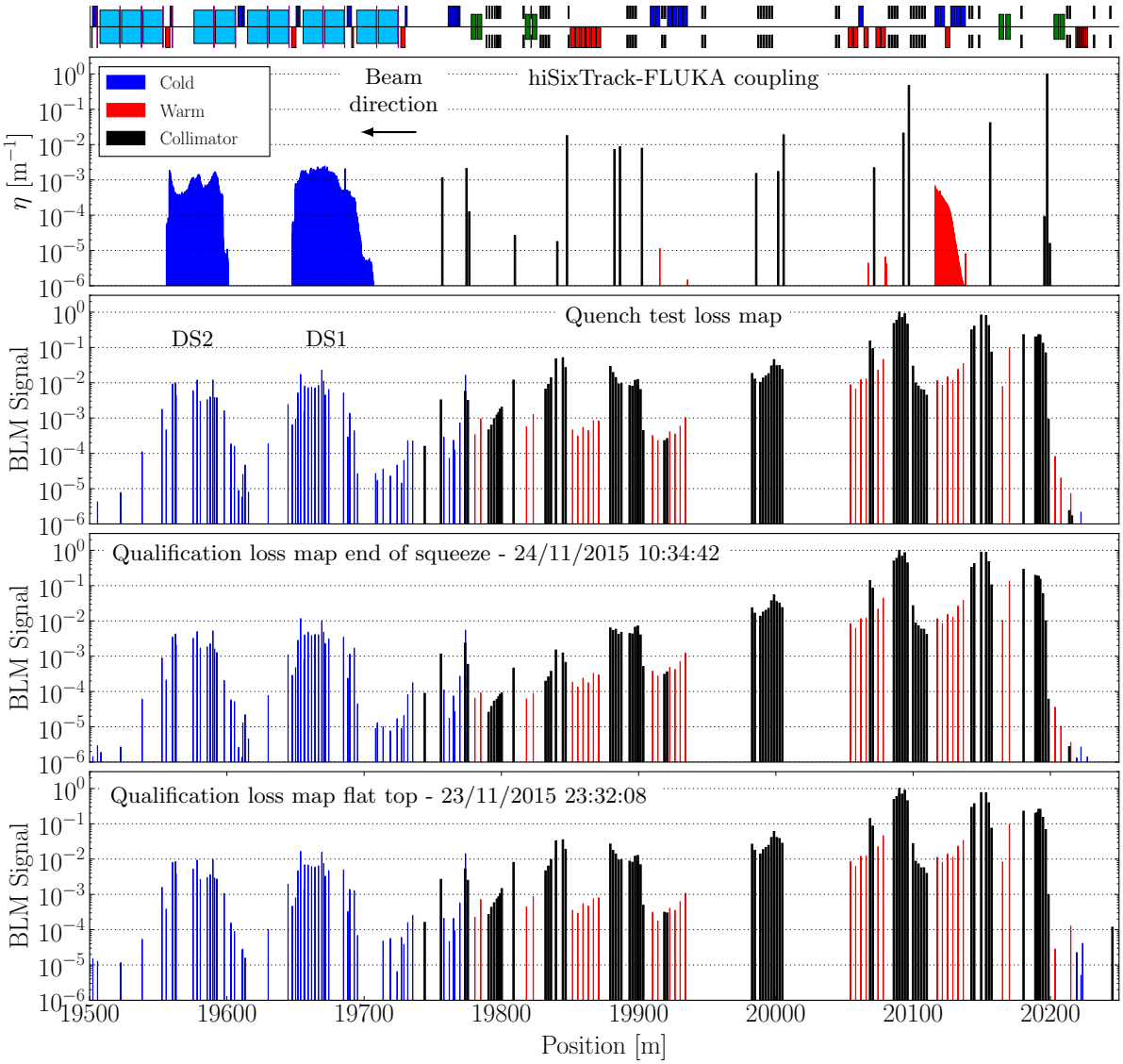

Figure 9.6: Top panel: loss map in the 2015 heavy-ion quench test configuration simulated with the hiSixTrack-FLUKA coupling. Second panel: loss map measured at the moment of quench. Third panel: qualification loss map at the end of squeeze. Bottom panel: qualification loss map measured at flat top.

Some of the pronounced C67 loss peaks are simulated in the hiSixTrack-FLUKA coupling but not measured in the qualification loss maps. From the zoom to IR7 shown in Fig. 9.6, it is visible that the measured losses in the TCLA collimators in IR7 are different between the EoS qualification loss map and the FT and quench test loss map. In the EoS loss map, the TCLA losses at some absorbers are lower by one order of magnitude.

These discrepancies are not understood and subject to further investigation. One possible reason could be different reference orbits between the measurements.

Losses in the DS1 and DS2 cluster

In the measured loss map at quench, the highest loss signal in the cold regions is occurs at the MBB.9L7 with a loss signal of $\mathcal{B}^{\mathrm{QT}}_{\mathrm{MBB9L7}} = (2.2 \pm 0.4) \times 10^{-2}$. The uncertainty is derived from the BLM signal variations observed during the excitation at which the quench occurred.

In the qualification loss map at flat top, the highest loss signal was measured at the MQY in the same cell, with a slightly lower loss signal of $\mathcal{B}^{\mathrm{lm,\,FT}}_{\mathrm{MQ9L7}} = (1.6 \pm 0.4) \times 10^{-2}$. For the EoS loss map, the measured signal yields $\mathcal{B}^{\mathrm{lm,\,EoS}}_{\mathrm{MQ9L7}} = (1.2 \pm 0.4) \times 10^{-2}$. This discrepancy is not considered important because the impact parameter and hence the fragment spectrum might be different in the measured loss maps.

In the simulated loss map, the highest loss peak in the cold regions is located at the MBB.9L7, in line with the measurement and the quench location. At this location, the cleaning inefficiency simulated with the hiSixTrack-FLUKA coupling is

$$\eta_{\mathrm{MBB9L7}} = 2.4 \times 10^{-3}\,\mathrm{m}^{-1}\,. \tag{9.8}$$

In order to better understand the energy deposited in the magnet coils, a detailed shower propagation study is carried out with FLUKA.

Energy Deposition Simulation with FLUKA

Based on the `toucMap` output from the hiSixTrack-FLUKA coupling, subsequent FLUKA simulations can be performed to study the energy deposited in the superconducting magnet coils and hence derive the quench limit in terms of the MQPD [S^{+}15b].

A detailed model of the IR7 geometry is used to simulate the interaction of the particles with the TCP material and the subsequent propagation of residual fragments and electromagnetic and hadronic showers. The propagation of residual particles and their interaction with collimators, surrounding beam pipes and other machine hardware is included in the simulation. This allows to simulate the BLM signals at the collimators and in the DS. The most important outcome of the simulation is to estimate the energy deposited in the magnet coils at the time of quench.

These simulations are carried out by the CERN FLUKA team and are very demanding in terms of computing time and post-processing of the data. At the time of writing, the energy deposition simulations by FLUKA are still ongoing.

9.3 Estimates on Performance Limitations

The experimental input gathered from the heavy-ion collimation quench test can be combined with the results of the cleaning simulations presented in Chap. 8.3, to estimate the maximum allowed stored beam energy for the different configurations of HL-LHC. This analysis will determine whether the target luminosity is achievable and if the upgrade with the TCLD collimators is required for future heavy-ion operation. The extrapolation of the stored beam energy and luminosity is also presented for the prospective operation with $^{129}\mathrm{Xe}^{54+}$ or $^{40}\mathrm{Ar}^{18+}$.

9.3.1 Strategy

Maximum Stored Beam Energy

The baseline for the estimate of the achievable stored beam energy is the maximum stored beam energy at $6.37\,Z$ TeV derived from the heavy-ion collimation quench test. Following Eq. (9.6), the maximum stored beam energy at $6.37\,Z$ TeV is (10.8 ± 0.8) MJ. The re-scaling to a beam energy of $7\,Z$ TeV requires taking into account the reduced quench limit with the higher magnet current. As introduced in Chap. 3.3.3, the quench limit for steady state losses is quantified by the minimum quench power density (MQPD). The most recent estimates for the MQPD scaling from $6.5\,Z$ TeV to $7.0\,Z$ TeV are summarized in Table 9.4. It is assumed that the MQPD is approximately 20% lower at $6.5\,Z$ TeV than at $6.37\,Z$ TeV [Ver16]. The MQPD scaling factors are derived from simulations and should be considered tentative and uncertain [Ver13].

To estimate the energy deposited in the IR7 DS magnets in every simulated configuration, the maximum average cleaning inefficiency η_{max}^{avg} is compared to $\eta_{max}^{avg,QT}$ from the cleaning simulation in the quench test configuration. The same impact parameter should be applied in all cases to make the simulated cleaning performances comparable. The simulations for HL-LHC were conducted with $b = 1\,\mu$m, because the largest cleaning inefficiency in the DS2 was simulated with this impact parameter. The loss map simulated for the quench test scenario with an impact parameter of $b = 1\,\mu$m is shown in Fig. 9.7.

The maximum allowed stored beam energy at $6.37\,Z$ TeV was derived from the quench test result using the design specification for the minimum beam lifetime, which is $\tau_{\mathrm{DR}} = 12$ min. So far, the minimum beam lifetime τ in operation at top energy with heavy-ion beams dropped rarely to values close to 12 min. Therefore, the extrapolation of the permitted stored beam energies for HL-LHC is also carried out for beam lifetimes up to $\tau = 60$ min. This requires re-scaling the maximum stored beam energy with the ratio τ/τ_{DR}. Such a comparison allows specifying a minimum beam lifetime required to reach the HL-LHC target.

Table 9.4: Estimated quench limit scaling from 6.37 Z TeV and 6.5 Z TeV to 7.0 Z TeV for the LHC main dipoles [Ver16]. Only the longest loss durations are shown, considering that collimation losses are assumed to be steady state losses. It should be kept in mind that these numbers have significant uncertainties.

Loss Duration [s]	$\frac{\text{MQPD}_{7.0}}{\text{MQPD}_{6.5}}$	$\frac{\text{MQPD}_{7.0}}{\text{MQPD}_{6.37}}$
0.25	0.74	0.59
0.65536	0.71	0.57
1.31072	0.68	0.54
5.24288	0.60	0.48
20.9715	0.55	0.44
83.8861	0.56	0.45

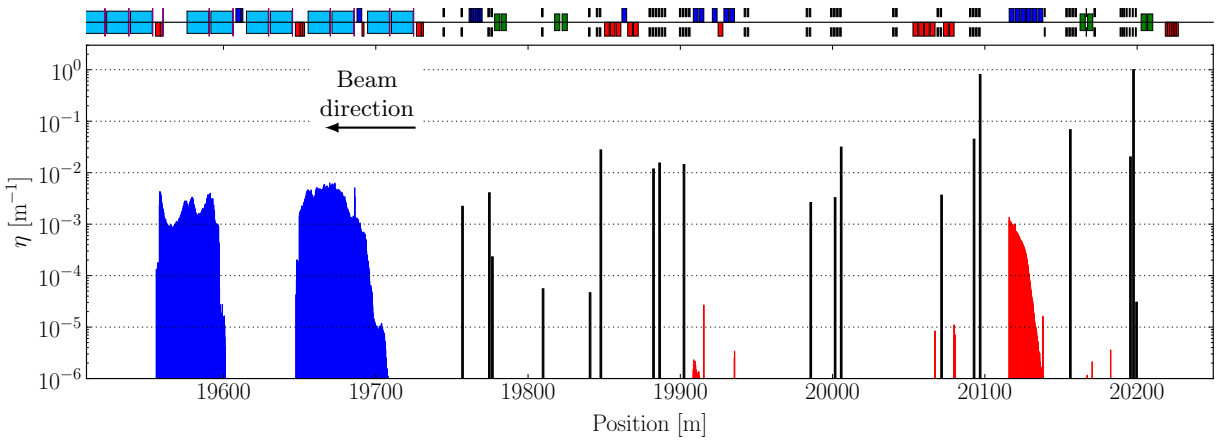

Figure 9.7: B2H cleaning inefficiency in IR7 simulated with the hiSixTrack-FLUKA coupling in the configuration of the heavy-ion collimation quench test at 6.37 Z TeV with an impact parameter of 1 μm.

Table 9.5: Maximum average cleaning inefficiencies in the IR7 DS clusters simulated with the hiSixTrack-FLUKA coupling for different LHC configurations. All simulations assume an impact parameter of 1 μm at the TCP.

Configuration	Ion	TCLDs	N_D [σ]	η^{avg}_{DS1} [m^{-1}]	η^{avg}_{DS2} [m^{-1}]
2015 Quench Test	^{208}Pb^{82+}	0	-	4.7×10^{-3}	2.5×10^{-3}
HL-LHC	^{208}Pb^{82+}	0	-	4.0×10^{-3}	4.7×10^{-3}
HL-LHC	^{208}Pb^{82+}	1	15	1.0×10^{-3}	4.2×10^{-3}
HL-LHC	^{208}Pb^{82+}	1	12	3.6×10^{-5}	2.7×10^{-3}
HL-LHC	^{208}Pb^{82+}	1	10	1.5×10^{-5}	2.6×10^{-3}
HL-LHC	^{208}Pb^{82+}	2	15	1.0×10^{-3}	1.4×10^{-4}
HL-LHC	^{208}Pb^{82+}	2	12	3.6×10^{-5}	1.5×10^{-6}
HL-LHC	^{208}Pb^{82+}	2	10	1.5×10^{-5}	2.5×10^{-6}
HL-LHC	^{129}Xe^{54+}	0	-	4.8×10^{-3}	4.3×10^{-3}
HL-LHC	^{40}Ar^{18+}	0	-	4.6×10^{-3}	1.9×10^{-3}

The maximum permitted stored beam energy $E_s^{\mathrm{max,HL}}$ in the studied scenario is then derived from the quench limit scaling, the ratio of maximum average cleaning inefficiency and the assumed beam lifetime by the following relation

$$E_s^{\mathrm{max,HL}} = E_s^{\mathrm{max,QT}} \times \frac{\tau}{\tau_{\mathrm{DR}}} \times \frac{\mathrm{MQPD}_{7.0}}{\mathrm{MQPD}_{6.37}} \times \frac{\eta^{avg,QT}_{max}}{\eta^{avg}_{max}} \,. \tag{9.9}$$

The quantity $E_s^{\mathrm{max,QT}}$ is the maximum stored beam energy at $6.37\,Z$ TeV derived from the heavy-ion collimation quench test (see Eq. (9.6)).

Given the rather large uncertainty of the quench limit estimate and the known limitations from the comparison of simulated cleaning inefficiencies, the estimates derived with this formula should be regarded as approximate. A better approach would be the simulation of energy deposition in the magnet, starting from the output generated with the hiSixTrack-FLUKA coupling. This type of simulation is envisaged for the future.

For the MQPD re-scaling, the most conservative scaling factor of 0.44 is chosen (loss duration 20.9715 s). As a comparison, the allowed stored beam energy is also estimated without accounting for the quench limit reduction. This value represents an upper limit.

Especially for the simulations with 2 TCLDs per beam, the extrapolation will deliver stored beam energies significantly above the HL-LHC target value of 24.1 MJ for $^{208}Pb^{82+}$ beams. At the time of writing, stored beam energies beyond the HL-LHC target are not reachable with the envisaged injector upgrades. The values for simulations with 2 TCLDs should rather be interpreted as a margin compared to the HL-LHC target, from perspective of the quench risk by collimation losses. But even if the injector performance should turn out to be better in the future, additional constraints arise from the collimation system, e.g. by the maximum power load the primary collimators can withstand without being damaged.

Achievable Luminosity

As shown in Eq. (3.2), the maximum stored beam energy cannot be directly translated into the luminosity. Assumptions have to be made about the bunch intensity and the number of bunches in the machine. The luminosity is proportional to the square of the bunch intensity, and linearly proportional to the number of bunches. The maximum luminosity can hence be reached if the stored beam energy is distributed over the fewest possible number of bunches.

The baseline for the luminosity calculations presented below is the most recent estimate for the HL-LHC bunch intensity yielding 2.1×10^8 ions/bunch for $^{208}Pb^{82+}$ ions [Jow16], 6×10^8 ions/bunch for $^{129}Xe^{54+}$ ions and 5×10^9 for $^{40}Ar^{18+}$ ions [M$^+$16a]. Note that for Ar and Xe, the bunch intensity corresponds to the value that is achievable at the extraction of the SPS. The assumed number of bunches is derived from the maximum stored beam energy and the bunch intensity, although no filling scheme is yet existing for the different cases.

All luminosities derived are calculated for IP2, assuming that all bunches are colliding. The crossing angle correction factor is not taken into account ($F = 1$), so all luminosities should be regarded as upper boundaries. Furthermore, the assumed beam parameters are $\beta^* = 0.5\,\mathrm{m}$, a normalized emittance of $\epsilon_N = 1.3\,\mu\mathrm{m}$ rad [Jow16] and the nominal revolution frequency of 11.245 kHz [B$^+$04b]. The assumptions are made to provide the best comparability between the different study cases.

9.3.2 Results

The maximum average cleaning inefficiencies in the two DS clusters derived from the different simulations are listed in Table 9.5. Based on these values, the maximum stored beam energy is derived with and without MQPD scaling by means of Eq. (9.9). The maximum stored beam energy is used to derive the achievable luminosity in IP2, as it was described above. The results of the study assuming a minimum beam lifetime of 12 min are listed in Table 9.6. The results are also graphically represented for different lifetimes in Fig. 9.8, Fig. 9.9 and Fig. 9.10.

Table 9.6: Extrapolated maximum stored beam energy and achievable peak nucleon-nucleon luminosity in IP2 for different HL-LHC configurations with and without MQPD scaling. A minimum beam lifetime of 12 min is assumed.The values derived for the case of 2 TCLDS with settings of $10\,\sigma$ and $12\,\sigma$, are not reachable in the LHC, because the required number of bunches can not be injected in the LHC. They are written in brackets and are only shown for comparison.

		Without MQPD scaling			With MQPD scaling		
	N_D [σ]	$E_s^{\mathrm{max,HL}}$ [MJ]	n_B	$\mathcal{L}_{\mathrm{NN,\,IP2}}^{\mathrm{max}}$ [cm^{-2} s^{-1}]	$E_s^{\mathrm{max,HL}}$ [MJ]	n_B	$\mathcal{L}_{\mathrm{NN,\,IP2}}^{\mathrm{max}}$ [cm^{-2} s^{-1}]
HL Target	-	*24.1*	*1248*	*9.7×10^{32}*	*24.1*	*1248*	*9.7×10^{32}*
No TCLD	-	10.8±0.8	560	$(4.3\pm0.5)\times10^{32}$	4.8 ±0.4	248	$(1.9\pm0.3)\times10^{32}$
1 TCLD	15	12.1±0.9	626	$(4.8\pm0.9)\times10^{32}$	5.3±0.4	274	$(2.2\pm0.2)\times10^{32}$
1 TCLD	12	18.8±1.4	974	$(7.8\pm0.9)\times10^{32}$	8.3±0.7	430	$(3.3\pm0.4)\times10^{32}$
1 TCLD	10	19.5±1.5	1010	$(7.8\pm0.9)\times10^{32}$	8.7±0.7	450	$(3.5\pm0.4)\times10^{32}$
2 TCLD	15	50.8±3.8	2630	$(2.0\pm0.2)\times10^{33}$	22.4±1.7	1160	$(9.1\pm0.9)\times10^{32}$
2 TCLD	12	[1410±105]	n.r.	$[(5.7\pm0.5)\times10^{34}]$	[623±47]	n.r.	$[(2.5\pm0.2)\times10^{34}]$
2 TCLD	10	[3384±251]	n.r.	$[(1.4\pm0.2)\times10^{35}]$	[1596±111]	n.r.	$[(6.4\pm0.5)\times10^{34}]$
Xe	-	10.6±0.8	292	$(7.7\pm0.7)\times10^{32}$	4.7±0.4	130	$(3.3\pm0.4)\times10^{32}$
Ar	-	11.0±0.9	110	$(2.1\pm0.2)\times10^{33}$	4.9±0.4	48	$(9.1\pm0.8)\times10^{32}$

Nominal HL-LHC without TCLD

The allowed stored beam energy for the HL-LHC configuration without TCLDs and considering a minimum beam lifetime of 12 min is extrapolated to be (4.8 ± 0.4) MJ with MQPD scaling and (10.8 ± 0.8) MJ without MQPD scaling. The nucleon-nucleon luminosity reachable with scaled MQPD yields $(1.9\pm0.3)\times10^{32}\,\mathrm{cm^{-2}\,s^{-1}}$. In the 2015 heavy-ion run, the peak nucleon-nucleon luminosity was approximately $1.6\times10^{32}\,\mathrm{cm^{-2}\,s^{-1}}$. The HL-LHC target nucleon-nucleon luminosity derived with the same assumptions on emittance, β^* and crossing angle is $9.7\times10^{32}\,\mathrm{cm^{-2}\,s^{-1}}$. The illustration in Fig. 9.8 shows also that the target value could not be reached, even if the minimum beam lifetime was 60 min.

Nominal HL-LHC with 1 TCLD

The improved cleaning performance with one TCLD collimator leads to an increase of the permitted stored beam energies. Including the MQPD scaling and assuming the design minimum beam lifetime of 12 min, the maximum stored beam energy yields (5.3±0.4) MJ for a TCLD setting of $15\,\sigma$ and (8.7±0.7) MJ for the tightest setting of $10\,\sigma$. The achievable nucleon-nucleon luminosity in IP2 increases accordingly to $(2.2\pm0.2)\times10^{32}\,\mathrm{cm^{-2}\,s^{-1}}$ for a TCLD half gap of $15\,\sigma$ and $(3.5\pm0.4)\times10^{32}\,\mathrm{cm^{-2}\,s^{-1}}$ with a half gap of $10\,\sigma$.

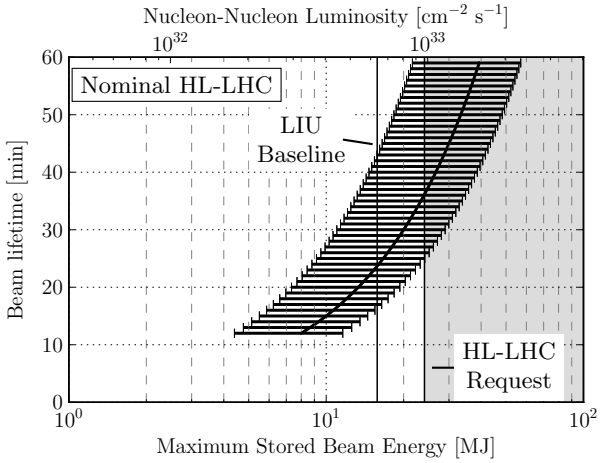

Figure 9.8: Maximum stored beam energy and achievable luminosity for HL-LHC with $^{208}Pb^{82+}$ ions without TCLD collimators. The lower limits are derived from the rescaling including the reduced MQPD. The upper limit is only re-scaled with the cleaning inefficiency. The vertical black lines show the target values for operation after the LIU upgrade and the present optimistic baseline for HL-LHC. The gray area shows stored beam energies which are not reachable with the presently envisaged injector upgrades.

The HL-LHC target stored beam energy could possibly be reached, if the TCLD is set to half gaps smaller than $12\,\sigma$ and the beam lifetime is larger than 38 min.

Nominal HL-LHC with 2 TCLDs

The drastic improvement of the cleaning performance with two TCLD collimators leads to significantly larger permitted stored beam energies. Already in the scenario with MQPD scaling, design minimum beam lifetime and the TCLDs set to the most relaxed setting of $15\,\sigma$, the allowed stored beam energy is (22.4±1.7) MJ. This corresponds to an achievable luminosity of $(9.1 \pm 0.9)\times10^{32}$ cm^{-2} s^{-1}, close to the design luminosity. All studied scenarios with tighter settings deliver stored beam energies beyond 600 MJ, showing that the quench risk of collimation losses would not restrict the LHC performance any more. Evidently, such large beam intensities are not reachable and would be restricted by other limitations. The conclusion of this study is hence, that the HL-LHC goal is reachable when two TCLDs per beam are installed in IR7 and set to a small enough half gap between $12\,\sigma$ and $15\,\sigma$.

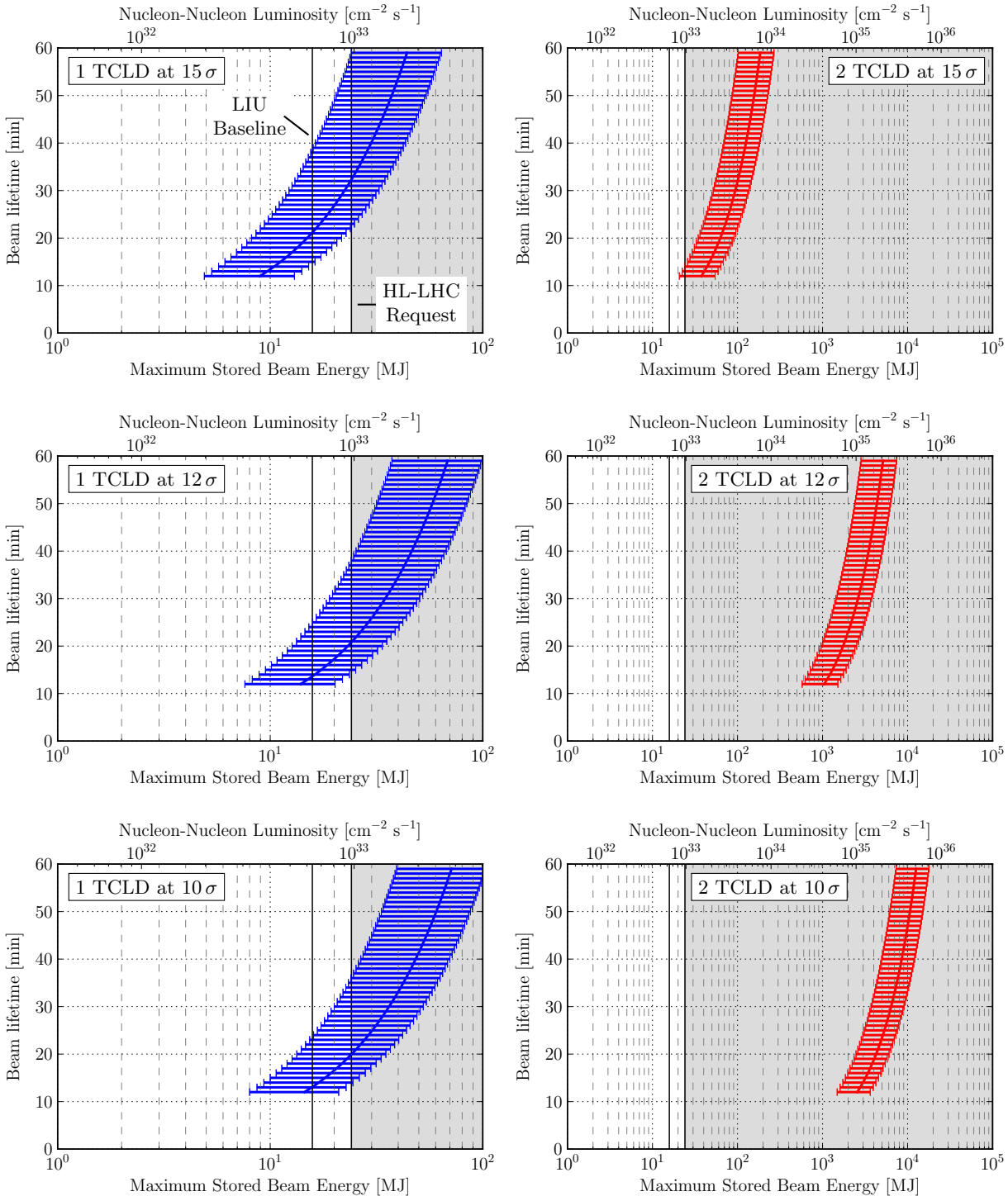

Figure 9.9: Maximum stored beam energy as a function of the beam lifetime for different HL-LHC scenarios with $^{208}Pb^{82+}$ beams. Left column: simulations with one TCLD per beam. Right column: simulations with two TCLDs per beam. The gray areas show stored beam energies which are not reachable with the presently envisaged injector upgrades. The vertical black lines show the target values for LIU and HL-LHC.

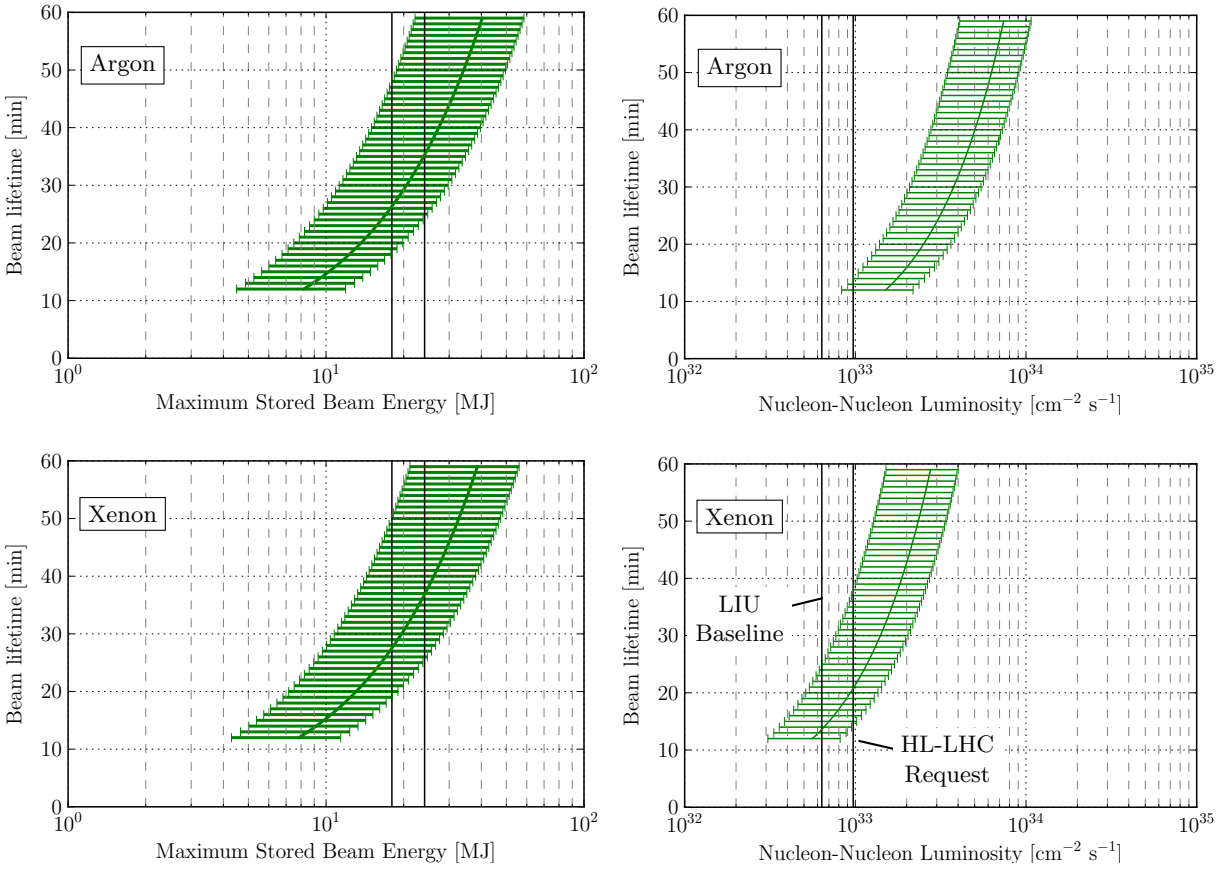

Figure 9.10: Left column: Maximum stored beam energy for Ar and Xe ions. Right column: achievable luminosity, assuming the same normalized emittance 1.3 μm rad as for $^{208}Pb^{82+}$ beams and bunch intensities of 5×10^9 ions/bunch for Ar and 6×10^8 ions/bunch for Xe. The vertical lines show the $^{208}Pb^{82+}$ design values after the LIU upgrade and for HL-LHC.

Argon and Xenon Ions

The cleaning inefficiency simulated for $^{40}Ar^{18+}$ and $^{129}Xe^{54+}$ are similar to the HL-LHC configuration with $^{208}Pb^{82+}$ beams, without TCLDs. Accordingly, the maximum stored beam energy is also similar for Ar and Xe. With MQPD scaling and a minimum beam lifetime of 12 min, the allowed stored beam energy yields (4.9±0.4) MJ for Ar and (4.7 ± 0.4) MJ for Xe.

However, for the case of Ar, the number of ions per bunch is higher by a factor of almost 20. Also the charge to mass ratio of Ar is larger than that of Pb, which increases the relativistic γ factor, assuming the same emittance as for Pb beams. Therefore, the achievable nucleon-nucleon luminosity with Ar is significantly larger compared to Pb beams. Including MQPD scaling and assuming a minimum beam lifetime of 12 min, the extrapolated nucleon-nucleon luminosity of Ar yields $(9.1 \pm 0.8) \times 10^{32}\,\mathrm{cm}^{-2}\,\mathrm{s}^{-1}$.

This is a significant improvement compared to $(1.9 \pm 0.2) \times 10^{32}\,\mathrm{cm}^{-2}\,\mathrm{s}^{-1}$ for Pb beams, when MQPD scaling is considered and no TCLDs are installed. The comparison shows that with Ar ions, the envisaged HL-LHC nucleon-nucleon luminosity of $9.7 \times 10^{32}\,\mathrm{cm}^{-2}\,\mathrm{s}^{-1}$ can almost be reached. The maximum nucleon-nucleon luminosity for Xe ions, including MQPD scaling and assuming a beam lifetime of 12 min, yields $(3.3 \pm 0.4) \times 10^{32}$. This is only slightly larger than for Pb and significantly below the HL-LHC target.

The comparison shows that higher luminosities are indeed possible when lighter ion species than $^{208}\mathrm{Pb}^{82+}$ are collided, although the cleaning inefficiency is comparable. While for Xe, the potential for luminosity increase is rather limited, the estimated nucleon-nucleon luminosity for Ar is significantly larger than for Pb. It should be kept in mind, that these estimates depend crucially on the assumed bunch intensity. The latter could be lower in the LHC at top energy. This should be taken into account in an updated study, as soon as reliable data on the achievable Ar bunch intensity in the LHC is available.

9.4 Summary and Conclusions

The 2015 LHC heavy-ion collimation quench test was the first experiment of its kind in which a quench was achieved. The MBB.9L7 quenched from the collimation debris, when a power of (15 ± 1) kW was deposited at the horizontal TCP for B2. Extrapolating from the TCP power load and the design value of the minimum beam life time, the upper limit for the achievable stored beam energy at 6.37 Z TeV was derived to be (10.8±0.8) MJ.

The cleaning inefficiency of the LHC in the quench test configuration was simulated with the hiSixTrack-FLUKA coupling and the result is in good agreement with the measured loss pattern. The output produced is used for a detailed shower propagation and energy deposition simulation. This study is carried out by the CERN FLUKA team and is still ongoing.

The experimentally gathered intensity limitation for 6.37 Z TeV was used to extrapolate intensity limitations for HL-LHC with and without TCLD collimators. This was achieved by re-scaling the intensity limit found for 6.37 Z TeV with a MQPD reduction factor and taking into account the maximum average cleaning inefficiency in the different scenarios. These studies show that the target intensity for HL-LHC can possibly not be reached if only one TCLD is installed per beam in IR7 and the minimum beam lifetime is 12 min. This should be further investigated, possibly with more detailed shower propagation studies in FLUKA. With sufficiently tight TCLD settings and a lifetime above 38 min, the target stored beam energy can possibly be reached.

With two TCLD collimators, the amount of collimation debris lost in the IR7 DS is reduced sufficiently to reach the HL-LHC goals if the TCLD half gap is set to sufficiently tight settings. With two TCLD collimators, the quench risk from collimation debris can potentially be eliminated as a limiting factor for the achievable stored heavy-ion beam energy.

The studies with Ar and Xe ions have shown that higher nucleon-nucleon luminosities can be reached also without TCLDs, especially if Ar ions were to be used in the LHC.

Within the remaining inevitable uncertainties, the HL-LHC simulations with the hiSixTrack-FLUKA coupling have delivered important new findings. They are going to be taken as a reference for future discussions about the required collimation system upgrades for HL-LHC.

10. Outlook

This chapter discusses potential reasons for remaining discrepancies between measurements and simulations with STIER or the hiSixTrack-FLUKA coupling. The outcome can be used in future applications to improve the agreement with measurements or to study the significance of loss predictions with the new simulation tools.

10.1 Possible Improvements for Future Simulations

The simulations with both STIER and the hiSixTrack-FLUKA coupling still show discrepancies to the measured loss maps. Some of the loss peaks which are measured are not simulated and vice versa. In this section, it is discussed, how these discrepancies could be understood and possible improvements for future upgrades of the simulation tools are outlined.

10.1.1 Orbit Fluctuations

Field errors and misalignments of the LHC magnets can lead to variations of the closed orbit. As it was discussed in Chap. 8.1.2, the loss location can, depending on the projected penetration depth d_p of the particle, be altered when the orbit does not coincide with the ideal orbit. For loss peaks which are simulated with either STIER or the hiSixTrack-FLUKA coupling, the simulation data can be consulted to find the projected penetration depth of the individual particles causing the losses and hence quantify the orbit offset required to alleviate these losses.

This principle can be illustrated at the example of the simulated and measured loss patterns for the 2011 and 2015 heavy-ion run. They are directly compared in Fig. 10.1. The arc loss peaks A1 to A4 are both measured and simulated in the heavy-ion run of 2011. Also in the hiSixTrack-FLUKA coupling simulation for the 2015 heavy-ion run they are predicted. However, in the 2015 qualification loss maps only the A1 and A4 loss spikes are visible, while at the A2 and A3 locations loss peaks are not measured. These discrepancies could potentially arise from orbit offsets, which shall be studied in the following.

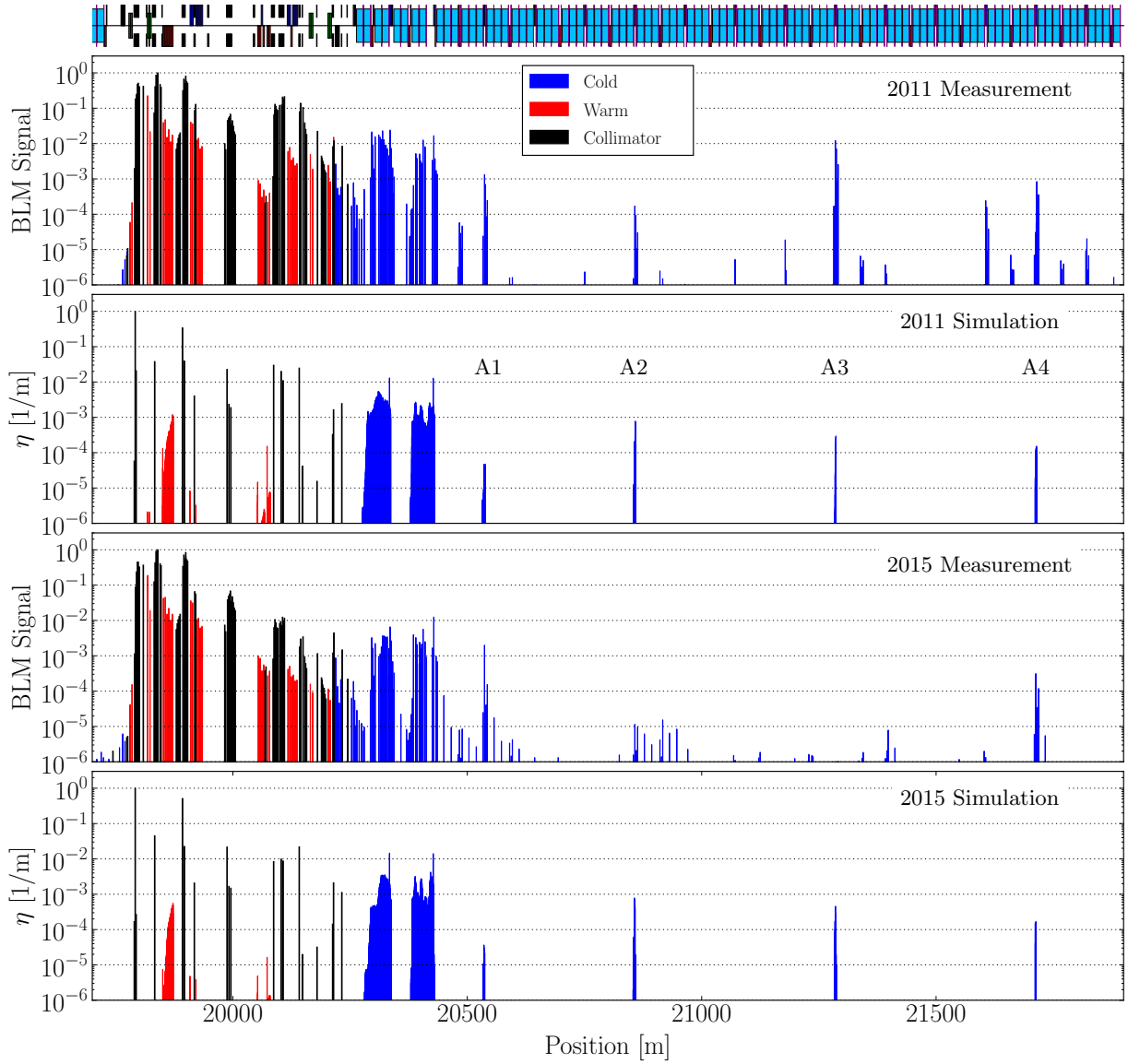

Figure 10.1: Measured and simulated B1H loss maps of the 2011 heavy-ion run at 3.5 Z TeV and the 2015 heavy-ion run at 6.37 Z TeV, zoomed to IR7. The simulations are carried out with the hiSixTrack-FLUKA coupling.

From the simulation data, the projected penetration depth for the particles impacting at the individual loss peaks can be derived. With this information, the expected loss reduction for a given orbit offset can be derived, assuming that the orbit offset shifts the beam away from the impacting side of the beam pipe. The so derived loss reduction as a function of the orbit offset Δx is shown for the 2011 and the 2015 heavy-ion run in Fig. 10.2. A key quantity in the following comparison is the orbit offset required to reduce the losses by 50% (see Fig. 10.2). This quantity is called Δx_{50} in the following. The values for Δx_{50} in the A1 to A4 loss peaks derived for the 2011 and 2015 heavy-ion run are listed in Table 10.1.

For the A1 loss peak, the required offset for 50% loss reduction simulated for the 2011 configuration is approximately $\Delta x_{50}^{2011} = 800\,\mu$m. In the simulation for the 2015 heavy-ion run, this quantity yields $\Delta x_{50}^{2015} = 1700\,\mu$m. This means that a larger orbit offset is required to alleviate the same amount of the A1 losses in the 2015 configuration. For orbit offsets of more than $2500\,\mu$m, the A1 loss peak is fully alleviated in both simulations. These values are rather large.

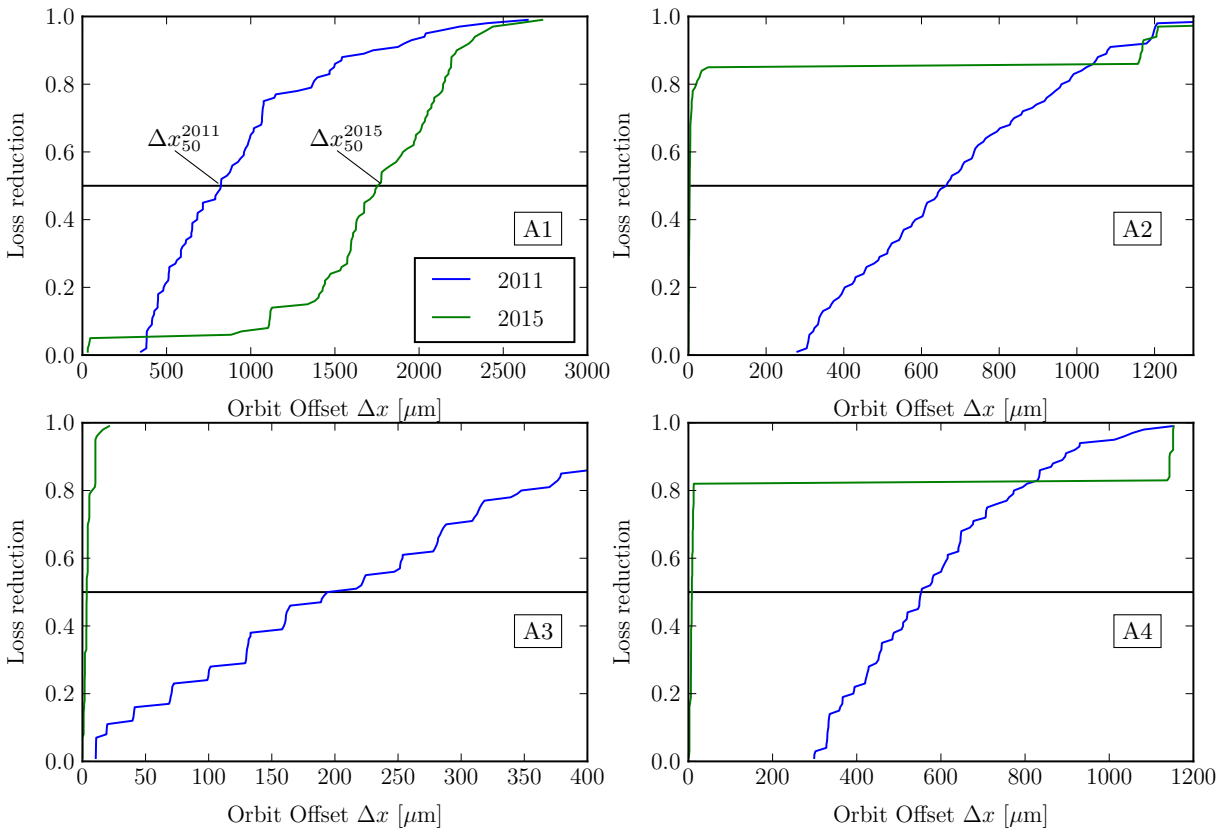

Figure 10.2: Loss reduction as a function of the orbit offset at the individual arc loss spikes A1 to A4 derived from the projected penetration depth. Data simulated with the hiSixTrack-FLUKA coupling for the 2011 and the 2015 heavy-ion run.

Table 10.1: Orbit offsets required to alleviate 50% of the energy lost at the A1 to A4 loss peaks.

	Δx_{50} [μm]			
Year	A1	A2	A3	A4
2011	800	650	190	550
2015	1700	6	4	9

For the A2 loss peak in the 2011 configuration which was both measured and simulated, Δx_{50}^{2011} yields 650 μm. In the 2015 heavy-ion run, the measured qualification loss map does not show a loss peak at the A2 location. The analysis of the simulated loss pattern shows that Δx_{50}^{2015} is only 6 μm for this simulation case. Hence, very small orbit variations can alleviate this loss peak which might be the reason for the discrepancy between simulation and measurement.

For the A3 loss peak, an orbit offset of $\approx 4\,\mu$m is sufficient to alleviate half of the losses in the 2015 configuration. For the 2011 simulation, the required offset yields $\approx 190\,\mu$m. Also for this loss spike, the discrepancy between measurement and simulation could be explained by small orbit fluctuations.

For the A4 loss peak, the simulation in of the 2015 heavy-ion run predicts $\Delta x_{50}^{2015} = 9\,\mu$m and that for the 2011 heavy-ion run $\approx 550\,\mu$m. In spite of the small penetration depth in the 2015 configuration, the A4 loss peak is measured in the qualification loss map. One possible reason could be that the particles which are not lost in the A2 and A3 arrive at the A4 loss peak with larger projected penetration depth and cause the losses measured at this location.

In conclusion, the study demonstrates that the loss distribution of heavy-ion collimation losses can, depending on the machine configuration, be altered by small variations of the beam orbit. A loss reduction of 50% of the simulated loss amplitude at the locations A2, A3 and A4 can be expected by very small orbit offsets between 4 μm and 9 μm in the 2015 heavy-ion configuration. The real orbit during operation can drift by significantly larger amounts. Within one fill, the orbit can drift by 50 μm [Wen16]. The reference orbit that is commissioned at the beginning of a run can be even further away from the magnet centers. The simulation results indicate that this is possibly the reason why A2 and A3 were not measured during the 2015 heavy-ion run. At the location of the A4 loss peak, the orbit could be shifted towards the beam pipe or the particles which would otherwise have been lost at the A2 and A3 could be lost there.

The studies show that it is important to take into account the projected penetration depth of simulated loss peaks. This can give valuable information to determine whether the simulated loss peak is probable to be measured or not.

Simulated loss spikes from particles impacting the aperture at a small projected penetration depth could be unobservable in the machine. As a counterexample, the impact parameter of the $^{207}Pb^{82+}$ fragments lost at the TCT2 in the study presented at Chap. 8.2 yields approximately 2 mm. As it was shown before, these losses were well predicted in the STIER simulation.

10.1.2 Aperture Misalignments

Besides orbit variations, also aperture misalignments of the LHC magnets can alter the loss position of secondary ion fragments. In the collimation simulations so far, only the ideal aperture is taken into account. Measurements of the aperture profile [H$^+$08a, Hag08] in the LHC magnets show that in reality the aperture can be shifted significantly with respect to the reference. The measured aperture in IR7 is illustrated in Fig. 10.3. Furthermore, the distribution of aperture misalignments with respect to the reference aperture in the arc magnets between IR7 and IR8 is illustrated in Fig. 10.4.

The standard deviation of this distribution is approximately 340 μm. The study of the projected penetration depth discussed in the previous subsection shows that such aperture offsets are sufficient to alleviate losses which would occur with the nominal aperture. For future cleaning simulations with heavy-ion beams, a framework could be established which incorporates the information about the measured aperture. This would possibly allow for a better understanding of existing discrepancies between simulations and measurements.

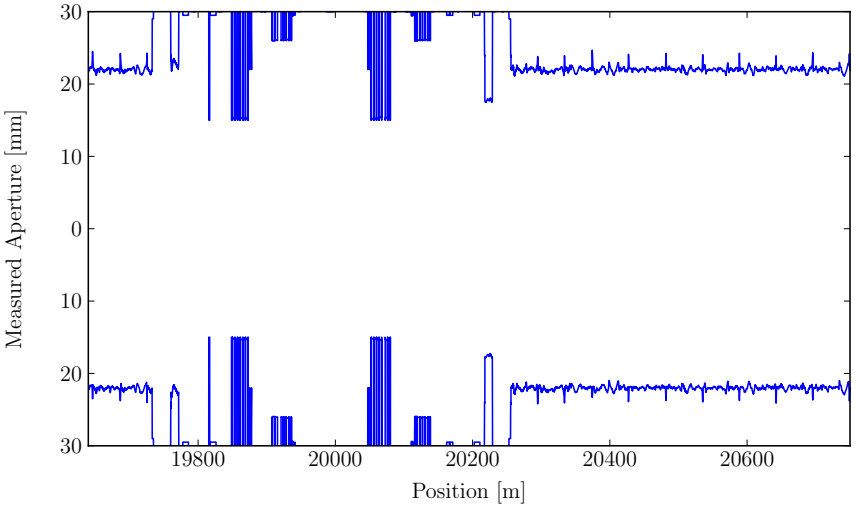

Figure 10.3: Measured horizontal aperture in the LHC magnets of IR7 and at the beginning of the arc between IR7 and IR8.

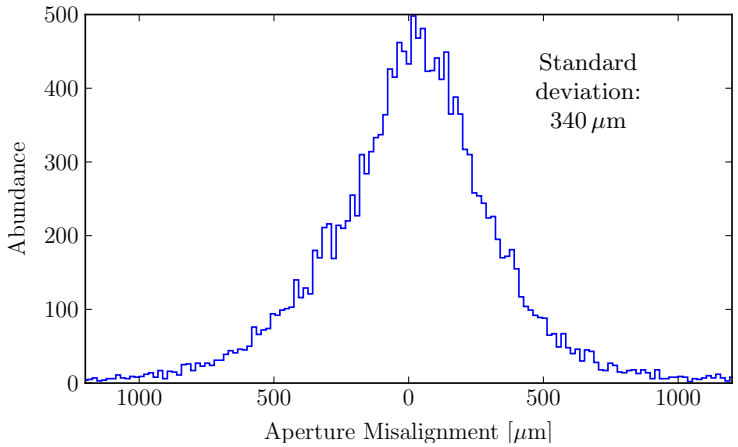

Figure 10.4: Distribution of aperture misalignments in the arc between IR7 and IR8.

10.2 Summary and Conclusions

In this chapter, it was shown that remaining discrepancies between measured and simulated heavy-ion loss maps can potentially be caused by orbit and aperture offsets. The projected penetration depth in the magnet aperture was used to study loss peaks in the arc downstream of IR7. Some of these loss peaks were simulated in the configuration of the 2015 heavy-ion run, but not measured during operation. The analysis unveiled that the projected penetration depth of the particles was smaller than typical orbit drifts or aperture misalignments, which might explain their absence in the measurement.

Future simulations could take these effects into account and hence predict the cleaning inefficiency even better than the existing tools.

Summary

With the CERN Large Hadron Collider (LHC), particle beams of unprecedented momentum became available for fundamental research. Besides the proton program, the LHC is operated with $^{208}Pb^{82+}$ beams, making it the third heavy-ion collider ever operated worldwide. The unprecedented stored beam energies in the LHC are a potential danger, because small fractions of it are sufficient to provoke the superconducting magnets to lose their superconductivity (quench), or even damage the machine hardware. The LHC is therefore equipped with a multi-stage collimation system to protect the machine from undesired beam loss. However, particles with rigidity offsets can still scatter out of the collimators. They can subsequently be absorbed by the superconducting LHC magnets which are in danger to quench. The dominating contribution to the cleaning inefficiency of the collimation system, defined as the ratio of energy lost in the superconducting magnets to the particles impacting on the collimators, is given by particles with changed magnetic rigidity

In this thesis, a new software to simulate the collimation performance of the LHC with heavy-ion beams is presented. Compared to proton collimation, the efficiency of the LHC collimation system for $^{208}Pb^{82+}$ beams is worse by more than two orders of magnitude. The reason for this is the large amount of residual heavy-ion fragments with different mass to charge ratio that is generated when heavy ions interact with the collimators. When the fragments enter the superconducting LHC magnets, they can be deviated into the magnet aperture and deposit energy in the superconducting magnet coils. Sophisticated simulation tools are required to simulate the efficiency of the collimation system in order to ensure safe operation that is uninterrupted by quenches. Such simulations allow understanding potentially critical beam losses and can be used to develop loss mitigation strategies. Collimation simulation tools must accurately simulate the interaction of beam particles with the collimators and follow the trajectory of the particles scattered out of the collimation system (tracking) to determine their loss location. The result of such simulations is the predicted distribution of losses in the ring (loss map), which can be compared to the loss distribution measured in operation.

Simulation software for heavy-ion collimation must hence take into account the nuclear and electromagnetic fragmentation inside the collimators and follow the particle trajectories of a wide range of different heavy ions inside the LHC magnets. The previous standard heavy-ion collimation simulation tool ICOSIM simulated the fragmentation in the LHC collimators in a simplified manner. In particular scattering and momentum changes from the fragmentation process are not taken into account in ICOSIM. Some important loss features that were measured in LHC operation could not be predicted with ICOSIM.

To understand if the simplified fragmentation algorithm in ICOSIM is the origin of the observed discrepancies, a new simulation framework, referred to as SixTrack with Ion-Equivalent Rigidities (STIER), was established. STIER was developed in order to estimate the impact of the various approximations used in ICOSIM. In particular, it is distinguished by a more realistic fragmentation model during the first passage through a collimator. In the STIER approach, the fragmentation at the most important primary collimator is simulated with the simulation software for particle-matter interaction FLUKA. The resulting distribution of heavy-ion fragments (including the correct angular coordinates and the particle energy) is then tracked as protons with ion-equivalent rigidities in the proton tracking software SixTrack. The particles start from the primary collimator. All other collimators are treated as perfect absorbers.

The STIER simulations have demonstrated that the accuracy of the cleaning simulations can be significantly improved if changes in transverse angle and in energy from the fragmentation process are included. In spite of not treating fragmentation in subsequent collimators, the STIER simulations are in good agreement with the measured data. It was therefore used to validate the collimation system in the 2015 LHC heavy-ion run at 6.37 Z TeV. In this operational period, high losses at the tertiary collimator close to the ALICE experiment occurred. STIER was employed to study the origin of these losses, showing that they are dominated by the isotope $^{207}\mathrm{Pb}^{82+}$ scattered out of the left jaw of the primary collimator. Based on this outcome, strategies for loss mitigation were worked out. They were later-on experimentally tested in the LHC. In these experiments, the LHC behaved as predicted by STIER and the loss reduction anticipated by the simulation could be quantitatively confirmed.

The experience obtained with STIER was used to implement heavy-ion SixTrack (hiSixTrack), a generic tracking tool supporting arbitrary ion types. The software is based on the standard version of SixTrack, but is extended to store information about the species of the tracked particle. In order to accurately simulate the magnetic bending for particles with different masses and charges, symplectic tracking maps were derived from a new accelerator Hamiltonian that is adapted for the treatment of isotopes different from the reference species. The new multi-isotopic tracking maps are implemented in hiSixTrack and have been studied to verify their symplecticity.

The particle tracks simulated with hiSixTrack have been benchmarked against STIER. With hiSixTrack, a new tracking tool became available that allows the symplectic tracking of arbitrary heavy-ion species with their physical momentum, mass and charge.

To allow simulating the fragmentation at the LHC collimators, hiSixTrack was coupled with FLUKA. The basis for this development was the SixTrack-FLUKA coupling, which was already implemented to actively exchange protons between both codes. The framework was adapted to exchange heavy ions between hiSixTrack and FLUKA. Today, the hiSixTrack-FLUKA coupling is the standard simulation software for heavy-ion collimation used at CERN. The cleaning simulations with the hiSixTrack-FLUKA coupling show an even better agreement with the measured data than STIER, mainly due to the inclusion of fragmentation at all collimators.

The hiSixTrack-FLUKA coupling was applied to study the cleaning performance in the future High Luminosity LHC (HL-LHC). Keeping the cleaning inefficiency at a low and tractable value is particularly important for this scenario, because the stored beam energies are going to be significantly increased. The simulations were also carried out with additional collimators (TCLD) in the dispersion suppressor of the betatron collimation region IR7, which are envisaged to be installed for HL-LHC. The analysis shows that the cleaning performance can be improved if the new TCLD collimators were installed in the LHC. With one TCLD collimator per beam, the cleaning inefficiency can be reduced by approximately 45%, if the collimator is set to a sufficiently small half gap. With two TCLD collimators per beam, the quench risk from particles scattered out of the collimators can be reduced by more than two orders of magnitude.

The cleaning performance was also simulated with other heavy-ion species than $^{208}\mathrm{Pb}^{82+}$. The study showed that the cleaning efficiency for $^{129}\mathrm{Xe}^{54+}$ and $^{40}\mathrm{Ar}^{18+}$, which are presently the most probable candidates for operation, is similar to what can be expected with $^{208}\mathrm{Pb}^{82+}$.

As a part of this thesis, a dedicated heavy-ion collimation quench test was designed and conducted in the LHC, to quantify the quench risk from collimation losses. In this experiment, carried out with $^{208}\mathrm{Pb}^{82+}$ beams at $6.37\,Z\,\mathrm{TeV}$ in late 2015, high steady state particle losses were induced at the primary collimator. The aim of the experiment was to quantify at which power load on the collimator the generated heavy-ion fragments would induce a quench of the superconducting LHC magnets. A magnet quench was achieved with a beam loss rate of (15 ± 1) kW. Assuming a minimum beam lifetime of 12 min (which is the design specification), an approximate estimate for the maximum stored beam energy at $6.37\,Z\,\mathrm{TeV}$ can be derived, which yields (10.8 ± 0.8) MJ.

The experimentally accessed quench limit was combined with the hiSixTrack-FLUKA coupling simulations to derive limitations in terms of stored beam energy also for future operation. Taking

into account that the quench limit at 7.0 Z TeV is lower than at 6.37 Z TeV, the analysis showed that the target stored beam energy, and hence luminosity for HL-LHC cannot be reached without TCLD collimators, if a minimum beam lifetime of 12 min is assumed. With one TCLD collimator per beam, the HL-LHC target can be only reached if the minimum beam lifetime was larger than 38 min. With two TCLD collimators per beam, the cleaning performance is improved significantly, such that the stored beam energy is not limited by the quench risk from collimation losses any more. The analysis further showed that the target luminosity can almost be reached also without TCLD collimators if the LHC were to be operated with $^{40}Ar^{18+}$ ions. The main reason for this improvement is the significantly larger bunch intensity compared to what is achievable with $^{208}Pb^{82+}$ beams.

In a brief outlook, remaining discrepancies between simulated and measured loss maps were studied, which can be used for future improvements of the simulation tools.

In summary, this thesis has introduced STIER and the hiSixTrack-FLUKA coupling as new simulation tools for heavy-ion collimation. They have been benchmarked against measured data, were used to make accurate predictions about the machine behavior, delivered input for the analysis of experimental data from the LHC and were used to define the required collimation system upgrades for HL-LHC.

At the time of writing, the hiSixTrack-FLUKA coupling is the most sophisticated tool to simulate heavy-ion collimation. It is going to be used for future heavy-ion collimation simulations and might be indispensable to understand and avoid potential limitations from beam losses, which need to be overcome to exploit the full potential of the LHC in heavy-ion operation.

Zusammenfassung

Mit dem CERN Large Hadron Collider (LHC) wurden Teilchenstrahlen von vorher unerreichter Energie für die Grundlagenforschung zugänglich. Neben dem Forschungsprogramm mit Protonenstrahlen wird der LHC mit Schwerionenstrahlen betrieben, womit er der dritte Speicherring weltweit ist, der Colliding-Beam-Experimente mit Schwerionen ermöglicht. Die große Strahlenergie, die im LHC gespeichert wird stellt ein Risiko für den Beschleuniger dar, da selbst kleinste Mengen dieser Energie ausreichen können, um einen Übergang der supraleitenden Magnete in den normalleitenden Zustand zu induzieren (Quench), oder sogar den Beschleuniger zu beschädigen. Aus diesem Grund ist der LHC mit einem mehrstufigen Kollimationssystem ausgestattet, das den Beschleuniger vor unerwünschten Strahlverlusten schützen soll. Trotzdem können Teilchen mit abweichenden magnetischen Rigidtäten aus den Kollimatoren gestreut werden und anschließend in den supraleitenden Magneten verloren gehen. Die Ineffizienz des Kollimationssystems wird definiert als die in supraleitenden Magneten verlorene Strahlenergie im Verhältnis zur Strahlenergie, die in den Kollimatoren verloren geht. Der größte Teil der Ineffizienz des Kollimationssystems stammt von Teilchen mit abweichender Rigidität.

In dieser Dissertation wird eine Software zur Simulation der Kollimationseffizienz mit Schwerionenstrahlen vorgestellt. Im Vergleich zur Kollimation von Protonen ist die Effizienz des Kollimationssystems mit Schwerionenstrahlen um zwei Größenordnungen reduziert. Die Ursache dafür ist die große Menge an Fragmenten mit anderen Massen und Ladungen, die entsteht wenn Schwerionen mit dem Kollimatormaterial wechselwirken. Wenn die Fragmente die supraleitenden LHC Magnete erreichen, werden sie in die Magnetapertur gelenkt und gehen dort verloren. Um einen sicheren und ununterbrochenen Betrieb des Beschleunigers zu gewährleisten werden anspruchsvolle Simulationen benötigt, die die Effizienz des Kollimationssystems simulieren können. Diese Simulationen erlauben es Strahlverluste, die möglicherweise gefährlich sein könnten, zu verstehen und Strategien zu entwickeln um sie zu reduzieren. Simulationen der Effizienz des Kollimationssystems simulieren die Wechselwirkung der Strahlteilchen mit den Kollimatoren und berechnen die Trajektorie der aus den Kollimatoren gestreuten Teilchen durch die Magnete des Beschleunigers.

Eine Software für die Simulation von Schwerionenkollimation muss deshalb Wechselwirkungen über die elektromagnetische und die starke Kraft mit dem Kollimatormaterial simulieren und die Trajektorie einer Vielzahl verschiedener Fragmente in den Magneten des LHC berechnen. ICOSIM, die bisherige Referenz für diese Art von Simulationen, berechnet die Fragmentierung in den Kollimationen in einem vereinfachten Modell. Insbesondere Streuung und der Transfer von Energie auf den erzeugten Atomkern wurden nicht berücksichtigt. Wichtige Strukturen in der gemessenen Verteilung der Fragmente im LHC wurden von ICOSIM nicht vorausgesagt.

Um zu verstehen ob die Ursache für die beobachteten Diskrepanzen in dem vereinfachten Modell zur Simulation der Fragmentierung zu suchen ist, wurde eine neue Software entwickelt, die die Bezeichnung SixTrack with Ion-Equivalent Rigidities (STIER) trägt. STIER zeichnet sich insbesondere durch ein realistischeres Modell zur Simulation der Fragmentierung aus, das bei der ersten Wechselwirkung mit einem Kollimator genutzt wird. STIER basiert auf der Software FLUKA zur Simulation der Wechselwirkung von Teilchen mit Materie, sowie auf SixTrack, einer Software für Teilchentransport in den Magneten eines Beschleunigers. In STIER wird die Wechselwirkung der Teilchenstrahlen mit dem primären Kollimator (der der größten Menge einfallender Teilchen ausgesetzt ist) mit FLUKA simuliert. Anschließend wird die Trajektorie der aus dem Kollimator gestreuten Teilchen mit SixTrack berechnet, wobei die Schwerionentrajektorien als Protonentrajektorien berechnen werden und den Protonen eine Rigidität zugewiesen wird, die jener des Schwerions entspricht. Im Gegensatz zu ICOSIM werden die Streuwinkel und die korrekten Teilchenenergien berücksichtigt. Alle anderen Kollimatoren werden in STIER als perfekte Absorber betrachtet.

Die Simulationen mit STIER haben aufgezeigt, dass die Übereinstimmung mit der gemessenen Verteilung von Strahlverlusten verbessert wird, wenn Änderungen des transversalen Winkels und der Energie berücksichtigt werden. Obwohl die Interaktionen mit allen weiteren Kollimatoren nicht simuliert werden, zeigen die Simulationen mit STIER eine gute Übereinstimmung mit den gemessenen Verteilungen von Kollimationsverlusten. Aufgrund dessen wurde STIER im Jahre 2015 genutzt um das Kollimationssystem für den Betrieb mit $^{208}\mathrm{Pb}^{82+}$ Schwerionen bei $6.37\,Z$ TeV zu validieren. Während des Betriebes wurden große Strahlverluste am tertiären Kollimator nahe des ALICE Experimentes gemessen. Mittels STIER wurde aufgezeigt, dass der dominierende Anteil an diesen Verlusten durch $^{207}\mathrm{Pb}^{82+}$ verursacht wird, das auf der linken Seite des primären Kollimators erzeugt wird. Diese Erkenntnisse wurden genutzt um Strategien zur Verringerung dieser Verluste zu entwickeln, die später im LHC experimentell getestet wurden. Die Experimente bestätigen die von STIER getroffenen Voraussagen.

Um die Übereinstimmung mit den gemessenen Daten weiter zu verbessern, wurde als Nachfolger von STIER die neue Software heavy-ion SixTrack (hiSixTrack) entwickelt. Diese ermöglicht die Berechnung der Trajektorie von beliebigen Schwerionen. Die Software hiSixTrack ist eine Erweiterung von SixTrack, die zusätzlich Informationen über Masse und Ladung der Teilchen speichert. Um die magnetische Ablenkung von Teilchen mit unterschiedlichen Massen und Ladungen akkurat zu berechnen wurden symplektische Transformationsregeln von einer verallgemeinerten Hamilton-Funktion abgeleitet. Diese ist geeignet die Dynamik von Teilchen mit Masse und Ladung zu berechnen, die nicht notwendigerweise mit jenen des Referenzteilchens übereinstimmen müssen. Die neuen generalisierten Transformationsregeln wurden in hiSixTrack implementiert, nachdem ihre Symplektizität sichergestellt wurde. Die mit hiSixTrack berechneten Trajektorien wurden mit von STIER simulierten Trajektorien verglichen um die Fehlerfreiheit der Implementierung zu gewährleisten. Mit hiSixTrack steht nun eine neue Software zur Verfügung, die zur symplektischen Berechnung von Trajektorien beliebiger Teilchenarten verwendet werden kann.

Um die Wechswelwirkung der Schwerionen mit den Kollimatoren zu simulieren wurde hiSixTrack mit FLUKA gekoppelt. Als Grundlage für diese Entwicklung diente das SixTrack-FLUKA coupling, das bereits implementiert war um Protonen zwischen SixTrack und FLUKA auszutauschen. Die zugrundeliegende Software wurde angepasst um den Austausch von Schwerionen zwischen hiSixTrack und FLUKA zu ermöglichen. Heute ist das hiSixTrack-FLUKA coupling die Standardsoftware zur Simulation von Schwerionenkollimation am CERN. Dank der Berücksichtigung von Fragmentierungsprozessen an allen Kollimatoren zeigt das hiSixTrack-FLUKA coupling eine noch bessere Übereinstimmung mit den gemessenen Daten als STIER.

Das hiSixTrack-FLUKA coupling wurde genutzt um die Effizienz des Kollimationssystems im High Luminosity LHC (HL-LHC) zu simulieren. Aufgrund der, im Vergleich zum LHC, stark vergrößerten gespeicherten Strahlenergie in HL-LHC ist es für letzteren besonders wichtig die Strahlverluste zu minimieren und kontrollieren. Die Effizienz des Kollimationssystems wurde außerdem mit zusätzlichen Kollimatoren des Typs TCLD simuliert, deren Installation für HL-LHC vorgesehen ist. Die Simulationen zeigen, dass mit der Installation eines TCLD Kollimators pro Strahl das Risiko eines strahlinduzierten Quenches um etwa 45% reduziert werden kann. Mit zwei TCLD Kollimatoren pro Strahl kann das Risiko eines Quenches sogar um zwei Größenordnungen reduziert werden.

Die Kollimationseffizienz wurde auch mit anderen Nukliden als $^{208}Pb^{82+}$ untersucht. Die Simulationen wurden mit $^{129}Xe^{54+}$ und $^{40}Ar^{18+}$ durchgeführt und zeigen, dass die erwarteten Strahlverluste zu jenen bei Betrieb mit $^{208}Pb^{82+}$ vergleichbar sind.

Im Rahmen dieser Dissertation wurde weiterhin ein Experiment zur Quantifizierung des Risikos eines strahlinduzierten Quenches durch Kollimationsverluste konzipiert und durchgeführt.

In diesem Experiment wurden hohe Strahlverluste eines $^{208}Pb^{82+}$ Strahls bei einer Energie von $6.37\,Z$ TeV am primären Kollimator erzeugt. So konnte eine Verlustrate am primären Kollimator identifiziert werden, bei der die Schwerionenfragmente einen Quench der supraleitenden Magnete induzieren. Dies geschah bei einer Verlustrate von (15 ± 1) kW. Auf dieser Grundlage kann die maximale gespeicherte Strahlenergie bei $6.37\,Z$ TeV abgeschätzt werden. Unter Berücksichtigung der minimalen Strahllebenszeit von 12 min (für die das Kollimationssystem konzipiert ist) ergibt sich für $^{208}Pb^{82+}$ Strahlen mit einer Teilchenenergie von $6.37\,Z$ TeV eine Limitierung der gespeicherten Strahlenergie auf (10.8 ± 0.8) MJ.

Die gewonnenen Daten wurden anschließend mit Simulationsergebnissen des hiSixTrack-FLUKA coupling kombiniert um die maximale Strahlenergie für den zukünftigen Betrieb des LHC abzuschätzen. Unter Berücksichtigung der Reduzierung der nötigen Verlustrate zur Induzierung eines Quenches von $6.37\,Z$ TeV zu $7.0\,Z$ TeV wurde gezeigt, dass die vorgesehene gespeicherte Strahlenergie und damit Luminosität ohne TCLD Kollimatoren nicht erreicht werden kann. Dies gilt, wenn eine minimale Strahllebensdauer von 12 min angenommen wird. Mit einem TCLD Kollimator pro Strahl können die Zielparameter für HL-LHC nur erreicht werden, wenn die minimale Strahllebenszeit größer als 38 min ist. Mit zwei TCLD Kollimatoren kann die Verlustrate so stark reduziert werden, dass die maximale gepeicherte Strahlenergie nicht mehr durch das Risiko eines strahlinduzierten Quenches limitiert wird. Weiterhin wurde festgestellt, dass die beabsichtigte Luminosität fast auch ohne TCLD Kollimatoren erreicht werden kann, wenn der LHC mit $^{40}Ar^{18+}$ betrieben würde. Der Hauptgrund dafür ist die im Vergleich zu $^{208}Pb^{82+}$ größere Bunchintensität, die mit diesen Schwerionen erreicht werden kann.

Abschließend wurden die verbleibenden Diskrepanzen zwischen Simulation und Messung diskutiert. Die gewonne Erkenntnisse können möglicherweise in Zukunft genutzt werden um die Übereinstimmung mit den gemessenen Strahlverlusten weiter zu verbessern.

Zusammenfassend wurden in dieser Arbeit STIER und das hiSixTrack-FLUKA coupling als neue Software zur Simulation der Effizienz von Schwerionenkollimation vorgestellt. STIER und das hiSixTrack-FLUKA coupling wurden mit gemessenen Daten verglichen, wurden genutzt um physikalische Prozesse im LHC vorherzusagen und lieferten substanzielle Erkenntnisse über die benötigten Erweiterungen des Kollimationssystems für HL-LHC.

Heute ist das hiSixTrack-FLUKA coupling die Software zur Simulation von Schwerionenkollimation mit der besten Übereinstimmung zum Experiment. Zukünftige Simulationen mit dem hiSixTrack-FLUKA coupling könnten unverzichtbar sein um potentielle Limitationen durch Strahlverluste zu überwinden. Damit könnte das hiSixTrack-FLUKA coupling dazu beitragen das volle Potential des LHC im Schwerionenbetrieb auszuschöpfen.

Appendix A.

A.1 Tracking Map Symplecticity

The symplecticity can be probed with the Jacobian of the tracking map. It can be shown [RS95] that a tracking map is symplectic if its Jacobian matrix $\mathcal{J}$ fulfills the symplectic condition:

$$\mathcal{J}^T S \mathcal{J} = S \,. \tag{A.1}$$

The Jacobian matrix is related to the initial coordinates and the final coordinates as follows:

$$\mathcal{J} = \frac{\partial(x^F, p_x^F, y^F, p_y^F, \sigma^F, p_\sigma^F)}{\partial(x^I, p_x^I, y^I, p_y^I, \sigma^I, p_\sigma^I)} = \begin{pmatrix} \frac{\partial x^F}{\partial x^I} & \frac{\partial x^F}{\partial p_x^I} & \frac{\partial x^F}{\partial y^I} & \frac{\partial x^F}{\partial p_y^I} & \frac{\partial x^F}{\partial \sigma^I} & \frac{\partial x^F}{\partial p_\sigma^I} \\ \frac{\partial p_x^F}{\partial x^I} & \frac{\partial p_x^F}{\partial p_x^I} & \frac{\partial p_x^F}{\partial y^I} & \frac{\partial p_x^F}{\partial p_y^I} & \frac{\partial p_x^F}{\partial \sigma^I} & \frac{\partial p_x^F}{\partial p_\sigma^I} \\ \frac{\partial y^F}{\partial x^I} & \frac{\partial y^F}{\partial p_x^I} & \frac{\partial y^F}{\partial y^I} & \frac{\partial y^F}{\partial p_y^I} & \frac{\partial y^F}{\partial \sigma^I} & \frac{\partial y^F}{\partial p_\sigma^I} \\ \frac{\partial p_y^F}{\partial x^I} & \frac{\partial p_y^F}{\partial p_x^I} & \frac{\partial p_y^F}{\partial y^I} & \frac{\partial p_y^F}{\partial p_y^I} & \frac{\partial p_y^F}{\partial \sigma^I} & \frac{\partial p_y^F}{\partial p_\sigma^I} \\ \frac{\partial \sigma^F}{\partial x^I} & \frac{\partial \sigma^F}{\partial p_x^I} & \frac{\partial \sigma^F}{\partial y^I} & \frac{\partial \sigma^F}{\partial p_y^I} & \frac{\partial \sigma^F}{\partial \sigma^I} & \frac{\partial \sigma^F}{\partial p_\sigma^I} \\ \frac{\partial p_\sigma^F}{\partial x^I} & \frac{\partial p_\sigma^F}{\partial p_x^I} & \frac{\partial p_\sigma^F}{\partial y^I} & \frac{\partial p_\sigma^F}{\partial p_y^I} & \frac{\partial p_\sigma^F}{\partial \sigma^I} & \frac{\partial p_\sigma^F}{\partial p_\sigma^I} \end{pmatrix} . \tag{A.2}$$

A.1.1 Thick Dipole

For simplicity and due to the lack of relevance for hiSixTrack, the symplecticity of the thick dipole is here only discussed in two dimensions. Following the tracking map shown in the Eqs. (7.65) to (7.68), the two-dimensional Jacobian matrix yields:

$$\mathcal{J} = \begin{pmatrix} C_x & \frac{S_x}{(1+\delta)\omega_x} & 0 & 0 \\ -S_x(1+\delta)\omega_x & C_x & 0 & 0 \\ 0 & 0 & 1 & \frac{L}{1+\delta} \\ 0 & 0 & 0 & 1 \end{pmatrix} . \tag{A.3}$$

The symplectic condition $\mathcal{J}^T \mathbf{S} \mathcal{J} = \mathbf{S}$ is fulfilled.

A.1.2 Thin Dipole

From the tracking map for the thin dipole, presented in Chap. 7.3.2, the following Jacobian can be derived:

$$\mathcal{J} = \begin{pmatrix} 1 & 0 & 0 & 0 & 0 & 0 \\ -L\,k_0\,\chi\,h_x & 1 & 0 & 0 & 0 & \frac{\beta_0}{\beta}\,L\,h_x \\ 0 & 0 & 1 & 0 & 0 & 0 \\ 0 & 0 & 0 & 1 & 0 & 0 \\ -\frac{\beta_0}{\beta}\,L\,h_x & 0 & 0 & 0 & 1 & -h_x\,x\,L\,\frac{\mathrm{d}}{\mathrm{d}p_\sigma}\frac{\beta_0}{\beta} \\ 0 & 0 & 0 & 0 & 0 & 1 \end{pmatrix} \tag{A.4}$$

This Jacobian fulfills the symplectic condition.

A.1.3 Thick Quadrupole

The Jacobian matrix of the thick quadrupole in four dimensions is given by:

$$\mathcal{J} = \begin{pmatrix} \cos(\omega_x L) & \frac{\sin(\omega_x L)}{(1+\delta)\omega_x} & 0 & 0 \\ -(1+\delta)\omega_x \sin(\omega_x L) & \cos(\omega_x L) & 0 & 0 \\ 0 & 0 & \cosh(\omega_x L) & \frac{\sinh(\omega_x L)}{(1+\delta)\omega_x} \\ 0 & 0 & (1+\delta)\omega_x \sinh(\omega_x L) & \cosh(\omega_x L) \end{pmatrix}. \tag{A.5}$$

The symplectic condition is fulfilled.

A.1.4 Thin Quadrupole

From the tracking map for the thin quadrupole, the following Jacobian can be derived:

$$\mathcal{J} = \begin{pmatrix} 1 & 0 & 0 & 0 & 0 & 0 \\ -K\,L & 1 & 0 & 0 & 0 & 0 \\ 0 & 0 & 1 & 0 & 0 & 0 \\ 0 & 0 & K\,L & 1 & 0 & 0 \\ 0 & 0 & 0 & 0 & 1 & 0 \\ 0 & 0 & 0 & 0 & 0 & 1 \end{pmatrix} . \tag{A.6}$$

This Jacobian fulfills the symplectic condition.

A.1.5 Accelerating RF Cavity

The Jacobian for the accelerating RF cavity yields:

$$\mathcal{J} = \begin{pmatrix} 1 & 0 & 0 & 0 & 0 & 0 \\ 0 & 1 & 0 & 0 & 0 & 0 \\ 0 & 0 & 1 & 0 & 0 & 0 \\ 0 & 0 & 0 & 1 & 0 & 0 \\ 0 & 0 & 0 & 0 & 1 & 0 \\ 0 & 0 & 0 & 0 & Q & 1 \end{pmatrix} , \tag{A.7}$$

with

$$Q = \chi\, q_0\, \frac{1}{\beta_0^2}\, \frac{U}{E_0}\, L\, \frac{2\pi\, h}{C}\, \cos\left(\frac{2\pi\, h}{C}\, \sigma + \phi\right) . \tag{A.8}$$

This Jacobian fulfills the symplectic condition.

A.2 IR2 Loss Mitigation Experiment - Loss Maps

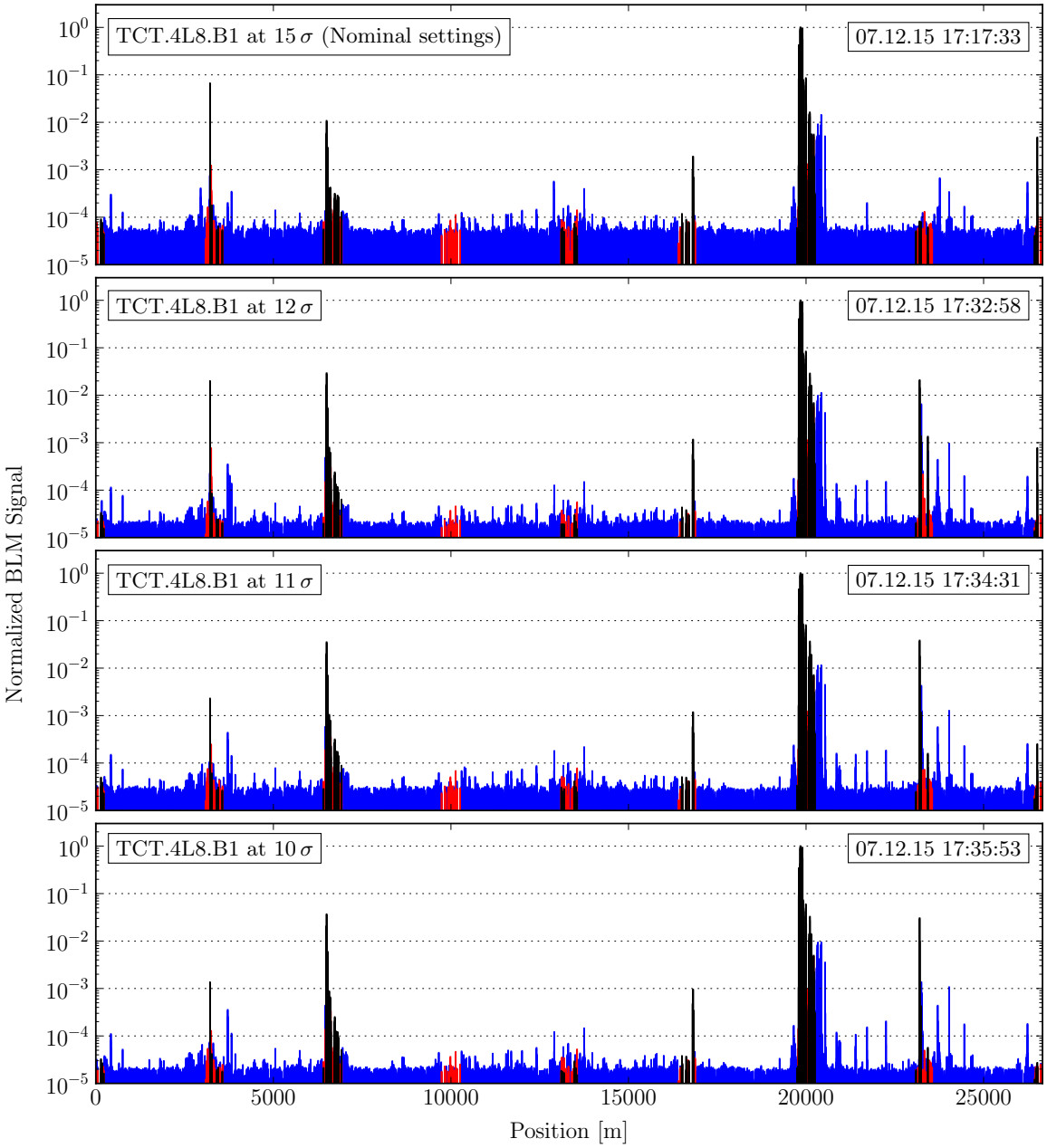

Figure A.1: Loss maps measured in the 2015 heavy-ion run with different settings of the TCTH.4L8.B1. Each loss map was measured the 07.12.2015

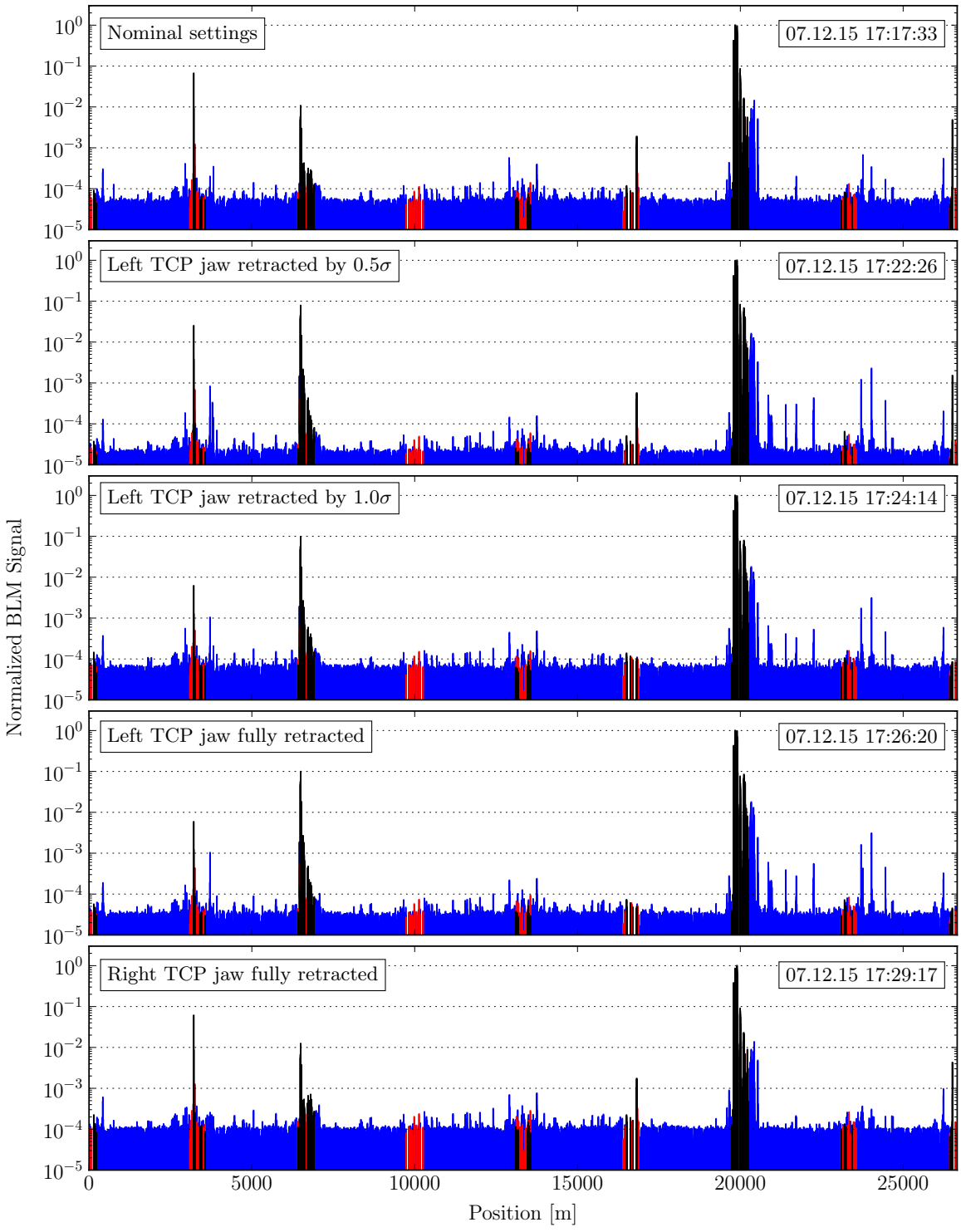

Figure A.2: Loss maps measured in the 2015 heavy-ion run with different TCP configurations. Each loss map was measured the 07.12.2015 at the times indicated at top right of each plot.

A.3 Loss Maps Simulated with the hiSixTrack-FLUKA Coupling

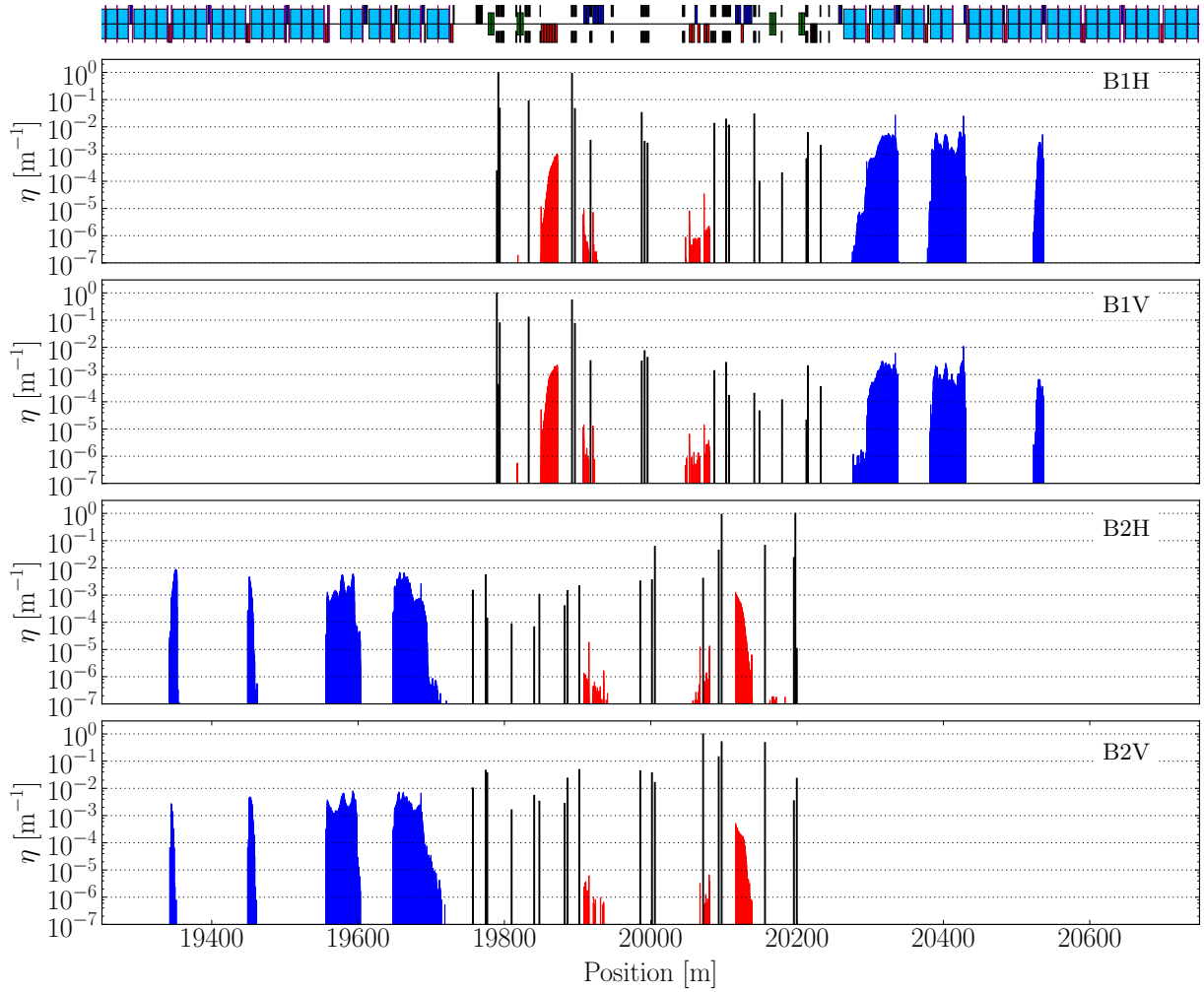

Figure A.3: Cleaning inefficiency simulated in the HL-LHC configuration at 7 Z TeV with $^{208}\mathrm{Pb}^{82+}$ beams for the different beams and planes.

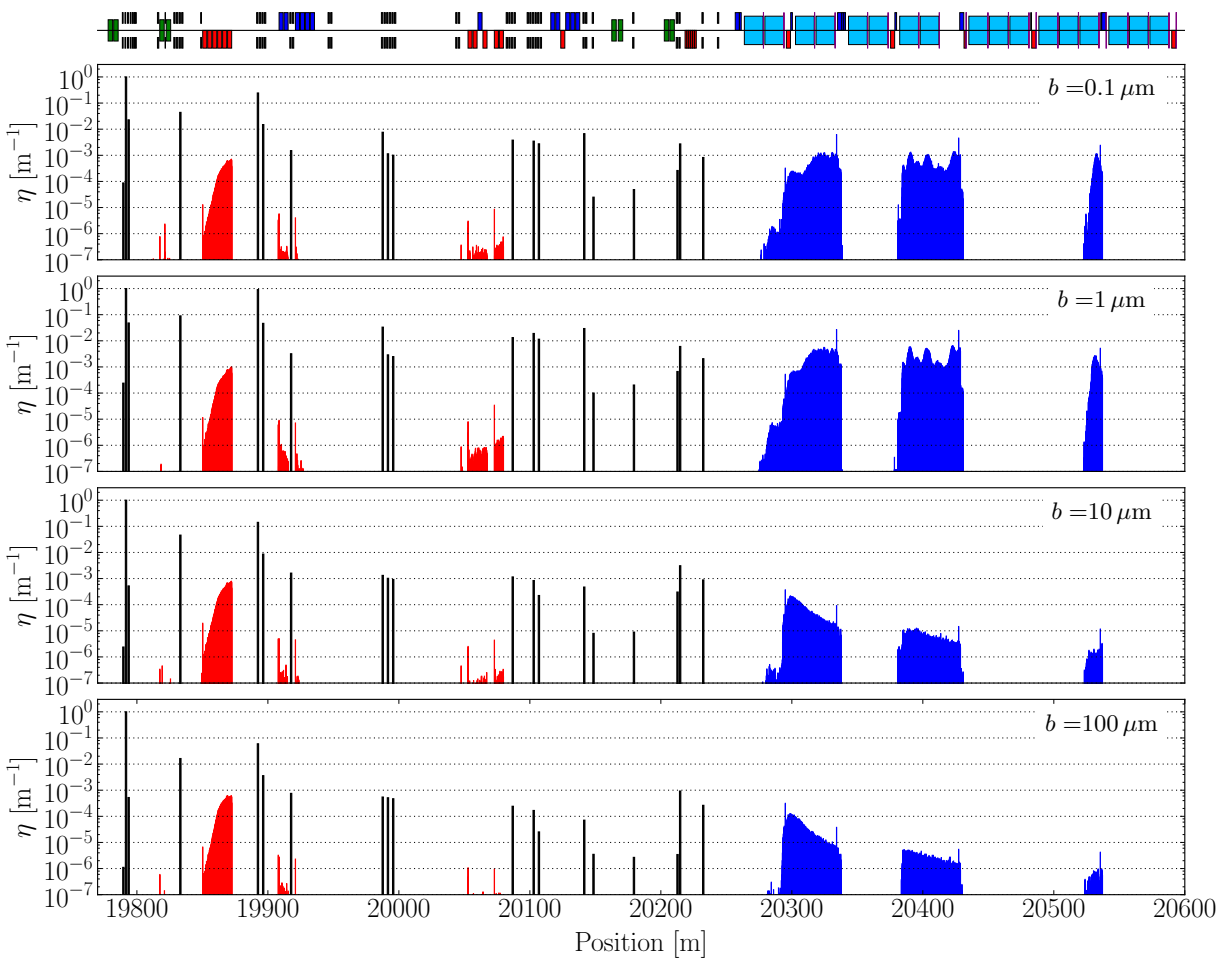

Figure A.4: Comparison of the cleaning inefficiency simulated with the hiSixTrack-FLUKA coupling for four different impact parameters $b = 0.1\mu$m, $1.0\,\mu$m, $10.0\,\mu$m, $100.0\,\mu$m.

A.4 Accelerator Hamiltonian in a Curved Coordinate System

In dipole magnets, the trajectory of the reference particle is curved. The motion of the particles in a dipole magnet is then most elegantly described in a curvilinear coordinate system. For the case of a purely horizontal and uniform bending magnet, the reference trajectory can be described by a bending radius ρ_0, as illustrated in Fig. A.5. Based on the geometry, the coordinates in the straight (x, y, z) and in the curved coordinate system (X, Y, S) can be related to each other. With a third order generating function, the momentum coordinates in the curved coordinate system and the new magnetic potentials can be calculated. The derivation presented in the following is based on [Wol14]. From the geometry shown in Fig. A.5, the new and old coordinates are related to each other by the simple equations:

$$\begin{aligned} x &= (\rho_0 + X)\,\cos\left(\frac{S}{\rho_0}\right) - \rho_0\,, \\ y &= Y, \\ z &= (\rho_0 + X)\,\sin\left(\frac{S}{\rho_0}\right)\,. \end{aligned} \tag{A.9}$$

One can construct a generating function of third order to calculate the particle momenta in the new coordinate system:

$$F_3(X, p_x, Y, p_y, S, p_z) = -\left[(\rho_0 + X)\,\cos\left(\frac{S}{\rho_0}\right) - \rho_0\right] p_x - Y\,p_y - \left[(\rho_0 + X)\,\sin\left(\frac{S}{\rho_0}\right)\right] p_z\,. \tag{A.10}$$

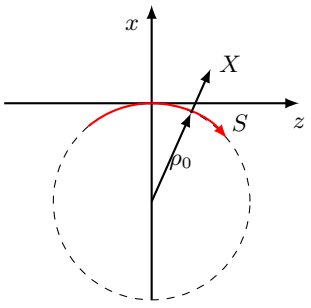

Figure A.5: Transformation of the straight coordinate system (x, y, z) into the curvilinear system (X, Y, S). Based on [Wol14].

The old and the new coordinates are then related by

$$x_i = -\frac{\partial F_3}{\partial p_i} \qquad P_i = -\frac{\partial F_3}{\partial X_i}\,. \tag{A.11}$$

The new momentum coordinates are given by

$$\begin{aligned} P_X &= p_x\,\cos\left(\frac{S}{\rho_0}\right) + p_z \sin\left(\frac{S}{\rho_0}\right)\,, \\ P_Y &= p_y\,, \\ P_S &= p_z\,\left(1+\frac{X}{\rho_0}\right)\cos\left(\frac{S}{\rho_0}\right) - p_x\,\left(1+\frac{X}{\rho_0}\right)\sin\left(\frac{S}{\rho_0}\right)\,. \end{aligned} \tag{A.12}$$

The vector potential is defined by

$$\begin{aligned} A_X &= A_x\,\cos\left(\frac{S}{\rho_0}\right) - A_z\,\sin\left(\frac{S}{\rho_0}\right)\,, \\ A_Y &= A_y\,, \\ A_S &= A_z\,\cos\left(\frac{S}{\rho_0}\right) + A_x\,\sin\left(\frac{S}{\rho_0}\right)\,, \end{aligned} \tag{A.13}$$

A.5 Implementation of hiSixTrack

The SixTrack source is saved altogether in the three files `sixtrack.s`, `lielib.s` and `dabnew.s`. To build the SixTrack executable, a compilation file `make_six` is executed with dedicated flags that activate given functionalities. Examples for such flags are the `collimat` flag to compile the collimation version of SixTrack. An excellent overview of the compilation of SixTrack is given in [F+13]. Specific functions of the SixTrack-FLUKA coupling are stored in an external module saved as `mod_fluka.f90`.

A.5.1 Variables in hiSixTrack

SixTrack tracks a variety of different arrays, to store information of the tracked particle bunch. Besides the obvious arrays `xv(i,j),yv(i,j),sigmv(j),dpsv(j)` containing information about the six-dimensional particle coordinates, other arrays store information about the particle energy and momentum as well as auxiliary quantities derived from them. In the process of tracking,

Table A.1: Variables in SixTrack [DM+16]. The variable `j` describes the particle index.

Variable	Description	Symbol	Unit	Definition
`napx`	number of tracked particles			
`npart`	maximum number of tracked particles			
	Reference particle properties			
`e0`	Energy of the reference particle	E_0	MeV	
`e0f`	Momentum of the reference particle	P_0	MeV/c^2	
`pma`	Proton rest mass	m_p	MeV/c^2	
	Particle arrays			
`xv(1,j)`	Horizontal coordinate	x	mm	Eq. (2.1)
`xv(2,j)`	Vertical coordinate	x	mm	Eq. (2.1)
`yv(1,j)`	Horizontal slope	x'	mrad	
`yv(2,j)`	Vertical slope	y'	mrad	
`sigmv(j)`	Path length difference	σ	mm	Eq. (7.27)
`dpsv(j)`	Relative momentum offset	δ	-	Eq. (2.15)
`oidpsv(j)`	Relative momentum offset	$\frac{1}{1+\delta}$	-	
`ejfv(j)`	Particle momentum	P	MeV/c	
`ejv(j)`	Particle energy	E	MeV	

the latter are re-initialized every time the particle momentum (and in hiSixTrack the particle species) may have changed, which is true for the collimators and accelerating elements. An overview of the most relevant particle arrays is given in Table A.1.

Some of these variables are redefined in hiSixTrack in order to be compatible with the generic multi-isotopic definitions introduced in Chap. 2.1.2. This includes the relative offset of the momentum per mass unit δ which is implemented in the SixTrack as the relative momentum offset. Furthermore, new variables are introduced to keep track of the particle species and to facilitate the implementation of the heavy-ion tracking maps. These variables are summarized in Table A.2. For the identification of the tracked particles, the mass number A, the charge multiplicity Z and rest mass m are stored in arrays. The latter is not important for the identification of the particle, but it is used to calculate χ. The information about the reference species A_0, Z_0, m_0 is read from `fort.3` with a newly introduced block `HION`, described in the next subsection.

The implementation of δ in both SixTrack and hiSixTrack is shown in List. A.1. The quantity $\frac{\delta}{1+\delta}$ follows the redefinition of δ.

Table A.2: Variables introduced or modified in hiSixTrack. The variable `j` describes the particle index.

Variable	Description	Symbol	Unit	Definition
	Reference particle properties			
`zz0`	Charge multiplicity of the reference ion species	Z_0	-	
`aa0`	Nucleon number of the reference ion species	A_0	-	
`nucm0`	Rest mass of the reference ion species	m_0	GeV/c^2	
	Particle arrays			
`nzz(j)`	Charge multiplicity of the tracked ion	Z	-	
`naa(j)`	Nucleon number of the tracked ion	A	-	
`nucm(j)`	Rest mass of the tracked ion	m	GeV/c^2	
`mtc(j)`	Relative mass to charge ratio	χ	-	Eq. (2.11)
`dpsv(j)`	Relative **momentum per mass** offset	δ	-	Eq. (2.10)
`moidpsv(j)`	Relative rigidity offset	$\frac{\chi}{1+\delta}$	-	Eq. (2.12)

```
!         dpsv  (j)   = (ejfv(j)-e0f)/e0f                    ! SixTrack
          dpsv  (j)   = (ejfv(j)*(nucm0/nucm(j))-e0f)/e0f    ! hiSixTrack
          oidpsv(j)   = one/(one+dpsv(j))
```

Listing A.1: Definition of δ in SixTrack and hiSixTrack.

The quantity `mtc(j)` represents the relative mass to charge ratio χ. Its definition in the SixTrack source is shown in List. A.2.

```
        mtc     (j) = (nzz(j)*nucm0)/(zz0*nucm(j))
```

Listing A.2: Definition of χ in hiSixTrack.

Note that instead of using the particle charge q, hiSixTrack uses the nuclear charge multiplicity Z, assuming that all electrons are removed from the tracked particle and the reference particle. If non-fully stripped ions should be tracked with hiSixTrack, the source has to be extended for an additional array storing the effective ion charge. The variable `moipdsv(j)` describes the auxiliary quantity $\frac{\chi}{1+\delta}$ representing the relative offset in magnetic rigidity.

While in SixTrack the particle mass is hard coded as a constant parameter `pma` that is applied for all particles, hiSixTrack requires a new implementation of mass-dependent equations in which the particle mass is a variable. Depending on the context, `pma` refers to the mass of the reference particle or of the tracked particle and is replaced in hiSixTrack by `nucm0` or `nucm(j)` accordingly. In List. A.3, the Einstein energy-momentum relation is shown as it is implemented in SixTrack and hiSixTrack for both the reference particle and for a tracked particle.

```
!         MOMENTUM OF THE REFERENCE PARTICLE
!         e0f=sqrt(e0**2-pma**2)              ! SixTrack
          e0f=sqrt(e0**2-nucm0**2)            ! hiSixTrack
!
!         ENERGY OF THE TRACKED ION j
!         ejv(j)=sqrt(ejfv(j)**2+pma**2)      ! SixTrack
          ejv(j)=sqrt(ejfv(j)**2+nucm(j)**2)  ! hiSixTrack
```

Listing A.3: Definition of the reference momentum P_0 and the energy E of the tracked ion in SixTrack and hiSixTrack.

A.5.2 Initialization of hiSixTrack

hiSixTrack is activated by calling the new `HION` block in the fort.3 file. This block acquires information on the reference particle species (A_0, Z_0, m_0). The code defining the HION block in the hiSixTrack source code is shown in List. A.4. An example input block to call hiSixTrack

for different heavy-ion reference species is given in List. A.5.

```
!     P. HERMES 01-07-2015
!     HEAVY ION BLOCK
 2400 read(3,10020,end=1530,iostat=ierro) ch
      if(ierro.gt.0) call prror(58)
      if(ch(1:1).eq.'/') goto 2400
      if(ch(:4).eq.next) goto 110
      ch1(:nchars+3)=ch(:nchars)//' / '
      read(ch1,*) aa0, zz0, nucm0
      nucm0 = nucm0  * 1.0D+03 !  [GeV/c^2] -> [MeV/c^2] ! hiSixTrack
      write(*,*) 'Heavy-ion reference species:', aa0, zz0, nucm0
      goto 110
```

Listing A.4: Definition of the information acquisition from the `fort.3` in the hiSixTrack source file.

```
HION
/1     1     0.9382723            /PROTONS
/40   18     37.215549            /ARGON IONS
/129  54     120.04664            /XENON IONS
208   82     193.68769            /LEAD IONS
NEXT
```

Listing A.5: New heavy-ion block in the fort.3 file to activate hiSixTrack. In the given example, the chosen reference ion species is $^{208}\mathrm{Pb}^{82+}$. Lines starting with '/' are commented out.

A.5.3 Initial Particle Distribution

In the framework of the SixTrack-FLUKA coupling, SixTrack provides subroutine `dist_readdis` to load an initial distribution from an external file. The subroutine is called by the `DIST` block in the fort.3 file. For hiSixTrack, the routine is adapted to read also A, Z and the particle mass m. Already the implementation in SixTrack foresaw different isotopes, so only minor changes are required to access the heavy-ion specific properties from the input file.

When the initial distribution is sampled from the input file, the acquired quantities are processed to populate the respective arrays for the tracking. The modification includes the new definition of δ, the correct nuclear rest mass (as shown in the previous subsection), the initialization of χ and auxiliary quantities derived from it. The relevant code is shown in List. A.6.

```
          call dist_readdis( napx, npart, enom, pnom, clight,
     &                         x, y, xp, yp, s, pc, aa, zz, m )
!         [...]
!         LOOP OVER ALL PARTICLES
          do j=1, napx
!             VALUES RELATED TO LOSSES
              nlostp(j) = j
              pstop (j) = .false.
!             VALUES RELATED TO MOMENTUM (MODIFIED IN HISIXTRACK)
              ejv   (j)   = sqrt(ejfv(j)**2+nucm(j)**2)
              dpsv  (j)   = (ejfv(j)*(nucm0/nucm(j))-e0f)/e0f
              oidpsv(j)   = one/(one+dpsv(j))
!             NEW IN HISIXTRACK
              mtc     (j) = (nzz(j)*nucm0)/(zz0*nucm(j))
              moidpsv (j) = mtc(j)*oidpsv(j)
              omoidpsv(j) = c1e3*((one-mtc(j))*oidpsv(j))
!         [...]
```

Listing A.6: Definition of the subroutine `dist_readdis` in hiSixTrack including the initialization of χ and auxiliary quantities as well as the redefined δ.

A.5.4 Implemented Heavy-Ion Tracking Maps

Some of the redefined tracking maps in hiSixTrack are shown in List. A.7 to List. A.9.

```
+cd kickv01h
+if .not.tilt
!             yv(1,j)=yv(1,j)+(strack(i)*oidpsv(j))        ! SixTrack
              yv(1,j)=yv(1,j)+(strack(i)*oidpsv(j))*mtc(j)  ! hiSixTrack
+ei
+if tilt
              yv(1,j)=yv(1,j)+(strackc(i)*oidpsv(j))*mtc(j)
              yv(2,j)=yv(2,j)+(stracks(i)*oidpsv(j))*mtc(j)
+ei
```

Listing A.7: Definition of the transfer map of an horizontal kicker dipole.

```
+cd kickv01v
+if .not.tilt
            yv(2,j)=yv(2,j)+(strack(i)*oidpsv(j))*mtc(j)   ! hiSixTrack
+ei
+if tilt
            yv(1,j)=yv(1,j)-(stracks(i)*oidpsv(j))*mtc(j) ! hiSixTrack
            yv(2,j)=yv(2,j)+(strackc(i)*oidpsv(j))*mtc(j) ! hiSixTrack
+ei
```

Listing A.8: Definition of the transfer map of a vertical dipole kick.

```
+cd kickvxxh
+if .not.tilt
            yv(1,j)=yv(1,j)+((strack(i)*oidpsv(j))*crkve)*mtc(j) ! hiSixTrack
            yv(2,j)=yv(2,j)-((strack(i)*oidpsv(j))*cikve)*mtc(j) ! hiSixTrack
+ei
+if tilt
            yv(1,j)=yv(1,j)+(oidpsv(j)*(strackc(i)*crkve+                &
     &stracks(i)*cikve))*mtc(j)
            yv(2,j)=yv(2,j)+(oidpsv(j)*(stracks(i)*crkve-                &!hr02
     &strackc(i)*cikve))*mtc(j)                                            !hr02
+ei
```

Listing A.9: Definition of the transfer map of a quadrupole.

A.6 Implementation of the hiSixTrack-FLUKA Coupling

A.6.1 Code Structure

The SixTrack-FLUKA coupling requires several changes with respect to the standalone tools to provide particle exchange between the different codes. The most important ingredient is the FlukaIO protocol, developed for this purpose [Ft12]. Before the set up of hiSixTrack, this protocol was already equipped with a function to send information about A, Z, m back and forth. Only minor modifications (implemented by V. Vlachoudis) were necessary to adapt the FlukaIO for the hiSixTrack-FLUKA coupling.

Both the FLUKA input and subroutines, as well as the SixTrack source are adapted to allow for the exchange of information about the heavy-ion species. These changes are summarized below.

A.6.2 Changes in FLUKA Input and Subroutines

This subsection gives a brief overview of the modifications at the FLUKA user routines, input file and compilation to allow for the accurate heavy-ion exchange and an appropriate fragmentation simulation.

Initialization and Particle Reception

The communication between FLUKA and the FlukaIO is established via the user routine `source.f` [Ft16]. The human interface to control the latter is the `SOURCE` card in the FLUKA input file. It is used to receive the particle distribution from SixTrack and write the `toucMap` file. For the coupling with hiSixTrack, the `source.f` user routine is modified to ensure the accurate initialization of the FLUKA particle variables (author: A. Mereghetti). The function to write the `toucMap` file is extended for heavy-ion applications by saving additional information on A, Z.

Sending Particles back to hiSixTrack

The particle bunch is sent back to hiSixTrack via the user routine `fluscw.f`, which is activated over the `USRBDX` card with the special `SDUM` keyword `BACK2ICO` (see [Ft16]). In this user routine the particles are selected and the `fort.66` file containing the correction data for the collimator losses is populated as shown in List. A.10. The user routine is activated when the boundary crossing condition is fulfilled (in this framework a transition from the vacuum surrounding the collimators to black absorber). The type of boundary crossing is defined in the `USRBDX` card, as shown in List. A.11, for the nominal SixTrack-FLUKA coupling on top and for the heavy-ion version on the bottom.

```
1      [...]
2              ESCO = -PLA + AM(IJ)
3 *            hiST: write all particles not sent back to fort.66
4              IF ( IJ .GT. 0 .OR. IJ .LT. -6 ) THEN
5                  WRITE(66,*)
6      &                 IJ, IBARCH(IJ), ICHRGE(IJ),ICPPNT,ESCO
7              RETURN
8              END IF
9      [...]
```

Listing A.10: Particle selection in the `fluscw.f` user routine to write the data to the collimator loss correction file `fort.66`.

```
*USRBDX          99.0    PROTON     -42.0   VAROUND  BLKROUND          BACK2ICO
*USRBDX        8000.0   1.0E-04     210.0                             &
USRBDX          99.0  ALL-PART     -42.0   VAROUND  BLKROUND          BACK2ICO
USRBDX      576000.0   1.0E-04     210.0
```

Listing A.11: USRBDX card in the FLUKA input for the nominal SixTrack-FLUKA coupling (commented out) and the heavy-ion version at the bottom.

Compilation

The computation of high-energy hadronic interactions in FLUKA requires the activation of the DPMJET-III [R$^+$00]. For this purpose, the linking of the user routines is done with a different linker, which is incorporated in the FLUKA `Makefile` in the framework of the hiSixTrack-FLUKA coupling where the usage of the default `lfluka` linker is replaced by `ldpm3qmd`.

Input File

Besides the changes on the `USRBDX` card mentioned above, minor changes at the FLUKA input make the framework compatible for heavy-ion applications. The `SDUM` of the `BEAM` card is changed from `PROTON` to `HEAVYION` with the subsequent definition of the main beam isotope. Furthermore, heavy-ion specific EMD and nuclear evaporation are activated by means of their dedicated cards, as shown in List. A.12.

```
* activate EMD and Evaporation for heavy-ions
PHYSICS          2.0                                              EM-DISSO
PHYSICS     3.0                                                   EVAPORAT
* maximum momentum per nucleon (3000 for 3.5Z TeV, 6000 for 6.37Z TeV)
BEAM           6000.                                              HEAVYION
HI-PROPE         82.      208.
*
```

Listing A.12: Changes in the FLUKA input for heavy-ion applications

A.6.3 Changes in hiSixTrack

Several modifications are required in hiSixTrack to adapt the software for the exchange of heavy-ions. The most important changes are done in the subroutine `kernel_fluka_entrance` and the `kernel_fluka_exit`.

```
      subroutine kernel_fluka_entrance( nturn, i, ix )
      use mod_fluka
      [...]
+ca hions                             ! load the commons specific to hiST
      [...]
      nnuc0 = 0                       ! nucleons sent to FLUKA
      ien0  = 0.0                     ! ion energy sent to FLUKA

      do j=1,npart                    ! initialize array of particle ids
         pids(j) = 0
      end do

      do j=1,napx
         nnuc0   = nnuc0 + naa(j)     ! count nucleons
         ien0    = ien0  + ejv(j)     ! count energy [GeV]
         pids(j) = fluka_uid(j)       ! array of SixTrack IDs sent to FLUKA
      end do

      ret = fluka_send( nturn, fluka_geo_index(ix), eltot, napx,        &
     & xv(1,:), yv(1,:), xv(2,:), yv(2,:), sigmv, ejv , naa(:), nzz(:), &
     &nucm(:) )

     [...]
     return
     end subroutine
```

Listing A.13: Send particles to FLUKA as implemented in hiSixTrack.

kernel_fluka_entrance This subroutine sends the particle bunch to FLUKA via the dedicated function `fluka_send`. For hiSixTrack, the number of nucleons (`nnuc0`) and the total particle energy (`ien0`) sent to FLUKA are counted before the particle bunch is sent to FLUKA. This information is compared to the total nucleon number and particle energy when the bunch of residual ions is sent back from FLUKA to SixTrack, to calculate the ion loss (see paragraph below). Furthermore a dedicated array (`pids(j)`) containing the hiSixTrack particle IDs of all particles sent to FLUKA is populated, to save the particle information about the particles lost at the collimator. The most important changes are shown in List. A.13.

kernel_fluka_exit

The subroutine `kernel_fluka_exit` is called when the particle bunch is sent back from FLUKA to hiSixTrack. It makes use of the `fluka_receive` subroutine defined in the `mod_fluka` module. After the bunch of residual particles is received by the `fluka_receive` function, the arrays

storing the particle momenta, δ, χ and other quantities are re-populated. Also, the number of out-scattered nucleons (`nnuc1`) and the integrated energy of the received particle bunch (`ien1`) are calculated. In a subsequent step, the latter are compared to `nnuc0` and `ien0` to calculate the collimator losses, which are saved into the `fort.208` file. In a last step, it is identified which particle IDs have been sent to FLUKA but not back to SixTrack. The corresponding particle information is then saved in to the `fort.209` file. The implementation in hiSixTrack is shown in List. A.14.

```
1
2       subroutine kernel_fluka_exit( nturn, i, ix )
3       [...]
4       ret = fluka_receive( nturn, fluka_geo_index(ix), eltot, napx,     &
5      &xv(1,:), yv(1,:), xv(2,:), yv(2,:), sigmv, ejv, naa(:),nzz(:)     &
6      & ,nucm(:) )
7       nnuc1 = 0                 ! init. number of nucleons leaving collimator
8       ien1  = 0.0               ! init. total energy leaving collimator
9       do j=1,napx
10         [...]
11 !       Update hiST arrays (naa, nzz, nucm are initialized by fluka_receive)
12         ejfv    (j) = sqrt((ejv(j)-nucm(j))*(ejv(j)+nucm(j))) ! ion momentum
13         rvv     (j) = (ejv(j)*e0f)/(e0*ejfv(j))               ! beta0/beta
14         dpsv    (j) = (ejfv(j)*(nucm0/nucm(j))-e0f)/e0f       ! delta
15         oidpsv  (j) = 1.0D+00/(1.0D+00+dpsv(j))               ! 1/(1+delta)
16         dpsv1   (j) = (dpsv(j)*1.0D+03)*oidpsv(j)             !
17         mtc     (j) = (nzz(j)*nucm0)/(zz0*nucm(j))            ! chi
18         moidpsv (j) = mtc(j)*oidpsv(j)                        ! chi/(1+delta)
19         omoidpsv(j) = 1.0D+03*((1.0D+00-mtc(j))*oidpsv(j))    !
20         nnuc1       = nnuc1 + naa(j)                          ! increase
   nucleon counter
21         ien1        = ien1  + ejv(j)                          ! increase energy
    counter
22       end do
23       ! hiSixTrack: if energy is lost at the collimator, write to fort.208
24         if ((ien0-ien1).gt.one) then
25             write(208,*), fluka_geo_index(ix), nnuc0-nnuc1,            &
26     &      (ien0-ien1)*1d-3
27         end if
28 !     hisix: check which particle ids have not been sent back
29 !            write their ids to fort.209
30       do j=1,npart                                    ! loop over all IDs
31     pid_q = zero
32     do k=1,napx                                  ! loop over pids received
33         if (pids(j).eq.fluka_uid(k)) then
34             pid_q = one
35         end if
36     end do
37     if (pid_q.eq.zero.and.pids(j).ne.zero) then
38               write(209,*), fluka_geo_index(ix), pids(j)
39     end if
40       end do
```

Listing A.14: Receive particles from FLUKA as implemented in hiSixTrack.

Publications

This is a summary of publications the author published during the work on the Ph.D. project.

Main Author

Journal Paper

P. D. Hermes, R. Bruce, J. M. Jowett, S. Redaelli, B. Salvachua, G. Valentino, D. Wollmann,
"*Measured and Simulated Heavy-Ion Beam Loss Patterns at the CERN Large Hadron Collider*"
Nuclear Instruments and Methods in Physics Research A 819 (2016) 73-83.

Proceedings

P. D. Hermes, R. Bruce, F. Cerutti, A. Ferrari, J. M. Jowett, A. Lechner, A. Mereghetti, D. Mirarchi, P. G. Ortega, S. Redaelli, B. Salvachua, E. Skordis, G. Valentino, V. Vlachoudis,
"*Simulation of Heavy-Ion Beam Losses with the SixTrack-FLUKA Active Coupling*"
Proceedings of IPAC 2016 (WEPMW029):2490-2493, Busan, Korea.

P. D. Hermes, R. Bruce, R. De Maria,
"*Symplectic Tracking of Multi-Isotopic Heavy-Ion Beams in SixTrack*"
Proceedings of IPAC 2016 (TUPMW015):1450-1453, Busan, Korea.

P. D. Hermes, R. Bruce, M. Fiascaris, H. Garcia, M. Giovannozzi, A. Mereghetti, D. Mirarchi, E. Quaranta, S. Redaelli, B. Salvachua, G. Valentino, R. Kwee-Hinzmann, E. Quaranta
"*Improved Aperture Measurements at the LHC and Results from their Application in 2015*"
Proceedings of IPAC 2016 (TUPMW014):1446-1449, Busan, Korea.

P. D. Hermes, R. Bruce, J. M. Jowett, S. Redaelli,
"*Betatron Cleaning for Heavy Ion Beams with IR7 Dispersion Suppressor Collimators*"
Proceedings of IPAC 2015 (TUPTY025):2057-2059, Richmond, VA, USA.

P. D. Hermes, R. Bruce, J.M. Jowett, S. Redaelli, B. Salvachua, G. Valentino, D. Wollmann,
"*Studies on Heavy Ion Losses from Collimation Cleaning at the LHC*"
Proceedings of HB 2014 (MOPAB43):138-142, East Lansing, MI, USA.

CERN Publications

P. D. Hermes, B. Auchmann, R. Bruce, W. Höfle, E. B. Holzer, M. Kalliokoski, G. Kotzian, A. Mereghetti, D. Mirarchi, E. Quaranta, S. Redaelli, G. Valentino, D. Valuch, D. Wollmann, M. Zerlauth, "*LHC Heavy-Ion Collimation Quench Test at 6.37Z TeV*"
CERN-ACC-NOTE-2016-0031, CERN, Geneva, Switzerland, (2016).

Co-Author

Proceedings

J.M. Jowett, R. Alemany-Fernandez, R. Bruce, M. Giovannozzi, P. D. Hermes, W. Höfle, M. Lamont, T. Mertens, S. Redaelli, M. Schaumann, J.A. Uythoven, J. Wenninger,
"*The 2015 Heavy-Ion Run of the LHC*"
Proceedings of IPAC 2016 (TUPMW027):1493-1496, Busan, Korea.

B. Salvachua, P. Baudrenghien, R. Bruce, H. Garcia, P. D. Hermes, S. Jackson, M. Jaussi, A. Mereghetti, D. Mirarchi, S. Redaelli, H. Timko, G. Valentino, A. Valloni, R. Kwee-Hinzmann,
"*Validation of Off-momentum Cleaning Performance of the LHC Collimation System*"
Proceedings of IPAC 2016 (WEPMW007):2427-2430, Busan, Korea.

D. Mirarchi, A. Bertarelli, R. Bruce, F. Cerutti, P.D. Hermes, A. Lechner, A. Mereghetti, E. Quaranta, S. Redaelli, R.B. Appleby, H. Garcia Morales, R. Kwee-Hinzmann,
"*Cleaning Performance of the Collimation System of the High Luminosity Large Hadron Collider*", Proceedings of IPAC 2016 (WEPMW030):2494-2497, Busan, Korea.

E. Quaranta, A. Bertarelli, F. Carra, P. D. Hermes, S. Redaelli, A. Rossi, K. Bunk, F. Carra, J. Guardia Valenzuela, C.L. Hubert, M. Tomut, P. Nocera, C. Porth, N. Simos,
"*Radiation-induced Effects on LHC Collimator Materials under Extreme Beam Conditions*"
Proceedings of IPAC 2016 (WEPMW032):2502-2505, Busan, Korea.

D. Mirarchi, R. Bruce, M. Giovannozzi, P. D. Hermes, S. Redaelli, B. Salvachua, G. Valentino, J. Wenninger, "*LHC aperture and ULO restrictions: are they a possible limitation in 2016?*"
Proceedings of the 6th Evian Workshop, Evian, France, (2015).

G. Valentino, R. Bruce, M. Fiascaris, H. Garcia, P. D. Hermes, A. Mereghetti, D. Mirarchi, R. Kwee, S. Redaelli, E. Quaranta, A. Rossi, R. Rossi, B. Salvachua, P. Theodoropoulos, A. Valloni, J. Wagner, "*Performance of the LHC collimation system during 2015*"
Proceedings of the 6th Evian Workshop, Evian, France (2015).

E. Skordis, R. Bruce, F. Cerutti, A. Ferrari, P.D. Hermes, A. Lechner, A. Mereghetti, P.G. Ortega, S. Redaelli, V. Vlachoudis,
"*Impact of Beam Losses in the LHC Collimation Regions*"
Proceedings of IPAC 2015 (TUPTY046):2116-2119, Richmond, VA, USA.

CERN Publications

B. Salvachua, A. Mereghetti, B. Auchmann, R. Bruce, P.D. Hermes, E.B. Holzer, D. Jacquet, M. Kalliokoski, D. Mirarchi, S. Redaelli, E. Skordis, G. Valentino, A. Valloni, D. Valuch, D. Wollmann, M. Zerlauth, "*Collimation Quench Test with 6.5 TeV Proton Beams*"
CERN-ACC-NOTE-2016-0015, CERN, Geneva, Switzerland (2016).

R. Bruce, P. D. Hermes, H. Garcia, R. Kwee-Hinzmann, A. Mereghetti, D. Mirarchi, S. Redaelli, B. Salvachua, P. Skowronski, G. Valentino, A. Valloni,
"*IR aperture measurement at β^* =40 cm*"
CERN-ACC-NOTE-2015-0037, CERN, Geneva, Switzerland (2015).

R. Bruce, H. Garcia, P.D. Hermes, R. Kwee-Hinzmann, A. Mereghetti, D. Mirarchi, E. Quaranta, S. Redaelli, B. Salvachua, G. Valentino, A. Valloni,
"*Collimation with tighter TCTs at β^* =40 cm*"
CERN-ACC-NOTE-2015-0036, CERN, Geneva, Switzerland (2015).

G. Valentino, G. Baud, R. Bruce, H. Garcia, P. D. Hermes, M. Gasior, R. Kwee, D. Mirarchi, J. Olexa, S. Redaelli, R. Rossi, B. Salvachua, A. Valloni, J. Wagner,
"*Characterization of Embedded BPM Collimators*"
CERN-ACC-NOTE-2015-0027, CERN, Geneva, Switzerland (2015).

Bibliography

[A+02a] R. W. Assmann et al. *Requirements for the LHC Collimation System.* Proceedings of EPAC 2002, Paris, France, (TUAGB001):197–199, 2002.
URL: http://epaper.kek.jp/e02/PAPERS/TUAGB001.pdf .

[A+02b] R. W. Assmann et al. *The Consequences of Abnormal Beam Dump Actions on the LHC Collimation System.* (LHC Project Note 293), 2002.
URL: http://lhc-collimation.web.cern.ch/lhc-collimation/files/dumpkick2.pdf .

[A+06] R. W. Assmann et al. *The final collimation system for the LHC.* Proceedings of EPAC 2006, Edinburgh, Scotland, (TUODFI01):986–988, 2006.
URL: http://accelconf.web.cern.ch/accelconf/e06/PAPERS/TUODFI01.PDF .

[A+11a] R. W. Assmann et al. *Collimator losses in the DS of IR7 and quench test at 3.5 Z TeV.* CERN-ATS-Note-2011-0042 MD, 2011.
URL: https://cds.cern.ch/record/1488931/files/ATSnote2012081.pdf .

[A+11b] R. W. Assmann et al. *Summary of MD on nominal collimator settings.* CERN-ATS-Note-2011-036 MD, 2011.
URL: https://cds.cern.ch/record/1353517/files/MD_ATS_Note-2011-036.pdf .

[A+12] R. W. Assmann et al. *Pb ions collimator losses in IR7 DS and quench test at 3.5 Z TeV.* CERN-ATS-Note-2012-081 MD, 2012.
URL: https://cds.cern.ch/record/1488931/files/ATSnote2012081.pdf? .

[A+14] G. Apollinari et al. *HL-LHC Preliminary Design Report.* CERN-ACC-2014-0300, 2014.
URL: https://cds.cern.ch/record/1972604/files/CERN-ACC-2014-0300.pdf .

[A+15] B. Auchmann et al. *Testing beam-induced quench levels of LHC superconducting magnets in Run I.* Phys. Rev. ST Accel. Beams, 18:061002, 2015.
URL: http://link.aps.org/doi/10.1103/PhysRevSTAB.18.061002 .

[AF+13] R. Alemany-Fernandez et al. *Operation and Configuration of the LHC in Run 1.* CERN-ACC-NOTE-2013-0041, 2013.
URL: https://cds.cern.ch/record/1631030/files/CERN-ACC-Note-2013-0041.pdf .

[Ass05] R. W. Assmann. *Collimators and Beam Absorbers for Cleaning and Machine Protection.* LHC Project Workshop XIV, Chamonix, France, 2005.
URL: https://cds.cern.ch/record/987838/files/cham-xiv-8_02.pdf .

[ASS14] A. N. Artemyev, V. G. Serbo, and A. Surzhykov. *Double lepton pair production with electron capture in relativistic heavy-ion collisions.* Eur. Phys. J. C, 74:2829, 2014.
URL: https://inspirehep.net/record/1281700/files/scoap3-fulltext.pdf .

[Ast08] A. Aste. *Bound-free pair production cross-section in heavy-ion colliders from the equivalent photon approach.* EPL, 81(6), 2008.
URL: http://phys-merger.physik.unibas.ch/~aste/epa_pair_production.pdf .

[B+99] J. Bosser et al. *LHC Beam Instrumentation.* Proceedings of PAC 1999, New York, USA, 1999, (THAR3):465–467, 1999.
URL: https://accelconf.web.cern.ch/accelconf/p99/PAPERS/THAR3.PDF .

[B+04a] H. H. Braun et al. *Collimation of heavy ion beams in LHC.* Proceedings of EPAC 2004, Lucerne, Switzerland, (MOPLT010):551, 2004.
URL: http://accelconf.web.cern.ch/AccelConf/e04/PAPERS/MOPLT010.PDF .

[B+04b] O. Brüning et al. *LHC Design Report (Volume I, The LHC Main Ring)*, volume CERN-2004-003-V-1. CERN, 2004.
URL: https://cds.cern.ch/record/782076/files/CERN-2004-003-V1.pdf .

[B+06] C. Bracco et al. *The final collimation system for the LHC.* Proceedings of EPAC 2006, Edinburgh, Scotland, (TUPLS018):1529–1531, 2006.
URL: http://accelconf.web.cern.ch/AccelConf/e06/PAPERS/TUPLS018.PDF .

[B+09a] T. Böhlen et al. *Energy Deposition Simulations and Measurements in an LHC Collimator and Beam Loss Monitors.* Proceedings of PAC 2009, Vancouver, Canada, (TH5RFP035):3525–3527, 2009.
URL: https://cds.cern.ch/record/1206844/files/th5rfp035.pdf .

[B+09b] R. Bruce et al. *Beam losses from ultra-peripheral nuclear collisions between $^{208}Pb^{82+}$ ions in the Large Hadron Collider and their alleviation.* Phys. Rev. ST Accel. Beams, 12(071002), 2009.
URL: http://lss.fnal.gov/archive/2009/pub/fermilab-pub-09-367-td.pdf .

[B+10] D. Belohrad et al. *The LHC Fast BCT system: A comparison of Design Parameters with Initial Performance.* Proceedings of BIW10, Santa Fe, New Mexico, USA, (TUPSM051):269–273, 2010.
URL: http://accelconf.web.cern.ch/Accelconf/BIW2010/papers/tupsm051.pdf .

[B+11a] T. Baer et al. *UFOs in the LHC.* Proceedings of IPAC 2011, San Sebastián, Spain, (TUPC137):1347–1349, 2011.
URL: https://accelconf.web.cern.ch/accelconf/IPAC2011/papers/tupc137.pdf .

[B+11b] A. Bertarelli et al. *Limits for Beam Induced Damage: Reckless or too Cautious?* Chamonix 2011 Workshop on LHC Performance, 2011.
URL: https://cds.cern.ch/record/1353855/files/AB_5_02.pdf .

[B+12] J. Beringer et al. *Review of Particle Physics.* Phys.Rev., D86:010001, 2012.
URL: http://pdg.lbl.gov/2015/download/rpp2014-Chin.Phys.C.38.090001.pdf .

[B+13a] F. Bordry et al. *The first Long Shutdown (LS1) for the LHC.* Proceedings of IPAC 2013, Shanghai, China, (MOZB202):44–48, 2013.
URL: https://cds.cern.ch/record/1575133/files/CERN-ACC-2013-0084.pdf .

[B+13b] R. Bruce et al. *Sources of machine-induced background in the ATLAS and CMS detectors at the CERN Large Hadron Collider.* Nucl. Instrum. Methods Phys. Res., Sect. A, 729(0):825 – 840, 2013.
URL: http://www.sciencedirect.com/science/article/pii/S016890021301190X .

[B+14a] V. Boccone et al. *Beam-machine Interaction at the CERN LHC.* Nuclear Data Sheets, 120:215–218, 2014.
URL: http://www.sciencedirect.com/science/article/pii/S009037521400502X .

[B+14b] T. T. Böhlen et al. *The FLUKA code: developments and challenges for high energy and medical applications.* Nuclear Data Sheets, 120:211–214, 2014.
URL: http://www.sciencedirect.com/science/article/pii/S0090375214005018 .

[B+14c] H. H. Braun et al. *Hadronic and electromagnetic fragmentation of ultrarelativistic heavy ions at LHC.* Phys. Rev. ST Accel. Beams, 17:021006, 2014.
URL: http://link.aps.org/doi/10.1103/PhysRevSTAB.17.021006 .

[B+14d] R. Bruce et al. *Simulations and measurements of beam loss patterns at the CERN Large Hadron Collider.* Phys. Rev. ST Accel. Beams, 17(081004), 2014.
URL: http://journals.aps.org/prstab/pdf/10.1103/PhysRevSTAB.17.081004 .

[B+15] R. Bruce et al. *Collimator Layouts for HL-LHC in the Experimental Insertions.* Proceedings of IPAC 2015, Richmond, VA, USA, (TUPTY028):2064–2067, 2015.
URL: http://accelconf.web.cern.ch/AccelConf/IPAC2015/papers/tupty028.pdf .

[B+16] R. Bruce et al. *LHC Run 2: Results and Challenges.* Proceedings of HB 2016, Malmö, Sweden, (MOAM5P50), 2016.
URL: https://hb2016.esss.se/prepress/papers/moam5p50.pdf .

[Bar09] J. Bartke. *Relativistic Heavy Ion Physics.* World Scientific Publishing, 2009.

[BAR15] R. Bruce, R. W. Assmann, and S. Redaelli. *Calculations of safe collimator settings and β^* at the CERN Large Hadron Collider.* Phys. Rev. ST Accel. Beams, 18(061001), 2015.
URL: http://link.aps.org/doi/10.1103/PhysRevSTAB.17.021006 .

[BBM12] O. Brüning, H. Burkhardt, and S. Myers. *The Large Hadron Collider.* Prog. Part. Nucl. Phys., 67(3):705 – 734, 2012.
URL: http://indico.cern.ch/event/184080/ .

[BC07] O. Brüning and P. Collier. *Building a behemoth.* Nature, 448:285–289, 2007.
URL: http://www.nature.com/nature/journal/v448/n7151/pdf/nature06077.pdf .

[BDS09] D. Bocian, B. Dehning, and A. Siemko. *Quench limit model and measurements for steady state heat deposits in LHC magnets.* IEEE Trans. Appl. Supercond., 19(3):2446–2449, 2009.
URL: http://ieeexplore.ieee.org/stamp/stamp.jsp?arnumber=5067228 .

[BLM16] LHC Beam Loss Monitoring System Homepage, April 2016.
URL: https://ab-div-bdi-bl-blm.web.cern.ch/ab-div-bdi-bl-blm/ .

[BMR14] R. Bruce, A. Marsili, and S. Redaelli. *Cleaning performance with 11T dipoles and local dispersion suppressor collimation at the LHC.* Proceedings of IPAC 2014, Dresden, Germany, (MOPRO042):170–173, 2014.
URL: https://cds.cern.ch/record/2003162/files/mopro042.pdf .

[BR16] O. Brüning and L. Rossi. *The High Luminosity Large Hadron Collider.* Advanced Series on Directions in High Energy Physics: Volume 24, 2016.

[Bra09] C. Bracco. *Commissioning scenarios and tests for the LHC.* PhD thesis, Ecole Polytechnique Fédérale de Lausanne, 2009.
URL: http://infoscience.epfl.ch/record/128806/files/EPFL_TH4271.pdf .

[BRS87] D. P. Barber, G. Ripken, and F. Schmidt. *A non-linear canonical formalism for the coupled synchro-betatron motion of protons with arbitrary energy.* DESY-87-036, 1987.
URL: `http://cds.cern.ch/record/178715/files/DESY-87-036.pdf` .

[C+12] B. V. Carlson et al. *Fermi breakup and the statistical multifragmentation model.* Nuclear Physics A, 876:77 – 92, 2012.
URL: `http://www.sciencedirect.com/science/article/pii/S0375947411006993` .

[CAS14] *Proceedings of CERN Accelerator School: Advanced Accelerator Physics Course, Trondheim, Norway*, 2014. CERN-2014-009.
URL: `https://cds.cern.ch/record/1507631/files/CERN-2014-009.pdf` .

[Col95] ALICE Collaboration. *Technical Proposal for A Large Ion Collider Experiment.* (CERN-LHCC-95-71), 1995.
URL: `https://cds.cern.ch/record/293391/files/cer-000214817.pdf` .

[Col08a] The ALICE Collaboration. *The ALICE experiment at the CERN LHC.* J. Instrum., 3(S08002), 2008.
URL: `http://iopscience.iop.org/article/10.1088/1748-0221/3/08/S08002/pdf` .

[Col08b] The ATLAS Collaboration. *The ATLAS Experiment at the CERN Large Hadron Collider.* J. Instrum., 3(S08003), 2008.
URL: `http://nordberg.web.cern.ch/nordberg/PAPERS/JINST08.pdf` .

[Col08c] The CMS Collaboration. *The CMS experiment at the CERN LHC.* J. Instrum., 3(S08004), 2008.
URL: `https://cds.cern.ch/record/1129810/files/jinst8_08_s08004.pdf` .

[Col08d] The LHCb Collaboration. *The LHCb Detector at the LHC.* J. Instrum., 3(S08005), 2008.
URL: `https://cdsweb.cern.ch/record/1129809/files/jinst8_08_s08005.pdf` .

[Col12a] ATLAS Collaboration. *Observation of a new particle in the search for the Standard Model Higgs boson with the ATLAS detector at the LHC.* Physics Letters B, 716(1):1–29, 2012.
URL: `http://www.sciencedirect.com/science/article/pii/S037026931200857X` .

[Col12b] CMS Collaboration. *Observation of a new boson at a mass of 125 GeV with the CMS experiment at the LHC.* Physics Letters B, 716(1):30–61, 2012.
URL: `http://www.sciencedirect.com/science/article/pii/S0370269312008581` .

[DDPM08] R. Denz, K. Dahlerupp-Petersen, and K. H. Mess. *Electronic Systems for the Protection of Superconducting Devices in the LHC.* Proceedings of EPAC 2008, Genoa, Italy, (WEPD010):2422–2424, 2008.
URL: https://accelconf.web.cern.ch/accelconf/e08/papers/wepd010.pdf .

[Dep16] CERN IT Department. *Batch System (Website).* 2016.
URL: http://information-technology.web.cern.ch/services/batch .

[Dir58] P. Dirac. *The Principles of Quantum Mechanics.* Oxford at the Clarendon Press, 4. edition, 1958.

[DM+16] R. De Maria et al. SixTrack Developer's Wiki, 2016.
URL: https://twiki.cern.ch/twiki/bin/view/LHCAtHome/SixTrack .

[DMFF15] R. De Maria, M. Fitterer, and M. Fjellstrom. *SixTrackLib Manual.* 2015.
URL: http://sixtrack.web.cern.ch/SixTrack/doc/physics_manual/sixphys.pdf .

[Duv01] V. Duvivier. *Cross section of LHC dipole.. Dipole LHC: Coupe transversale.* 2001.
URL: http://cds.cern.ch/record/843195 .

[F+03] A. Fassò et al. *The physics models of FLUKA: status and recent developments.* Proceedings of CHEP 2003, La Jolla, California, USA, (MOMT005), 2003.
URL: http://www.slac.stanford.edu/econf/C0303241/proc/papers/MOMT005.PDF .

[F+13] M. Fjellstrom et al. Particle Tracking in Circular Accelerators Using the Exact Hamiltonian in SixTrack. Master's thesis, Lulea University of Technology, Lund, Sweden, 2013.
URL: https://pure.ltu.se/ws/files/87616086/LTU-EX-2013-76674531.pdf .

[FJ14] W. Fischer and J. M. Jowett. *Ion Colliders.* Reviews of Accelerator Science and Technology, 07:49–76, 2014.
URL: http://www.worldscientific.com/doi/abs/10.1142/S1793626814300047 .

[FLS65] R. P. Feynman, R. B. Leighton, and M. Sands. *The Feynman Lectures on Physics.* Vol. II. Addison-Wesley, 1965.

[FSFR05] A. Ferrari, P. R. Sala, A. Fasso, and J. Ranft. *FLUKA: A multi-particle transport code (Program version 2005).* CERN-2005-10 (2005), INFN/TC_05/11, SLAC-R-773 , 2005.
URL: https://cds.cern.ch/record/898301/files/CERN-2005-010.pdf .

[Ft12] The CERN FLUKA team. FlukaIO twiki, 2012.
URL: https://twiki.cern.ch/twiki/bin/view/FlukaTeam/FlukaIO .

[Ft16] The CERN FLUKA team. SixTrack-FLUKA coupling twiki, 2016.
URL: https://twiki.cern.ch/twiki/bin/view/FlukaTeam/ .

[G+11] R. Garoby et al. *Plans for the Upgrade of the LHC Injectors.* Proceedings of IPAC 2011, San Sebastián, Spain, (WEPS017):2517–2519, 2011.
URL: http://accelconf.web.cern.ch/accelconf/ipac2011/papers/weps017.pdf .

[GMBR16] H. Garcia-Morales, R. Bruce, and S. Redaelli. *Beam Cleaning in Experimental IRs in HL-LHC for the Incoming Beam.* Proceedings of IPAC 2015, Richmond, VA, USA, (TUPTY066):2181–2183, 2016.
URL: http://accelconf.web.cern.ch/AccelConf/IPAC2015/papers/tupty066.pdf .

[Gri13] D.J. Griffiths. *Introduction to electrodynamics*, volume 4. Pearson, 2013.

[Gua05] G. Guaglio. *Reliability of the beam loss monitors system for the Large Hadron Collider at CERN.* PhD thesis, Université Blaise Pascal, Clermont-Ferrand, France, 2005.
URL: https://tel.archives-ouvertes.fr/tel-00128836/document .

[GvW14] P. Granieri and R. van Weelderen. *Deduction of Steady-State Cable Quench Limits for Various Electrical Insulation Schemes with Application to LHC and HL-LHC Magnets.* IEEE Trans. Appl. Supercond., 24, 2014.
URL: http://ieeexplore.ieee.org/stamp/stamp.jsp?arnumber=6719512 .

[H+03] H. Hahn et al. *The RHIC design overview.* Nucl. Instr. Meth. Phys. Res. A, 499(2-3):245–263, 2003.
URL: http://www.sciencedirect.com/science/article/pii/S0168900203013688 .

[H+05] E.B. Holzer et al. *Beam loss monitoring system for the LHC.* CERN-AB-2006-009 BI, 2005.
URL: https://cds.cern.ch/record/930275/files/ab-2006-009.pdf .

[H+08a] P. Hagen et al. *WISE: A Simulation of the LHC Optics including Magnet Geometrical Data.* Proceedings of EPAC 2008, Genoa, Italy, (TUPP091):1744–1746, 2008.
URL: http://accelconf.web.cern.ch/AccelConf/e08/papers/tupp091.pdf .

[H+08b] E.B. Holzer et al. *Development, Production and Testing of 4500 Beam Loss Monitors.* Proceedings of EPAC 2008, Genoa, Italy, (TUPC037):1134, 2008.
URL: http://accelconf.web.cern.ch/accelconf/e08/papers/tupc037.pdf .

[H+14] P. D. Hermes et al. *Studies on Heavy Ion Losses from Collimation Cleaning at the LHC*. Proceedings of HB 2014, East-Lansing, MI, USA, (MOPAB43):138–142, 2014.
URL: http://accelconf.web.cern.ch/AccelConf/HB2014/papers/mopab43.pdf .

[H+15] P. D. Hermes et al. *Betatron Cleaning for Heavy Ion Beams with IR7 Dispersion Suppressor Collimators*. Proceedings of IPAC 2015, Richmond, VA, USA, (TUPTY025):2057–2059, 2015.
URL: http://accelconf.web.cern.ch/AccelConf/IPAC2015/papers/tupty025.pdf .

[H+16a] P. D. Hermes et al. *LHC Heavy-Ion Collimation Quench Test at 6.37Z GeV*. CERN-ACC-NOTE-2016-0031 MD, 2016.
URL: https://cds.cern.ch/record/2136828/files/CERN-ACC-Note-2016-0031%20MD.pdf .

[H+16b] P. D. Hermes et al. *Measured and Simulated Heavy-Ion Beam Loss Patterns at the CERN Large Hadron Collider*. Nucl. Instr. Meth. Phys. Res. A, 819:73–83, 2016.
URL: http://www.sciencedirect.com/science/article/pii/S0168900216002175 .

[H+16c] P. D. Hermes et al. *Simulation of Heavy-Ion Beam Losses with the SixTrack-FLUKA Active Coupling*. Proceedings of IPAC 2016, Busan, Korea, (WEPMW029):2490–2493, 2016.
URL: http://accelconf.web.cern.ch/AccelConf/ipac2016/papers/wepmw029.pdf .

[Hag08] P. Hagen. *WISE - User Guide and Implementation Notes*. LHC Project Report 1056, CERN, Geneva, Switzerland, 2008.
URL: https://cds.cern.ch/record/1089857/files/lhc-project-report-1056.pdf .

[HBDM16] P. D. Hermes, R. Bruce, and R. De Maria. *Symplectic Tracking of Multi-Isotopic Heavy-Ion Beams in SixTrack*. Proceedings of IPAC 2016, Busan, Korea, (TUPMW015):1450–1453, 2016.
URL: http://accelconf.web.cern.ch/AccelConf/ipac2016/papers/tupmw015.pdf .

[Her03] W. Herr. *Concept of luminosity*. Proceedings of CERN Accelerator School: 5th Intermediate Accelerator Physics Course, 2003. CERN-2006-002.
URL: https://cds.cern.ch/record/941318/files/p361.pdf .

[Hol08] N. Holden. Development of the ICOSIM Program and Application to Magnetised Collimators in the LHC. Technical Report CERN-AB-Note-2008-054, 2008.
URL: https://cds.cern.ch/record/1151294/files/AB-Note-2008-054.pdf .

[HRS95] K. Heinemann, G. Ripken, and F. Schmidt. *Construction of Nonlinear Symplectic Six-Dimensional Thin-Lens Maps by Exponentiation.* DESY-95-189, 1995.
URL: `http://arxiv.org/pdf/acc-phys/9510005v1.pdf` .

[Iwa09] Y. Iwasa. *Case studies in superconducting magnets: design and operational issues.* Springer Science & Business Media, 2 edition, 2009.

[J+96] J. B. Jeanneret et al. *Quench Levels and Transient Beam Losses in LHC Magnets.* LHC Project Report 44, CERN, Geneva, Switzerland, 1996.
URL: `https://ab-div-bdi-bl-blm.web.cern.ch/ab-div-bdi-bl-blm/literature/lhc-project-report-44_quenchlevels_bernard.pdf` .

[J+11] J. M. Jowett et al. *First Run of the LHC as a Heavy-Ion Collider.* Proceedings of IPAC 2011, San Sebastián, Spain, (TUPZ016):1837, 2011.
URL: `https://accelconf.web.cern.ch/accelconf/IPAC2011/papers/tupz016.pdf` .

[J+12] J. M. Jowett et al. *Heavy Ions in 2012 and the Programme up to 2022.* Chamonix 2012 Workshop on LHC Performance, 2012.
URL: `https://cds.cern.ch/record/1492972/files/JJ_4_06.pdf` .

[J+13a] J. M. Jowett et al. *Future heavy-ion performance of the LHC.* Presentation at Review of LHC and Injector Upgrade Plans Workshop, 2013.
URL: `https://indico.cern.ch/event/260492/` .

[J+13b] J. M. Jowett et al. *Proton-Nucleus Collisions in the LHC.* Proceedings of IPAC 2013, Shanghai, China, (MOODB201):49, 2013.
URL: `http://accelconf.web.cern.ch/AccelConf/IPAC2013/papers/moodb201.pdf` .

[J+16a] J. M. Jowett et al. *Bound-Free Pair Production in LHC Pb-Pb Operation at 6.37Z per Beam.* Proceedings of IPAC 2016, Busan, Korea, (TUPMW028):1497–1500, 2016.
URL: `http://accelconf.web.cern.ch/AccelConf/ipac2016/papers/tupmw028.pdf` .

[J+16b] J. M. Jowett et al. *The 2015 Heavy-Ion Run of the LHC.* Proceedings of IPAC 2016, Busan, Korea, (TUPMW027):1493–1496, 2016.
URL: `https://accelconf.web.cern.ch/accelconf/IPAC2011/papers/tupz016.pdf` .

[JJ84] M. Jacob and K. Johnsen. *A Review of Accelerator and Particle Physics at the CERN Intersecting Storage Rings.* (CERN 84-13), 1984.

[Jow16] J. M. Jowett. *Private Communication.* 2016.

[Kal15] M. Kalliokoski. *BLM Thresholds for 2015 Ion Quench Tests.* CERN Engineering Change Request, (LHC-BLM-ECR-0043), 2015.

[Lam05] M. Lamont. *Estimates of Annual Proton Doses in the LHC.* (LHC Project Note 375), 2005.
URL: https://cds.cern.ch/record/893060/files/project-note-375.pdf .

[Lec14] A. Lechner. *BLM thresholds for post-LS1 LHC operation: UFOs and orbit bumps in the arcs and straight sections.* Presentation at Workshop on Beam-Induced Quenches, 16.09.2014, 2014.
URL: https://indico.cern.ch/event/323249/ .

[Lee12] S.Y. Lee. *Accelerator physics.* World scientific Singapore, 2012.

[Lef08] Christiane Lefèvre. The CERN accelerator complex. Dec 2008.
URL: https://cds.cern.ch/record/1260465 .

[M+01] H. Meier et al. *Bound-free electron-positron pair production in relativistic heavy-ion collisions.* Phys.Rev., 63:032713–1 – 032713–7, 2001.
URL: http://journals.aps.org/pra/pdf/10.1103/PhysRevA.63.032713 .

[M+12] A. Mereghetti et al. *The FLUKA Linebuilder and Element Database: Tools for building complex Models of Accelerator Beam Lines.* Proceedings of IPAC 2012, New Orleans, Louisiana, USA, (WEPPD071):2687–2689, 2012.
URL: http://accelconf.web.cern.ch/AccelConf/IPAC2012/papers/WEPPD071.PDF .

[M+13a] A. Mereghetti et al. *SixTrack-FLUKA active coupling for the upgrade of the SPS Scrapers.* Proceedings of IPAC 2013, Shanghai, China, (WEPEA064):2657–2659, 2013.
URL: https://accelconf.web.cern.ch/accelconf/IPAC2013/papers/wepea064.pdf .

[M+13b] V. Moens et al. *Comparison of LHC Beam Loss Maps Using the Transverse Damper Blow Up and Tune Resonance Crossing Methods.* Proceedings of IPAC 2013, Shanghai, China, (MOPWO050):1008–1010, 2013.
URL: https://accelconf.web.cern.ch/accelconf/IPAC2013/papers/mopwo050.pdf .

[M+15] M. Meddahi et al. *LHC Injectors Upgrade (LIU) Project at CERN.* Proceedings of IPAC 2015, Richmond, VA, USA, (THPF093):3915–3918, 2015.
URL: http://accelconf.web.cern.ch/AccelConf/IPAC2015/papers/thpf093.pdf .

[M+16a] D. Manglunki et al. *CERN's Fixed Target Primary Ion Programme.* Proceedings of IPAC 2016, Busan, Korea, (TUPMR027):1297–1300, 2016.
URL: http://cds.cern.ch/record/2207350/files/tupmr027.pdf .

[M+16b] D. Mirarchi et al. *Cleaning Performance of the Collimation System of the High Luminosity Large Hadron Collider.* Proceedings of IPAC 2016, Busan, Korea, (WEPMW030):2494–2497, 2016.
URL: http://accelconf.web.cern.ch/AccelConf/ipac2016/papers/wepmw030.pdf .

[MAD] MAD - Methodical Accelerator Design. Last accessed: 16.09.2016.
URL: http://cern.ch/madx/ .

[Man14] D. Manglunki. *Performance of the Injectors with Ions after LS1.* Proceedings of RLIUP: Review of LHC and Injector Upgrade Plans, Archamps, France, pages 157–162, 2014.
URL: https://cds.cern.ch/record/1629486/files/CERN-2014-006.pdf .

[MB83] S. K. Mtingwa and J. D. Bjorken. *Intrabeam scattering.* Part. Acc., 13:115–143, 1983.
URL: https://cds.cern.ch/record/140304/files/p115.pdf .

[Mer16] T. Mertens. *Private Communication.* 2016.

[P+16a] G. Papotti et al. *Macroparticle-induced Losses during 6.5 TeV LHC Operation.* Proceedings of IPAC 2016, Busan, Korea, (TUPMW023):1481–1484, 2016.
URL: http://accelconf.web.cern.ch/AccelConf/ipac2016/papers/tupmw023.pdf .

[P+16b] G. Papotti et al. *Operation of the LHC with Protons at High Luminosity and High Energy.* Proceedings of IPAC 2016, Busan, Korea, (WEOCA01):2066–2068, 2016.
URL: https://accelconf.web.cern.ch/accelconf/IPAC2011/papers/tupz016.pdf .

[Piw74] A. Piwinski. *Intra-Beam Scattering.* Proceedings of the IXth International Conference on High Energy Accelerators, Stanford, CA, USA, (SLAC-R-839):405–409, 1974.
URL: http://www.slac.stanford.edu/cgi-wrap/getdoc/slac-r-839-a.pdf .

[Pla16] Plansee. Tungsten heavy alloys (website), 2016.
URL: https://www.plansee.com/en/materials/tungsten-heavy-metal.html .

[Pro95] *Proceedings of CERN Accelerator School: 5th Advanced Accelerator Physics Course*, 1995. CERN-1995-006.
URL: https://cds.cern.ch/record/254747/ .

[Psh16] I. A. Pshenichnov. *Private Communication*. 2016.

[Q+15] E. Quaranta et al. *Collimation cleaning at the LHC with advanced secondary collimator materials*. Proceedings of IPAC 2015, Richmond, VA, USA, (TUPTY029):2068–2071, 2015.
URL: https://cds.cern.ch/record/2114397/files/tupty029.pdf .

[Q+16] E. Quaranta et al. *Towards Optimum Material Choices for HL-LHC Collimator Upgrade*. Proceedings of IPAC 2016, Busan, Korea, (WEPMW031):2498–2501, 2016.
URL: http://accelconf.web.cern.ch/AccelConf/ipac2016/papers/wepmw031.pdf .

[R+00] S. Rösler et al. *The Monte Carlo Event Generator DPMJET-III*. Proceedings of the Monte Carlo 2000 Conference, Lisbon, Portugal, pages 1033–1038, 2000.
URL: http://link.springer.com/chapter/10.1007%2F978-3-642-18211-2_166 .

[R+12a] S. Redaelli et al. *Aperture Measurements in the LHC Interaction Regions*. Proceedings of IPAC 2012, New Orleans, Louisiana, USA, (MOPPD062):508–510, 2012.
URL: http://accelconf.web.cern.ch/accelconf/ipac2012/papers/moppd062.pdf .

[R+12b] S. Redaelli et al. *Combined Ramp and Squeeze at the Large Hadron Collider*. Proceedings of IPAC 2012, New Orleans, Louisiana, USA, (MOPPC016):157–159, 2012.
URL: https://accelconf.web.cern.ch/accelconf/IPAC2012/papers/moppc016.pdf .

[R+12c] S. Redaelli et al. *Quench tests at the Large Hadron Collider with Collimation Losses at 3.5 Z TeV*. Proceedings of HB 2012, Beijing, China, (MOP245):157–161, 2012.
URL: https://accelconf.web.cern.ch/accelconf/HB2012/papers/mop245.pdf .

[R+14] S. Redaelli et al. Collimator BLM threshold strategy, 2014. Proceedings of the Workshop on Beam-Induced Quenches, CERN, Geneva, Switzerland.
URL: https://indico.cern.ch/event/323249/ .

[RARD05] S. Redaelli, R. W. Assmann, and G. Robert-Demolaize. *LHC Aperture and Commissioning of the Collimation System*. Proceedings of LHC Project Workshop - Chamonix XIV, 2005.
URL: https://cds.cern.ch/record/293391/files/cer-000214817.pdf .

[RD+05a] G. Robert-Demolaize et al. *A new Version of SixTrack with Collimation and Aperture Interface*. Proceedings of PAC 2005, Knoxville, Tennessee, USA, (FPAT081):4084, 2005.
URL: http://accelconf.web.cern.ch/AccelConf/p05/PAPERS/FPAT081.PDF .

[RD+05b] G. Robert-Demolaize et al. *A New Version of Sixtrack with Collimation and Aperture Interface.* Proceedings of PAC 2005, Knoxville, TN, USA, (FPAT081):4084–4086, 2005.
URL: http://epaper.kek.jp/p05/PAPERS/FPAT081.PDF .

[Red13] S. Redaelli. *The collimation system: defence against beam loss.* CERN Courier, 2013.
URL: http://cerncourier.com/cws/article/cern/54384 .

[Red16] S. Redaelli. *Private Communication.* 2016.

[Ree03] J. R. Rees. *Symplecticity in Beam Dynamics: An Introduction.* SLAC-PUB-9939, Stanford Linear Accelerator Center, Stanford, CA, USA, 2003.
URL: http://www.slac.stanford.edu/cgi-wrap/getdoc/slac-pub-9939.pdf .

[Rip85] G. Ripken. *Non-linear canonical equations of coupled synchro-betatron motion and their solution within the framework of a non-linear 6-dimensional (symplectic) tracking program for ultra-relativistic protons.* DESY-85-084, 1985.
URL: http://cds.cern.ch/record/162762/files/desy%2085-084_001.pdf .

[RS95] G. Ripken and F. Schmidt. *A symplectic Six-Dimensional Thin-Lens Formalism for Tracking.* CERN-SL-95-12 (AP), 1995.

[S+07] R. Schmidt et al. *LHC Machine Protection.* LHC Project Report 1053, CERN, Geneva, Switzerland, 2007.
URL: https://cds.cern.ch/record/1076302/files/lhc-project-report-1053.pdf .

[S+13a] M. Sapinski et al. *Beam induced quenches of LHC magnets.* Proceedings of IPAC 2013, Shanghai, China, (THPEA045):3243–3245, 2013.
URL: http://accelconf.web.cern.ch/AccelConf/IPAC2013/papers/thpea045.pdf .

[S+13b] E. Skordis et al. *FLUKA Energy deposition simulations for quench tests.* Talk at the LHC Collimation Review 30.05.2013, 2013.
URL: https://indico.cern.ch/event/251588/ .

[S+14a] B. Salvachua et al. *Collimation quench test with 4 TeV proton beams.* CERN-ATS-Note-2014-0036, 2014.
URL: https://cds.cern.ch/record/1708365/files/CERN-ACC-NOTE-2014-0036.pdf .

[S+14b] B. Salvachua et al. *Handling 1 MW Losses with the LHC Collimation System.* Proceedings of IPAC 2014, Dresden, Germany, (MOPRO043):174–177, 2014.
URL: http://accelconf.web.cern.ch/AccelConf/IPAC2014/papers/mopro043.pdf .

[S+14c] M. Serluca et al. *HI-Lumi LHC Collimation Studies with Merlin Code.* Proceedings of IPAC 2014, Dresden, Germany, (MOPRI077):784–787, 2014.
URL: https://inspirehep.net/record/1314145/files/mopri077.pdf .

[S+15a] M. Schaumann et al. *LHC BFPP Quench Test with Ions (2015).* CERN-ACC-NOTE-2015-0024, 2015.
URL: https://cds.cern.ch/record/2127951/files/CERN-ACC-Note-2016-0024.pdf .

[S+15b] E. Skordis et al. *Impact of Beam Losses in the LHC Collimation Regions.* Proceedings of IPAC 2015, Richmond, VA, USA, (TUPTY046):2116–2119, 2015.
URL: https://cds.cern.ch/record/2141844/files/tupty046.pdf .

[S+16] B. Salvachua et al. *Collimation quench test with 6.5 TeV proton beams.* CERN-ACC-NOTE-2016-0015, 2016.
URL: https://cds.cern.ch/record/2123852/files/CERN-ACC-NOTE-2016-0015.pdf .

[Sch94] F. Schmidt. *SixTrack Version 4.2.16 Single Particle Tracking Code Treating Transverse Motion with Synchrotron Oscillations in a Symplectic Manner - User's Reference Manual.* 1994. CERN/SL/94-56 (AP).
URL: http://sixtrack.web.cern.ch/SixTrack/doc/manual/six.pdf .

[Sch06] F. Schmidt. *MAD-X a worthy successor for MAD8?* Proceedings of ICAP04, St. Petersburg, Russia, 558(1):47 – 49, 2006.
URL: http://www.sciencedirect.com/science/article/pii/S0168900205020929 .

[Sch15] M. Schaumann. *Heavy-Ion Performance of the LHC and Future Colliders.* PhD thesis, RWTH Aachen, Germany, 2015.
URL: https://cds.cern.ch/record/2065692/files/CERN-THESIS-2015-195.pdf .

[Scr15] R. Scrivens. *Beam parameter from Linac3 to the PSB stopper.* CERN EDMS: 1570447, 2015.
URL: https://edms.cern.ch/document/1570447/1/TAB3 .

[Sie13] A. Siemko. Safeguarding the superconducting magnets, 2013.
URL: http://cerncourier.com/cws/article/cern/54383 .

[SSS10] S. Sarkar, H. Satz, and B. Sinha. *The Physics of the Quark-Gluon Plasma*, volume 785. Springer Verlag, Heidelberg, 2010.

[Tam14] C. Tambasco. An improved scattering routine for collimation tracking studies at LHC. Master's thesis, 2014. CERN-THESIS-2014-014.
URL: https://cds.cern.ch/record/1690529/files/CERN-THESIS-2014-014.pdf .

[Tin04] M. Tinkham. *Introduction to superconductivity*. Courier Corporation, 2 edition, 2004.

[TJ94] T. Trenkler and J.B. Jeanneret. *K2: A Software Package evaluating Collimation Systems in Circular Colliders (Manual)*. CERN SL Note, SL/Note 94-105 (AP), 1994.
URL: `https://cds.cern.ch/record/703539/files/CERN-SL-Note-94-105.pdf` .

[V+11] G. Valentino et al. *Semi-Automatic Beam-Based Alignment Algorithm for the LHC Collimation System*. Proceedings of IPAC 2011, San Sebastián, Spain, (THPZ034):3768–3770, 2011.
URL: `http://accelconf.web.cern.ch/accelconf/ipac2011/papers/thpz034.pdf` .

[V+15] G. Valentino et al. *Characterization of Embedded BPM Collimators*. CERN-ACC-Note-2015-0028, 2015.
URL: `https://cds.cern.ch/record/2054942/files/CERN-ACC-Note-2015-0028.pdf?` .

[Ver13] A. Verweij. *Quench limits: extrapolation of quench tests to 7.0 TeV*. Presentation at LHC Collimation Review, 30.05.2013, 2013.
URL: `https://indico.cern.ch/event/251588/other-view?view=standard` .

[Ver16] A. Verweij. *Private Communication*. 2016.

[W+08] T. Weiler et al. *Beam Cleaning and Beam Loss Control*. Proceedings of HB 2008, Nashville, Tennessee, USA, (WGD08):359–362, 2008.
URL: `https://accelconf.web.cern.ch/accelconf/HB2008/papers/wgd08.pdf` .

[Web12] LHC Collimation Group Website. *Tracking Code for Collimation Studies*. 2012.
URL: `http://lhc-collimation-project.web.cern.ch/lhc-collimation-project/code-tracking.htm` .

[Wen16] J. Wenninger. *Private Communication*. 2016.

[Wie99] H. Wiedemann. *Particle accelerator physics I: basic principles and linear beam dynamics*, volume 1. Springer Verlag, 1999.

[Wol14] A. Wolski. *Beam Dynamics in High Energy Particle Accelerators*. World Scientific, 2014.

[Z+05] C. Zamantzas et al. *The LHC Beam Loss Monitoring System's Real-Time Data Analysis Card.* Proceedings of DIPAC 2005, Lyon, France, (POW019):280–282, 2005.
URL: http://accelconf.web.cern.ch/AccelConf/d05/PAPERS/POW019.PDF .

List of Symbols

A	Nuclear mass number (number of nucleons in the nucleus).
A_0	Nuclear mass number of the reference particle.
A_m	Average nuclear mass number of the collimator material.
$\mathbf{A}$	Magnetic vector potential.
B	Magnetic field.
b	Impact parameter.
β	Relativistic β.
β_x/β_y	Horizontal/vertical betatron function.
$B\,\rho$	Magnetic rigidity.
c	Speed of light.
χ	Mass to charge ratio relative to the reference particle.
d_p	Projected penetration depth.
d	Distance traversed in the collimator material.
δ	Momentum per mass offset relative to reference particle.
$\bar{\delta}$	Dirac delta distribution.
$1+\delta_{\text{eff}}$	Rigidity offset with respect to the reference particle.
D_x	Horizontal periodic dispersion function.
$\tilde{D}_x$	Local horizontal dispersion function.
ϵ_N	Normalized transverse RMS emittance.
E	Particle energy.
E_s	Total stored beam energy.
η	Cleaning inefficiency.
η_{DS1}^{avg}	Maximum average cleaning inefficiency in the DS1 loss cluster.
η_{DS2}^{avg}	Maximum average cleaning inefficiency in the DS2 loss cluster.
η_{max}^{avg}	Maximum average cleaning inefficiency in all superconducting LHC magnets.
η^{int}	Integrated cleaning inefficiency.
η^{max}	Peak cleaning inefficiency.
g	Quadrupole gradient.

γ	Relativistic Lorentz factor.
h_x	Curvature of the reference trajectory.
$\mathcal{J}$	Jacobian matrix.
k	Quadrupole focusing strength.
$\mathcal{L}$	Instantaneous luminosity.
$\mathcal{L}^{\text{int}}$	Integrated luminosity.
$\mathcal{L}_{\text{NN}}$	Nucleon-nucleon luminosity.
m	Particle rest mass.
m_0	Rest mass of the reference particle.
n_B	Number of bunches per beam.
N_B	Number of ions per bunch (bunch intensity).
N_D	Normalized TCLD half gap.
N_P	Normalized primary collimator half gap.
N_S	Normalized secondary collimator half gap.
$\Delta N_{S,P}$	Retraction of the secondary collimators in σ.
P_0	Absolute value of the reference particle momentum vector.
P	Absolute value of the particle momentum vector.
$\mathbf{p}$	Canonical momentum.
q	Particle charge.
q_0	Charge of the reference particle.
$\mathbf{q}$	Canonical coordinate.
ρ_0	Ideal bending radius in a magnet.
ρ_m	Density of a material.
R_P	Radius of projectile nucleus.
R_T	Radius of target nucleus.
$\mathbf{S}$	Symplectic matrix.
s	Longitudinal parameter, distance from IP1.
τ	Beam lifetime.
τ_{DR}	LHC design minimum beam lifetime (12 min).
τ_L	Loss duration.

x	Horizontal coordinate.
X_0	Radiation length.
y	Vertical coordinate.
Z	Nuclear charge number (number of protons in the nucleus).
z	Longitudinal coordinate in straight coordinate system.
Z_0	Nuclear charge number of the reference particle.
Z_m	Nuclear charge number of the collimator material.

List of Acronyms

ADT	Transverse damper, can induce white noise excitation to provoque beam loss.
B1	LHC Beam 1, rotating in clockwise direction.
B1H	Horizontal plane of Beam 1.
B1V	Vertical plane of Beam 1.
B2	LHC Beam 2, rotating in counter-clockwise direction.
B2H	Horizontal plane of Beam 2.
B2V	Vertical plane of Beam 2.
BCT	Beam current transformator. Measures the beam intensity.
BFPP	Bound-free pair production.
BLM	Beam loss monitor.
BPM	Beam position monitor. Measures the transverse position of the beam.
CFC	Carbon fiber composite, material of primary and secondary collimators.
DS	Dispersion suppressor.
EMD	Electromagnetic dissociation.
EoS	End of Squeeze.
FEDB	FLUKA element database.
FLUKA	Fluktuierende Kaskade, simulation tool for particle-matter interaction.
FT	Flat Top.
ICOSIM	Ion Collimation Simulation.
IR	Insertion region.
IT180	Inermet 180.

LHC	Large Hadron Collider.
MAD-X	Methodical Accelerator Design, software to simulate beam dynamics.
MB	Bending dipole magnet.
MQ	Quadrupole magnet.
NF	Nuclear fragmentation.
PPD	Projected penetration depth.
RS	BLM running sum.
SPS	Super Proton Synchrotron.
STIER	SixTrack with Ion-Equivalent Rigidities.
TCLD	Target collimator long dispersion suppressor.
TCP	Target collimator primary (primary collimator).
TCSG	Target collimator secondary (secondary collimator).
TCT	Target collimator tertiary (tertiary collimator).
UFO	Unidentified falling object.

Acknowledgments

I would like to thank everyone who contributed to the success of my PhD project.

Many thanks to my university supervisor Prof. Dr. Johannes Wessels for giving me the possibility of accomplishing my Master and PhD thesis at CERN, while being part of his working group at the University of Münster.

Special thanks to my CERN supervisor Dr. Roderik Bruce. Thank you very much for the intelligent structuring of the thesis work and for the many interesting and inspiring discussions!

It was a great experience to be part of the LHC collimation team and I would like to thank the whole team for making my three years at CERN such a pleasure: Roderik Bruce, Maria Fiascaris, Hector Garcia Morales, Regina Kwee-Hinzmann, Aurelien Marsili, Alessio Mereghetti, Daniele Mirarchi, Elena Quaranta, Stefano Redaelli, Adriana Rossi, Roberto Rossi, Belen Salvachua, Alessia Valloni, Gianluca Valentino and Joschka Wagner. Many thanks to Dr. Stefano Redaelli for welcoming me in his team and for his constant support during my PhD time.

Thanks for constant support during my thesis work to John Jowett, Riccardo de Maria and Massimo Gionvannozzi.

My acknowledgments to the CERN FLUKA team for the help with the setup of the hiSixTrack-FLUKA coupling: F. Cerutti, A. Ferrari, A. Lechner, A. Mereghetti, P. G. Ortega, E. Skordis, V. Vlachoudis.

Many thanks to my office mates: D. Mirarchi, E. Quaranta, T. Mertens, M. Schaumann.

For proof-reading my thesis I would like to thank R. Bruce, B. Holzer, E. Sicking, A. Mereghetti and M. Breitenfeld.

But also outside of work some important people in my life contributed to this thesis, by giving me inspiration and by making my time outside work worthwhile. Most importantly, my wife Julia, with whom I shared all the happy and the hard times during the last three years. She was my haven of tranquility and graced my life with pleasure and ease.

I thank my family Stefanie, Wolfgang, Vanessa, Johanna, Maria and Litwina for everything they did for me.

For interesting coffee breaks and activities outside CERN, I would like to thank Robert Mertzig, Andy Langner and Martin Breitenfeld.

I would like to thank Sam Ringle for our stimulating friendship and his constant presence in my life for over two decades. I am also very grateful to Alex Senzig, not only for his musical contributions, but also for his loyal friendship which enriched my life for many years now.

Last but not least I would like to thank Andy, Robert, Martin, Eva Dietz, Eva Sicking, Vanessa, Georg, Desi, Gabriele, Werner and many more.

Lebenslauf

Name	Pascal Dominik Hermes
Geburtsdatum	30.04.1987
Geburtsort	Saarlouis
Staatsangehörigkeit	Deutsch
Eltern	Stefanie Hermes, geb. Peifer
	Wolfgang Hermes

Schulausbildung

08/1993 - 06/1997	Grundschule Saarlouis Steinrausch
08/1998 - 07/2003	Integrierte Gesamtschule Dillingen/Saar
08/2003 - 07/2006	Technisch Wissenschaftliches Gymnasium Dillingen/Saar
07/2006	Allgemeine Hochschulreife

Studium

04/2007 - 09/2007	**Studium der Humanmedizin**
	Westfälische Wilhelms-Universität Münster
10/2007 - 03/2011	**Studium der Physik**
	Westfälische Wilhelms-Universität Münster
09/2009 - 08/2010	**Studium der Physik - ERASMUS**
	Université Paris Sud XI, Orsay, Frankreich
05/2010 - 08/2010	**Bachelorarbeit in Physik**
	"Conception de l'Injecteur et
	des Diagnostics du Faisceau pour le Projet SuperB"
	Laboratoire de l'Accélérateur Linéaire, Orsay, Frankreich
03/2011	**Bachelor of Science**
	Westfälische Wilhelms-Universität Münster

03/2011 - 07/2013	**Studium der Physik**
	Westfälische Wilhelms-Universität Münster
04/2012 - 04/2013	**Masterarbeit in Physik**
	"Development of high β^* optics for ALICE"
	Westfälische Wilhelms-Universität Münster
	Europäische Organisation für Kernforschung, Genf, Schweiz
07/2013	**Master of Science**
	Westfälische Wilhelms-Universität Münster

Promotionsstudium

10/2013	**Beginn der Dissertation**
	Institut für Kernphsyik, Westfälische Wilhelms-Universität Münster
	Europäische Organisation für Kernforschung, Genf, Schweiz
	Betreut von Prof. Dr. Johannes P. Wessels und Dr. Roderik Bruce